論文 / 著書情報
Article / Book Information

題目(和文)	多相交流アークを用いたインフライト溶融によるガラス製造
Title(English)	Investigation of In-Flight Melting of Glass Raw Materials by Multi-Phase AC Arc
著者(和文)	LiuYaping
Author(English)	Yaping Liu
出典(和文)	学位:博士(工学), 学位授与機関:東京工業大学, 報告番号:甲第9529号, 授与年月日:2014年3月26日, 学位の種別:課程博士, 審査員:渡邉　隆行,馬場　俊秀,関　宏也,田巻　孝敬,奥野　喜裕
Citation(English)	Degree:Doctor (Engineering), Conferring organization: Tokyo Institute of Technology, Report number:甲第9529号, Conferred date:2014/3/26, Degree Type:Course doctor, Examiner:,,,,
学位種別(和文)	博士論文
Type(English)	Doctoral Thesis

Investigation of In-Flight Melting of Glass Raw Materials by Multi-Phase AC Arc

Tokyo Institute of Technology

Yaping Liu

2014

Contents

1. Introduction

The innovative in-flight melting technology was developed to melt granulated glass raw materials with energy saving and environmental benefits. A stable 12-phase alternating current (AC) arc plasma has been successfully applied to melt granulated glass powders in this dissertation. The discharge characteristics of multi-phase AC arc and its effect on the in-flight melting of glass particles were investigated.

The research direction of material processing by thermal plasmas, and the glass melting technology using thermal plasmas, are introduced to indicate the necessity of this work in this chapter.

1.1 Thermal Plasmas

1.1.1 Definition of the Plasma State

The term “plasma” was first introduced by Irving Langmuir (1881-1957) in 1923 to describe the jellylike behavior of those regions of an electrical discharge capable of showing a certain periodic variation or movement of the free electrons. It was not until the early 50th however, that the concept of a plasma as a distinct state of a gas was fully appreciate. Now the term plasma is often referred to as the fourth state of matter. As the temperature increases, molecules become more energetic and the state of the matter transforms in the sequence: solid, liquid, gas and plasma. In the last stages, molecules in the gas dissociate to form a gas of atoms and then a gas of freely moving charged particles, electrons and positive ions. This state is

called the plasma state.

In contrast to an ordinary gas, plasmas are electrically conducting due to the presence of free charge carriers. Plasma is characterized by a mixture of electrons (e), ions (i), and neutral gas atoms/molecules (g) moving in random directions that on the average is electrically neutral ($n_e \cong n_i$). Plasma in not only the most energetic state of matter, but also the most challenging for scientists. The temperature of the charged particles in plasma can be so high that their collisions can result in thermonuclear reactions. It is estimated that more than 99% of the matter in the universe exists in the plasma state. Plasmas occur naturally, such as auroras and lightning, but also can be man-made. Plasma generation and stabilization in the laboratory and in industrial devices is not easy, but very promising for many modern applications, including thermonuclear synthesis, electronics, lasers, and many others.

Plasmas offer two main characteristics for practical applications. First, they can have temperatures and energy densities higher than those produced by ordinary chemical methods. Second, plasmas are able to produce, even at low temperatures, energetic species that can initiate chemical reactions which are difficult or impossible to obtain using ordinary chemical mechanisms. The energetic species generated cover a wide spectrum of species, for example, charged particles including electrons, ions, and radicals, highly reactive neutral species such as reactive atoms (e.g., O, F, etc.), reactive molecular fragments, photons of different wavelength, and excited atomic states.

Pressure has a strong influence on plasma, affecting its respective luminosity, energy, or temperature and its components of the plasma state. Since plasmas occur over a wide range of pressures, it is customary to classify them in terms of electron temperatures (T_e) and electron number densities (n_e). The electron temperature is expressed in electron volt (eV); one electron volt is equal to approximately 11,600 K. Man-made plasma range from slightly above room

temperatures comparable to the interior of stars. Electron densities span over 15 orders of magnitudes. However, most plasmas of practical significance have electron temperatures of 1-20 eV with electron densities in the range 10^6-10^{18} cm^{-3}. Not all particles need to be ionized to become plasma; a common condition is for the gases to be partially ionized. Under the latter conditions one must examine the particle densities to determine if it is plasma.

The local thermodynamic equilibrium (LTE) is a state in which all species of particles in plasma (neutral atoms, molecules, ions, electrons) from the volume are considered at the same volume corresponds to the same temperature T ($T_i \simeq T_e \simeq T_g$). In the case of LTE, there are valid the following relations: Maxwell distribution, Boltzmann distribution and the Saha's ionization equation. When the LTE conditions are met, the plasma is termed thermal plasma. Conversely, when different constituents of the plasma have different energy levels, the plasma is termed a nonequilibrium plasma or nonthermal plasma. In this case, the electrons have the highest, the ions a significantly lesser, and neutral gas species the least energy ($T_e > T_i > T_g$). Physics, engineering aspects, and application areas are quite different for thermal and nonthermal plasmas. Thermal plasmas are usually more powerful, while nonthermal plasmas are more selective. However, these two very different types of ionized gases have much more features in common and both are plasmas.

1.1.2 Generation of Thermal Plasmas

Artificial plasma is formed by electric charges passing through gas. There are two types of discharges commonly used for the generation of thermal plasmas: the electric arc discharge (direct current and alternating current), and the high frequency (radio frequency) induction discharge. Thermal plasmas generated by electric arcs are normally produced in devices called plasma torches. In the electric arc discharge, the plasma generating current flows from one

electrode to the other through the plasma. The electrodes are in intimate contact with the plasma and experience the highest heat fluxes. The size of the plasma column is determined by the balance of electric power dissipation with heat loss by conduction, radiation and convection. For the same power input, a plasma gas with high thermal conductivity or with high radiative power loss values will have a smaller cross section, therefore higher energy densities. Energy densities increase for the following gases in the order in which they are listed: argon, nitrogen, helium, hydrogen.

(a) DC Arc Plasmas

DC arc plasma torches are usually divided in two categories (Fig. 1.1): transferred and non-transferred. In transferred plasma torches the electric arc strikes between an electrode of the torch and a metal (or other material) bath (at the beginning of the operation the metal is normally solid, melting during operation) located inside the vessel. The electrode can be a metal, such as thoriated tungsten or a graphite rod (which would have a central hole for the passage of gas). The gas is injected in the plasma torch and heated by the electric arc established between the inside electrode and the metal pool. These devices are normally employed in metallurgical processes or for treatment of some solid residues (such as ashes).

In non-transferred plasma torches the electric arc strikes between two electrodes inside the torch. The electrodes can be made of different metals (or even oxides) and geometries. The arc is generated with the injection of plasma-forming gas (Ar, N_2 and O_2 et al.) between a rod-type cathode and a nozzle-type anode, which has to be cooled sufficiently with water to avoid the melting problem on the anode surface. The thermal plasma is obtained when passing a gas inside the torch. The gas will be heated by the electric arc, forming a plasma jet at the exit of the torch. This type of plasma torch is usually employed in powder spraying and for the

treatment of liquid residues (or solid fines).

The transferred plasma torch has higher energy efficiency than the non-transferred type, since almost all the heat is directed transferred to the material to be treated.

(b) Multi-Phase AC Arc Plasma

In AC plasma type of generator, the gas is heated by the energy of alternating current of industrial frequency. Sine waves are by far one of the most important types of AC waveform used in electrical engineering. An AC waveform is constantly changing its polarity every half cycle alternating between a positive maximum value and a negative maximum value respectively with regards to time. This means that the AC waveform is a “time-dependent signal” with the most common type of time-dependent signal being that of the periodic waveform. The most widely used method of igniting the AC electrical arc is by shortening the gap between the electrodes by a gas-discharge channel formed as a result of supplying to the electrodes a high voltage pulse with high-frequency from an oscillator. The single-phase and the three-phase AC power supply have already been proposed for the fields in welding and cutting of metals, steelmaking, synthesis of nanoparticles and spheroidization of particles (Gold et al. 1981).

Three-phase AC system is readily available and it is almost universally used to distribute electrical power. A multi-phase system with more than three-phase AC can be supplied by connecting more than one set of three-phase systems. Techniques for processing industrial waste by arc plasma which generates among six carbon electrodes using a 6-phase AC current power supply and its applications were described (Matsuura et al. 1994a; Matsuura et al. 1997). It seems as if this system was driven by the DC power supply instead of actual commercial AC power supply (60 Hz) because the continuing smoothly discharge action. To obtain a more effective arc plasma generator by expanding its volume, a 12-phase AC power supply was

developed (Matsuura et al. 1994b). Figure 1.2 shows the electrical circuit diagram and schematic connection diagram for generating of 12-phase AC arc. The most important advantage of this system is that there are large numbers of discharging paths among electrodes in comparison with the case of the single-phase and three-phase AC systems. This 12-phase AC discharge for synthesis of carbon nanotubes (CNTs) was proposed (Matsuura et al. 2007). The optimum temperature for CNTs synthesis was approximately in the range from 1000 to 1250 °C. The multi-walled CNTs of 20~40 nm in diameter were produced.

(c) RF Thermal Plasmas

The schematic of the RF thermal plasmas is shown in Fig. 1.3. An inductively-coupled torch usually consists of a cylindrical tube with a few centimeters in diameter, surrounded by an RF coil (2~5 turns). High frequency electric current passes through the coil where the resulting high frequency magnetic field is induced along the axis of the discharge tube. A separate coaxial cooling flow is often provided within the tube to avoid excessive heating of the quartz. The torches can be operated at RF powers ranging from 1 kW to 15 kW and gas flow (inside the tube) from 1 to 30 L/min. The high frequencies (RF) of about 0.1~100 MHz is usually required. Powerful RF discharges and power supplies generate noises and interfere with radio communication systems. To avoid this undesirable effect, most RF sources use the 13.56 MHz (corresponding wavelength is 22 m) industrial standard frequency. High temperature region of RF plasma can be effectively used in heating up the solid precursors if they are injected along the centerline of the torch. The absence of an electrode is also advantageous for the synthesis of high purity materials. Compared with a non-transferred DC plasma torch, the competitive advantage of a RF plasma torch is not only its high enthalpy available along the centerline but also relatively long residence time of axially injected precursors.

1.1.3 Thermal Plasma Processing of Materials

Thermal plasmas are used in industrial processes because of: a) high temperatures reached in the plasma jets; b) high energy densities of the plasmas; c) possibility of using different plasma gases depending on the application desired. Thermal plasmas with temperatures of around 10,000 K and more are particularly suitable for material processing, e.g. for coating, melting, cutting, welding, spheroidizing of powder particles, and synthesizing of materials including production of nano-particles. They are also of increased interest in waste destruction or material synthesis. Thermal plasma processes work at atmospheric pressure and use electric power originating from DC, AC, or RF sources.

(a) Plasma Coating

Plasma spraying is part of thermal spraying that is a method in which a metal or ceramic powder is injected into hot gas plasma, the particles in flight melted to molten droplets and then projected at high velocity onto a substrate to form coatings (Pawlowski 1995; Fauchais et al. 2001). More than 97% of plasma spraying in manufactures is performed with DC plasma torches, the rest being carried out with RF inductively coupled discharges. The first industrial plasma spray torches (DC arcs) appeared in the 1960s, but only about a decade later soft vacuum plasma spraying was introduced in industry (Pawlowski 1995). In the 1980s, process robotization was started, together with the development of RF plasma torches for spraying (Jurewicz et al. 1985; Boulos and Jurewicz 1989). The 1990s were mainly devoted to the implementation of robust sensors able to work in the harsh environment of spray booths and new torches (Fauchais 2004). This decade has also seen the development of new plasma torches such as DC torches using axial injection (Hawthorne et al 1997; Moreau et al. 1995), rotating

mini-torches to spray within cylinders (Nicoll 1994), Triplex torches with three cathodes and a segmented anode (Zierhut et al. 1998), and supersonic RF torches (Mailhot et al. 1997).

A major advantage of thermal spray processes is the extremely wide variety of materials that can be used to produce coatings (Tucker 1994). The particles or droplet are accelerated in the range of 50 to >1000 m/s. The high particle temperature and speeds achieved result in significant droplet deformation on impact at a surface, producing thin layers or lamellae, often called “splats,” that conform and adhere to the substrate surface. Solidified droplets build up rapidly, particle by particle, to form continuous rapidly solidified layers. This process includes complex multiphase flow with disperse particles, heat transfer, and conversion of thermal to kinetic energy. Individual splats are generally thin (~1 to 20 μm), and each droplet cools at very high rates (>10^6 K/s for metals) to form uniform, very fine-grained coatings or deposits. Sprayed deposits usually contain some level of porosity, typically between 0 and ~10%, some unmelted or partially melted particles, fully melted and deformed “splats”, metastable phases and oxidation from entrained air. Over the past five decades, researches have allowed a much better understanding of interactions between particles and plasma and the development of simplified sensors in booths. However, studies about the formation of splats and their layering, i.e. coating formation, are still in their infancy and much is still to be done.

Plasma spraying of micrometer-sized powder is a well-established process (American Society for Metal 1982; Pawlowski 1995). Using nano sized powder as feedstock to generate nanostructured coatings presents new challenges as well as new opportunities (Shaw et al. 2000). Due to the low mass and the resultant instability to be carried in a moving gas stream, the individual nanoparticles cannot be thermal sprayed and deposited on a substrate. To overcome this problem, a reconstitution of individual nanoparticles into spherical micro-sized granules is necessary. The second difficulty is to retain grain sized at the nanometer regime in the coating

(Shaw et al. 2000). Plasma sprayed nanostructured TiO_2-Al composite coatings (Chwa et al. 2005), Al_2O_3-TiO_2 coatings (Shaw et al. 2000), zirconia coatings (Liang and Ding 2005) and Ti-Ru-Fe-O coatings (Irissou et al. 2002) were prepared. The interfacial microstructure, toughness and failute modes of the plasma sprayed nano coatings were characterized in the case of Al_2O_3-13wt% TiO_2 (Bansal et al. 2003). The plasma sprayed nanostructured zirconia coatings reported possess a higher wear resistance than their conventional counter parts. The higher wear resistance of the nanostructured coatings is attributed to their optimized microstructure and improved micro-hardness (Ding et al. 2003). The superior properties of plasma sprayed nanostructured alumina-titania coatings (Jordan et al. 2001), WC-Co coatings (Kim et al. 2006), and Al_2O_2-3wt% TiO_2 coatings (Lin et al. 2004) were reported as compared to their conventional counter parts. If properly deposited, nanostructured ceramic coatings could provide improved properties for variety of applications, including wear resistant and thermal barrier coatings.

(b) Plasma Spheroidization and Densification

Spheroidized particles provide a more homogeneous and stable flow while feeding. This allows feeds to run at faster or slower rates without clogging problem in industrial processes. Such products, characterized by an irregular shape and a strong tendency to agglomerate were classified (Geldart 1973). For this reason, densification of such agglomerated particles is necessary. Plasma processing is the most versatile technique for spheroidization of metal and ceramic powder particles and it is actually simple with respect to other plasma processes. It takes place in thermal plasmas, either DC or RF plasma torches, by means of in-flight heating and melting of feed material while passing through the discharge in the form of irregularly shaped or crushed powders. Equipment similar to that used for plasma spraying but the particle

size may be substantially (>100 mm) larger than that used for plasma spraying. Molten spherical droplets formed in this way are gradually cooled down under free-fall conditions. Porosity is also removed when the material is melted, resulting into better material to use in powder metallurgy applications and denser coatings. The particles' time of flight must be sufficient for complete solidification before reaching the bottom of reactor chamber. Finer particles are entrained by plasma gases and recovered in a filter. Different atmospheric pressure thermal plasmas are applied for the treatment of powders. A number of studies have been reported on the effects of plasma parameters on the spheroidizing proportion, heat-transfer mechanism and moving history of particles involved in the process (Ye et al. 2004; Shanmugavelayutham and Selvarajan 2004; Boulos 1991; Jordan 1971). In particular, effective powder densification and spheroidization have been demonstrated in atmospheric pressure RF-ICP discharge by Tekna Plasma System Inc. Their technique has the ability to melt relative large particles and operates with a wide range of gases. Thermal plasma treatment of powders results not only in their spheroidization and densification but also in physical and chemical transformations.

(c) Nanoparticle Synthesis

Thermal plasmas offer the advantages of very high temperatures and steep temperature gradients are attractive methods for the synthesis of fine powders down to the nanometer size range (Taylor and Pirzada 1994; Boulos 1991). The supersaturation of vapor species, which provides the driving force for particle condensation, can be very large in thermal plasmas, leading to the production of ultrafine particles by homogeneous nucleation (Pfender 1998). These synthesis processes are usually taken by means of DC arcs or RF discharges.

One of the most effective methods for nanoparticle preparation with thermal plasmas is hydrogen plasma-metal reaction (HPMR) method, which is developed by Ohno and Uda (1984,

1989). Dissociated hydrogen atom in the arc plasmas dissolves into molten metal and enhances the vaporization of metal elements when hydrogen atoms are emitted from the molten metal. Various kind of metal nanoparticles (Ag, Al, Co, Cr, Cu, Fe, Mn, Mo, Ni, Pd, Sc, Si, Ta, Ti, V, and W) were prepared by the HPMR method and the vaporization phenomena from molten metal were investigated (Ohno and Uda 1984, 1989; Ohno 1992). Metal nanoparticles of Mg, Ni, Co, Cu, and Fe were prepared by the HPMR method with 50%-H_2 for the application of the hydrogen storage material (Shao et al. 2004; Shao et al. 2008). These nanoparticles had a granular structure and the particle size ranges from several nanometers to tens of nanometers. In the case of Mg, contrastingly, the average particle size was about 300 nm. The difference of particle sizes between Mg and the other metals was explained by the difference of the vaporization rates. The vaporization rate of Mg was much higher than that of the other metals resulting in the higher metal-vapor concentration in the growth region. Novel carbon materials with nanometer dimensions, such as fullerences and nanotubes, have been synthesized using the DC arc discharge between the carbon electrodes. When metals were evaporated together with carbon, the nanoparticles of the metal carbide and/or the carbon-coated metal as well as carbon nanotubes were obtained (Brunsman et al. 1994; Saito et al. 1997a; Saito et al. 1997b; Ando et al. 2000; Ryu et al. 2009).

In the case of RF plasma, the plasma is inductively heated by RF electrical power of some tens of kW and a frequency of MHz order, the diameter is 30-50 mm, so the plasma volume is relatively large. The axial plasma velocity is as low as 10 m/s and the residence time in the high-temperature plasma frame is as long as some tens of milliseconds, which is long enough for chemical reactions to proceed. Since RF torch needs no electrode for sustaining plasma, it has been widely adopted to prepare nanoparticles of metal alloy and intermetallic compounds, oxide, nitride. Titanium dioxide (TiO_2) nanoparticles are continuously receiving

attention for use as photocatalysts, photonic crystals, photovoltaic cells, and gas sensors and have been prepared using RF thermal plasma (Li and Ishigaki 2004; Li et al. 2006; Ishigaki and Li 2007; Ishigaki 2008). A pulse modulated induction thermal plasmas (PMITP) system and an arbitrary waveform-modulated induction thermal plasma (AMITP) system have been developed. The PMITP system can modulate the coil current sustaining the induction thermal plasma into a rectangular waveform. Such a millisecond modulation can perturb the thermal plasma markedly. It can then change the temperature and radical densities as well as the gas flow field in the thermal plasma in time domain (Tanaka et al. 2009).

Further investigations of the nanoparticle growth mechanism by RF thermal plasma were conducted to clarify the effects of several cooling methods on the formation mechanisms of nanoparticles (Shigeta and Watanabe 2008a), because it has been reported that the nanoparticles formation is dramatically promoted by the forced cooling of the plasma flow with cold rings (Watanabe and Okumiya 2004), radial gas injection (Bilodeau and Proulx 1996; Desilets et al. 1997; Shigeta et al. 2004), and counterflows (Kong and Lau 1990; Shigeta and Watanabe 2008b).

(d) Plasma Waste Destruction

Incineration has been increasingly used for reduction of the waste. However, the problems are high off-gas flow rates and the consequent high cost of off-gas clean-up, as well as the production of residues containing hazardous materials. The principle advantages that plasma offers to treatment processes are high energy densities, high temperatures, and use of electricity as the energy source. In general, non-transferred arc processes are preferred for treatment of liquids and gases, because of the more uniform temperature and the availability of reactive species. RF plasmas and even microwave plasmas have also been shown to be commercially

viable in small-scale applications.

The pioneering plasma waste treatment process was the Pyroplasma process developed by Westinghouse in the early 1980s (Barton and Mordy 1984; Joseph and Barton 1987; Heberlein 1989). Destruction of PCBs to the 99.999999% level was demonstrated for 850 kW torch power and 4-12 L/min input flow. The system is no longer in operation. The PLASCON process, developed by CSIRO and SRL Plasma Ltd in Australia in the 1990s, uses a DC plasma torch with a tungsten cathode and can be up to 150 kW. The process can destroy a wide range of liquids and gases. Ten plants are currently operating in Australia, Japan, USA and Mexico, destroying halons and CFCs, hydrofluorocarbons (HFCs), PCBs, insecticides and the waste liquid from herbicide manufacture. Typical feed rates are about 100 kg/h for halons and CFCs, with destruction level to 99.9999%. The PLASCON process has benn well characterized by thermodynamic, chemical kinetic and fluid dynamic modeling studies, particularly its application to halons and CFCs (Watanabe and Shimbara 2003; Murphy and McAllister 1998, 2001; Deam et al. 1995;). A microwave plasma technology was developed by Mitsubishi Heavy Industries Ltd and launched in 2000. In this case, a thermal plasma is generated by 2.45 GHz microwaves in a coaxial cavity. The plasma operates on a small-scale with feed rates of about 2 kg/h and power level of 2 kW to destruct mixture of CFCs or HCFCs with steam. Tokyo Institute of Technology have developed a DC plasma torch running on steam (Watanabe and Shimbara 2003; Watanabe et al. 2005). This process has now been scaled up, in cooperation with Kyronenprorede Co. Ltd, into a mobile system, initially for treatment of PCBs and asbestos. Electrical power of 180 kW will be used to generate the plasma, and estimated treatment rates are 200 l/h for PCB and 0.5 m^3/h for asbestos.

1.1.4 Plasma and Particle Measurements in Thermal Spray

Growing demands on the quality of thermally sprayed coatings requires reliable methods to monitor and optimize the spraying processes. Thus, the importance of diagnostic methods is increasing. A critical requirement of diagnostics methods in thermal spray is the accurate measurement of temperatures. This refers to the hot working gases as well as to the in-flight temperature of the particles. Thermal plasma temperature is a key parameter in the study of intrinsic properties as well as in the control and optimization of industrial processes. The in-fight measurement of particle parameters provides information, which is useful in the optimization of the coating process.

(a) Plasma Temperature Measurement

The techniques used for plasma temperature measurement are mainly enthalpy probe, optical emission spectroscopy, laser scattering, and recently developed computer tomography.

Enthalpy probes were developed in the 1960s and their applicability has been approved in many cases (Fincke et al. 1993a; Rahmane et al. 1995). The enthalpy probe is a water-jacketed gas sampling and stagnation probe for studying the enthalpy, temperature, and velocity of hot and plasma gas flow field. The probe itself consists of double-walled tubing usually made of stainless steel, which is cooled by a high pressure water circuit. Furthermore, the measured gas can be sampled to analyze its composition by integrating a mass spectrometer. Examples are the investigation of the impact of the ambient atmosphere on the characteristics of the plasma jet (Capetti and Pfender 1989).

The optical emission spectrum (OES) of plasma is a common technology for the investigation of plasmas, because it does not interact with the plasma (Gherardi et al. 2000; Gheradi and Massines 2000; Popa 1996; Griem 1964; Lochte-Holtgreven 1968). The set-up at the experiment is very simple, only diagnostic ports are necessary which provide a line-of-sight

through the plasma. In OES, the spectrum of the radiation emitted by the plasma is sliced and its intensity measured as function of the wavelength. The most widely used spectroscopic method for the determination of T is the Boltzmann plot method which employs the ratio of integrated line intensities for two or more atomic lines.

(b) In-Flight Particle Temperature Measurement

Measurements on in-flight particles can be categorized as single particle technique where each particle is observed “one at a time” and ensemble techniques, where the sensor observed a plume of particles simultaneously. The former techniques require a limited measurement volume to avoid interferences from other nearby particles. In contrast, in ensemble measurements the information is linked to a large number of particles and the techniques can be used with heavily loaded jets. However, the measurements can only be performed where the particle radiation is not hindered by that of plasma; i.e., in the plasma plume or close to it.

Most of the systems are based on CCD cameras or linear arrays of photodiodes and/or fast pyrometers in the plasma plume. Thus, sensors are based on the detection of thermal radiation emitted by the surface of hot particles. A two-color technique described for measuring the temperature of burning droplets of liquid fuel as early as 1958 (Gurevich and Shetinberg 1958). Later, It was reported that the first application of an absolute radiance technique to the measurement of single-particle temperature in a plasma torch. The sample volume consisted of a chord through the flow field, defined by the back projection of the optical systems limiting aperture through the imaging light collection optics (Kruszewska and Lesinski 1977). The methods based on two-color pyrometry, were further developed between 1987 and 1991 (Vardelle et al. 1980, 1986; Moreau et al. 1990; Mishin et al. 1985, 1987). To overcome the large depth of the field of view of the lenses used, a coincidence technique allows us to limit the

length of the measuring volume to about 200 μm for the same diameter (Vardelle et al. 1983). Single particle temperature measurement was integrated with laser scattering for the simultaneous measurement of particle size and temperature (Fincke et al. 1988). This same idea was extended to the simultaneous measurement of particle size, velocity and temperature by integration with laser Doppler velocimetry and laser scattering (Fincke et al. 1990; Fincke et al. 1993b). When a laser Doppler velocimetry (LDV) is incorporated, the crossing of the LDV laser beams defines the measurement volume. The integration with laser scattering, or with laser Doppler velocimetry, has the advantage that relatively cold particles, or very small particles, produce a signal from the laser illumination even though they may not have sufficient intrinsic radiance to be detected by the temperature measurement channels.

The ensemble measurement technique has been applied to the thermal spray process since at least 1973 (Jantzsche 1973) then periodically rediscovered (Xu et al. 1988; Kuroda et al. 1989). A two-color pyrometer was designed for ensemble measurements (measuring volume 5 mm in diameter and 500 mm in length) (Swank et al. 1995), has been successfully incorporated into a closed-loop controller for the plasma spray process (Fincke et al. 1995a, b). It was later commercialized as the in-flight particle pyrometer (IPP) (Fincke et al. 2001). Similarly Stratonics Co has proposed an imaging pyrometer using a CCD camera (Craig et al. 2000), similar to the Spray Watch of Oseir (Vattulainen et al. 2001), using a custom double dichromic mirror to achieve the spectral resolving capability. Finally, the DPV-2000 (Moreau et al. 1990) has been widely used in thermal spray research. In this technique, the depth of field of the instrument optics and the limiting aperture generally define the measurement volume. The Accuraspray (Bisson et al. 2001) of Tecknar are also equipped with two-color pyrometers. Of course, many factors can perturb temperatures, as analyzed by Hollis and Neiser (1998). At last it must be underlined that all pyrometers must be very regularly calibrated (Mates et al. 2002).

(c) In-Flight Particle Velocity Measurement

According to the particle velocity range, their residence time in the measurement volume is rather short (in the 1-10 μs range). Thus, this technique requires the use of relatively high speed detectors and electronics with bandwidths of the order of 0.1-1 MHz. During the seventies and eighties, several methods based on laser doppler anemometry (Doppler effect or time-of-flight between two laser spots) were developed (Fauchais et al. 1989, 1992; Vardelle et al. 1995). These methods allowed measuring velocities in the bright core of a plasma jet, especially, with the time-of-flight method, for velocities higher than 500 m/s in high power (≈100 kW) soft vacuum plasma spraying. However, they were not applicable to a dense stream of particles, as in spray conditions, and the complexity of alignment of optical components was not adapted to spray booths. A phase doppler anemometry (PDA) was developed which also giving the particle diameter (Fincke et al. 1990; Swank et al. 1995). For high velocities (over 400 m/s with particle sizes as low as 3 μm in diameter) a laser two focus points (2-F) is used, the separation of the two focus points being adjusted to the particle velocity (Kowalsky et al. 1991). The advantages and drawbacks of PDA and 2-F are discussed in (Smith et al. 1995).

The time of flight method, using pyrometers as detectors in the plasma plume, developed first by Boulos et al. (Sakuta and Boulos 1987, 1988a, b) for RF plasmas has been adapted to DC plasma jets (Moreau et al. 1990) and then to industrial sensors such as DPV-2000 (Moreau et al. 1994, 1995). When hot particles in the plasma jet or in combustion flame passed near the focal plane of the set-up, two slits in the sensing head generated a well-separated bi-peak pulse. Knowing the time between both pulse, and the distance between slots, the velocity was calculated, the waveforms of the thermal radiation signals being important for the measurement precision (Li et al. 2003), which is generally better than 5%. A new device called Accuraspray

has been developed (Bisson et al. 2001; Marple et al. 2001) by Tecknar that, contrary to DPV-2000, provides ensemble average data corresponding to a measurement volume 3 mm in diameter and 25 mm in length.

A new method, the particle-shape-imaging has recently been presented. It measures the size, shape and velocity of particles through a laser-assisted shadow-image technique (Landes et al. 2002). Finally, velocity and concentration of hot particles are measured by CCD cameras (Vattulainen et al. 2001; Bertrand et al. 2002). The velocity is deduced from traces of particles obtained with a given exposure time (from 1μs to tens μs). With the commercial set-up Spray Watch (Vattulainen et al. 2001), used in spray booths, a recent development allows us to capture cold and/or hot and fast particles with the help of a laser illuminating the particles and whose pulse length is between 0.1 and 1.5 μs (Largo et al. 2003).

(d) In-Flight Particle Size Measurement

Particle size can also be estimated from the measurement of the absolute radiance emitted by a particle once the temperature is obtained. Simultaneous measurement of particle size, velocity, and temperature of combusting coal particles was demonstrated (Tichenor et al. 1984). This technique used an image plane coded aperture to obtain particle size, a transit timing technique to determine velocity, and two-color pyrometry to determine temperature. It was demonstrated at temperatures up to 1660 K on 100 to 500 μm coal particles at flow velocities of less than 10 m/s. The difficulty is that it is necessary to assume spherical particles and know precisely the emissivity of hot particles (that is the most critical point) at the temperature measured with the two-color pyrometer. Moreover, all particles are not necessarily detected by the system, especially the smallest one. Thus, the precision of this measurement is relatively poor (at the best 30 %). That is why such measurements must be calibrated, for

example by collecting particles in water or in oil. Such calibration is especially important with wire arc spray, where the size distribution of droplets is unknown compared to other spray processes (Planche et al. 2004). DPV-2000 measurements were achieved at the same locations into the jet as those previously chosen for the capture of the particles. In this way, the calibration of the diameter parameter by the DPV-2000 could be made. Of course, diameter measurements are not possible with ensemble measurements.

1.2 Glass Melting Technology

The process of manufacturing quality glass is comprised of six basic steps: (1) raw material selection, (2) batch preparation (i.e. weighing and mixing raw materials), (3) melting and refining, (4) conditioning, (5) forming, and (6) post-processing (i.e. annealing, tempering, polishing or coating). The technologies employed in each step depend on the product manufactured. After melting of the batch material is completed, the temperature of the furnace is typically increased to lower the melt viscosity and activate refining agents to remove bubbles from the melt (refining), and subsequently lowered to condition the glass for forming. The melting and refining of glass in furnaces is the most energy-intensive process step in glass production. Since thermal plasma is a powerful tool for rapid production of materials and to solve a range of environmental problems, the introduction of new technologies by using thermal plasma in glass industry was proposed.

1.2.1 Conventional Glass Melting Technology

Common heating methods are combustion-heating (oxy-fuel, air-fuel burners) and direct electrical heating (Joule heating), as well as combinations of both (electric boosting). The design of the ancient 1867 Siemens furnace has evolved steadily over some 140 years to meet

basic financial or technological risk. The raw materials are melted and held at 1500°C~1600°C for a prolonged time in the high temperature melting zone of the furnace to remove bubbles and to make the melts uniform. The residence time is estimated to be about 7 days for LCD (liquid Crystal Display) panel glass and to be about 1.5 days for bottle glass. The energy for glass production is roughly allocated into 20% for melting, 60% for heat loss caused by exhaust gas and 20% for radiation loss from the furnace wall. Many ideas have been applied to improve efficiency on the Siemens type furnaces and the efficiency values have been increased step by step (Dantsis et al. 1980; Bondarev et al. 1977; Dzyuze 2004; Shamp et al. 1995; Kuzyak 1960).

1.2.2 Alternative Glass Melting by Thermal Plasmas

A number of glass melting technologies that have been developed and tested both melting and refining by non-conventional methods during the second half of the 20th century as glassmakers have sought to solve critical industry problems. The Submerged Combustion Melting (SCM) is based on enhancing heat transfer by mixing the fuels and oxidant with the raw materials (Dolf and Marceau 1966). From 1984 to 1990, the Advanced Glass Melter (AGM) was developed to drastically improve the heating efficiency by introducing a glass batch directly into an oxygen gas or air stream to be melted within the burner flame (Tiwary et al. 1988). In addition to the typical non-Siemens type glass melters of SCM and AGM, plasma arc using in the electrical melters have also been researched in the past.

(a) Glass Plasma Melter

The British Glass Industry explored the plasma melter to compare the efficiencies of electrical plasma-arc and submerged electrode melting of soda-lime-silica glass in 1994. Three non-transferred DC arc plasma torches (120° angle between electrodes projected on horizontal

plane) are immersed in a batch pile contained in a ceramic container (Ross and Tincher 2004). Each torch generates a small low power DC plasma arc. To each torch is connected one of the three phases of a triple phase AC supply. The electric current will partly pass through the melt and will heat the melt by the Joule principle. The project successful demonstrated high melting efficiency. Some barriers to further development have been materials for construction, insufficient funding, scale-up to commercial production, limited glass composition, and high net cost. British Glass efforts ended without any commercial applications. However, in small tonnage, specialized applications that require intermittent production or rapid product changes, plasma technology would provide a flexible melting system (Dalton and Langton 1994).

(b) Arc Plasma Melter

Johns-Manville Corporation (JM) actively investigated glass melting using arc plasmas to melt E-glass batch as well as E-glass and insulation scrap glass. (Williams et al. 1991; Cusick et al. 1996). The schematic of arc plasma melter is shown in Fig. 1.4. They demonstrated discontinuous fibrous glass applications at high melting rates up to 1200 lb/h. However, JM did not address the assessment of glass quality and the relationship between the plasma melting process and glass quality. For business and technique reasons, JM terminated the project in the mid-1990s, and it has not been commercialized.

(c) High Intensity Plasma Glass Melter

Plasmelt Glass Technologies, LLC company partnered with Johns Manville and AGY have conducted a project-High Intensity Plasma Melting-from 2003 to 2006 (Gonterman and Weinstein 2006). The schematic of the melter is shown in Fig. 1.5. The plasma is generated between a DC anode and cathode torch. The torches do not contact the melt. This plasma

technology seems to be suitable for glasses that require high-temperatures or for special glass types with low production volumes. However, the energy consumption is higher compared to fossil fuel fired glass furnace for large volume glass production. It is quite clear that, similar to the British program, principle limitations are torch materials and design and the development of an overall stable and controlled operating process.

(d) Innovative In-Flight Melting Technology

In Japan, the project on the development of the innovative glass melting process based on the in-flight meting (IFM) technique was proposed by the National Institute for Materials Science, Tokyo Institute of Technology, Asahi Glass Co., Ltd., Toyo Glass Co., Ltd. and New Glass Forum in 2007. It was accepted as the National Project “Energy Innovation Program/ Development for Innovative Glass Melting Process Technology” by New Energy and Industrial Technology Development Organization (NEDO).

The conventional Siemens type melting technique is illustrated in Fig. 1.6. In the air-fuel-fired furnace, the heat transfer from above burner flame to glass melt is so low that the conventional melting technology is energy-intensive and time-consuming, especially in the melting and refining process. In addition, many emissions are generated due to the usage of fossil fuel, which brings more environmental pollution. In contrast, the principle of the in-flight glass melting technique is shown in Fig. 1.7. In the in-flight melting, the glass materials are charged into an oxygen gas stream to be introduced directly into an oxy-fuel burner flame similar to the AGM melter. The burner flame including glass materials in the in-flight melting corresponds to the burner flame radiation zone in the Siemens type melting. The glass materials for the in-flight melting are granulated as 100~300 μm size particles by spray drying. The particles of granular glass materials are melted while passing the burner flame for about 10

msec and converted into glass melt droplets. Employing granular glass batch accelerates the reactions among the raw materials in granules and makes it possible to melt within a short flight time in a flame. Moreover, the granular materials heating principally avoid the segregation of silica sand during melting. This is another effect enhancing the melting of glass materials and is an advantage which the AGM technique cannot produce (Inoue et al. 2012). The oxy-fuel burner can be combined with a multi-phase AC arc or RF plasma torch. The heating system is selected from three types, an oxy-fuel burner type, a thermal plasma type and an oxy-fuel burner-plasma hybrid type, according to the glass compositions.

The innovative in-flight glass melting technique will trigger the revolution in the glass production to push up the glass industry into a new era. According to Table 1.1, the energy consumption can be reduced about 60% compared to a typical Siemens type melting system. The new technique is also applicable to the melting of special glasses with small production scales and will be able to accelerate the production of new functional glasses which are seemed to be difficult to fabricate using the current popular Siemens type melting furnaces.

After completing the project, the in-flight melting technique is expected to be applied at first to the small scale glass production like car lamp lenses, colored glasses etc. Extension to the production of LCD panel glasses, small bottles and bulbs etc. will follow around 2017. The larger scale glass production like bottle, filament fiber, solar panel cover glass etc. will start around 2023. Application to huge scale glass production of sheet glass for buildings and cars is expected to start around 2027 depending on the preceding developments where the benefits of energy saving will be fully enjoyed.

1.3 Objective of This Work

As mentioned above, oxy-fuel burner, thermal plasmas and their combination can be

selected as the heat source in the in-flight melting technique. This dissertation is focused on the multi-phase AC arc plasma and its feasibility for the in-flight glass melting. The multi-phase AC arc possesses the following advantages for material synthesis and processing; high energy efficiency, large plasma volume, low velocity, easy scale-up, and low cost. As a new type of the thermal plasma generation system, the characteristics of multi-phase AC arc should be investigated. Due to the constantly changing of the AC waveform in the multi-phase AC arc electric power, the space and time homogeneous of plasma is important to understand.

The particles of raw material are directly flight into the plasma during in-flight treatment. As the in-flight time of particle in the plasma region is similar or even shorter than an AC cycle, the in-situ measurement of particles provides important information of plasma-particle interaction, which is useful in the optimization of the process. The in-flight particle measurement was carried out to investigate the in-flight melting behavior of glass raw materials by 12-phase AC arc with various methods.

The in-flight glass melting is totally different from the conventional melting method from the principle. The evaluation of the melted particles could demonstrate the effectiveness of the in-flight melting technique. The high reaction rate among the raw materials in granules within a short flight time in plasma would be predicted. Several analysis methods were conducted to examine the properties of the melted glass particles.

The objective of this study is clearly divided into three parts: 1) to investigate the plasma characteristics, 2) to investigate the relationship between multi-phase AC arc and in-flight glass melting behavior. In particular, (i) the spatial characteristics of the arc on the in-flight particles, (ii) the temporal characteristics of the arc on the in-flight particles, and 3) to analyze the properties of melted glass particles by multi-phase AC arc and hybrid plasma.

1.4 Contents of This Dissertation

Figure 1.8 shows the flowchart of this dissertation. Characterizations of in-flight particles were carried out by two different measurement methods thus described in two independent chapters. In-flight glass melting experiments were conducted by two heat sources which are separated into two chapters. The contents of each chapter in this dissertation are as follows:

In Chapter 2, the discharge behavior and the spatial and temporal characterizations of multi-phase AC arc plasma under different operating conditions were carried out by using a high speed video camera synchronized with current and voltage measurement. The effects of the electrode configurations, the electrode gap distance, the shield gas flow rate, the electrode diameter, and the gas flow characteristic on the plasma uniformity were investigated.

In Chapter 3, the in-flight particle diagnostics performed with optical system DPV-2000 and spectroscopic diagnostics were investigated theoretically and experimentally. It pointed out a possible method to estimate the accuracy of in-flight particle temperature measurement. The effects of carrier gas flow rate on the particle spatial characteristics at different measured radial position in the plasma region were investigated. In addition, the parameters described in Chapter 2 that could have influence on the plasma spatial property were also investigated with particle diagnostics. Therefore, the electrode configuration and the electrode diameter on the particle behavior at different measured radial position in the plasma region were characterized.

In Chapter 4, the fluctuation of particle temperature within millisecond in plasma region was studied by a high speed camera equipped with a band-pass filter system. The influence of the plasma temporal fluctuation on the in-flight particle temperature was evaluated. The effects of the electrode configuration, the carrier gas flow rate on the particle temperature fluctuation and the FFT characteristic were discussed.

In Chapter 5, the in-flight treatment of alkali-free glass raw materials by multi-phase AC arc was conducted. The effect of powder feed rate, the electrode configuration, and the carrier gas flow rate on the melting behavior was investigated. Results of the crystal structure, the morphology, the particle size distribution, and the composition of melted powders are given.

In Chapter 6, the combination of the multi-phase AC arc and oxygen burner as the heat source in the in-flight melting technology was introduced. The experiments results using this so-called “hybrid plasmas” were compared with the multi-phase AC arc. Furthermore, the effect of primary size of SiO_2 in the raw material on the melting process was investigated. The different melting behaviors due to the high temperature region and residence time in the two heat sources were discussed.

In Chapter 7, all the result in this dissertation are summarized, and the direction for future research of the multi-phase AC arc and the in-flight glass melting technique on industrial application is also stated.

References

American Society for Metals. ASM Metals Handbook. Vol. 5, Surface Cleaning, Finishing, and Coating, 9th Edition, (Pub.) ASM Int. Metal Parks, OH, U. S. (1982).

Ando, Y., X. Zhao, H. Kataura, Y. Achiba, K. Kaneto, M. Tsuruta, S. Uemura and S. Iijima. “Multiwalled carbon nanotubes prepared by hydrogen arc.” *Diamond and Related Materials* **9**, 847-851 (2000).

Bansal, P., N. P. Padture and A. Vasiliev. “Improved interfacial mechanical properties of Al_2O_3-13wt% TiO_2 plasma-sprayed coatings derived from nanocrystalline powders.” Acta Materialia, **51**(10), 2959-2970 (2003).

Barton, T. G. and J. A. Mordy. “The destruction of halogenated organic chemicals by plasma pyrolysis.” *Canadian Journal of Physiology and Pharmacology* **62**(8), 976-978 (1984).

Bertrand, P., I. Smurnov and M. Ignatiev. “Low cost industrial type diagnostic system for powder jet visualisation, particle-substrate interaction and coating growth.” *Proc. 5th IEEE International Conference on Intelligent Transportation Systems* 66-71, Essen, Germany (2002).

Bilodeau, J. F. and P. Proulx. “A mathematical model for ultrafine iron powder growth in a thermal plasma.” *Aerosol Science and Technology* **24**(3), 175-189 (1996).

Bisson, J. F., M. Lamontagne, C. Moreau, L. Pouliot, J. Blainard and F. Nadeau. Thermal Spray: New Surfaces for a New Millenium. 705-711, (Eds.) C. C. Berndt et al., (Pub.) ASM Int. Materials Park, OH, U.S. (2001).

Bondarev, K. T., O. N. Popov, V. A. Inshii and A. S. Bokova. “Some features of the refractory lining of design elements in glass furnaces.” *Glass and Ceramics* **34**(11), 700-703 (1977).

Boulos, M.I. and J. Jurewicz. “Process of Depositing Particulate Material on a Substrate.” U. S. Patent, 4,853,250 (1989).

Boulos, M. I. “Thermal plasma processing.” *IEEE Transactions on Plasma Science* **19**(6), 1078-1089 (1991).

Brunsman, E. M., R. Sutton, E. Bortz, S. Kirkpatrick, K. Midelfort, J. Williams, P. Smith, M. E. McHenry, S. A. Majetich, J. O. Artman, M. Degraef and S. W. Staley. “Magnetic-Properties of Carbon-Coated, Ferromagnetic Nanoparticles Produced by A Carbon-Arc Method.” *Journal of Physics D: Applied Physics* **75**(10), 5882-5884 (1994).

Capetti, A. and E. Pfender. “Probe Measurements in Argon Plasma Jets Operated in Ambient Argon.” *Plasma Chemistry and Plasma Processing* **9**(2), 329-341 (1989).

Chwa, S. O., D. Klein, F. L. Toma, G. Bertrand, H. Liao, C. Coddet and A. Ohmori. “Microstructure and mechanical properties of plasma sprayed nanostructured TiO_2-Al composite coatings.” *Surface and Coating Technology* **194**(2-3), 215-224 (2005).

Craig, J. E., R. A. Parker and D. Y. Lee. Thermal Spray: Surface Engineering via Applied Research. 51-66, (Ed.) C. C. Berndt, (Pub.) ASM Int. Materials Park, OH, U.S. (2000).

Cusick, M. J., M. A. Weinstein, and L. E. Olds. “Method for the melting, combustion or incineration of materials and apparatus therefor.” U. Patent, 5,548,611 (1996).

Dalton, D. A. and E. Langton. “Plasma and electrical systems in glass manufacturing.” *Electro-Technologies for Waste Processing and Purification, IEE Colloquium on* 3/1-2 (1994).

Dantsis, T. Y., A. A. Zeibots, L. A. Bisnietse, M. V. Marena, S. N. Gushchin and V. B. Kutin. “Improving the system of heating small glass furnaces with new burner equipment.” *Glass and Ceramics* **37**(7), 362-364 (1980).

Deam, R.T., A. R. Dayal, T. McAllister, A. E. Mundy. R. J. Western, L. M. Besley, A. J. D. Farmer, E. C. Horrigan and A. B. Murphy. “Interconversion of chlorofluorocarbons in -plasmas.” *Journal of the Chemical Society, Chemical Communications* **3**, 347-348 (1995).

Desilets, M., J. F. Bilodeau and P. Proulx. “Modelling of the reactive synthesis of ultra-fine powders in a thermal plasma reactor.” *Journal of Physics D: Applied Physics* **30**(13), 1951-1960 (1997).

Ding, C. X., H. Chen, X. Y. Liu and Y. Zeng. “Plasma sprayed nanostructured zirconia coatings for wear resistance.” Thermal Spray 2003: Advancing the science & applying the technology, 455-458, (Eds.) C. Moreau and B. Marple, (Pub.) ASM Int., Material Park, OH, U. S. (2003).

Dolf, H. R. and W. E. Marceau. “Method of melting glass with submerged combustion heaters and apparatus therefor.” U. S Patent, 3,260,587 A (1996).

Dzyuze, V. Y. “Current trends in production of glass containers.” *Glass and Ceramics* **61**(4), 101-105 (2004).

Fauchais, P., J. F. Coudert and M. Vardelle. “Diagnostics in thermal plasma processing.” *Plasma Diagnostics*,**1**, 349-446, (Eds.) O. Auciello and D. L. Flamm, Academic Press, Lodon, U. K. (1989).

Fauchais, P., J. F. Coudert, M. Vardelle , A. Vardelle and A. Denoirjean. “Diagnostics of thermal spraying plasma jets.” *Journal of Thermal Spray Technology* **1**(2), 117-128 (1992).

Fauchais, P., A. Vardelle and B. Dussoubs. “Quo Vadis Thermal Spraying?” *Journal of Thermal Spray Technology* **10**(1), 44-66 (2001).

Fauchais, P. and M. Vardelle. Thermal Spray 2003: Advancing the Science and Applying the Technology. **2**, 1165-1173, (Eds.) C. Moreau and B. Marple, (Pub.) ASM Int. Materials Park, OH, U.S. (2003).

Fauchais, P. “Understanding plasma spraying.” *J. Phys. D: Appl. Phys*., **37**, R86-R108 (2004).

Fincke, J. R., C. L. Jeffery and S. B. Englert. “In-flight measurement of particle size and temperature.” *Journal of Physics E: Scientific Instruments* **21**(4), 367-370 (1988).

Fincke, J. R., W. D. Swank and C. L. Jeffrey. “Simultaneous measurement of particle size, velocity and temperature in thermal plasmas.” *IEEE Transactions on Plasma Science* **18**(6), 948-957 (1990).

Fincke, J. R., W. D. Swank, S. C. Snyder and D. C. Haggard. “Enthalpy probe performance in compressible thermal plasma jets.” *Review of Science Instruments* **64**(12), 3585-3593 (1993a).

Fincke, J. R., W. D. Swank, C. L. Jeffery and C. A. Mancuso. “Simultaneous measurement of particle size, velocity and temperature.” *Measurement Science and Technology* **4**(5), 559-565 (1993b).

Fincke, J. R., W. D. Swank and D. C. Haggard. Thermal Spray Science and Technology. 117-122, (Eds.) C. C. Berndt and S. Sampath, (Pub.) ASM Int. Materials Park, OH, U.S. (1995a).

Fincke, J. R., W. D. Swank and D. C. Haggard. Thermal Spray Science and Technology. 123-128, (Eds.) C. C. Berndt and S. Sampath, (Pub.) ASM Int. Materials Park, OH, U.S. (1995b).

Fincke, J. R., D. C. Haggard, W. D. Swank. “Particle temperature measurement in the thermal spray process.” *Journal of Thermal Spray Technology* **10**(2), 255-266 (2001).

Geldart, D. “Types of Gas Fluidization.” *Powder Technology* **7**(5), 285-292 (1973).

Gherardi, N., G. Gouda, E. Gat, A. Ricard and F. Massines. “Transition from glow silent discharge to micro-discharges in nitrogen gas.” *Plasma Sources Science and Technology* **9**(3), 340-346 (2000).

Gherardi, N. and F. Massines. “Mechanisms controlling the transition from glow silent discharge to streamer discharge in nitrogen.” *IEEE Transactions on Plasma Science* **29**(3), 536-544 (2001).

Gold, D., C. Bonet, G. Chauvin, A. C. Mathieu, G. Gerinaert and J. Millet. “A 100-kW Three-Phase AC Plasma Furnace for Spheroidization of Aluminum Silicate Particles.” *Plasma Chemistry and Plasma Processing* **1**(2), 161-178 (1981).

Gonterman, J. R. and M. Weinstein. “High Intensity Plasma Glass Melter Project.” Final DOE (USA Department of Energy) Report. Award number: DE-FC36-03GO13093, Plasmelt Glass Technologies, LLC report. Boulder Co, USA (2006).

Griem, H. R. Plasma Spectroscopy, (Pub.) McGraw-Hill, New York (1964).

Gurevich, M. A. and V. B. Shetinberg. *Soviet Physics-Technical Physics* **3**, 368-375 (1958).

Hantzsche, H. *Proc. 7th International Metal Spraying Conference* 1-4, Edison Welding Institute, Columbus, OH, U. S. (1973).

Hawthorne, H. M., L. C. Erickson, D. Ross, H. Tai and T. Troczynski. “The microstructural dependence of wear and indentation behaviour of some plasma-sprayed alumina coatings.” *Wear*, **203-204**, 709-714 (1997).

Heberlein, J. V. R. “Adaption of plasma torches to new applications of plasma technology.” *Proc. Workshop of Industrial Applications of Plasma Chemistry*, (Ed.) M. I. Boulos, (Pub.) Universita di Bari, Bari, Italy (1989).

Hollis, K. and R. Neiser. “Analysis of the nonthermal emission signal present in a molybdenum particle-laden plasma-spray plume.” *Journal of Thermal Spray Technology* **7**(3), 383-391 (1998).

Inoue, S., T. Watanabe, T. Yano, O. Sakamoto, K. Satoh, S. Kawachi and T. Iseda. “Future of Glass Melting Through the In-Fight Melting Technique.” Processing, Properties, and Applications of Glass and Optical Materials: Ceramic Transactions, **231**, 37-44, (Eds.) A. K. Varshneya, H. A. Schaeffer, K. A. Richardson, M. Wightman and L. D. Pye. (2012).

Irissou, E., M. Blouin, L. Roue, J. Huot, R. Schulz and D. Guay. “Plasma-sprayed nanocrystalline Ti-Ru-Fe-O coatings for the electrocatalysis of hydrogen evolution reaction.” *Journal of Alloys and Compounds* **345**(1), 228-237 (2002).

Ishigaki, T. and J. G. Li. “Synthesis of functional nanocrystallites through reactive thermal

plasma processing." *Science and Technology of Advanced Materials* **8**(7-8), 617-623 (2007).

Ishigaki, T. "Synthesis of ceramic nanoparticles with non-equilibrium crystal structures and chemical compositions by controlled thermal plasma processing." *Journal of the Ceramic Society of Japan* **116**(1351), 462-470 (2008).

Jordan, E. H., M. Gell, Y. H. Sohn, D. Goberman, L. Shaw, S. Jiang, M. Wang, T. D. Xiao, Y. Wang and P. Strutt. "Fabrication and evaluation of plasma sprayed nanostructured alumina-titania coatings with superior properties." *Materials Science and Engineering* **301**(1), 80-89 (2001).

Jordan, G. R. "Induction plasma torches." *Review of Physics in Technology* **2**(128), 128-145 (1971).

Joseph, M. F. and T. G. Barton. "Pyrolysis of hazardous waste with a mobile plasma arc system." Management of Hazardous and Toxic Wastes (Amsterdam: Elsevier Applied Science) (1987).

Jurewicz, J., R. Kaczmarek and M.I. Boulos. "Radio Frequency Plasma Deposition of Metals and Alloys Under Reduced Pressure." *7th International Symposium on Plasma Chemistry* 1131-1136, Eindhoven, The Netherlands (1985).

Kim, J. H, H. S. Yang, K. Baik, B. G. Seong, C. H. Lee and S. Y. Hwang. "Development and properties of nanostructured thermal spray coatings." *Current Applied Physics* **6**(6), 1002-1006 (2006)

Kong, P. C. and Y. C. Lau. "Plsma Synthesis of Ceramic Powders." *Pure and Applied Chemistry* **62**(9), 1809-1816 (1990).

Kowalsky, K. A., D. R. Marunts, M. F. Smith and W. L. Oberkampf. Thermal Spray: Research and Applications. 587-592, (Ed.) T. F. Bernicki, (Pub.) ASM Int. Materials Park, OH, U.S. (1991).

Kruszewska, B. and J. Lesinski. "Temperature distributions of solid particles in a plasma stream." *Revue de Physique Appliquée* **12**(9), 1209-1200 (1977).

Kuroda, S., T. Fukushima, S. Kitahara and H. Fujimori. *Thermal Spraying: 12th International Conference* 145-153, The Welding Institute, Abington, OXON, U. K. (1989).

Kuzyak, V. A. "Electric boosting of glass heating in flame tank furnaces." *Glass and Ceramics* **15**(11), 586-591 (1958).

Landes, K. D., V. T. Streibl and J. Zeirhert. *Proc. 5th IEEE International Conference on Intelligent Transportation Systems* 47-51, Essen, Germany (2002).

Largo, J., E. Hämäläinen and K. Krikka. Thermal Spray 2003: Advancing the Science and Applying the Technology. 1113-1119, (Eds.) C. Moreau and B. Marple, (Pub.) ASM Int. Materials Park, OH, U.S. (2003).

Li, C. J., T. Wu, C. X. Li and B. Sun. “Effect of spray particle trajectory on the measurement signal of particle parameters based on thermal radiation.” *Journal of Thermal Spray and Technology* **12**(1), 80-94 (2003).

Li, J. G., X. H. Wang, H. Kamiyama, T. Ishigaki and T. Sekiguchi. “RF plasma processing of Er-doped TiO_2 luminescent nanoparticles.” *Thin Solid Films* **506-507**, 292-296 (2006).

Li, Y. L. and T. Ishigaki. “Controlled one-step synthesis of nanocrystalline anatase and rutile TiO_2 powders by in-flight thermal plasma oxidation.” *The Journal of Physical Chemistry B* **108**(40), 15536-15542 (2004).

Liang, B. and C. X. Ding. “Thermal shock resistances of nanostructured and conventional zirconia coatings deposited by atmospheric plasma spraying.” *Surface and Coating Technology* **197**(2-3), 185-192 (2005).

Lin, X. H., Y. Zeng, C. X. Ding and P. Y. Zhang. “Effects of temperature on tribological properties of nanostructured and conventional Al_2O_3-3wt% TiO_2 coatings.” Wear, **256**(11-12), 1018-1025 (2004).

Lochte-Holtgreven, W. Plasma Diagnostics, (Pub.) North-Holland, Amsterdam (1968).

Mailhot, K., F. Gitzhofer and M. I. Boulos. Thermal Spray: A United Forum for Scientific and Technological Advances, 21-25, (Ed.) C. C. Berndt, (Pub.) ASM Int., Material Park, OH, U. S. (1997).

Marple, B. R., J. Voyer, J. -F. Bisson and C. Moreau. “Thermal spraying of nanostructured cermet coatings.” *Journal of Materials Processing Technology* **117**(3), 418-423 (2001).

Mates, S. P., D. Basak, F. S. Biancaniello, S. D. Ridder and J. Geist. “Calibration of a Two-Color Imaging Pyrometer and Its Use for Particle Measurements in Controlled Air Plasma Spray Experiments.” *Journal of Thermal Spray Technology* **11**(2), 195-205 (2002).

Matsuura, T., O. Tago, H. Tshujino and K. Taniguchi. “Experimental Study of the Arc Plasma Generated by 6-Phase Alternating Currents.” *IEEJ Transactions on Industry Applications* **114**(1), 101-102 (1994a).

Matsuura, T., O. Tago, H. Tshujino and K. Taniguchi. *Proc. International Conference on Modeling, Simulation and Identification* Wakayama, Japan, 78 (1994b).

Matsuura, T., K. Taniguchi and K. Makida. “Techniques for Processing Industrial Waste Using Arc Plasma Generated by the Six-Phase Current.” *Journal of the Japan Society of Waste Management Experts* **8**(1), 9-15 (1997). (in Japanese).

Matsuura, T., K. Taniguchi and T. Watanabe. “A new type of arc plasma reactor with 12-phase alternating current discharge for synthesis of carbon nanotubes.” *Thin Solid Films* **515**(9), 4240-4246 (2007).

Mishin, J., M. Vardelle, J. Lesinski and P. Fauchais. *Proc. 7th International Symposium on*

Plasma Chemistry IUPAC, Eindhoven, 724-729 (1985).

Mishin, J., M. Vardelle and P. Fauchais. “Two-colour pyrometer for the statistical measurement of the surface temperature of particles under thermal plasma conditions.” *Journal of Physics E: Scientific Instruments* **20**(6), 620-625 (1987).

Moreau, C., P. Cielo, M. Lamontagne, S. Dallaire and M. Vardelle. “Impacting Particle Temperature Monitoring During Plasma Spray Deposition.” *Measurement Science and Technology* **1**(8), 807-815 (1990).

Moreau, C., P. Gougeon, M. Lamontagne, V. Lacasse, G. Vaudreuil and P. Cielo. Thermal Spray Industrial Applications. 431-437, (Eds.) C. C. Berndt and S. Sampath, (Pub.) ASM Int. Materials Park, OH, U.S. (1994).

Moreau, C., P. Gougeon, A. Burges and D. Ross. Thermal Spray Science and Technology. 141-147, (Eds.) C. C. Berndt and S. Sampath, (Pub.) ASM Int. Materials Park, OH, U.S. (1995).

Murphy, A. B. and T. McAllister. “Destruction of ozone-depleting substances in a thermal plasma reactor.” *Applied Physics Letters* **73**(4), 459-461 (1998).

Murphy, A. B. and T. McAllister. “Modeling of the physics and chemistry of thermal plasma waste destruction.” *Physics of Plasmas* **8**(5), 2565-2571 (2001).

Nicoll, A. R. Thermal Spray: Industrial Applications, 7-13, (Eds.) C. C. Berndt and S. Sampath, (Pub.) ASM Int., Material Park, OH, U. S. (1994).

Ohno, S. and M. Uda. “Generation Rate of Ultrafine Metal Particles in Hydrogen Plasma-Metal Reaction.” *Journal of the Japan Institute of Metals* **48**(6), 640-646 (1984).

Ohno, S. and M. Uda. “Preparation for Ultrafine Particles of Fe-Ni, Fe-Cu and Fe-Si Alloys by Hydrogen Plasma-Metal Reaction.” *Journal of the Japan Institute of Metals* **53**(9), 946-952 (1989).

Ohno, S. “The Vaporization Phenomenon of Molten Metal During “Hydrogen Plasma-Metal” Reaction.” *Journal of High Temperature Society* **19**(3), 105-111 (1992).

Pawlowski, L. The Science and Engineering of Thermal Spray Coatings, 1st Edition. (Pub.) John Wiley & Sons Ltd, England, U. K. (1995).

Pfender, E. “Thermal Plasma Technology: Where Do We Stand and Where Are We Going?” *Plasma Chemistry and Plasma Processing* **19**(1), 1-31 (1999).

Planche, M. P., H. Liao and C. Coddet. “Relationships between in-flight particle characteristics and coating microstructure with a twin wire arc spray process and different working conditions.” *Surface and Coating Technology* **182**(2-3), 215-226 (2004).

Popa, S. D. “Vibrational distributions in a flowing nitrogen glow discharge.” *Journal of Physics D: Applied Physics* **29**(2), 411-415 (1996).

Rahmane, M., G. Soucy and M. I. Boulos. “Analysis of the enthalpy probe technique for

thermal plasma diagnostics." *Review of Scientific Instruments* **66**(6), 3424-3431 (1995).

Ross, C. P. and G. L. Tincher. "Glass Melting Technology: A Technical and Economic Assessment." *Glass Manufacturing Industry Council* (2004).

Ross, C. P. "Innovative glassmelting technologies," *American Ceramic Society Bulletin* **83**(1), 18-20 (2004).

Ryu, T. G., H. Y. Sohn, K. S. Hwang and Z. Z. G. Fang. "Plasma Synthesis of Tungsten Carbide Nanopowder from Ammonium Paratungstate." *Journal of the American Ceramic Society* **92**(3), 655-660 (2009).

Saito, Y., T. Masumoto and K. Nishikubo. "Encapsulation of TiC and HFC crystallites within graphite cages by arc discharge." *Carbon* **35**(12), 1757-1763 (1997a).

Saito, Y., T. Matsumoto and K. Nishikubo. "Encapsulation of carbides of chromium, molybdenum and tungsten in carbon nanocapsules by arc discharge." *Journal of Crystal Growth* **172**(1-2), 163-170 (1997b).

Sakuta, T. and M. I. Boulos. *Proc. 8th International Symposium on Plasma Chemistry* IUPAC, Tokyo, 371-377 (1987).

Sakuta, T. and M. I. Boulos. "熱プラズマ中を飛行する微粒子の温度、速度およびサイズの同時測定手法" *Transactions of the Institute of Electrical Engineers of Japan* **108-A**(9), 389-396 (1988a). (in Japanese).

Sakuta, T. and M. I. Boulos. "Novel approach for particle velocity and size measurement under plasma conditions." *Review of Scientific Instruments* **59**(2), 285-291 (1988b).

Shamp, D. E., T. F. Stark, J. R. Elliott and L. E. Howard. "Oxygen fired glass furnace with burners in the upstream end." U. S Patent, 5,417,732 (1995).

Shanmugavelayutham, G. and V. Selvarajan. "Plasma spheroidization of nickel powders in a plasma reactor." *Bulletin of Material Science* **27**(5), 453-457 (2004).

Shao, H. Y., Y. T. Wang, H. R. Xu and X. G. Li. "Hydrogen storage properties of magnesium ultrafine particles prepared by hydrogen plasma-metal reaction." *Materials Science and Engineering: B-Solid State Materials for Advanced Technology* **110**(2), 221-226 (2004).

Shao, H. Y., T. Liu, Y. T. Wang, H. R. Xu and X. G. Li. "Preparation of Mg-based hydrogen storage materials from metal nanoparticles." *Journal of Alloys and Compounds* **465**(1-2), 527-533 (2008).

Shaw, L. L., D. Goberman, R. Ren, M. Gell, S. Jiang, Y. Wang, T. D. Xiao and P. R. Strutt. "The dependency of microstructure and properties of nanostructured coatings on plasma spray conditions." *Surface and Coatings Technology* **130**(1), 1-8 (2000).

Shigeta, M., T. Watanabe and H. Nishiyama. "Numerical investigation for nano-particle synthesis in an RF inductively coupled plasma." *Thin Solid Films* **457**(1), 192-200 (2004).

Shigeta, M. and T. Watanabe. “Numerical investigation of cooling effect on platinum nanoparticle formation in inductively coupled thermal plasmas.” *Journal of Applied Physics* **103**(7), 15 (2008a).

Shigeta, M. and T. Watanabe. “Two-dimensional analysis of nanoparticle formation in induction thermal plasmas with counterflow cooling.” *Thin Solid Films* **516**(13), 4415-4422 (2008b).

Smith, M. F., T. J. O’Hern, J. E. Brockmann, R. A. Neiser and T. J. Roeme. Thermal Spray: Sciences and Technology. 105-110, (Eds.) C. C. Berndt and S. Sampath, (Pub.) ASM Int. Materials Park, OH, U.S. (1995).

Swank, W. D., J. R. Fincke and D. C. Haggard. Thermal Spray: Sciences and Technology. 111-116, (Eds.) C. C. Berndt and S. Sampath, (Pub.) ASM Int. Materials Park, OH, U.S. (1995).

Tanaka, Y., T. Nagumo, H. Sakai, Y. Uesugi, Y. Sakai and K. Nakamura. “Effect of current modulation on nanopowder synthesis using induction thermal plasmas.” *19th International Symposium on Plasma Chemistry* Bochum, Germany (2009).

Taylor, P. R and S. A. Pirzada. “Thermal plasma processing of materials: A review.” *Advanced Performance Matertials* **1**(1), 35-50 (1994).

Tichenor, D. A., R. E. Mitchell, K. R. Hencken and S. Niksa. “Simultaneous in situ measurement of the size, temperature and velocity of particles in a combustion environment.” *20th Symposium (International) on Combustion* Pittsburgh, America 1213-1221 (1984).

Tiwary, R., D. Stickler and J. Woodroffe. “Rapid Heating of a Glass Batch in an Advanced Glass Melter.” *Journal of the American Ceramic Society* **71**(9), 748-753 (1988).

Tucker, R. C. “Thermal Spray Coatings.” *Surface Engineering*, **5**, 497-509, ASM Handbook, (Pub.) ASM Int. (1994).

Vardelle, A., J. M. Baronnet, M. Vardelle and P. Fauchais. “Measurements of the Plasma and Condensed Particles Parameters in a DC Plasma Jet.” *IEEE Transactions on Plasma Science* **8**(4), 418-424 (1980).

Vardelle, M., A. Vardelle, P. Fauchais and M. I. Boulos. “Plasma-particle momentum and heat transfer: Modelling and measurements.” *American Institute of Chemical Engineers* **29**(2), 236-243 (1983).

Vardelle, M., A. Vardelle, A.C. Leger, P. Fauchais and D. Gobin. “Influence of particle parameters at impact on splat formation and solidification in plasma spraying processes.” *Journal of Thermal Spray Technology* **4**(1), 50-58 (1995).

Vattulainen, J., E. Hämäläinen, R. Hernberg, P. Varisto and Mäntyla. “Novel method for in-flight particle temperature and velocity measurements in plasma spraying using a

single CCD camera." *Journal of Thermal Spray Technology* **10**(1), 94-104 (2001).

Watanabe, T. and S. Shimbara. "Halogenated hydrocarbon decomposition by steam thermal plasmas." *High Temperature Materials and Processes* **7**(4), 455-474 (2003).

Watanabe, T. and H. Okumiya. "Formation mechanism of silicide nanoparticles by induction thermal plasmas." *Science and Technology of Advanced Materials* **5**(5-6), 639-646 (2004).

Watanabe, T., T. Tsuro and A. Takeuchi. "Water plasma generation under atmospheric pressure for effective CFC destruction." *Proc. 17th International Symposium on Plasma Chemistry* Toronto, Canada, (Eds.) J. Mostaghimi et al., (University of Toronto) (2005).

Williams, J. K., C. P. Heanley, and L. E. Olds. "Method of melting materials and apparatus therefor." U.S Patent, 5,028,248 (1991).

Xu, X., G. Chen and Y. Shen. 1st Plasma-Technik-Symp., 99-103, (Eds.) H. Eschnauer, P. Huber, A. Nicoll and S. Sandmeier, Plasma-Technik, Lucerne, Switz. (1988).

Ye, R., T. Ishigaki, J. Jurewicz, P. Proulx and M. I. Boulos. "In-Flight Spheroidization of Alumina Powders in Ar-H_2 and Ar-N_2 Induction Plasmas." *Plasma Chemistry and Plasma Processing* **24**(4), 555-571 (2004).

Zierhut, J., P. Haslbeck, K. D. Landes, G. Barbezat, M. Muller and M. Schutzl. Thermal Spray: Meeting the Challenges of the 21st Century, 1375-1379, (Eds.) C. Coddet, (Pub.) ASM Int., Material Park, OH, U. S. (1998).

Table 1.1 Energy saving effect

Consumption energy for 100 t/d	In-flight glass melting	Conventional glass melting
Energy for heating of raw material and cullet	1800 kl	1800 kl
Heat loss of exhaust gas	1300 kl	4400 kl
Heat loss of furnace wall	120 kl	1500 kl
Making energy of oxygen gas	480 kl	0 kl
Crushing energy of raw material	140 kl	0 kl
Energy saving by preheating of raw material	-370 kl	0 kl
Loss on defective product	630 kl	2500 kl
Total of energy consumption (kl/furnace/year)	4100	10200
Energy reduction rate	**60%**	

(a)

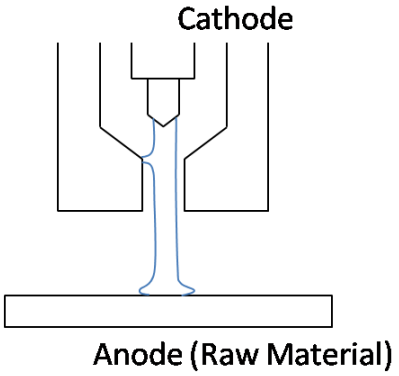

(b)

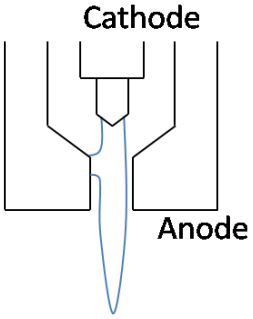

Fig. 1.1 The schematic illustration of the arc generating system of (a) transferred and (b) non-transferred arc

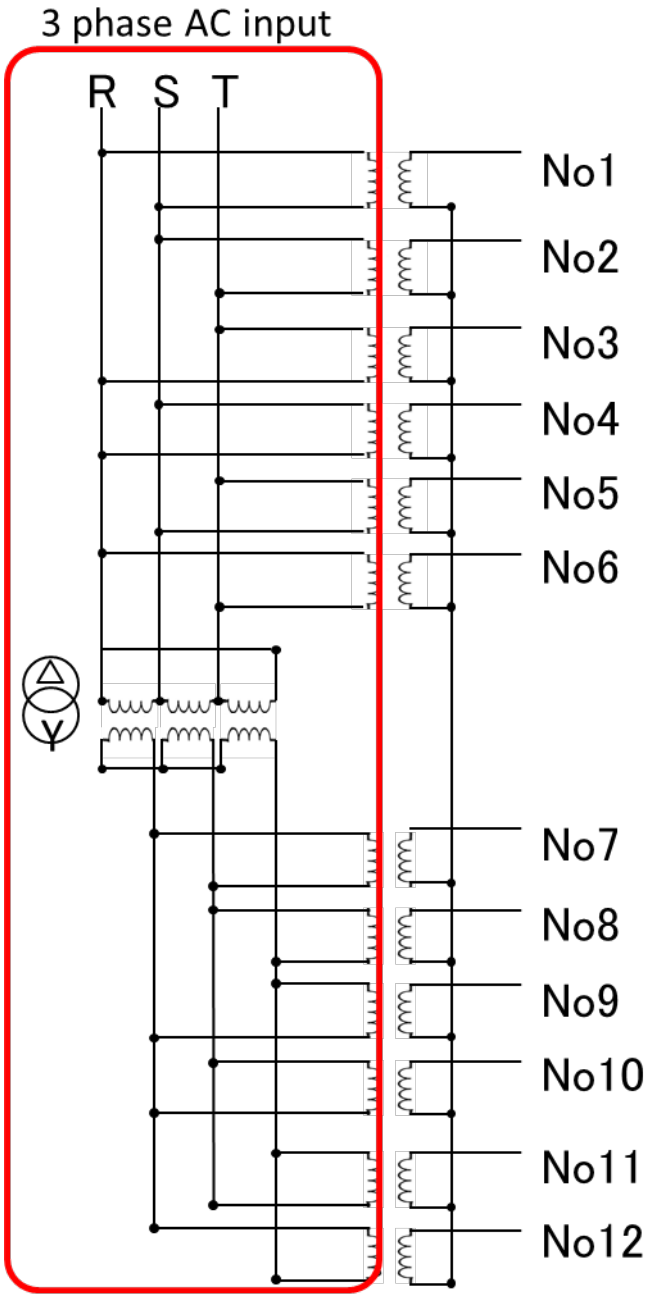

Fig. 1.2 The electrical circuit diagram and schematic connection diagram for generating of 12-phase AC arc

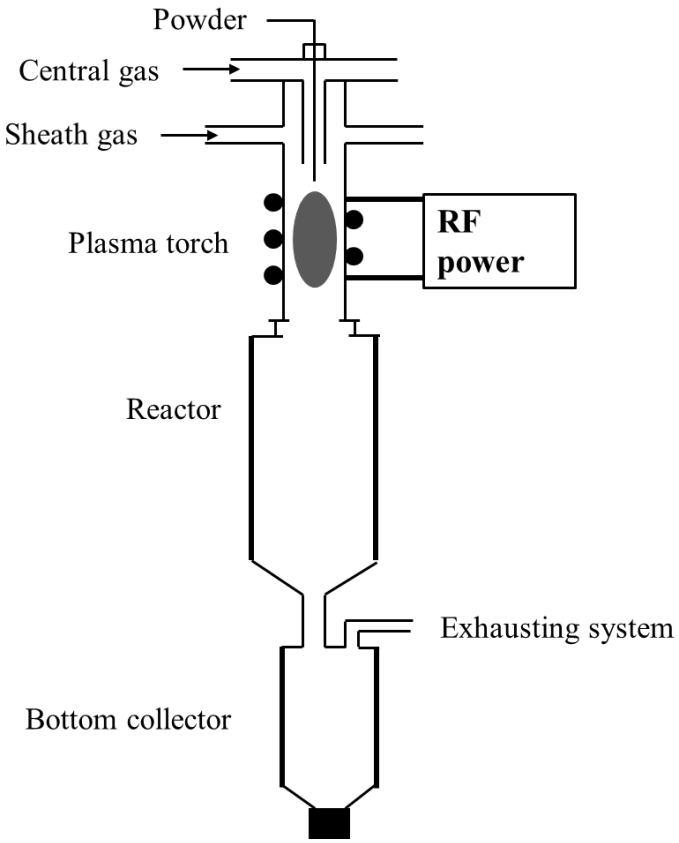

Fig. 1.3 The schematic illustration of the arc generating system of RF plasmas

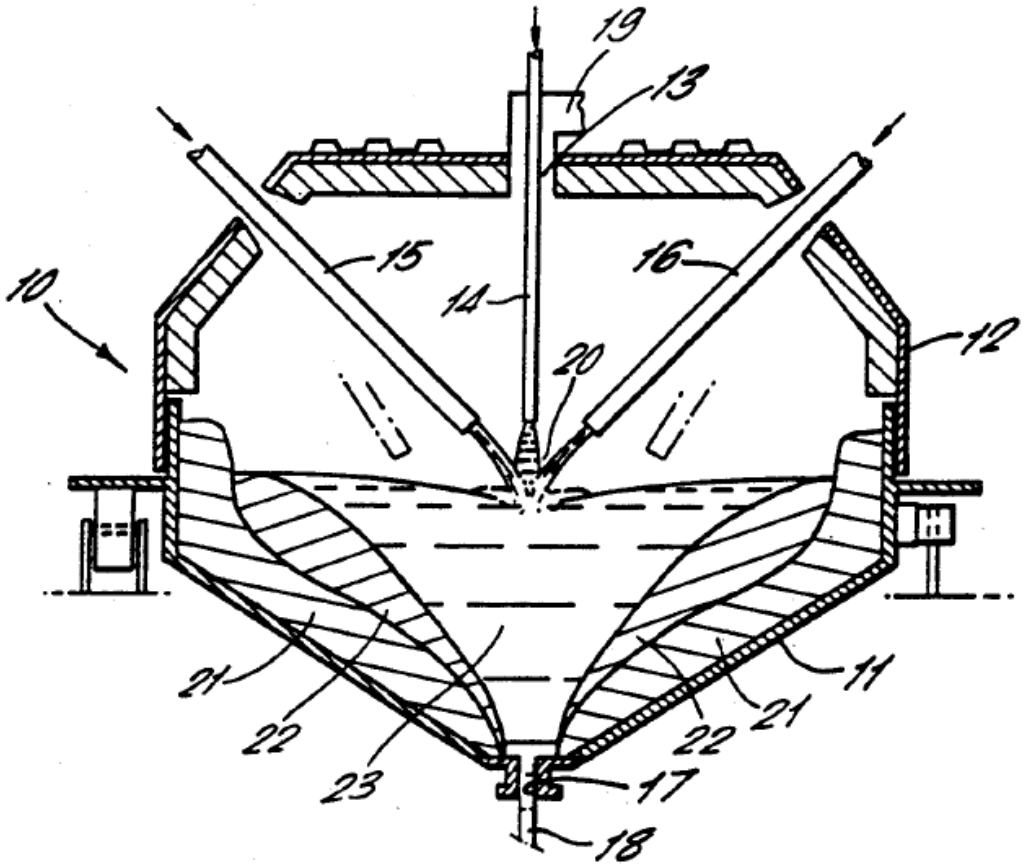

10. melting furnace	11. rotatable shell	12. fixed upper shell
13. central feed hole	14. feed tube	15. plasma electrode
16. plasma electrode	17. outlet orifice	18. stream of molten material
19. port for venting the off-gases	20. plasma arc zone	21. solid shell for protection of wall
22. scummy melt	23. hottest liquid zone	

Fig. 1.4 Schematic of arc plasma melter. (Williams et al. 1991)

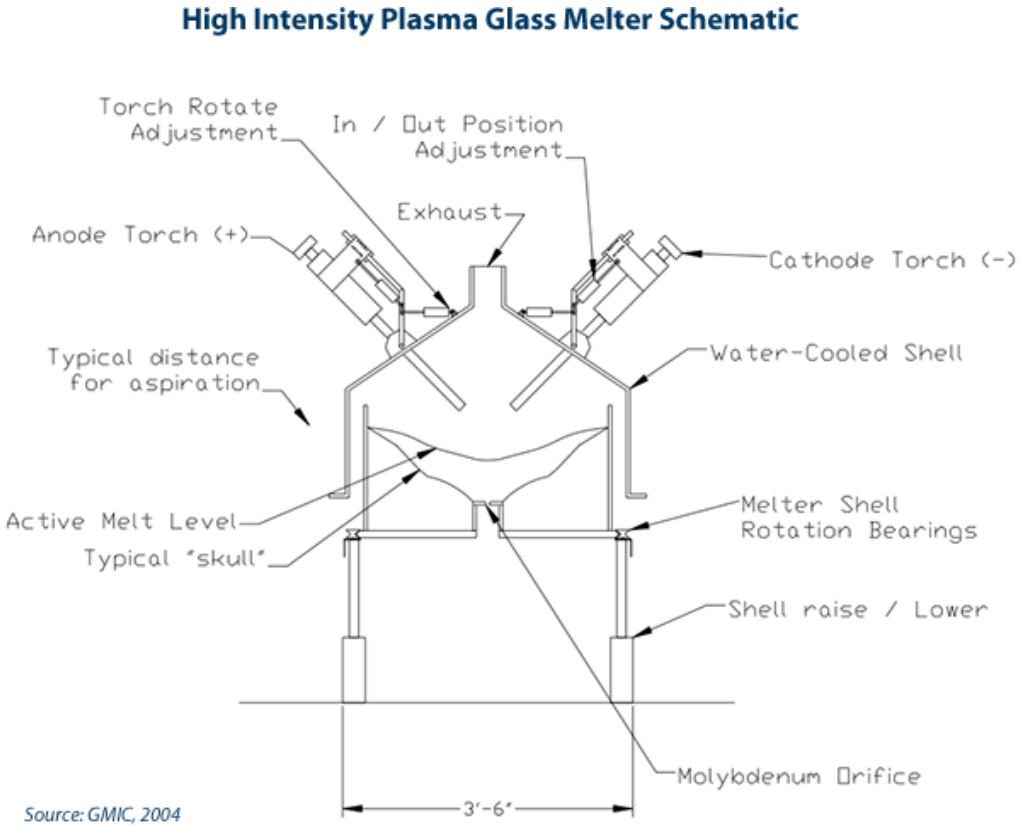

Fig. 1.5 Schematic of high intensity plasma glass melter. (Gonterman and Weinstein, 2006)

(a)

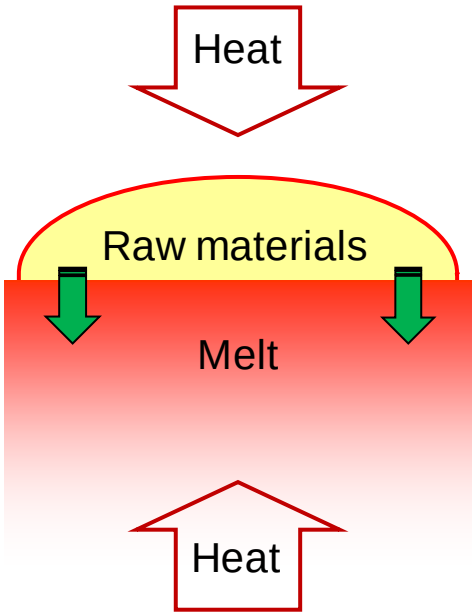

(b)

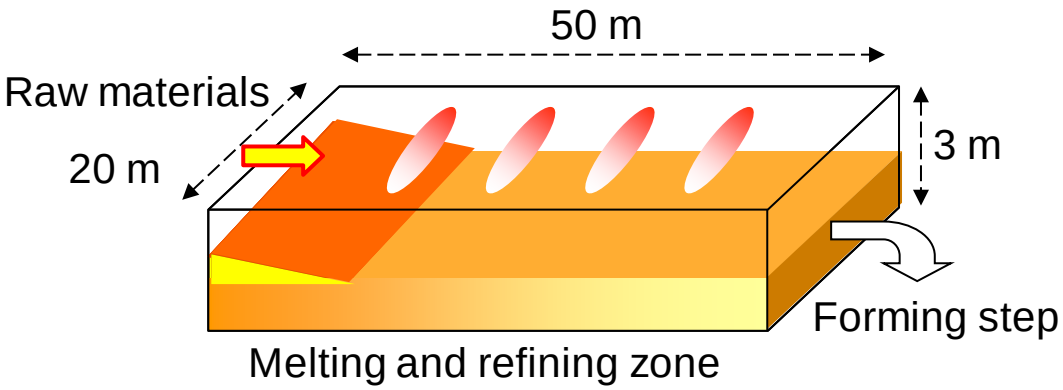

Fig.1.6 Conventional glass melting: (a) concept of conventional technology and (b) tank furnace of Siemens type

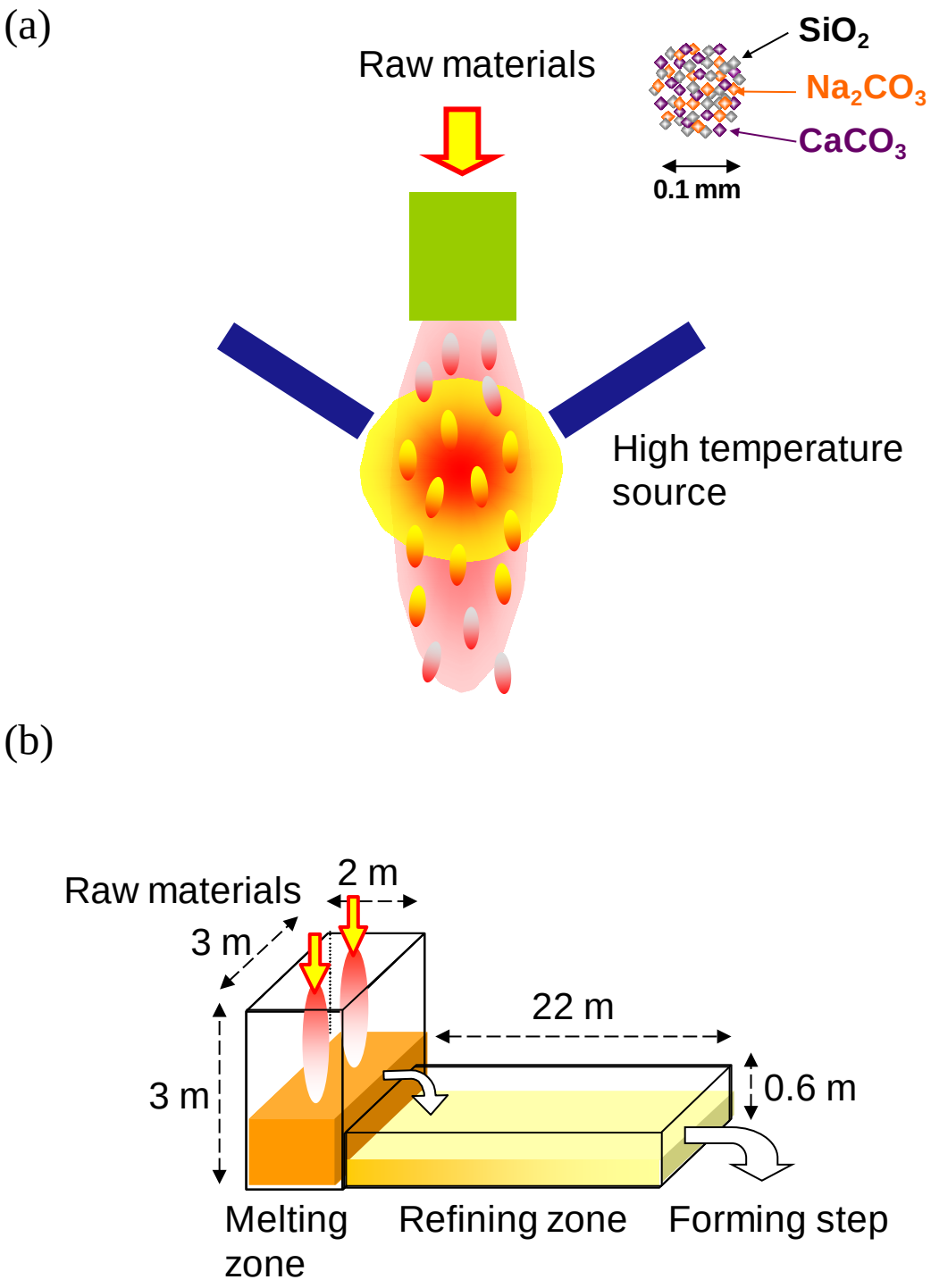

Fig.1.7 In-flight glass melting: (a) concept of new technology and (b) tank furnace of in-flight melting type

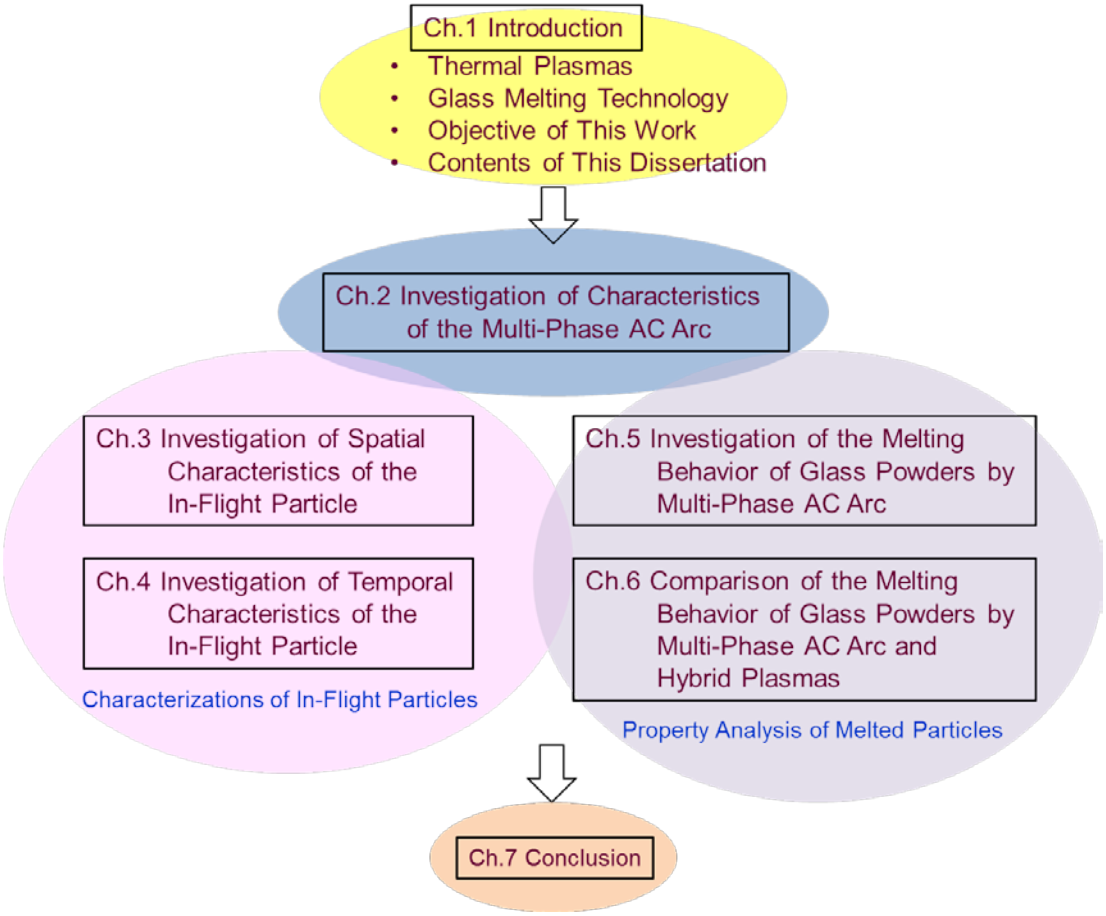

Fig. 1.8 The flow chart of this study

2. Investigation of Characteristics of the Multi-Phase AC Arc

Arc plasma as an energy source with high energy efficiency has been applied to the in-flight glass production. In particular, the multi-phase AC arc is one of the most suitable heat sources for the in-flight glass melting because it possesses many advantages such as high energy efficiency, large plasma volume and low gas velocity. In order to evaluate the feasibility of applying the multi-phase AC arc to the in-flight glass melting, this chapter talks about the characteristics of arc discharge behavior analyzed by a high-speed camera. As the multi-phase AC arc has large discharge volume about 100 mm, the uniformity of arc distribution and instability of discharge have great influence on the in-flight particles during the short time of several milliseconds. The origin for the time-transient characteristics of multi-phase AC arc is the AC waveform changes its vale or amplitude constantly. Therefore, the periodic fluctuations present in multi-phase AC arc have been studied. The change in spatial characteristics is caused by the arrangement of 12 electrodes in the space and the changes of anode or cathode due to AC current. For generating homogeneous plasma, it is necessary to know how external parameters influence the plasma properties. Thus, the dependence on parameters like electrode configuration, gap distance, gas flow, electrode diameter, and gas flow method is the objective of investigation. The aim of this chapter is to examine the influence of various parameters on the plasma homogeneity and therefore, its adaptability on the powder treatment.

2.1 Introduction

In the case of the DC arc plasma, considerable works have been devoted to characterize the properties of the arc plasma and to investigate the arc behavior and arc instability (Sander et al. 1982). In the arc welding field, the transferred DC arc has been mostly used. Most important instability of the transferred arc is derived from the arc electrode attachment. The arc inside the torch has been studied experimentally (Duan and Heberlein 2002; Coudert et al. 1996; Ramasamy and Selvarajan 2000) and numerically (Miloshevsky et al. 2000; Trelles et al. 2006, 2009; Selvan and Ramachandran 2006). The effects of the arc current, the torch configuration, working gas, and its flow rate on the arc-electrode attachment have been systematically investigated by the high-speed video observation synchronized with the measurement of arc voltage (Iwao et al. 2005; Yang et al. 2006), spectroscopic diagnostics (Zhou and Heberlein 1995), and the laser Thomson scattering analysis (Yang and Heberlein 2007a, b). The Schlieren imaging method has been also applied to investigate the arc behavior for the plasma cutting torch (Kim et al. 2009). It can be concluded that the arc behavior and the stability must be studied to enhance the efficiency and the productivity of the arc plasma processes.

The existing single- or three-phase AC power supplies have a characteristic of intermittent discharge due to the polarity transition. A new type of arc reactor with multiphase AC discharge has been developed to obtain stable and continuous arc by transformers converting 3-phase AC to 6- or 12-phase AC. Among various thermal plasma reactors, the multi-phase AC arc process has the following advantages: high energy efficiency, large plasma volume (about 100 mm in diameter), low flow velocity (5~20 m/s), easy scale up, and low cost. In glass production with the multi-phase AC arc, granulated raw glass materials are injected above the furnace and penetrated through the plasma region to be melted and vitrified within milliseconds. Therefore, the study of the discharge behavior, the high-temperature distribution,

and the fluctuation of plasma are necessary and important. However, the characteristics of the multi-phase AC arc have less intensively researched because it is still a new type of plasma generation reactor. In this chapter, a stable 12-phase AC arc was generated by transformers at a commercial electric power system and the arc behavior was characterized by high-speed video observations synchronized with voltage measurements. The spatial and temporal uniformity of arc discharge pattern will be investigated.

2.2 Experimental

2.2.1 Experimental Setup

Figure 2.1 shows the photograph of the multi-phase AC arc apparatus. The system is operated under atmospheric pressure. Fig. 2.2 shows the schematic diagram of the experimental setup. It consists of 12 electrodes, a reaction chamber and AC power supply. The 12 electrodes are symmetrically arranged rotating on the axis and divided into two layers to increase the plasma volume in the longitudinal direction. The angle between the upper six inclined electrodes and the six lower horizontal electrodes is 30º. The electrodes are made of 2%-thoriated tungsten with 6 mm in diameter. They are cooled by city water at a flow rate of 3 L/min, and Ar gas (99.9%) is injected around each electrode to prevent it from oxidation at a flow rate of 5 L/min. The water cooled arc chamber is made of stainless steel. A servomotor system is used to precisely control the electrode position and diameter of plasma.

12 sets of arc welding transformers with a single-phase AC (DAIHEN B-300, Japan) were used to realize the power supply for the generation of 12-phase AC arc. The idea voltage waveforms follow the phase sequence 1~12 are shown in Fig. 2.3. The applied voltage between each electrode and the neutral point of the coil of the transformer can be calculated by the following equation:

$$V_i^N = V_m^N \sin\left[\omega t - 2\pi(i-1)/12\right],\ (i=1,\ 2...12) \tag{2.1}$$

where V_i^N indicates the applied non-load voltage for each electrode number *i* and V_m indicates the amplitude of the non-load voltage (about 220 V). ω is the angular velocity and ω=2π*f*, *f* is the frequency of AC (50 Hz). In the case of 6-phase AC arc discharge, the voltage was applied to electrode No. 1, 2...6. The input of the three-phase AC power supply was connected to 200 V (50 Hz) commercial power lines. A period AC cycle is 20 ms so the phase transition time is 1.67 ms (20÷12 phase). The phase shift between each voltage waveform of a 12-phase AC power source is therefore 30° (360° ÷12 phase). Figure 2.4 shows the electrical circuit diagram and temporary connection diagram directly to the corresponding electrodes of the reactor. The primary coils of transformers are divided into two parts: one is the delta configuration and the other is the wye or Y configuration. The neutral points of the secondary coils in the transformers are connected to each other. The turn's ratio of the windings between the primary and secondary coils of the transformers is set to $1/\sqrt{3}$. The detailed electrical circuit and vector diagrams for converting from 3-phase AC to 12-phase AC were reported by Matsuura et al. (2007).

Figure 2.5 gives a schematic illustration of the experimental setup for the arc discharge behaviors measurement by a high-speed video camera in the 12-phase AC arc plasma system. An oscilloscope synchronized with the high-speed camera measured the current and voltages of the 12 electrodes.

2.2.2 Description of Different Electrode Configurations

Figure 2.6 illustrates one of the electrode arrangements for generating the 12-phase AC arc called Clockwise (CW) pattern. The arrows represent the maximum voltage difference at different times in one discharge cycle. The phase transition time was 1.67 ms from one electrode to the next one. In CW discharge pattern, all the electrodes are arranged counter-clockwise

according to the phase sequence. The maximum voltage difference is between the diametrically opposed pairs. Figure 2.7 shows another electrode arrangement named Flip-flop (FF) pattern, which interval phases are connected counter-clockwise by odd and even order.

2.2.3 Experimental Conditions

The process parameters in the investigation of arc discharge behavior including the electrode configuration, the electrode gap distance, the shield gas flow rate, the tungsten electrode diameter, and the gas flow method. The discharge conditions for the 12-phase AC arc in the Clockwise and Flip-flop pattern are shown in Table 2.1. The measurement conditions for arc discharge behavior in all experiments are given in Table 2.2. The high-speed video camera (Photron, FASTCAM SA WTI, Japan) recorded at a speed of 10000 frames/s with a shutter speed of 0.37 μs. The oscilloscope (Yokogawa, ScopeCorder DL850, Japan) recorded at a sampling rate of 10^6 Hz. Table 2.3 shows the experimental conditions for studying the effect of electrode gap distance. Besides the general electrode distance of 100 mm for the in-flight glass melting, a smaller gap distance, 80 mm, was also investigated. As the adjustment of the flow rate cost much time in the case of 12-phase AC arc, and the electrode erosion is expected to be substantial with Ar flow rate of 3 L/min, the effect of Ar shield gas flow rate on the discharge behavior was conducted in 6-phase AC arc (Table 2.4). The experiments presented above are all performed using tungsten electrode diameter of 6 mm. For a comparison with the old setup that used smaller electrode diameter of 3.2 mm, experiments were taken both in the CW and the FF pattern (Table 2.5). An orifice ring which can create swirl flow of Ar gas was made for the 3.2 mm electrode. Experimental conditions for the effect of swirl flow are shown in Table 2.6. For 6-phase AC arc, the effect of Ar gas flow rate was also investigated.

2.2.4 Experimental Procedures

The ignition procedure of multi-phase AC arc and the discharge behavior measurement by high-speed camera were conducted in the following manner.

- Preparation of electrodes

1) Check out if the electrode tip has come out from the water-cooled jacket nozzle exit and adjust the length to 5 mm.
2) If there is an oxide film on the electrode surface, remove it by using a grinding machine.
3) Insert the 12 electrodes from the side of the chamber. Connect the inlet and outlet cooling-water tube of electrode part and jacket part, respectively. Connect the Ar shield gas tube.
4) Use the servomotor to control the electrode position. One pair of the opposite electrodes at the upper layer are set to the gap distance of 2~3 mm for arc ignition. The other four electrodes at the upper layer are set to the diameter of 60 mm. The six lower electrodes are set to the diameter of 80 mm.
5) According to the experiment electrode configuration, connect the power cable to each electrode.
6) Adjust the power transformer corresponding to each electrode and set it to the target current value.

- Preparation of arc ignition (manipulate the operator control panel)

1) Put in the breaker for multi-phase AC arc (300 A), and then the main breaker in the operator panel.
2) Start the cooling-water system for the chiller unit, the cooling-water pump for the chamber, electrode and jacket, respectively.
3) Start the exhaust gas equipment (bag filter system).

4) Introduce the Ar shield gas into the electrode.

5) Put in the break (1~12) for the electrodes of the welding transformers.

6) Turn on the operation switch (1~12) for each electrode.

7) Turn on the power switch of high frequency generating equipment to ignite the arc. If the arc does not ignited, operate the servomotor to adjust the electrode gap distance. (One can also check whether current is flowing from the board of the operator control panel)

8) After the main arc is ignited, turn off the power switch of high frequency generating immediately. Retreat the electrodes until reach the gap distance of 100 mm.

- Observation of arc discharge behavior

1) Make sure the high-speed camera are installed above the chamber before ignition of the arc. Place a shading glass (thickness of 2.6 mm) in front of the camera lens.

2) After the multi-phase AC arc discharge become stable at the desired gap distance, adjust the camera such as zoom, lens aperture and focus to clearly observe the discharge behavior.

3) Set the frame rate and shutter speed of the camera and record the discharge behavior.

- Stop the arc discharge

1) Push the stop button on the board of the operator control panel to stop the discharge.

2) Stop the Ar shield gas five minutes after the arc stop to prevent the high-temperature of the electrode.

3) Keep on the water cooling until the temperature falls to the room temperature.

4) Turn off the breaker of the welding transformers. Turn off the breaker of the cooling water system for all parts. Turn off the bag filter system and the breaker. At last turn off the main breaker in the operator panel.

2.2.5 High Speed Image Analysis

The high speed image process for analysis the fluctuation of arc luminance area was conducted in the following procedures.

1) The captured video images were selected at pixel of 768×766 and saved to individual images as bitmaps in an interval time of 0.1 ms.
2) Convert each BMP file to CSV document.
3) Document image binarization by using C code programme. Define the calculate region and set the threshold value to 50. Then each pixel in an image is converted into one bit as “1” or “0” according to the threshold value.
4) Calculate the white luminance area according to pixel scale to obtain the arc luminance area (mm^2) of each image.
5) Program batch process of the 4000 high-speed images to acquire the time fluctuation of luminance area in the range of 400 ms.

The following shows the procedures of image analysis to obtain the arc existence time in one AC cycle.

1) The captured video images were selected at pixel of 768×766 and saved to individual images as bitmaps in an interval time of 0.1 ms.
2) Convert each BMP file to CSV document.
3) Document image binarization by using C code programme with threshold value of 20.
4) Accumulate the binary images of 10 discharge cycles (200 ms).
5) Convert the accumulate document into contour map which the colour indicates the arc existence time in one discharge cycle. The luminance area is assumed to be the arc existence area or the high-temperature area.

2.3 Results and Discussion of Spatial Characteristics of the Multi-Phase AC Arc

2.3.1 Discharge Behavior of the Multi-Phase AC Arc

Figure 2.8 shows the stable discharge with an electrode separation across a diameter of 100 mm observed by high-speed camera with the frame rate of 5000 fps and shutter speed of 25 μs. The luminance area is the arc existence area or the high temperate area. The discharges appear brighter in the center, indicating higher plasma temperature at the arc center.

The discharge behavior in the CW pattern in one discharge cycle of 20 ms is shown in Fig. 2.9 with the camera frame rate of 10000 fps and shutter speed of 0.37 μs. The maximum electrical field is between opposite in CW electrode configuration, hence the main arc is ignited between opposite electrode. The discharge behavior indicates multi-paths of the arc among the different electrodes. Due to the discharge between upper and lower layers, the arc channels are complex combinations of parallel and antiparallel discharges. There are mainly two discharge forms can be observed in CW pattern. One is characterized with parallel long arcs across the central, such as in the time of 7.0 and 13.0 ms. The main feature of another discharge form is two interval electrodes are connected with two small arcs by discharge with the same electrode between them, which can be seen in time of 1.0 and 8.0 ms. Observing the discharge photos from the high-speed video, the same discharge form appeared periodically and has an anti-clockwise rotation.

Fig. 2.10 shows the discharge behavior in the FF pattern. Compared to the CW pattern, it has couples of strong and medium-length arcs. The arc discharge almost takes place between two electrode intervals and no arc path is apparent in the central region. Observing the discharge photos from the high-speed video, almost the same discharge route repeated after 10 ms and shift in counter-clockwise.

From the above results, in 12-phase AC arc, the arcs are always existed in the nozzle cross section and both of the discharges act as a diffuse large volume of plasma. The continuous discharge was caused by the easier re-ignition due to the co-existing other arcs, which is the biggest advantages compared to single- or three-phase AC arc. Each electrode displays a series of behavior like arc swing, extinction and re-ignited according to the phase rotation of the 12-phase AC power source. The swing of discharge point is caused by the Lorentz force derived from other arcs. The most special feature of discharge in the multi-phase AC arc compared to the other electric arc discharges is the arc movement and rotation in a large discharge volume. This characteristic is expected to perform efficient gas heating in large space range. The difference in the behavior of the different electrode configurations can be considered in terms of the difference arc path lengths and the effects of alternative paths provided by the ionized gas from arcs between other electrodes.

2.3.2 Effect of Electrode Configuration on the Spatial Characteristics of Arc

The different plasma shapes and electric arc column indicate the diverse discharge path and arc temperature distribution for each configuration. The analysis of the high-speed video images was carried out to estimate the arc existence area for the 12-phase AC arcs. The luminance area of each image was analyzed at threshold of 15 and accumulated in ten discharge cycles. It was then averaged by ten to obtain a relatively reasonable data represents for one discharge cycle.

Figure 2.11 (a) shows the distribution of arc existence time with CW pattern at discharge diameter of 100 mm. The color of the contour maps indicates the length of time (ms) where the arc existed. In order for a better comparison, the time table was set to a range of 10 ms. It can be seen that the arc existence time is the longest near the electrode region. Moreover, the CW

pattern exhibits a relatively uniform distribution of plasma region as the arc existed everywhere in the whole space.

Figure 2.11 (b) gives the arc existence time distribution in FF pattern. Compared to the CW pattern, it shows no existence of arc in the center region. This result is in agreement with the high-speed video. The difference of the arc existence area in the two electrode patterns was caused by the different arc discharge paths. According to the snapshots as explained before, there is long arc across the central in CW pattern and the same discharge path shifts counter-clockwise in one AC cycle. While in the FF pattern, there is no arc path in the central region. Another big difference between two electrode patterns is the arc existence time between the adjacent electrodes. CW pattern shows a short time of arc existence at the edge around the discharge region. In the case of FF pattern, the arc existed area seems to be constricted towards the nozzle exit. These phenomena should take into account the arc swing motion.

Figures 2.12 (a) and (b) give the contour maps of the existence time of the arc around the electrode region both in the CW and FF patterns. The arc swing angle in CW pattern is apparently wider than that of FF pattern. As has been pointed out before, the swing of discharge point is caused by the Lorentz force derived from other arcs. The arc re-ignition in CW pattern is occurred between the adjacent electrodes due to the strong Lorentz force generated by the next electrode. So the re-ignition occurs from the side of the electrode surface. For the same reason, the arc extinguished from the other side of the surface due to strong Lorentz force generated by the next electrode. The arc behavior near electrode has been researched deeply in our previous works (Tsuruoka 2011). In the case of FF pattern, according to the phase shifting order which has been shown in Fig. 2.7, the next maximum of arc voltage occurs at the opposite side. The Lorentz force by the other arcs is relatively small due to the long distance thus the arc swing is small. It can be indicated that larger arc swing angle attributed to the wider distributed

high-temperature region.

The spatial characterization of different electrode configurations showed important understanding for the multi-phase AC arc. In CW pattern, the electrodes were initially connected in diametrically opposed pairs, thus a large volume of ionized gas can be generated filling the region between the electrodes. So that large volume coalesced discharges are produced. In FF pattern, the high-temperature region was most effectively constricted toward the nozzle axis but could not diffuse to the center. The probability of the existence of arc can be considered concentrated between the electrodes around the edge of the conduction zone. From the above analysis results, the high-temperature region can be controlled according to the processing requirements by different electrode configurations. Moreover, the spatial uniformity in the whole arc region is important for the efficiency of particle treatment.

2.3.3 Effect of Electrode Gap Distance on the Spatial Characteristics of Arc

The electrode gap distance is important on the processing capacity during the powder treatment of the multi-phase AC arc because the electrode distance is directly related to the high-temperature volume of the plasma. However, longer electrode distance leads to higher arc voltage of the discharge. Figures 2.13 (a) and (b) show the arc existence time of the 12-phase AC arc during a discharge cycle with CW pattern at electrode distance of 100 and 80 mm, respectively. Wider electrode distance leads to larger high-temperature volume resulting in the larger processing capacity. On the other hand, decrease the distance of separation between electrodes resulted in the longer arc existence time in the center, which can be related to the more durable arc between the opposite electrodes.

The similar result in the case of the FF pattern can be obtained from Fig. 2.14. When shorten the distance among the 12 electrodes, the couples of arc between the adjacent or interval

electrodes moved close to the central. It resulted in the long time of arc existence in the center area although the FF pattern has short discharged arcs.

In the multi-phase AC arc, the current kept about the same value. The farther apart the electrodes are, the greater the voltage required to recreate the same unit of current flow. When the electrode moved closer towards each other, the resistance decrease resulted in the lower arc voltage. Above all, the reduction of the gap distance results in an improved homogeneity of the plasma. From a viewpoint of material processing, the multi-phase AC arc is a suitable heat source that the electrode gap distance can be adapted for the process needs such as the amount of material and input power.

2.3.4 Effect of Argon Shield Gas Flow Rate on the Spatial Characteristics of Arc

According to our previous study of the electrode erosion mechanism in the multi-phase AC arc (Tanaka et al. 2013a, b), the tungsten becomes the main species in the arc during the anodic period when it started to evaporate. In a general running condition, the Ar gas flow rate is set at 5 L/min and the average erosion rate for each electrode is about 0.3 mg/min. If the shield gas flow rate decrease below 5 L/min, the erosion rate of electrode could increase sharply (Ikeba 2013). As the adjustment of the flow rate cost time during the experiment in the case of 12-phase AC arc, and the electrode erosion is expected to be substantial with Ar flow rate of 3 L/min, the effect of Ar shield gas flow rate on the discharge behavior was conducted in the case of 6-phase AC arc.

Figure 2.15 shows the arc existence time of the 6-phase AC arc (electrode distance of 100 mm) during one AC cycle in CW pattern at different Ar flow rates of 3, 5 and 10 L/min. With increasing the gas flow rate of Ar, the arc existence area is more concentrated in the center region. This is due to the “thermal pinch effect” thus the arc cross section decreased, and the

axial magnetic field is applied to the forced elongated arc. As the gas flow rate increases, the arc voltage increases because the elongated arc demands more power to sustain itself.

Figure 2.16 shows the contour map of the existence time of arc and the swing angle at different Ar gas flow rate corresponding to the Fig. 2.15. When focus on the single electrode, increase the gas flow rate leads to the narrow arc swing angle. It seems like the arc column becomes narrow and longer. However, large amount of shield gas flow may cause the cooling effect that could reduce the stability of plasma.

From the above studies, it indicates that other than shorten the electrode distance, increase the injection shield gas flow can also result in the longer arc existence time in the center. This can help to enhance the thermal efficiency in the powder treatment. However, the optimal gas flow rate must be considered with the electrode erosion rate and the plasma stability. In other words, the large plasma volume and uniform high temperature distribution can be obtained by optimize the parameters of electrode distance as well as the Ar gas flow rate.

2.3.5 Effect of Tungsten Electrode Diameter on the Spatial Characteristics of Arc

In our previous study of the electrode temperature and molten area, it has been found that the erosion rate of 3.2 mm diameter was higher than that of 6 mm electrode (Ikeba 2013). For the sake of experiment's convenience and also to increase the running time of the multi-phase AC arc system, the tungsten electrode with 6 mm is usually used. Therefore, the arc spatial characteristics using different diameter of electrode are important in the in-flight particle process.

Figures 2.17 (a) and (b) show the arc existence time of the 12-phase AC arc during one cycle in CW pattern with tungsten diameter of 3.2 mm and 6 mm, respectively. The high-temperature region is broadened with decrease the electrode diameter. Figure 2.18 shows

the arc existence time of the 12-phase AC arc during one cycle in FF pattern with tungsten diameter of 3.2 mm and 6 mm, respectively. Similar with the CW pattern, the smaller diameter of tungsten leads to wider arc distribution around electrode.

Figure 2.19 gives the comparison contour map of different electrode diameters at Ar flow rate of 5 L/min in CW pattern. The smaller diameter of electrode leads to the increase of the swing angle. In the case of larger diameter of electrode, the discharge point is more concentrated on narrow area. This can be related to the different ignition condition for two electrode sizes.

Figure 2.20 shows the representative waveforms of current and voltage with different electrode diameters in CW pattern. The re-ignition voltage (the first peak when the voltage becomes positive) of the smaller electrode is lower, which means the electrode is easier to discharge with adjacent electrodes. Also, the re-ignition is occurred at the side surface of electrode, thus the arc swing angle is wider. This phenomenon will cause the wider molten area in the electrode surface, also relate to the higher electrode erosion. Moreover, larger molten area leads to lower tip temperature. It can be expected that the average temperature in the plasma with small electrode diameter is lower than that of larger diameter.

The tungsten electrode diameter can have significant difference in the process by multi-phase AC arc. Considering for the low erosion rate of electrode and efficient thermal heating, using larger electrode size is better. One point is that the arc re-ignition voltage increased due to small molten area. However, under usual experiment condition, the plasma is very stable with the 6 mm electrode. If the process adds some other external parameters such as an oxy-fuel flame, it is necessary to consider the disturbance on the plasma instability.

2.3.6 Effect of Argon Swirl Flow on the Spatial Characteristics of Arc

An orifice ring with four holes was set at the nozzle exit inside of the torch to make clockwise swirling or vortex flow of Ar shield gas. The schematic of the plasma torch with tungsten diameter of 3.2 mm and the orifice ring is shown in Fig. 2.21. This ring was specially customized for tungsten diameter of 3.2 mm, therefore, no experiment was done with the 6 mm electrode. Experimental conditions for the investigation of effect of Ar swirl flow are listed in Table 2.6. The 6-phase (CW pattern) and 12-phase (CW and FF pattern) AC arc with swirl flow were investigated. Moreover, the different flow rate of Ar with 3, 5 and 10 L/min in the 6-phase AC arc were compared.

Figure 2.22 shows the snapshots of the re-ignition in 6-phase AC discharge with the usual straight flow method and the representative waveforms of arc voltage and current. The yellow arrow in the snapshot at time of 0.4 ms indicates the re-ignition of arc. In the 6-phase AC arc with CW pattern, the re-ignition also occurred between adjacent electrodes. Once the arc was generated, it moves toward the main arc region periodically.

Figure 2.23 shows the snapshots of the re-ignition in 6-phase AC discharge with the swirl ring and the synchronized voltage and current waveforms. It was thought that with the design of swirl or vortex flow of the shielding gas, low pressure in the core center and high pressure at the edge of the swirling flow cause higher re-ignition voltage. This can also be seen from the snapshots at time of 0.4 ms in Figs. 2.22 and 2.23 that the arc occurs easily in the case of direct gas flow. Moreover, the mean value of the arc voltage is smaller in the case of swirl flow. This indicates that after the re-ignition, it is easier to sustain the discharge.

Figures 2.24 give the arc existence area averaged in one discharge cycle at different Ar gas flow rate (a) with and (b) without the swirl flow in the 6-phase AC arc. With both gas flow methods, increase the Ar gas flow rate caused extension of the high-temperature region toward to the center. Moreover, under the swirl flow of Ar gas, it is expected to develop a stronger gas

flow in the axial direction out of the nozzle, thus the high-temperature region distributed wider in the center as shown in Fig. 2.24 (b).

Figures 2.25 represent the contour map of the existence time of 6-phase AC arc at Ar gas flow rate of 5 L/min and the arc swing angle was evaluated (a) with and (b) without the swirl flow. The swirling flow clearly affects the arc swing angle thus caused different spatial characteristics of the arc. The vortex injection of the plasma shield gas can help the constriction of the arc column. However, the re-ignition of arc also becomes more difficult due to the high pressure at the edge. Thus the arc voltage fluctuation is expected to be higher.

The 12-phase AC arcs with the swirl flow were also investigated and the results of CW and FF pattern are shown in Figs. 2.26 and 2.27, respectively. In both electrode patterns, the arc was more concentrated to the central area compared to the result without swirl ring. This phenomenon is similar with the case of 6-phase that has been discussed in Fig. 2.24.

Base on the above results of two kinds of gas flow patterns, the vortex flow pattern exhibits forced-elongated arc which was more constricted locally than the straight flow pattern. The gas flow pattern clearly affects the arc ignition condition thus fatherly affect the spatial characteristics of plasma. The constricted arc column is expected to provide high energy for material treatment. However, the increasing in the re-ignition voltage should be taken into account to lower the instability of multi-phase AC arc.

2.4 Results and Discussion of Temporal Characteristics of the Multi-Phase AC Arc

2.4.1 Effect of Electrode Configuration on the Plasma Fluctuation

The spatial homogeneous of plasma have been discussed above through evaluation of the arc distribution in one AC cycle. The multi-phase AC arc does not only have spatial

instability but also display time variance feature due to the arc experiences discharge, distinction and re-ignition according to the applied AC current. The temporal fluctuation of plasma should be decreased to achieve uniform heating of in-flight particles. Therefore, various factors have been investigated.

Fluctuation of the multi-phase AC arc was characterised by the luminance area. Results of time variation of arc luminance area in CW and FF patterns during 400 ms period are presented in Fig. 2.28. It can be noted that the average values of the fluctuation are similar to each other, while the fluctuation amplitude of CW pattern is higher than that of FF pattern. As can be seen from Figs. 2.9 that the maximum electrical field is between opposite in CW electrode configuration, hence the main arc is ignited between opposite electrodes. Additionally a number of alternative paths also exist in the complex discharge behavior of CW pattern. The multi arcs exist at same moment can cause complex Lorentz force from other arcs. It can be assumed that the real arc path may differ from the idea electric discharge path. Due to the transient variation of different discharge patterns, the arc luminance area changed immediately thus cause large fluctuation. In contrast to the CW pattern, FF pattern provides a well-defined conducting path between intervals or nearby electrodes which can be seen from Fig. 2.10. The multi arcs are separated from each other so the Lorentz force driven by other arcs is relatively small. The arc length keeps regular and similar result in the small fluctuation of luminance area.

As the luminance areas in CW and FF patterns show different spatial distribution that has been discussed in the section 2.3.3, the time variation of arc luminance area at different analyzed diameter of 60, 80 and 100 mm are compared as shown in Fig. 2.29. The results of CW and FF pattern in time period of 100 ms are presented in Fig. 2.30 with different considered diameters. The average value of luminance area is obviously increased along with the calculated

diameter, which is consistent with the above discharge images. Also, the FF pattern leads to relatively low fluctuation amplitude of the luminance area compared to the CW pattern at the same considered diameter. In the in-flight treatment, the diameter of the particles plume may change due to powder feeding condition. The instability of arc luminance area at different space diameter would be an important factor in the uniformity of particles.

The multi-phase AC arc shows temporally fluctuation due to AC power frequency of 50 Hz. The plasma features repeated after a period of 20 ms. If this characteristic time is relatively long or comparable to the powder residence time in the plasma, the fluctuation of arc is expected to affect the injection raw materials. One possible perspective to avoid the fluctuation of arc on the injected powders is to decrease the fluctuation from the original power source, such as using a higher frequency larger than 500 Hz.

2.4.2 Fast Fourier Transformation of Arc Luminance Area

The CW and FF pattern display the rotating discharge behavior in the clockwise direction. The periodicity of the fluctuation of plasma high-temperature region can be understood by considering the Fast Fourier Transform (FFT) analyzes. The results of the frequency spectra of arc luminance area at analyzed diameter of 100 mm of CW and FF patterns are shown in Figs 2.31 (a) and (b), respectively. Both of the patterns display a remarkable peak of 300 Hz. As the supply frequency of multi-phase AC arc is 50 Hz, six pairs of electrodes discharge will display a harmonic frequency of 300 Hz. The FFT signal of arc fluctuation with the FF pattern shows clear peaks than the CW pattern. This can be explained by the stable well defined arcs which show a regular periodical fluctuation.

The frequency spectra of arc luminance area at analyzed diameter of 80 mm of CW and FF patterns are shown in Fig. 2.32. The frequency which has the most significance in both of the

electrode patterns is 300 Hz. Moreover, the 100 Hz becomes obvious in the CW pattern, due to the luminance area reaches the maximum value every 10 ms. Figure 2.33 shows the frequency spectra of arc luminance area at analyzed diameter of 60 mm with CW and FF patterns. Despite of the peak at 300 Hz, CW appears a couple of harmonic frequencies at similar strength. However, FF pattern reveals no other strong peaks. This is possibly due to the long arc path across the center region in CW pattern, while almost no arc exists in the case of FF pattern.

Figure 2.34 summarize the amplitude of frequency spectra with different analyzed diameters in CW pattern. The amplitude of the typical 300 Hz increases with the larger analysis discharge area. In the whole plasma region, the frequency of 50 Hz becomes the main species. Figure 2.35 gives the amplitude of frequency spectra with different analyzed diameters in FF pattern. The 300 Hz is the most significant peak regardless of the different analysis diameters. While the frequencies of 50 and 100 Hz are kept relatively the same, which means no representative features for the FF pattern discharge.

If the particle residence time in the plasma is shorter than the periodical arc fluctuation, the particle characteristics such as temperature is likely to be affected by the arc. Thus the evaluation on the arc fluctuation and fluctuation frequency are important.

2.5 Conclusion

The multi-phase AC arc discharge behavior was observed by a high-speed video camera and the high speed image analysis was conducted to investigate the spatial and temporal characteristics of arc. Experimental parameters such as the electrode configuration, the electrode distance, the Ar shield gas flow rate and the electrode diameter were changed and the results were compared. The obtained results in this chapter are summarized as follows.

1) The multi-phase AC arc produces a large volume of discharge plasma suitable for particle

in-flight treatment. From the discharge photos, CW pattern is characterized by the main arc between opposite electrodes rotating in the clockwise direction combined with several small alternative arc paths. On the other hand, FF pattern has a couple of strong and short discharged arcs.

2) The spatial uniformity of multi-phase AC arc was investigated for different electrode configurations. High-temperature area of CW pattern was wider than that of FF pattern. The arc swing angle was contributed to the larger high-temperature distribution of the multi-phase AC arc. The control of high-temperature region can be achieved by adjusting electrode configuration.

3) The high-temperature region in the central area can be enlarged by reducing the electrode distance or increase the Ar gas flow rate. The swirl gas flow of Ar extends the arc length in the axial direction thus makes the plasma distribution more concentrated to the central area.

4) The temporal uniformity of multi-phase AC arc was investigated. Experimental results have shown that the arc fluctuation was related with the transition of discharge patterns. Due to the transient variation of different discharge paths, the arc luminance area changed immediately thus cause large fluctuation in CW pattern. In the case of FF pattern, the arc length is regular results in the smaller fluctuation of luminance area in the whole discharge region.

5) The periodicity properties of arc fluctuation were investigated by FFT spectra. Both electrode patterns possess the typical frequency of 300 Hz of 12-phase AC arc that originated from the supply frequency of 50 Hz. Arc luminance area analyzed at different plasma area shows slight difference in the FFT spectra. CW pattern has arc path between opposite electrode and rotates in clockwise direction. Therefore, a couple of peaks can be observed in the FFT spectra even in the small analyzed diameter.

References

Coudert, J. F., M. P. Planche and P. Fauchais. “Characterization of DC Plasma Torch Voltage Fluctuations.” *Plasma Chemistry and Plasma Processing* **16**(1), 211S-227S (1996).

Duan, Z. and J. Heberlein. “Arc Instabilities in a Plasma Spray Torch.” *Journal of Thermal Spray Technology* **11**(1), 45-51 (2002).

Ikeba, T. “インフライト溶融ガラス製造に用いる多相交流アークの電極現象の解析.” *Chapter 4, Master Thesis, Tokyo Institute of Technology* (2013). (in Japanese).

Iwao, T., P. Cronin, D. Bendix and J. V. Heberlein. “Anode Attachment Instability and Anode Heat Transfer for High Intensity Arcs with Lateral Gas Flow.” *IEEE Transactions on Plasma Science* **33**(3), 1123-1128 (2005).

Kim, S., J. V. Heberlein, J. Lindsay and J. Peters. “Control of fluid dynamic instability in oxygen plasma arc cutting.” *Proc. 19th International Symposium on Plasma Chemistry* Bochum, Germany (2009).

Matsuura, T., K. Taniguchi and T. Watanabe. “A new type of arc plasma reactor with 12-phase alternating current discharge for synthesis of carbon nanotubes.” *Thin Solid Films* **515**(9), 4240-4246 (2007).

Milosheevsky, G. V., G. S. Romanov, V. I. Tolkach and I. Yu. Smurov. “Simulation of the Dynamics of Two-Phase Plasma Jet in the Atmosphere.” *Proc. of 3th International Conference on Plasma Physics and Plasma Technology* Minsk, Belarus, September, 244-247 (2000).

Ramasamy, R. and V. Selvarajan. “Current-Voltage Characteristics of a Non-Transferred Plasma Spray Torch.” *European Physical Journal D*, **8**(1), 125-129 (2000).

Sanders, N., K. Etemadi, K.C. Hsu and E. Pfender. “Studies of the anode region of a high-intensity argon arc.” *Journal of Applied Physics* **53**(6), 4136-4145 (1980).

Selvan, B. and K. Ramachandran. “Comparison Between Two Different Three-Dimensional Arc Plasma Torch Simulations.” *Journal of Thermal Spray Technology* **18**(5-6), 846-857 (2006).

Tanaka, M., T. Ikeba, Y. Liu, S. Choi and Takayuki Watanabe. “High-Speed Visualization of Electrode Erosion in Multi-Phase Alternating Current Arc.” *Journal of Fluid Science and Technology* **8**(2), 160-171 (2013a).

Tanaka, M., T. Ikeba, Y. Liu, S. Choi and Takayuki Watanabe. “Investigation of Electrode Erosion Mechanism of Multi-Phase AC Arc by High-Speed Video Camera.” *Journal of Physics: Conference Series* **441**, 012015 (2013b).

Trelles, J. P., E. Pfender and J. Heberlein. “Multiscale Finite Element Modeling of Arc

Dynamics in a DC Plasma Torch." *Plasma Chemistry and Plasma Processing* **26**(6), 557-575 (2006).

Trelles, J. P., C. Chazelas, A. Vardell and J. V. R. Heberlein. "Arc Plasma Torch Modeling." *Journal of Thermal Spray Technology* **18**(5-6), 728-752 (2009).

Tsuruoka, Y. "多相交流アークの放電現象の解析." *Chapter 3, Master Thesis, Tokyo Institute of Technology* (2011). (in Japanese).

Yang, G., P. Cronin, J.V. Heberlein and E. Pfender. "Experimental investigations of the anode boundary layer in high intensity arcs with cross flow." *Journal of Physics D: Applied Physics* **39**(13), 2764-2774 (2006).

Yang, G. and J. V. Heberlein. "Anode attachment modes and their formation in a high intensity argon arc." *Plasma Sources Science and Technology* **16**(3), 529-542 (2007a).

Yang, G. and J. V. Heberlein. "Instabilities in the anode region of atmospheric pressure arc plasmas." *Plasma Sources Science and Technology* **16**(4), 765-773 (2007b).

Zhou, X. and J. V. Heberlein. "Characterization of the arc cathode attachment by emission spectroscopy and comparison to theoretical predictions." *Plasma Chemistry and Plasma Processing* **16**(1), S229-S244 (1995).

Table 2.1 Experimental conditions for effect of electrode configuration

Discharge conditions		
Number of phase	12	
Electrode configuration	Clockwise (CW) pattern	Flip-flop (FF) pattern
Power	40~45 kW	35~40 kW
Electrode distance	100 mm	100 mm
Ar flow rate (each electrode)	5 L/min	5 L/min
Tungsten electrode diameter	φ6.0 mm	φ6.0 mm

Table 2.2 Measurement conditions for arc discharge behavior

High-speed camera	FASTCAM SA WTI (Photron)
Frame rate	10000 fps
Shutter speed	0.37 μs
Oscilloscope	ScopeCorder DL850 (Yokogawa)
Sampling rate	10^6 Hz

Table 2.3 Experimental conditions for effect of electrode gap distance

Discharge conditions		
Number of phase	12	
Electrode configuration	Clockwise (CW) pattern	Flip-flop (FF) pattern
Power	35~45 kW	30~40 kW
Electrode distance	80, 100 mm	80, 100 mm
Ar flow rate (each electrode)	5 L/min	5 L/min
Tungsten electrode diameter	φ6.0 mm	φ6.0 mm

Table 2.4 Experimental conditions for effect of Ar shield gas flow rate

Discharge conditions	
Number of phase	6
Electrode configuration	Clockwise (CW) pattern
Power	14~15 kW
Electrode distance	80, 100 mm
Ar flow rate (each electrode)	3, 5, 10 L/min
Tungsten electrode diameter	φ6.0 mm

Table 2.5 Experimental conditions for effect of tungsten electrode diameter

Discharge conditions		
Number of phase	12	
Electrode configuration	Clockwise (CW) pattern	Flip-flop (FF) pattern
Power	35~45 kW	30~40 kW
Electrode distance	100 mm	100 mm
Ar flow rate (each electrode)	5 L/min	5 L/min
Tungsten electrode diameter	φ3.2 mm	φ3.2 mm

Table 2.6 Experimental conditions for effect of the Ar swirl flow

Discharge conditions			
Number of phase	6	12	12
Electrode configuration	Clockwise (CW) pattern	Clockwise (CW) pattern	Flip-flop (FF) pattern
Ar swirl flow	without with	with	with
Power	14~15 kW	35~45 kW	30~40 kW
Electrode distance	100 mm	100 mm	100 mm
Ar flow rate (each electrode)	3, 5, 10 L/min	5 L/min	5 L/min
Tungsten electrode diameter	φ3.2 mm	φ3.2 mm	φ3.2 mm

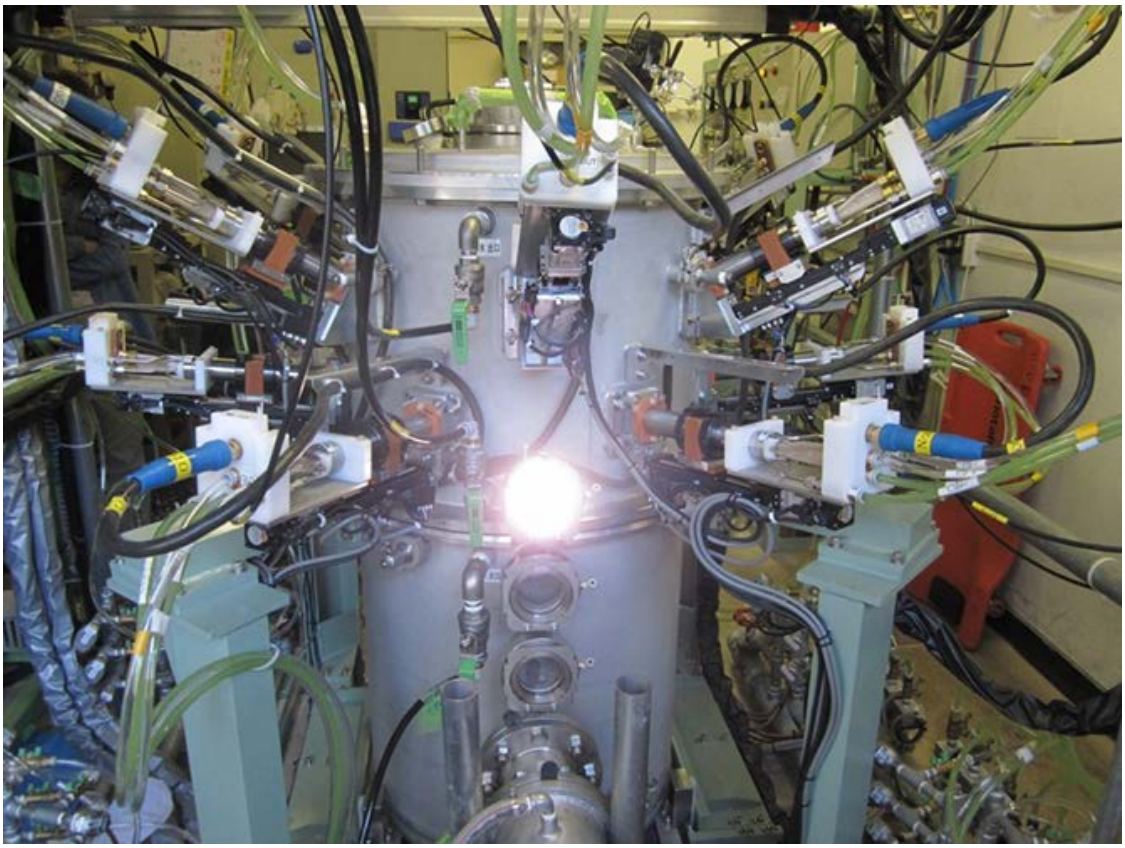

Fig. 2.1 The photograph of the multi-phase AC arc apparatus

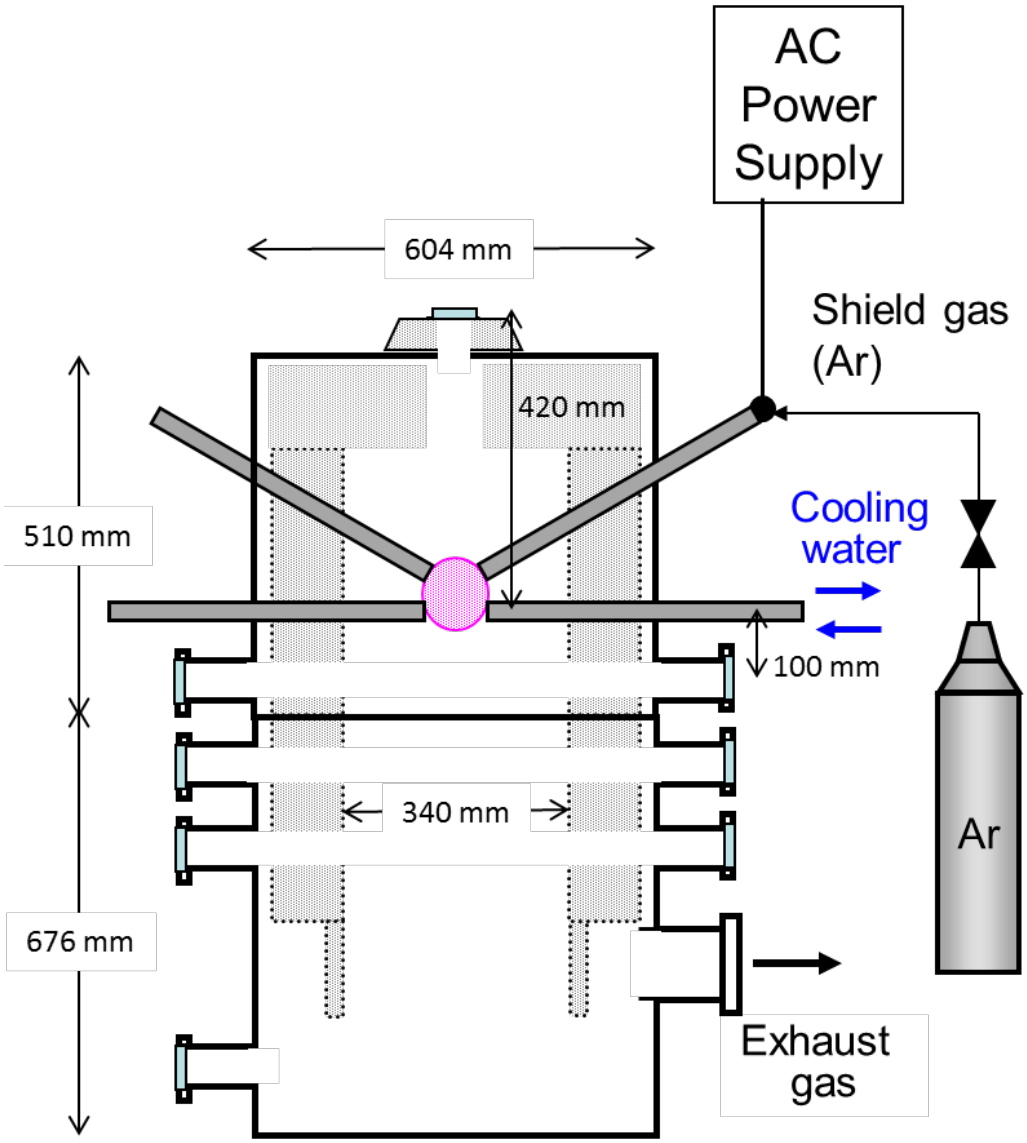

Fig. 2.2 The schematic of the multi-phase AC arc generating setup

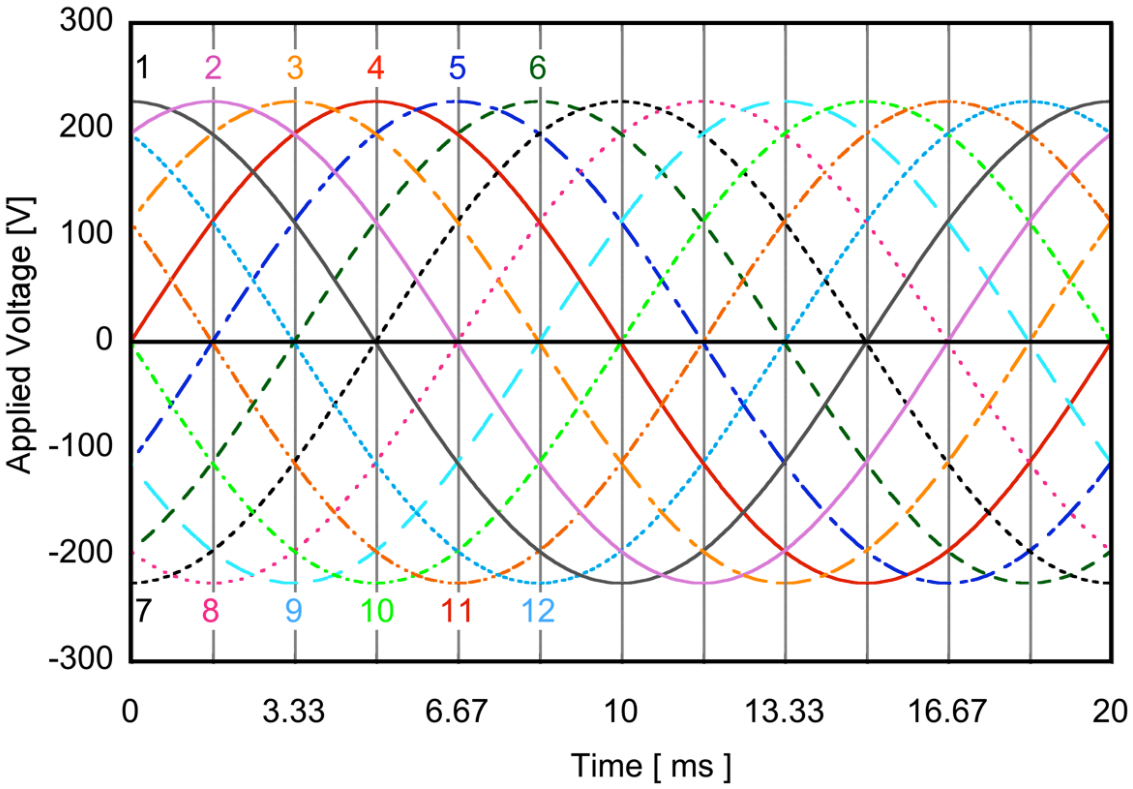

Fig. 2.3 The ideal voltage applied on each electrode

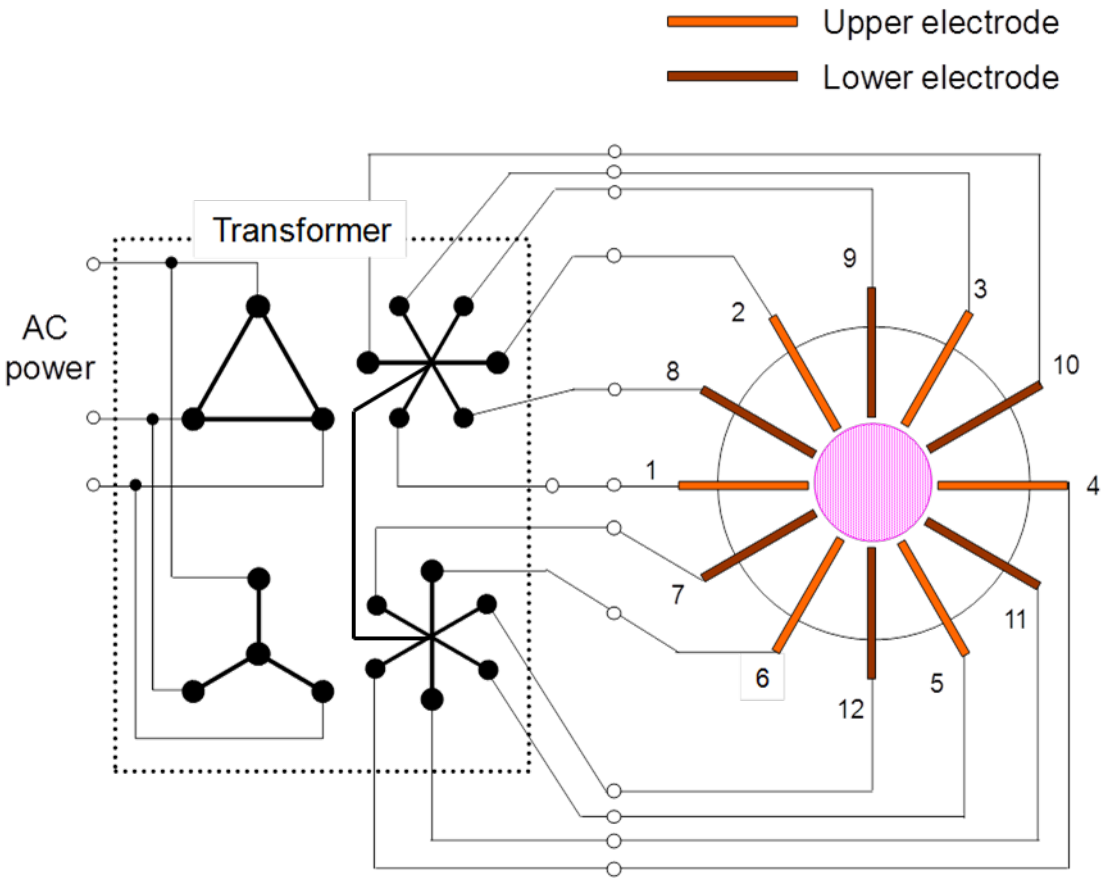

Fig. 2.4 The electrical circuit diagram and schematic connection diagram of 12-phase AC arc generation

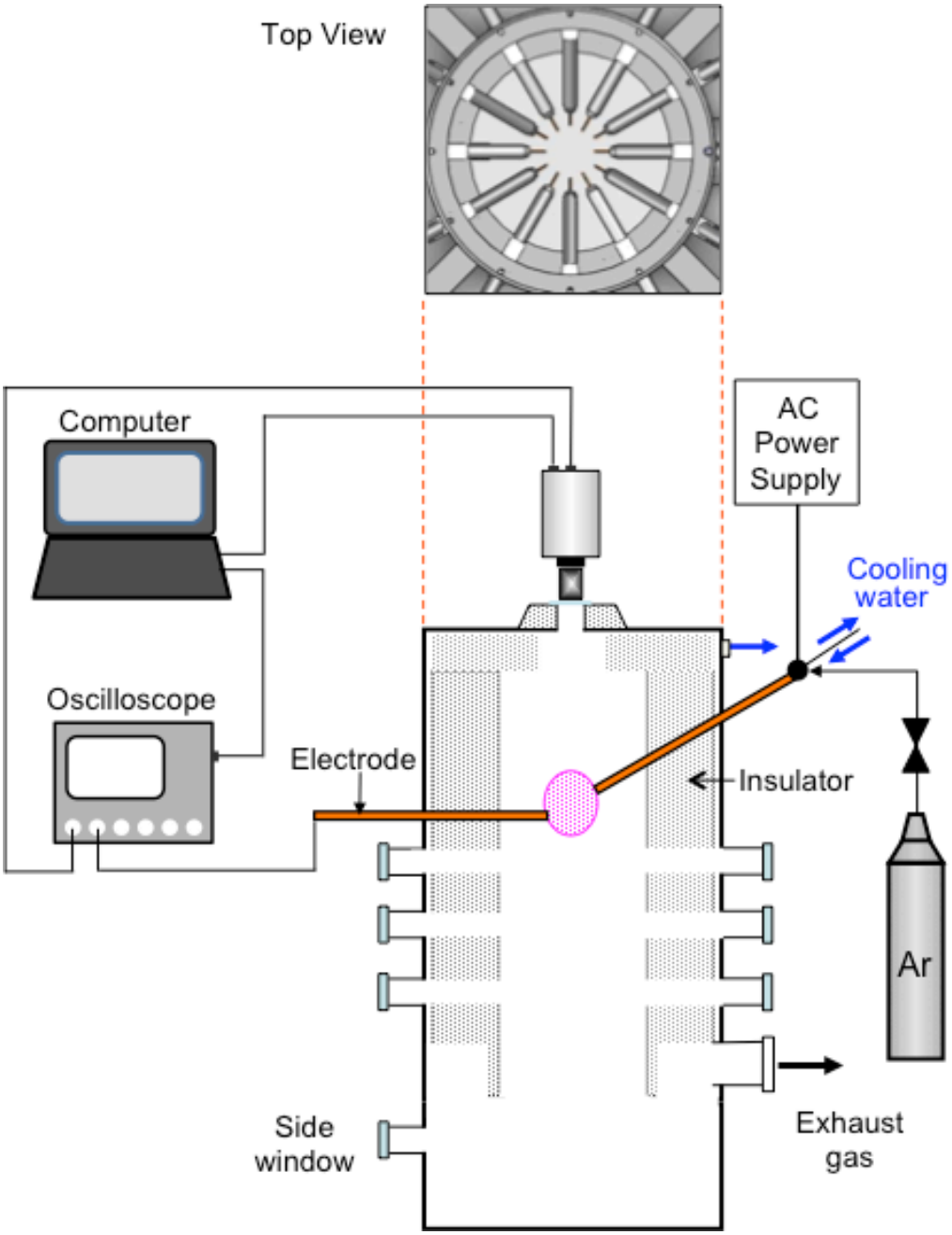

Fig. 2.5 The Schematic of the multi-phase AC arc apparatus with arc discharge behavior measurement system

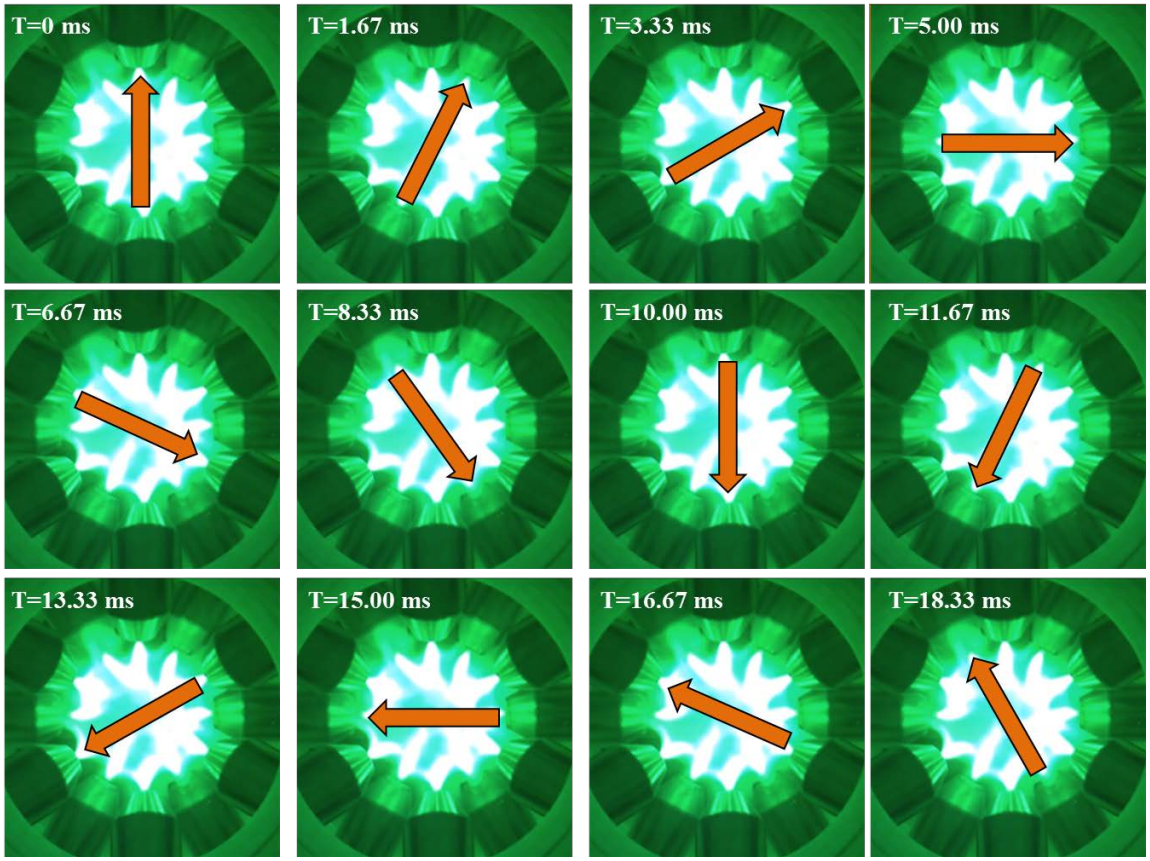

Fig. 2.6 The electrode configurations of 12-phase AC arc with the Clockwise pattern

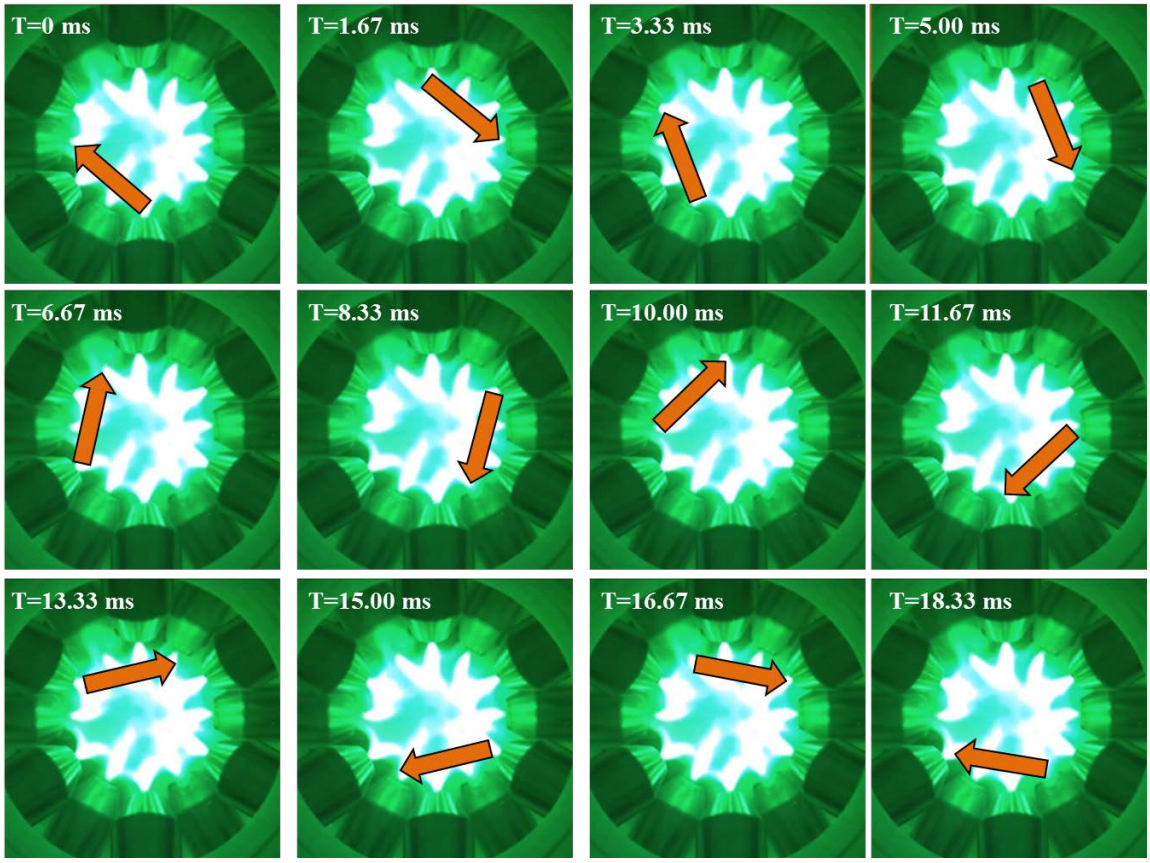

Fig. 2.7 The electrode configurations of 12-phase AC arc with the Flip-flop pattern

Fig. 2.8 The snapshot of 12-phase AC arc discharge under long exposure time of high-speed camera

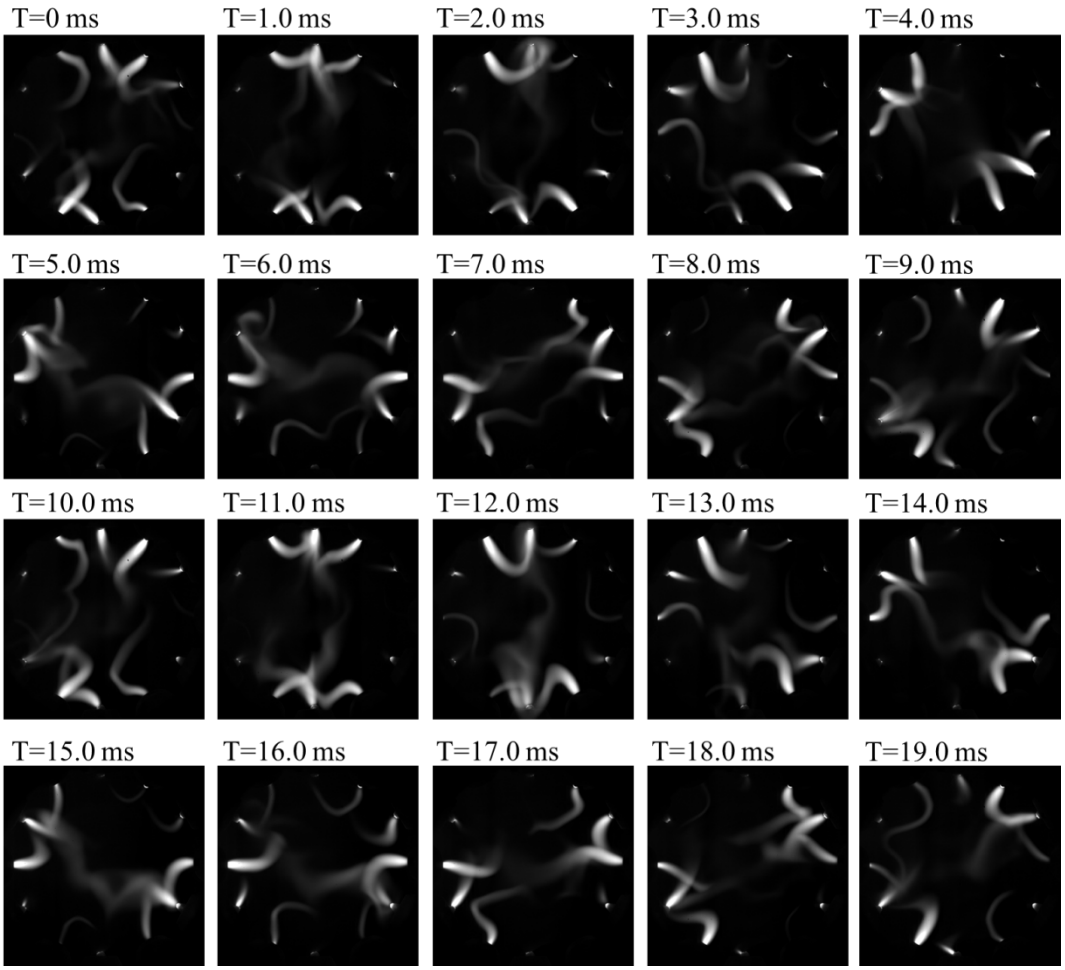

Fig. 2.9 The snapshots of 12-phase AC arc with CW pattern

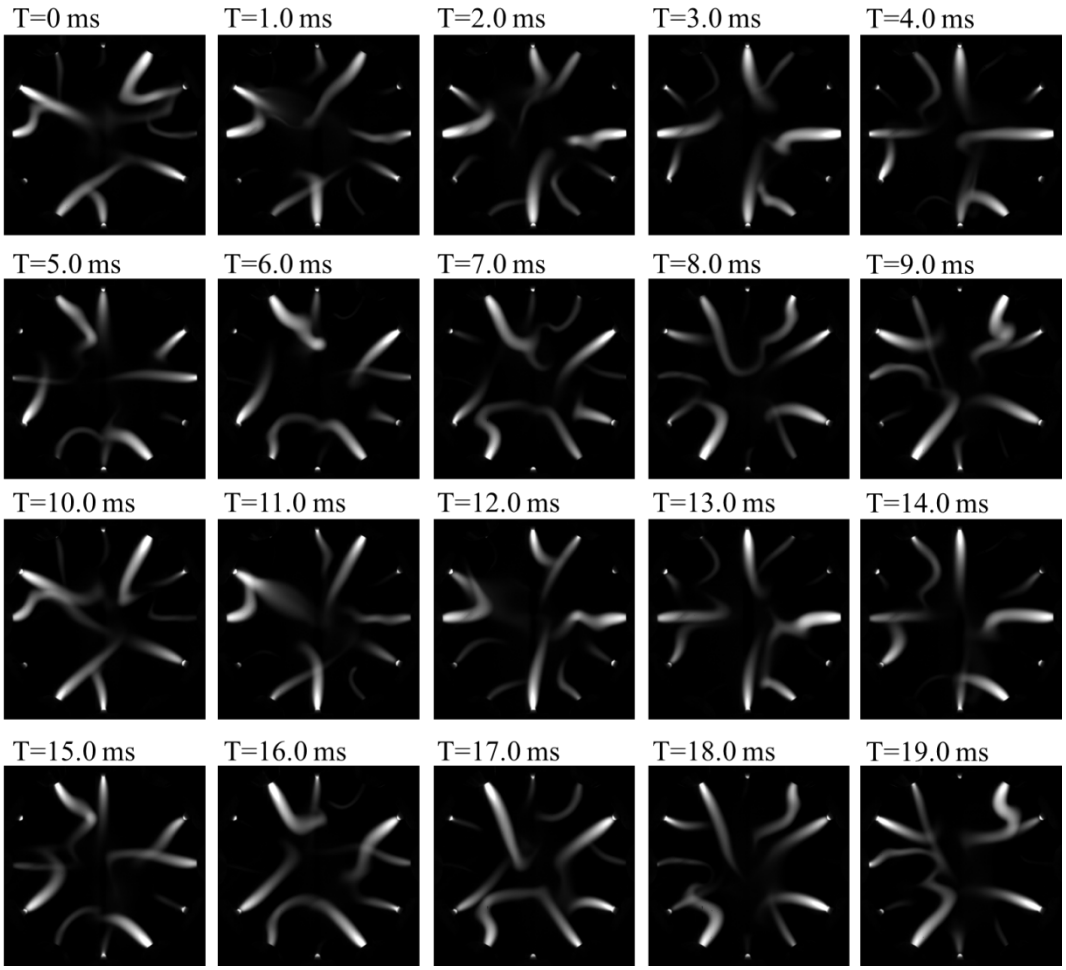

Fig. 2.10 The snapshots of 12-phase AC arc with FF pattern

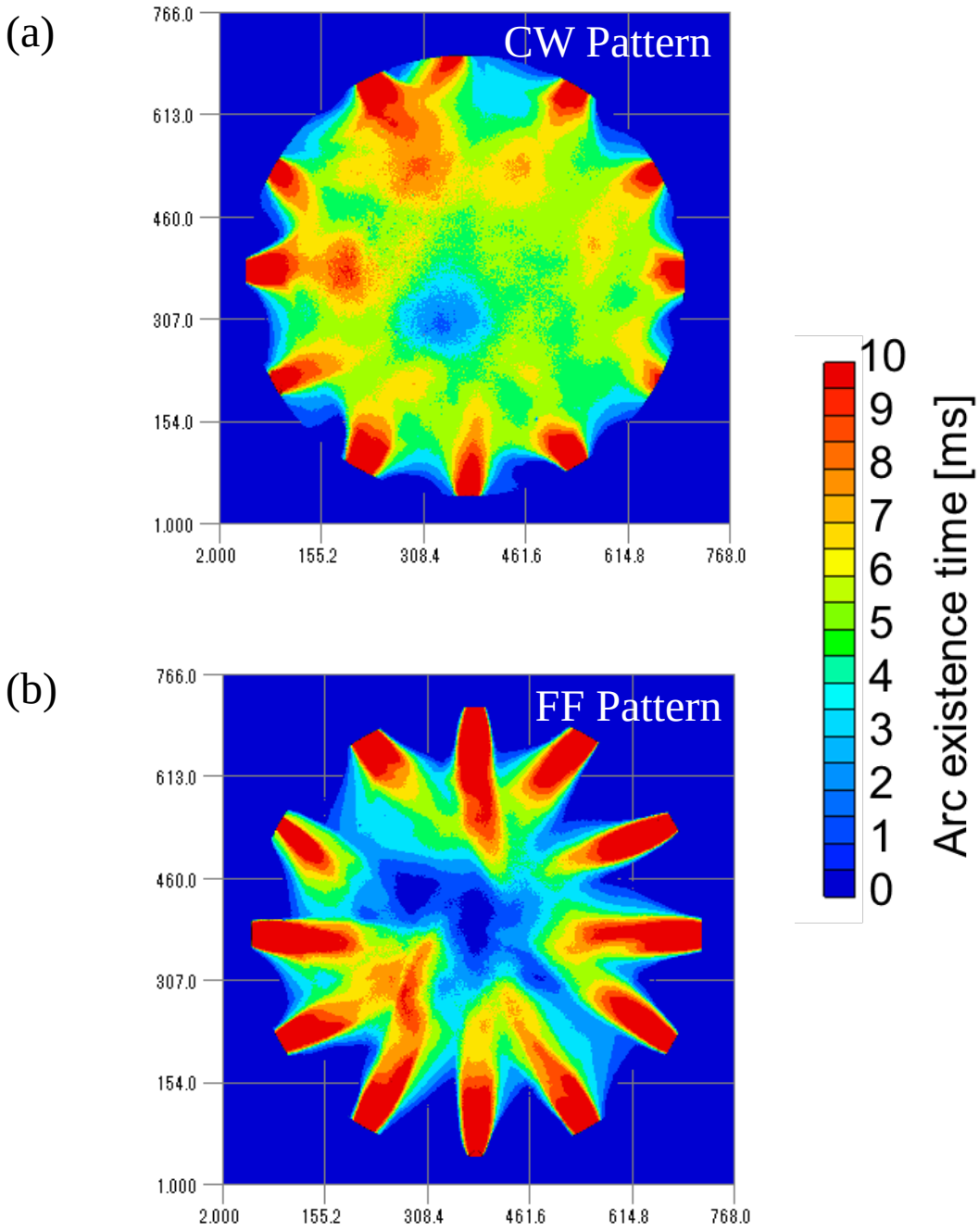

Fig. 2.11 Arc existence time of the 12-phase AC arc during an AC cycle with electrode distance of 100 mm in (a) CW pattern and (b) FF pattern

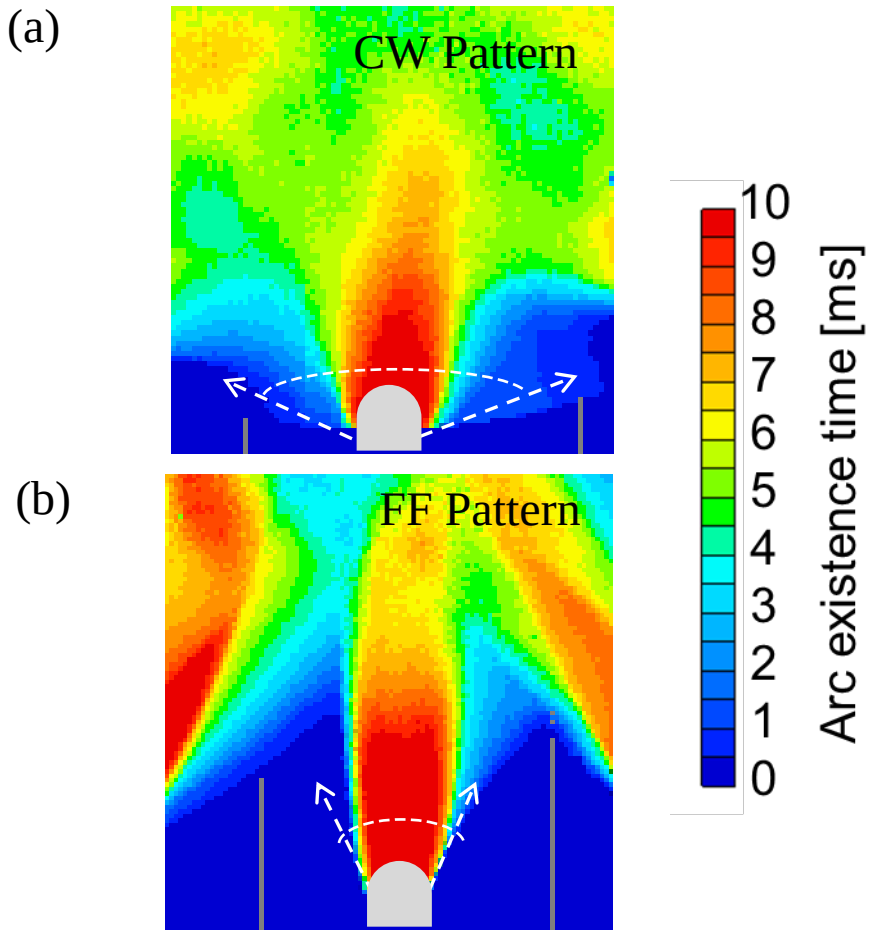

Fig. 2.12 Contour map of the existence time of 12-phase AC arc at argon gas flow rate of 5 L/min with different electrode configurations: (a) CW pattern and (b) FF pattern

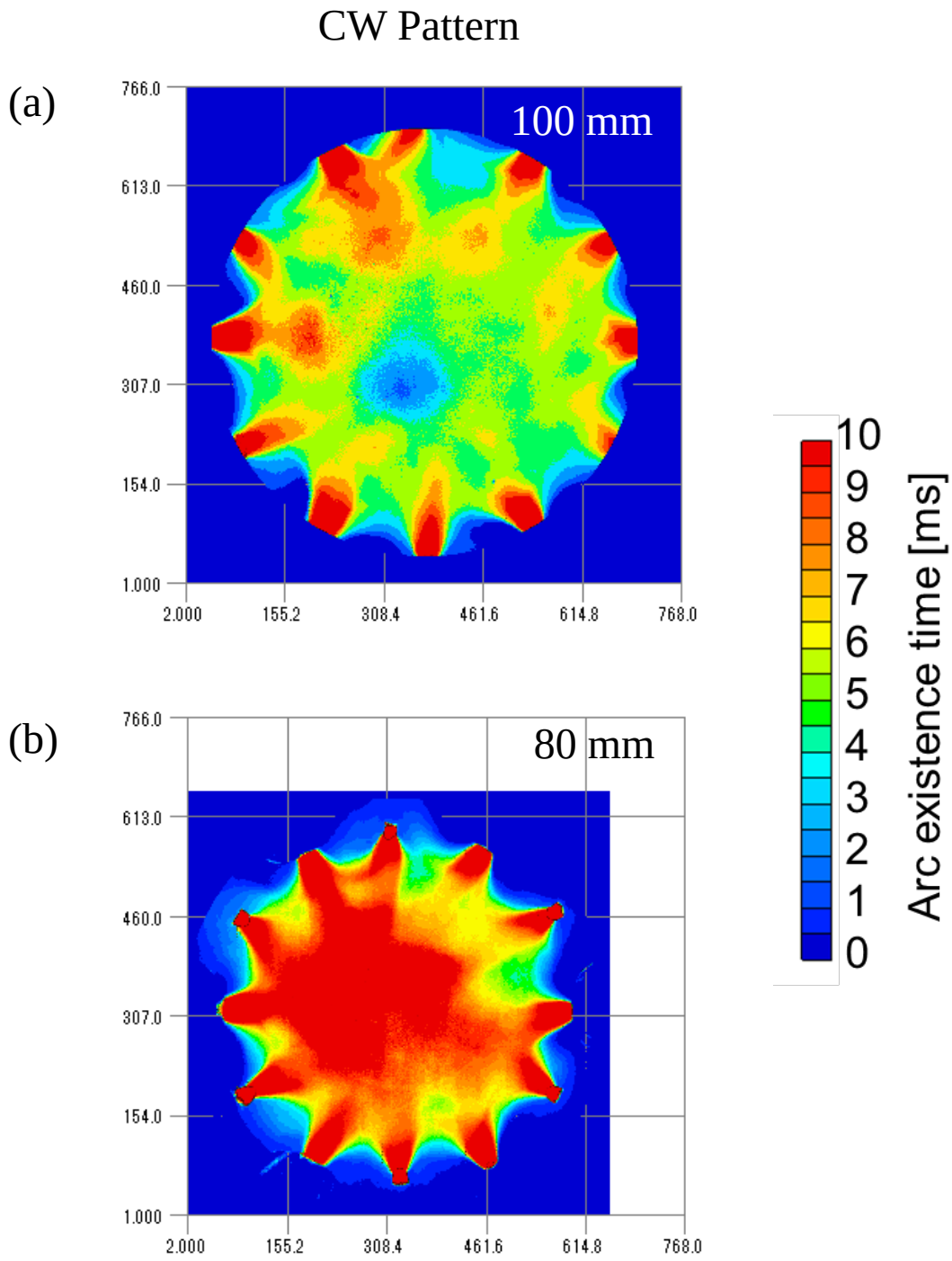

Fig. 2.13 Arc existence time of the 12-phase AC arc during an AC cycle in CW pattern at different electrode distances (a) 100 mm and (b) 80 mm

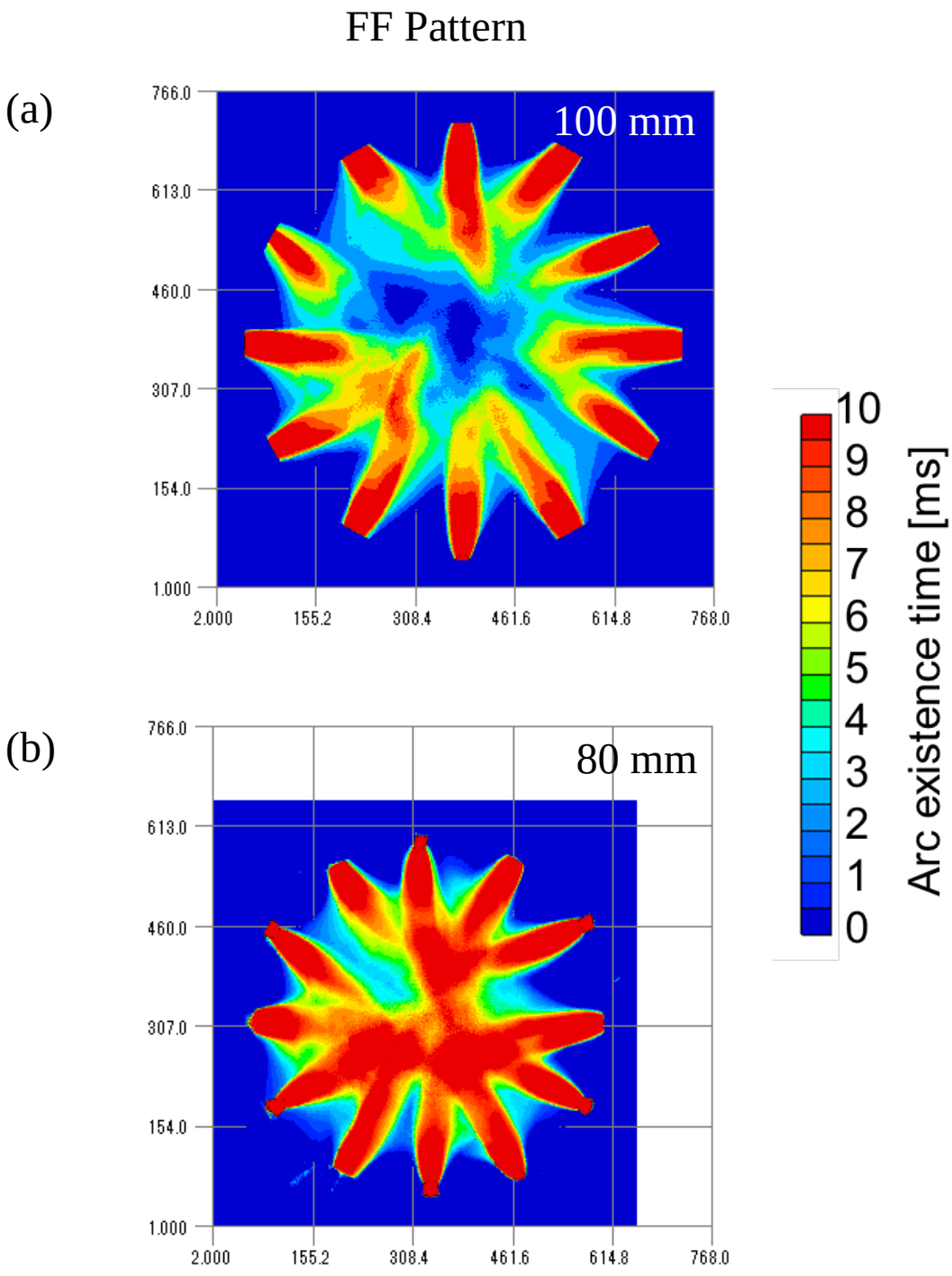

Fig. 2.14 Arc existence time of the 12-phase AC arc during an AC cycle in FF pattern at different electrode distances (a) 100 mm and (b) 80 mm

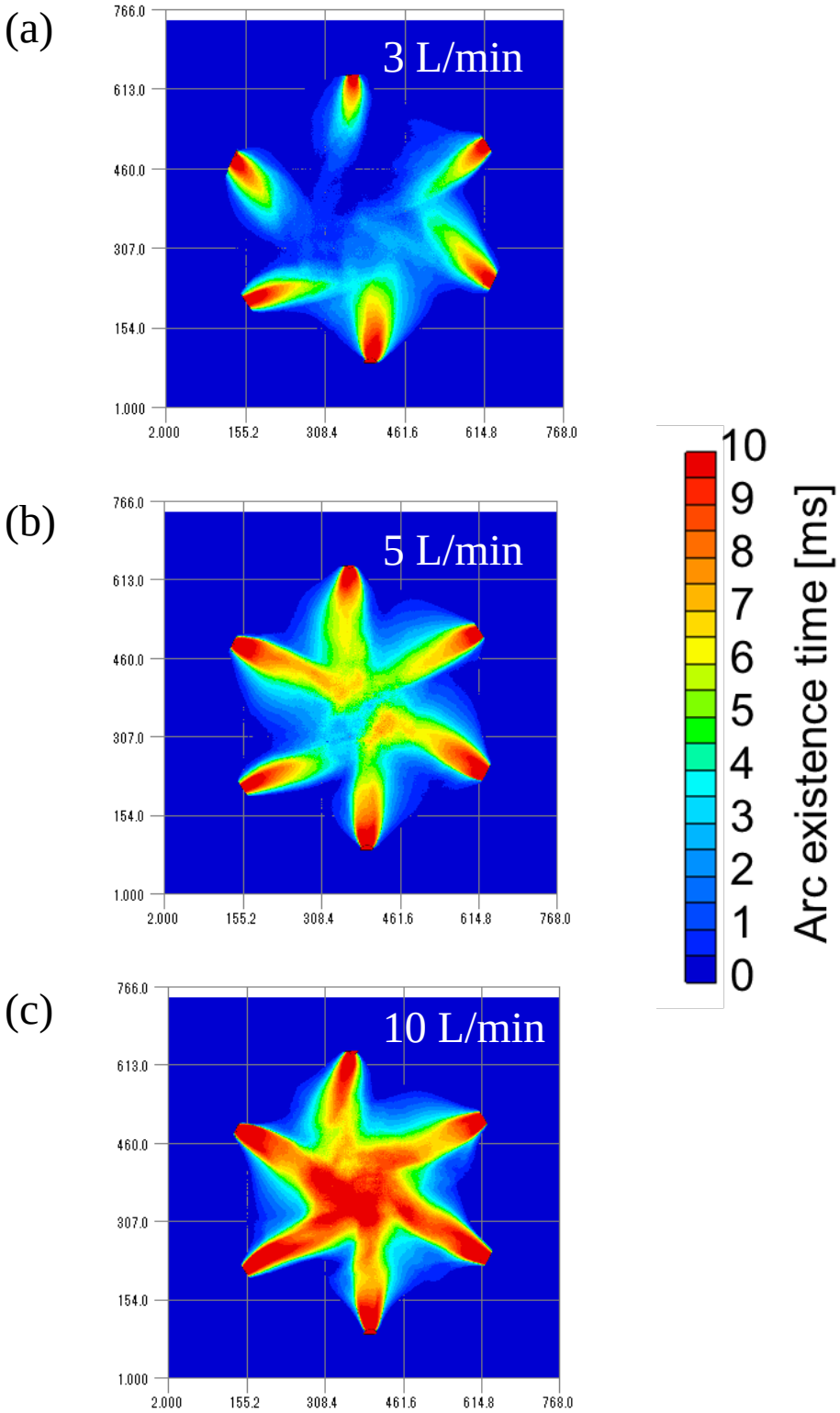

Fig. 2.15 Arc existence time of the 6-phase AC arc during an AC cycle in CW pattern with tungsten diameter of 6 mm at argon gas flow rate of (a) 3 L/min, (b) 5 L/min and (c) 10 L/min

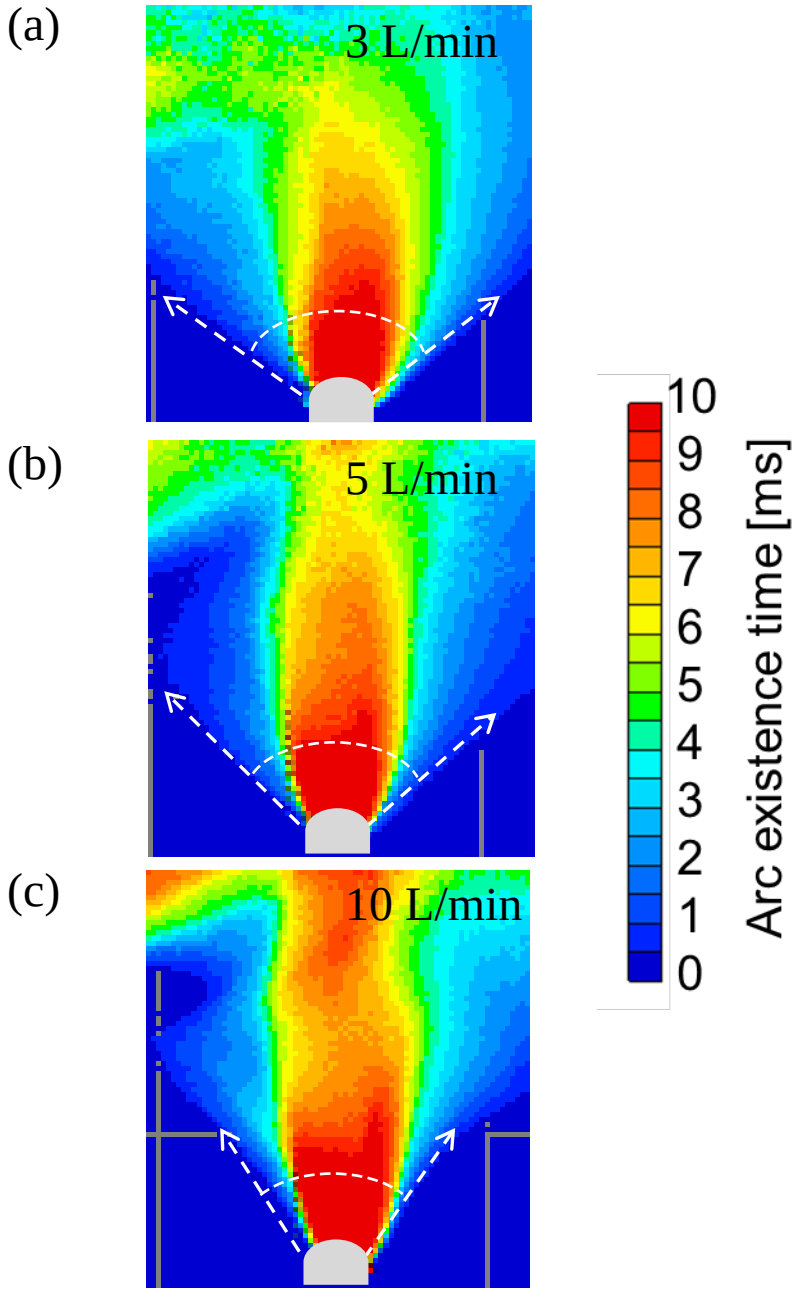

Fig. 2.16 Contour map of the existence time of the 6-phase AC arc during an AC cycle in CW pattern with tungsten diameter of 6 mm at argon gas flow rate of (a) 3 L/min, (b) 5 L/min and (c) 10 L/min

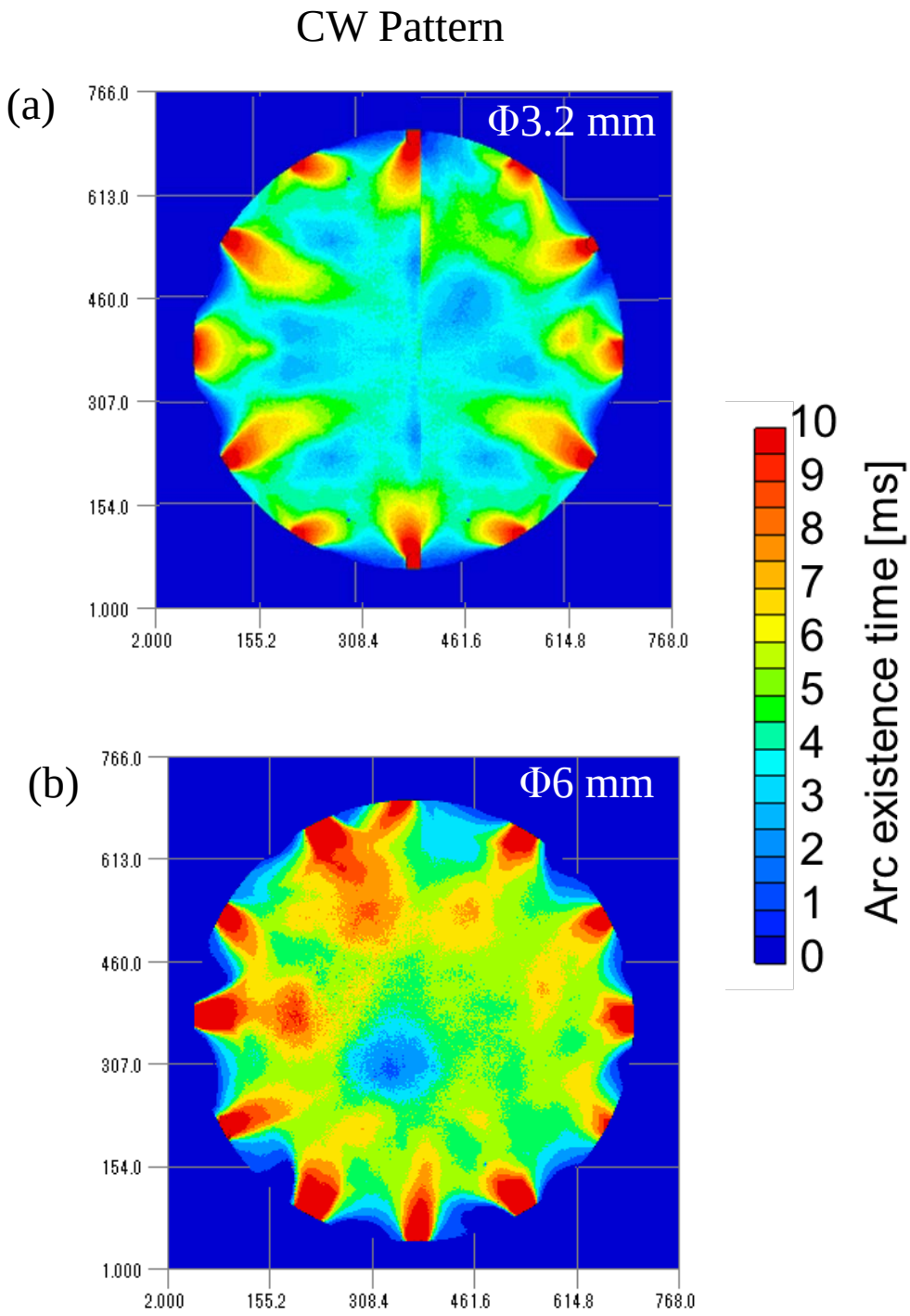

Fig. 2.17 Arc existence time of the 12-phase AC arc during an AC cycle in CW pattern with different tungsten diameters: (a) 3.2 mm and (b) 6 mm

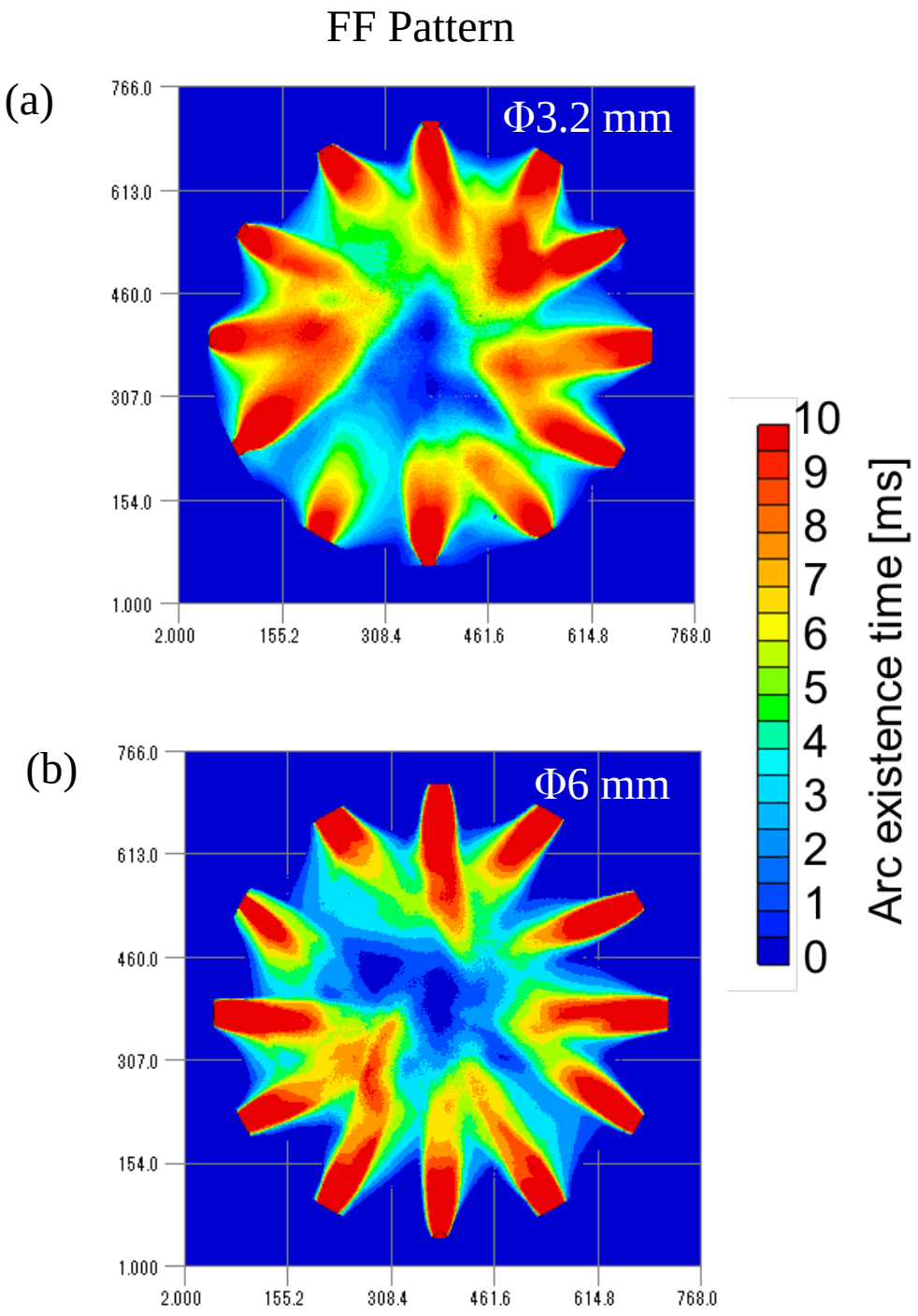

Fig. 2.18 Arc existence time of the 12-phase AC arc during an AC cycle in FF pattern with different tungsten diameters: (a) 3.2 mm and (b) 6 mm

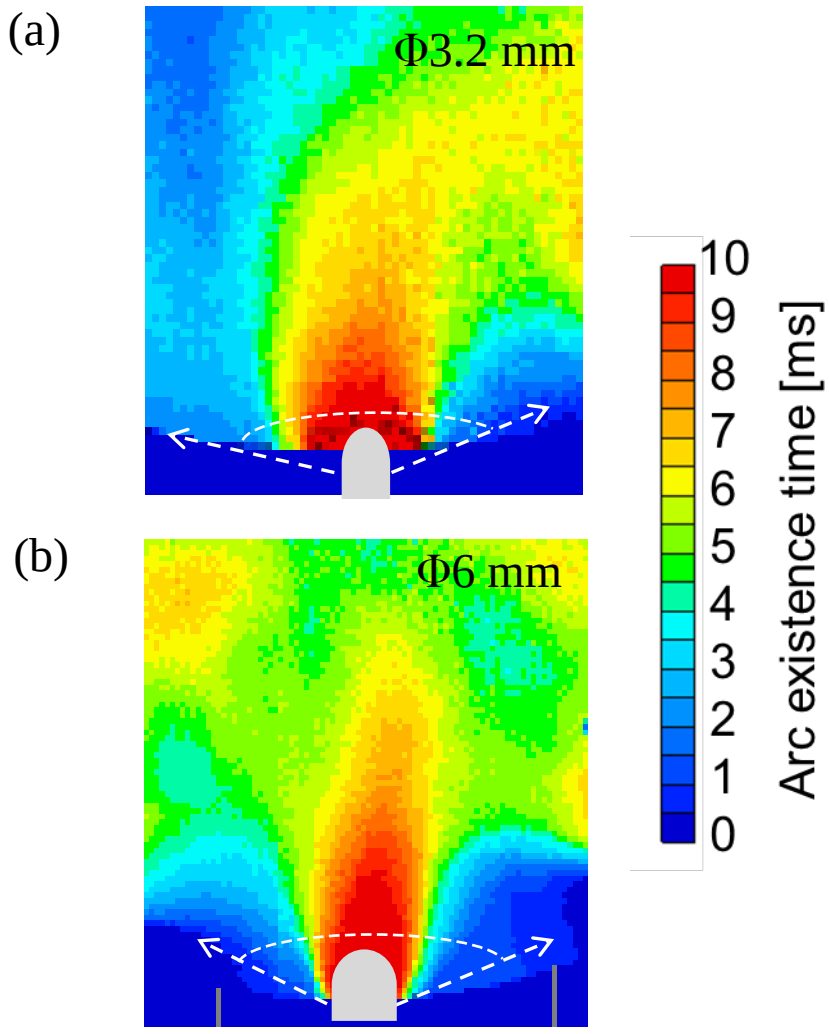

Fig. 2.19 Contour map of the existence time of 12-phase AC arc in CW pattern at argon gas flow rate of 5 L/min with different tungsten diameters: (a) 3.2 mm and (b) 6 mm

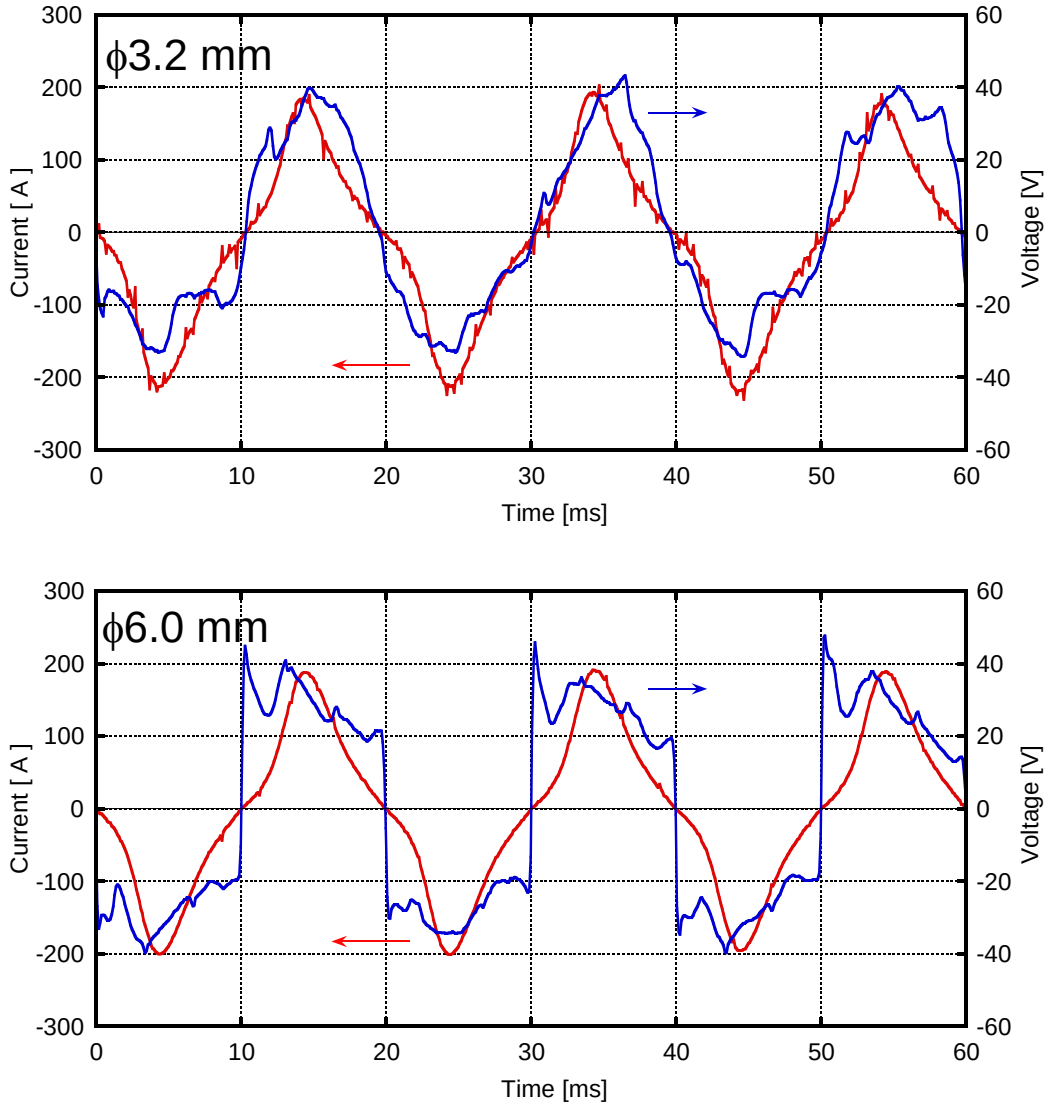

Fig. 2.20 Representative waveforms of current and voltage in CW pattern with different tungsten diameters: (a) 3.2 mm and (b) 6 mm

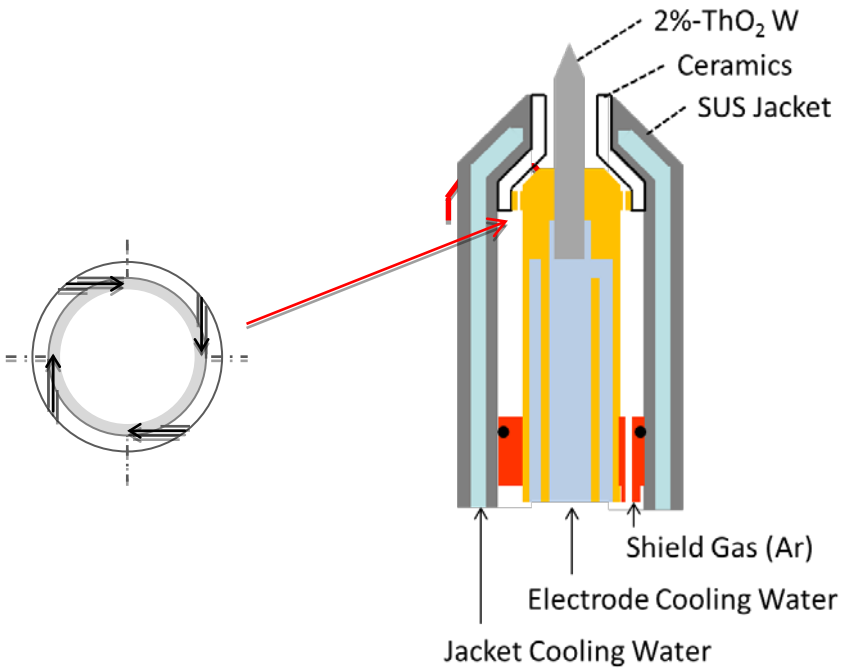

Fig. 2.21 Schematic of plasma torch with tungsten diameter of 3.2 mm and the orifice ring to create swirl flow of argon gas

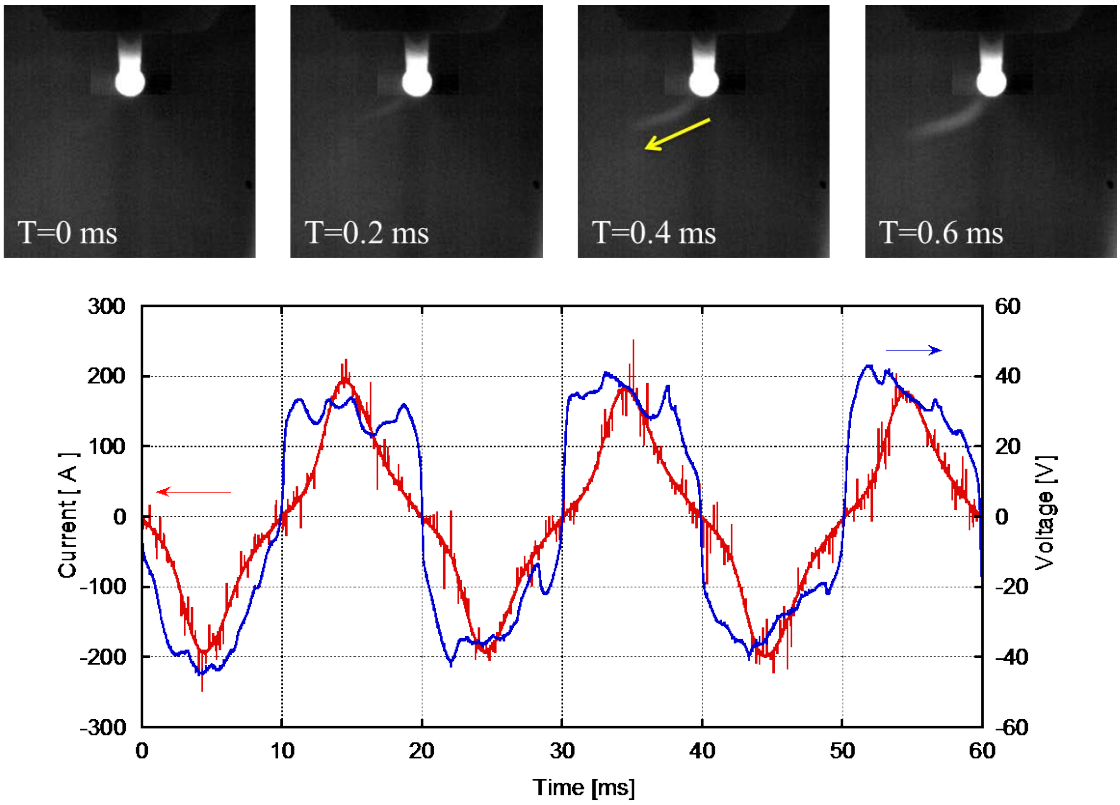

Fig. 2.22 Snapshots of 6-phase AC discharge behavior without the swirl ring and the synchronized voltage and current waveform

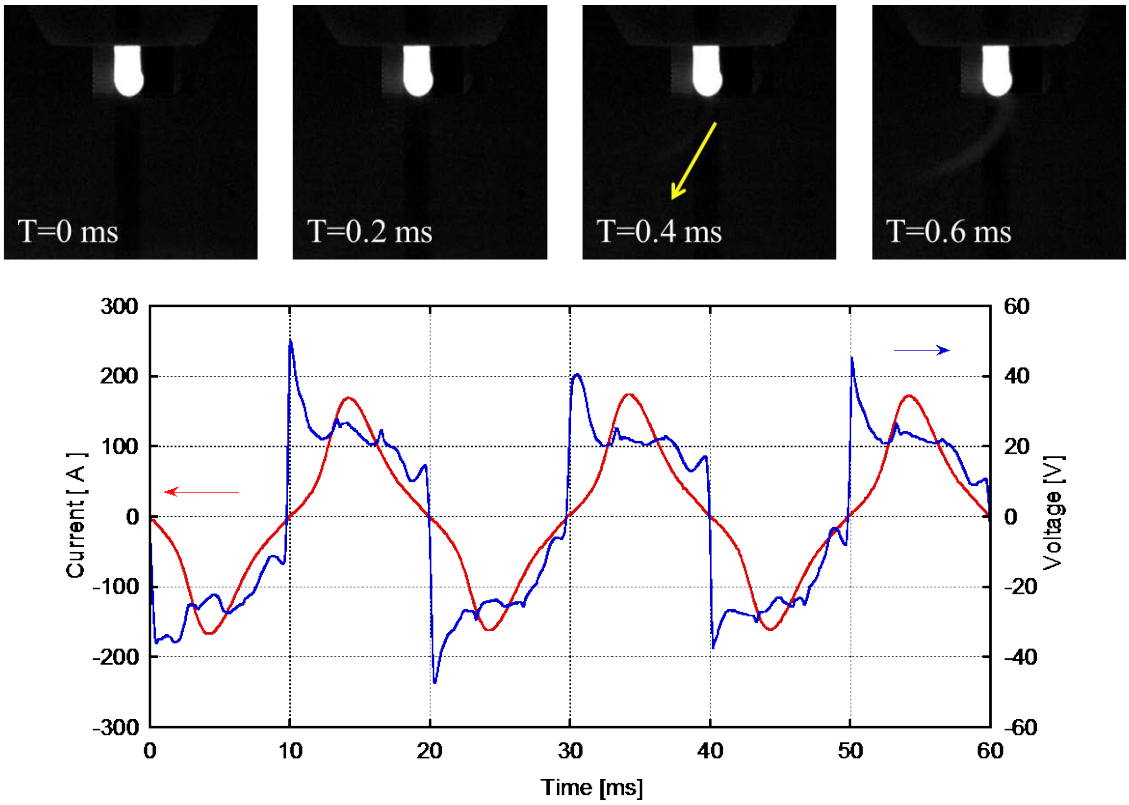

Fig. 2.23 Snapshots of 6-phase AC discharge behavior with the swirl ring and the synchronized voltage and current waveform

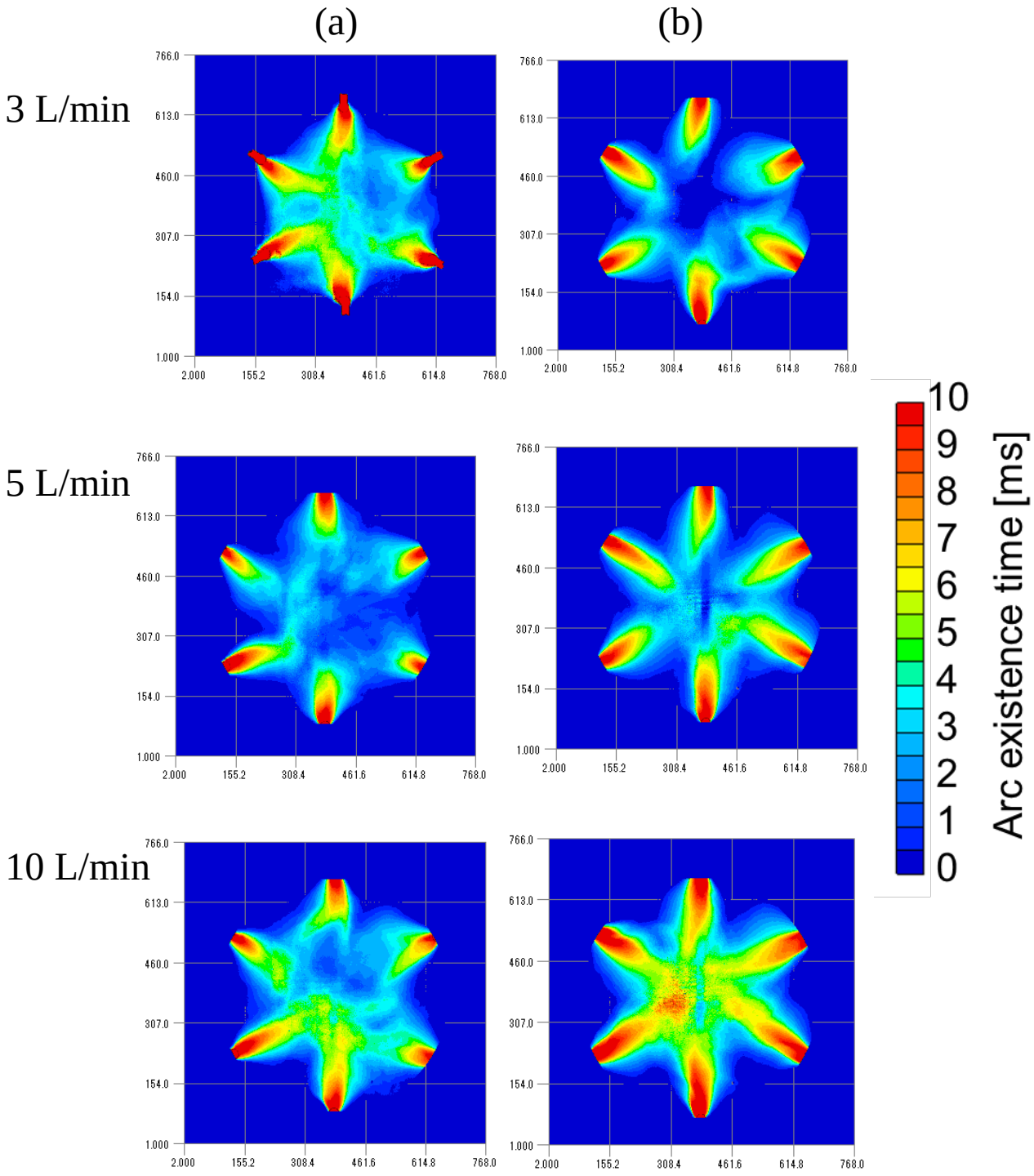

Fig. 2.24 Arc existence time of the 6-phase AC arc during an AC cycle with tungsten diameter of 3.2 mm at Ar gas flow rate of 3, 5, 10 L/min (a) without the swirl ring and (b) with swirl ring

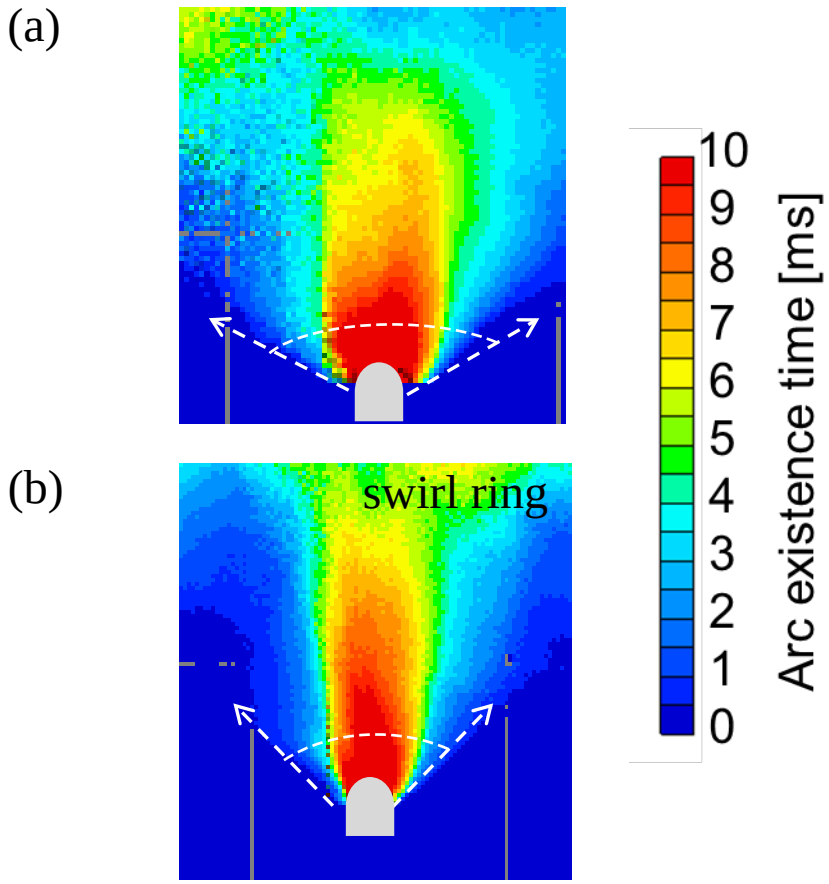

Fig. 2.25 Contour map of the existence time of 6-phase AC arc with tungsten diameter of 3.2 mm at argon gas flow rate of 5 L/min: (a) without the swirl ring and (b) with the swirl ring

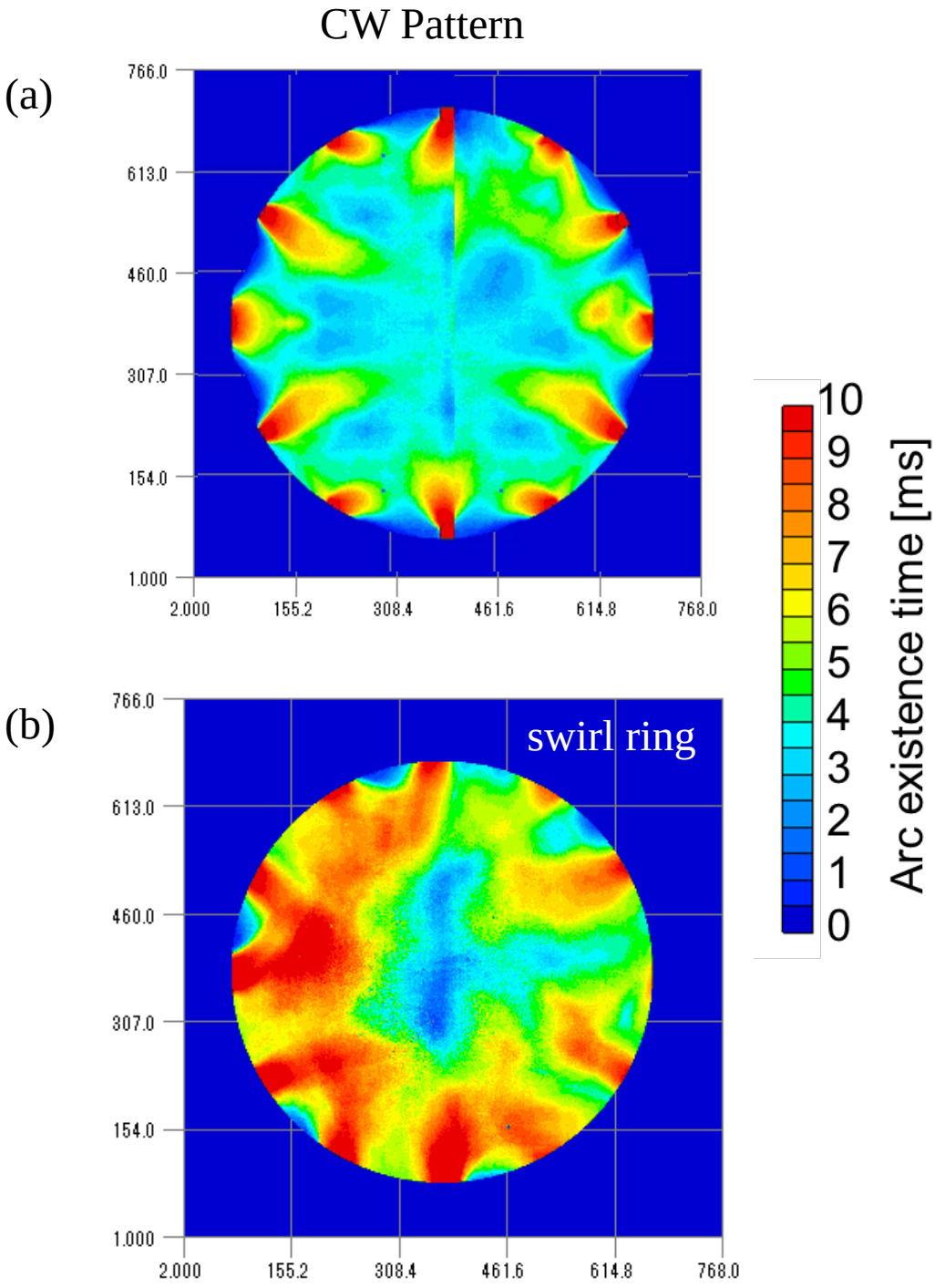

Fig. 2.26 Arc existence time of the 12-phase AC arc in CW pattern with tungsten diameter of 3.2 mm at Ar gas flow rate of 5 L/min (a) without the swirl ring and (b) with swirl ring

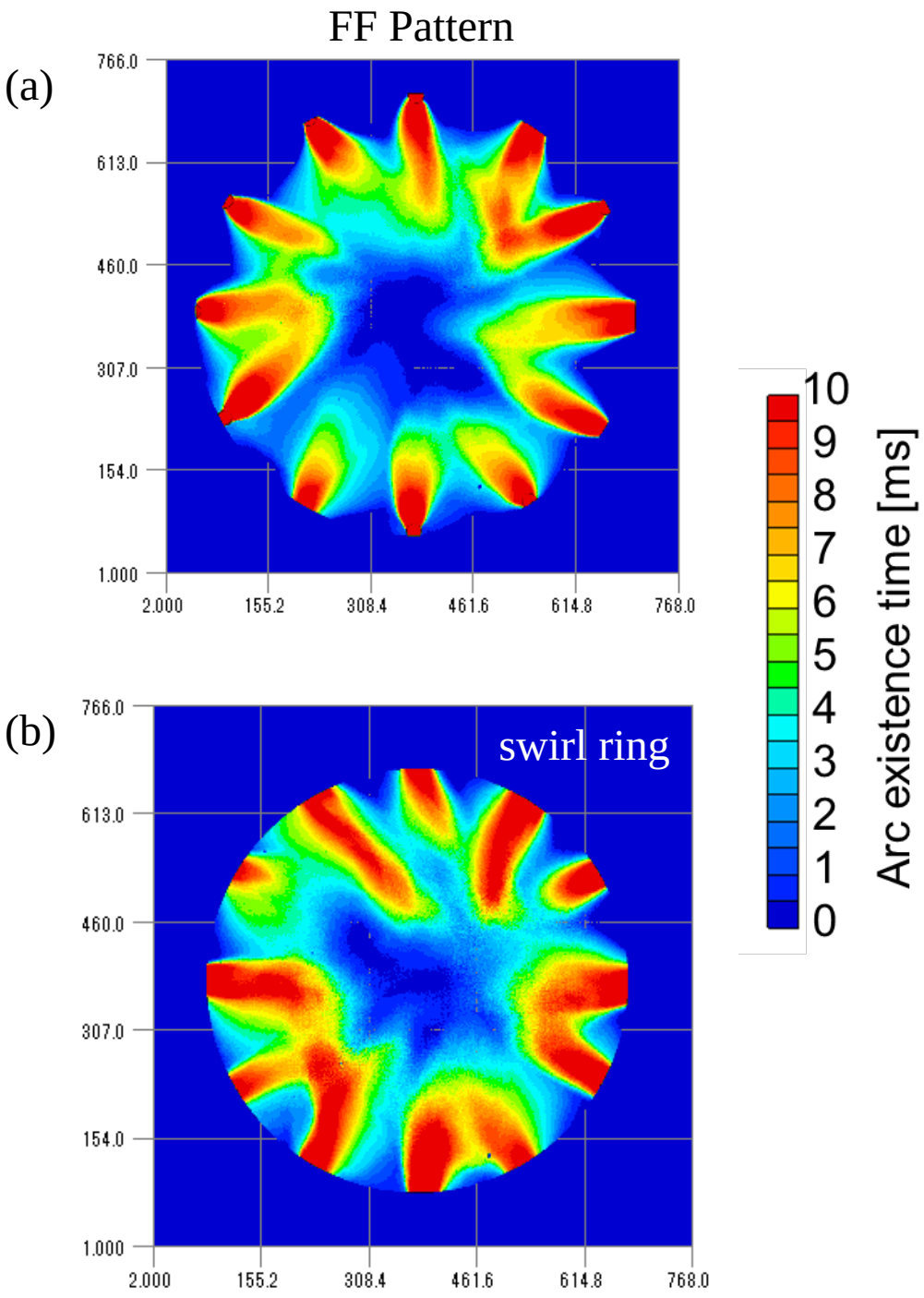

Fig. 2.27 Arc existence time of the 12-phase AC arc in FF pattern with tungsten diameter of 3.2 mm at Ar gas flow rate of 5 L/min (a) without the swirl ring and (b) with swirl ring

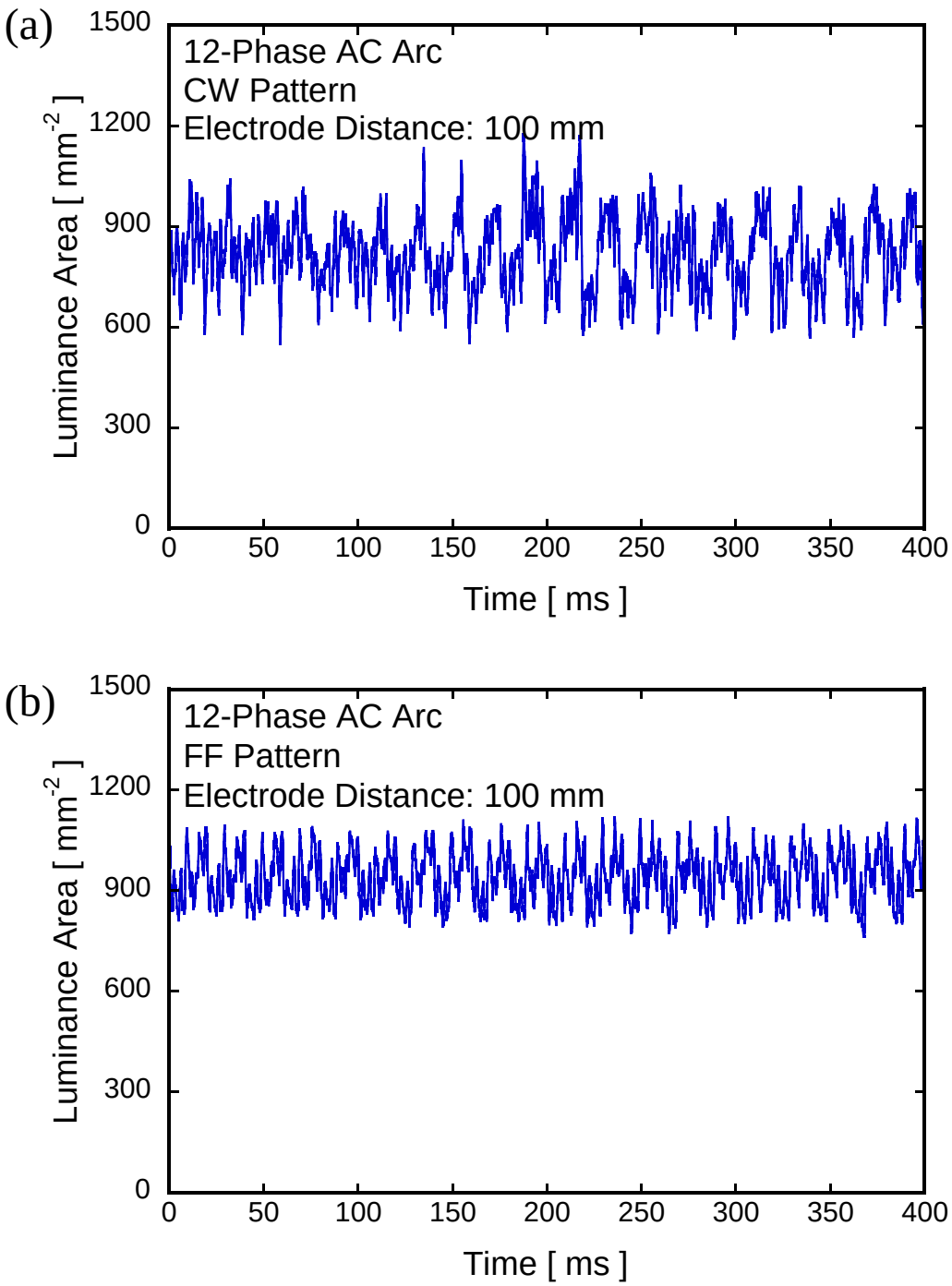

Fig. 2.28 Time variation of arc luminance area: (a) CW pattern and (b) FF pattern

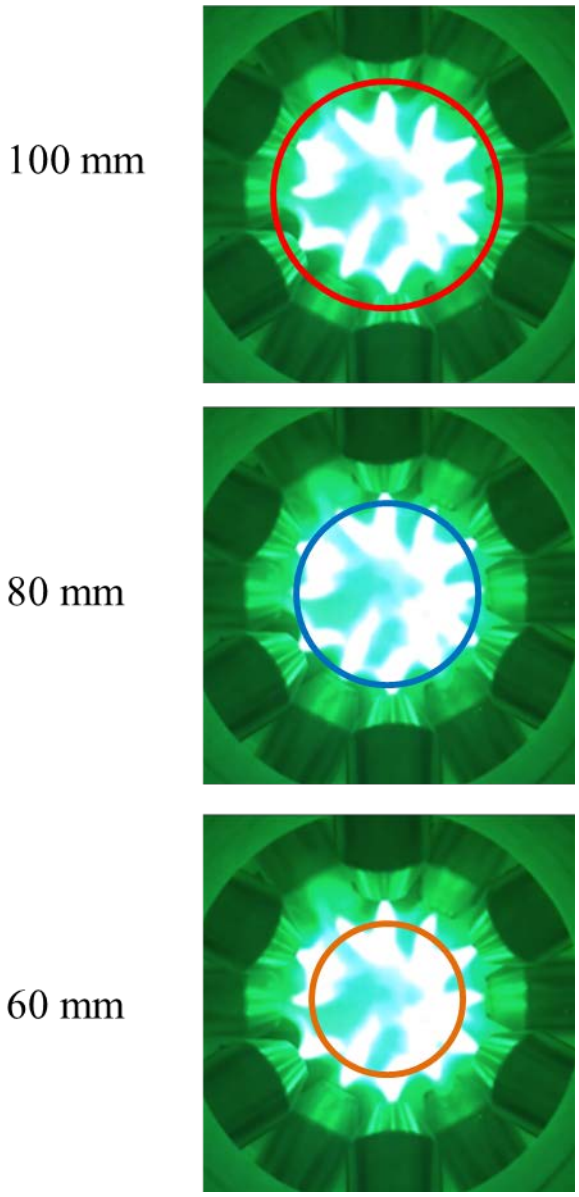

Fig. 2.29 Schematic of evaluated arc luminance area at different diameters

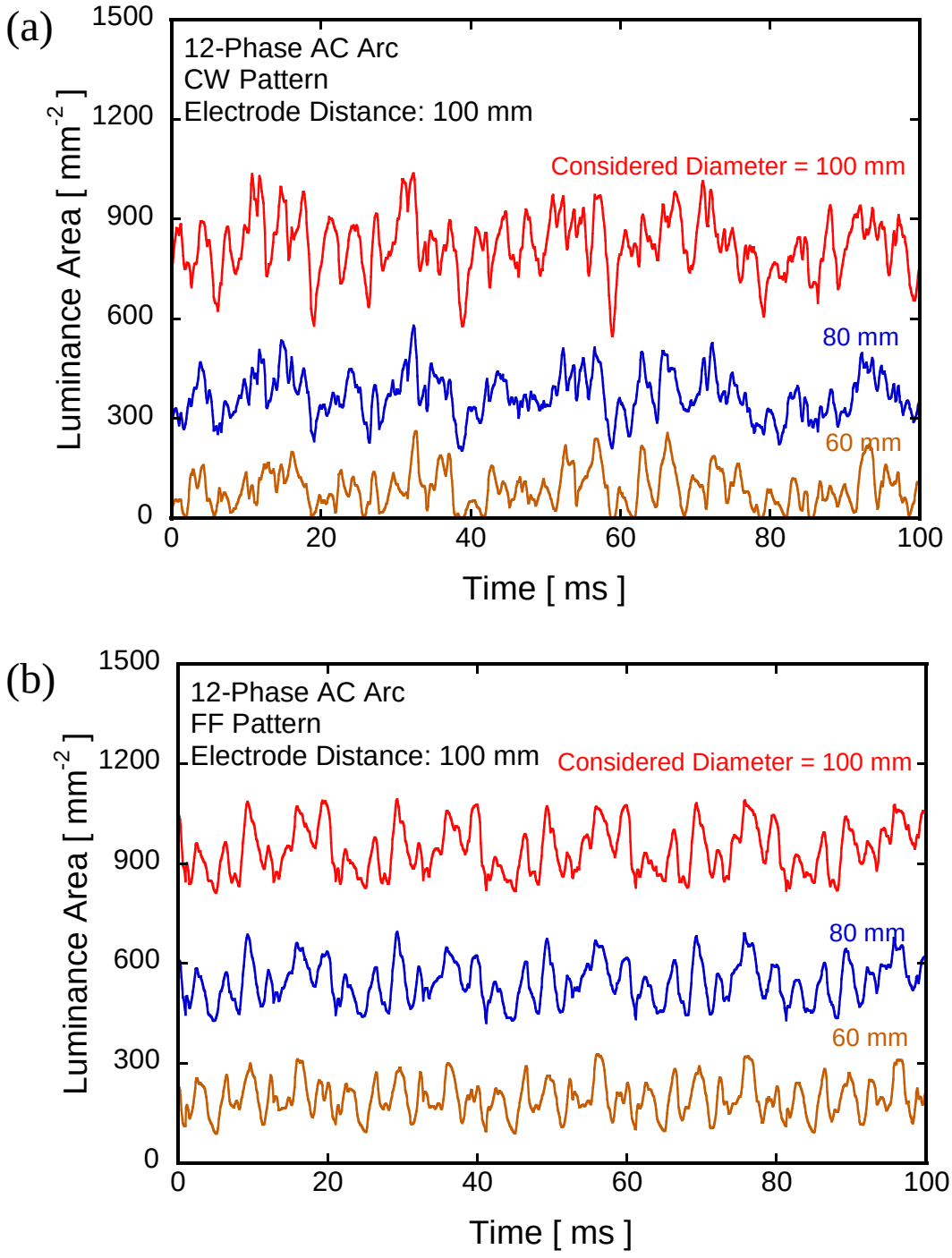

Fig. 2.30 Time variation of arc luminance area at different analyzed diameters of 60, 80 and 100 mm: (a) CW pattern and (b) FF pattern

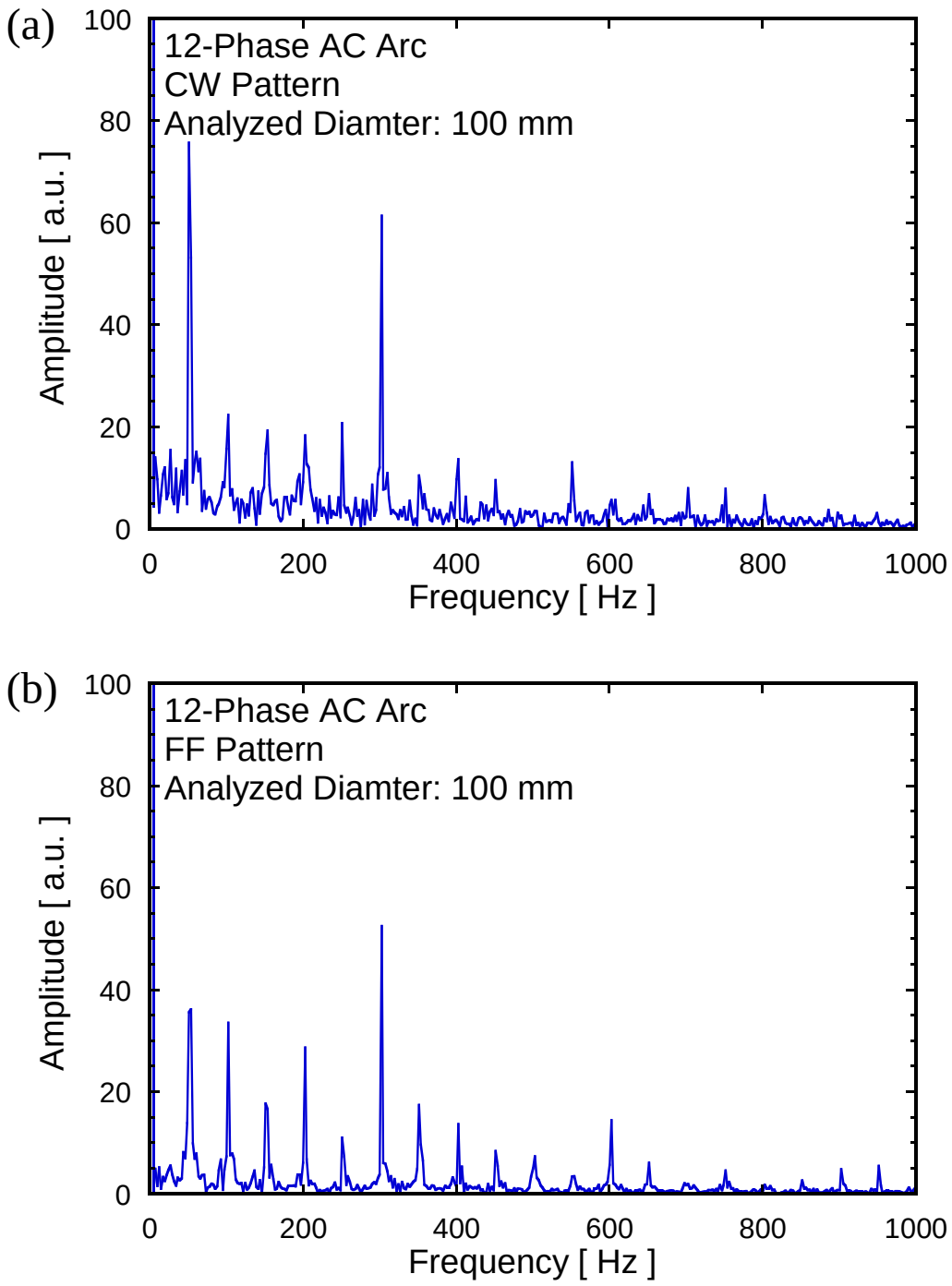

Fig. 2.31 Frequency spectra of arc luminance area at analyzed diameter of 100 mm: (a) CW pattern and (b) FF pattern

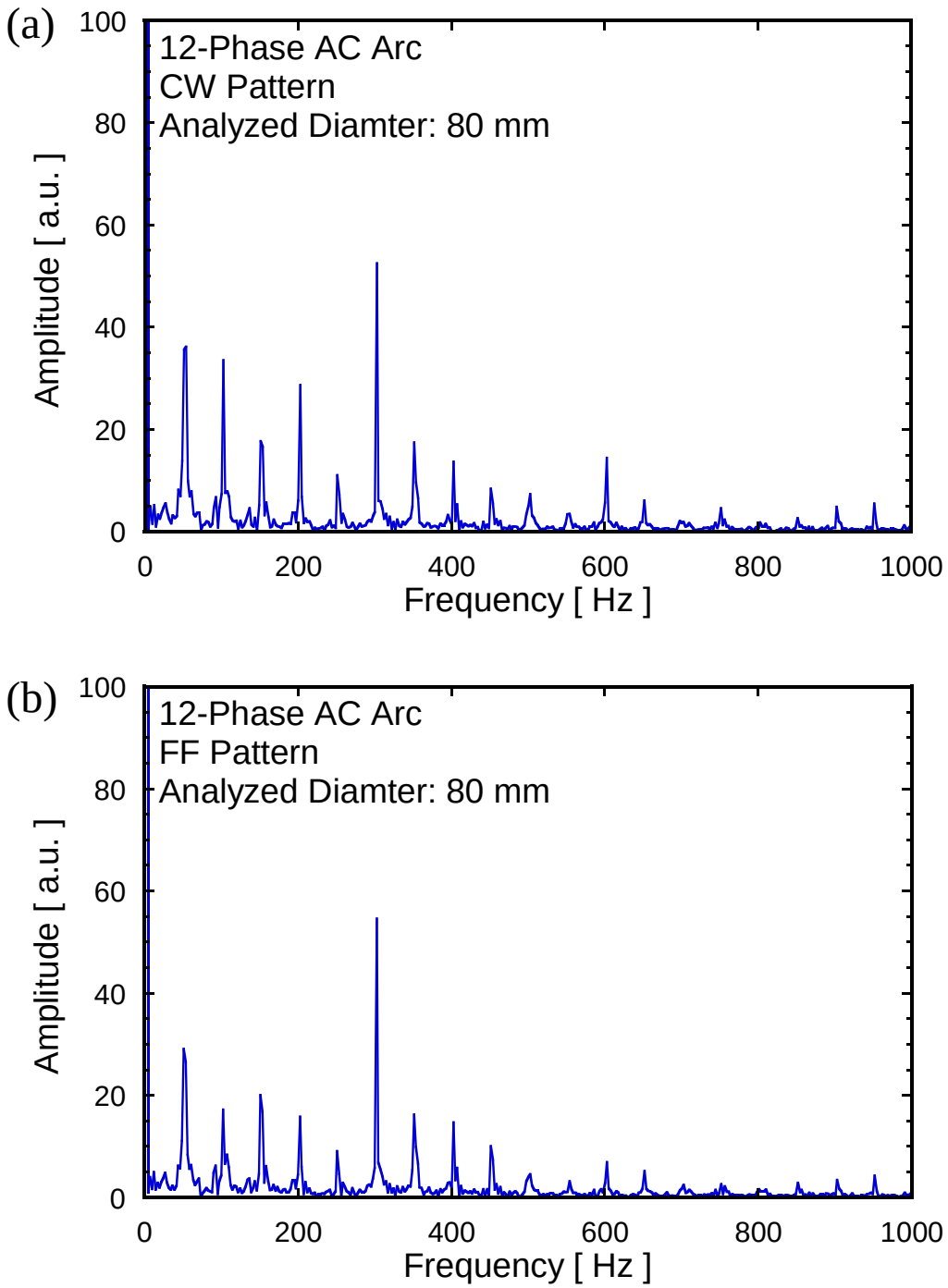

Fig. 2.32 Frequency spectra of arc luminance area at analyzed diameter of 80 mm: (a) CW pattern and (b) FF pattern

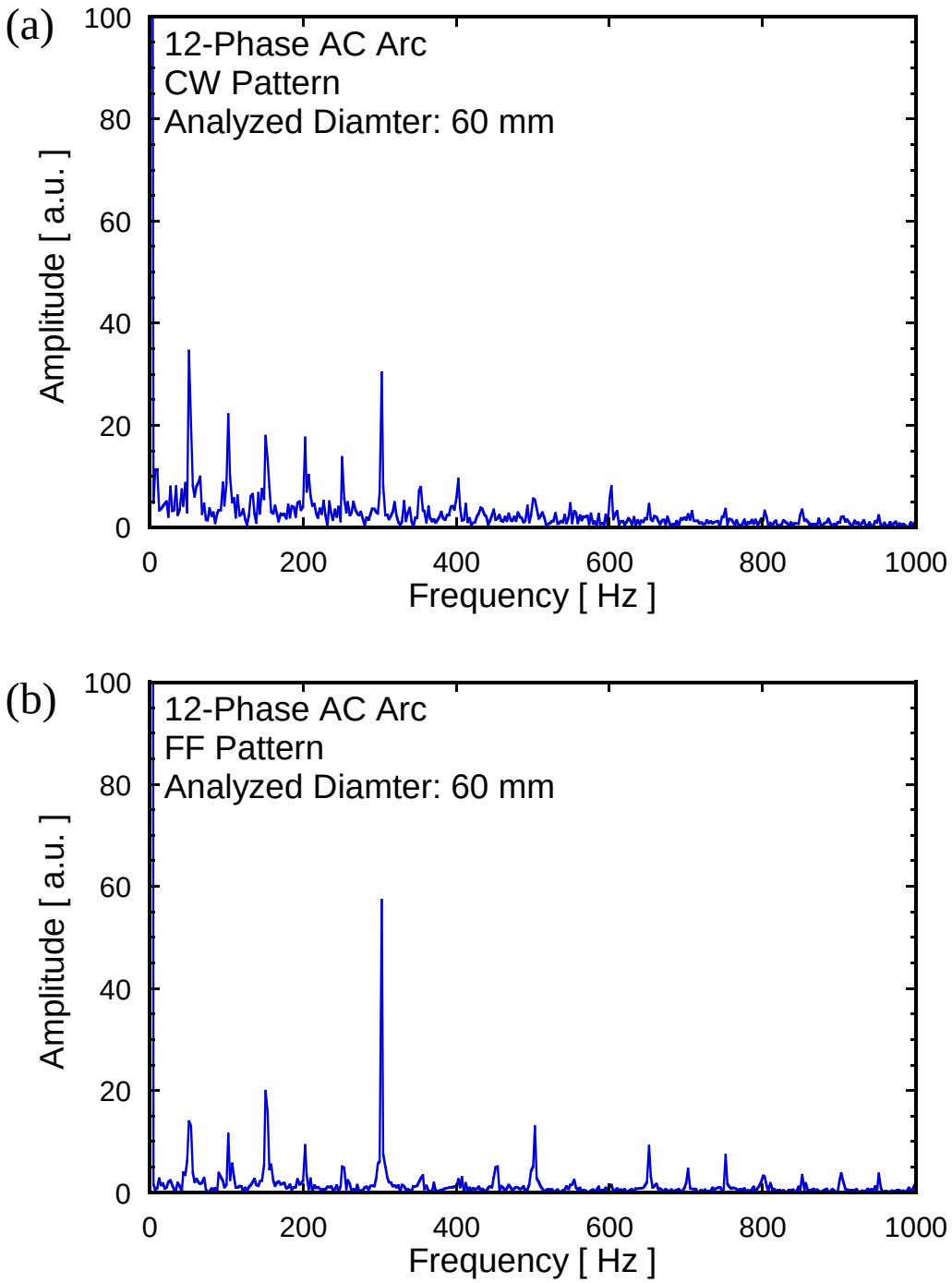

Fig. 2.33 Frequency spectra of arc luminance area at analyzed diameter of 60 mm: (a) CW pattern and (b) FF pattern

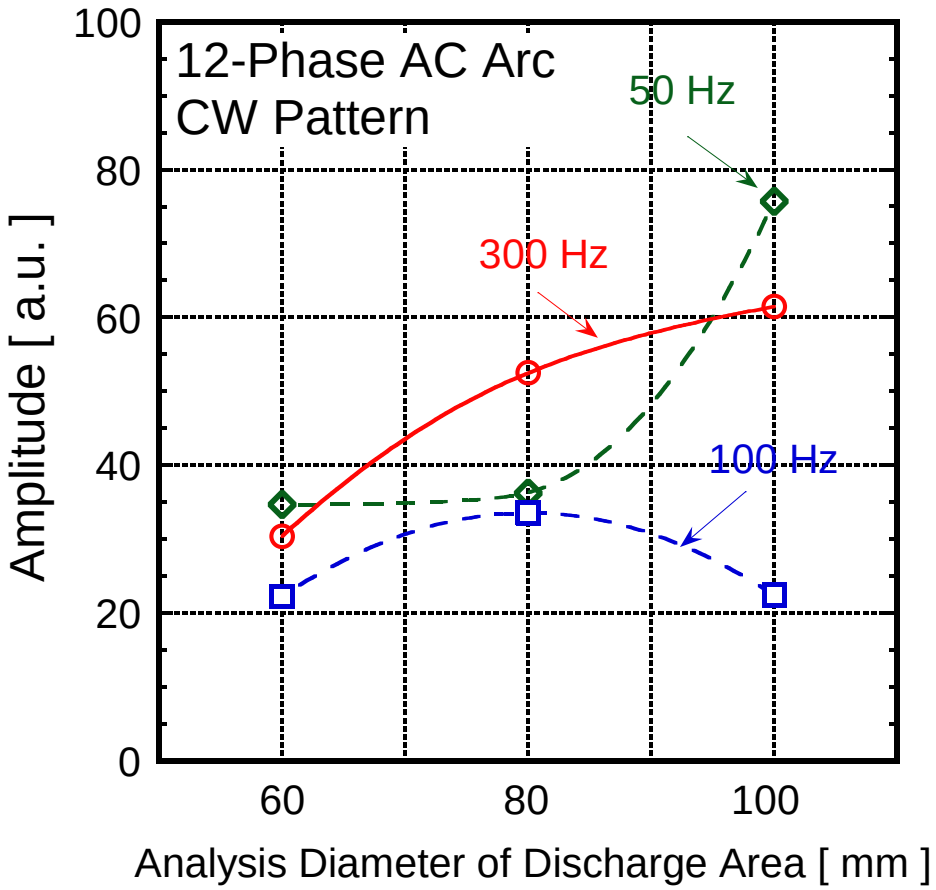

Fig. 2.34 Amplitude of frequency spectra with different analyzed diameters in CW pattern

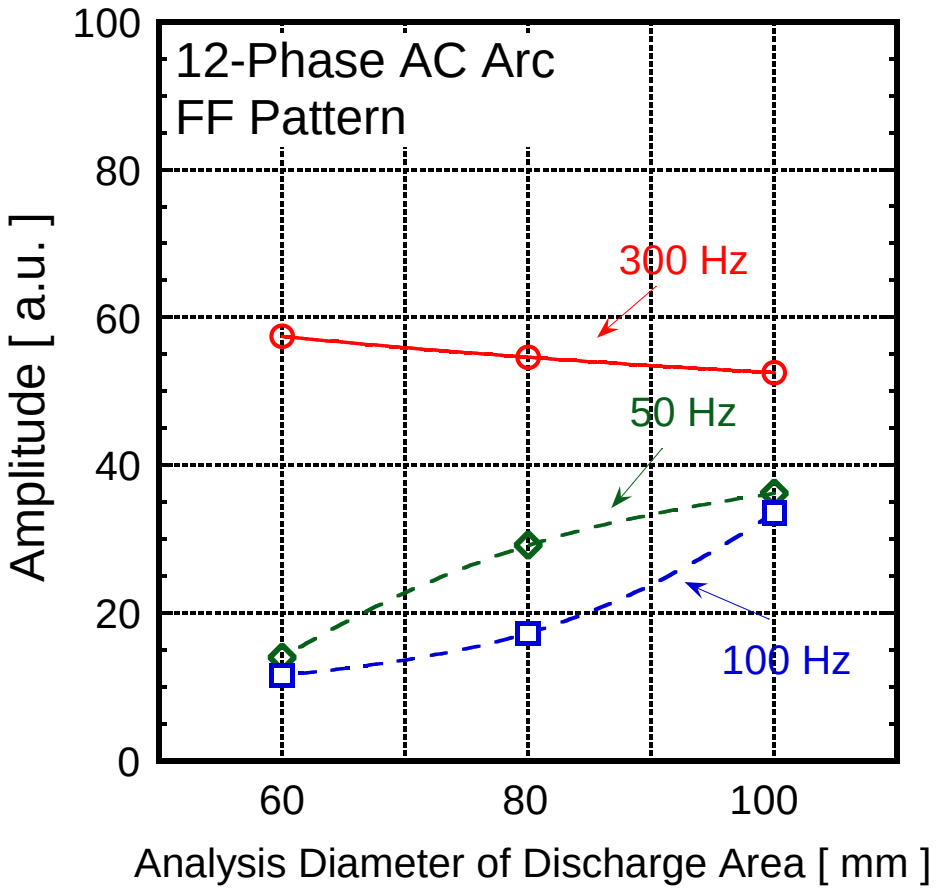

Fig. 2.35 Amplitude of frequency spectra with different analyzed diameters in FF pattern

3. Investigation of Spatial Characteristics of the In-Flight Particles

In the in-flight melting process by multi-phase AC arc, powder materials are injected into the plasma region. Then it is important to study interaction between the plasma flow and injected powder particles. In-flight particle measurements of the surface temperature and velocity are important for understanding of melting behavior of glass particles during in-flight melting by multi-phase AC arc plasma. In this chapter, by using a single particle measurement method with optical system, the information of particle in-flight can be obtained. However, the use of optical pyrometry for particle surface temperature has inevitable uncertainties due to non-thermal emission signals from the plasma plume. This chapter presents spectroscopic measurements of the non-thermal signals which were found to be caused mainly by the plasma emissions scattered by the particles and the radiation emitted by vapor. After that, the accuracy of thermal radiation measurement was estimated and surface temperature of in-flight glass particle was corrected. In addition, the plasma spatial characteristics which have been presented in Chapter 2 are expected to have influence on the in-flight particle characteristics. Therefore, the effects of the electrode configuration, the carrier gas flow rate and the measured radial position in the plasma region on the particle spatial characteristics were investigated. The particle velocities and temperatures with varied radial distance were evaluated considering mean and standard deviation associated to each condition. The standard deviation of the measured velocity, temperature and diameter in different electrode configurations and electrode diameters

were discussed summarily.

3.1 Introduction

In the thermal spraying, in-flight particle characteristics can be measured by using various optical techniques. The widely used diagnostic equipment based on the two-color pyrometry principle and time-of-flight techniques has been applied in both laboratories and industries. The particle diagnostic systems differ in ensemble and single particle measurements. It was reported that measurement of particle temperature close to plasma torch exit is difficult to be carried out by ensemble measurement, because the plasma radiation is stronger than the particle radiation in the large measurement volume (Mauer et al. 2007). Along with the thermal radiation emitted by particles, it is inevitable that several non-thermal signals will also be collected by optical lens.

The effect of these non-thermal emission signals have been investigated by several researchers. Sakuta and Boulos (1988) calculated the visibility of the nickel radiative signal and plasma background in order to determine in what condition it would be difficult to observe the particle through its own emission. Gougeon and Moreau (1993) have quantified the Nickel particle-reflected plasma light received by detectors from spectroscopic measurement. It was found that scattered light degrades the accuracy of temperature calculation especially the smaller, cooler, closer to the torch exit particles. Hollis and Neiser (1998) described a method to estimate the non-thermal signals by spectral analysis from the plasma/Mo particle plume. The results showed that emissions from plasma radiation and vaporized particle species must be considered into temperature estimation. Furthermore, their calculations showed that the plasma light scattered by particles has significant effect on the increase of the argon emission line intensity up to 120%, which would induce a significant temperature measurement error. Salhi et

al. (2005) measured the quantity of plasma light scattered by cold copper particles by DPV-2000 in order to calculate the true surface temperature. Results showed the importance to remove the non-thermal radiation for more accurate temperature measurements.

3.2 Experimental

3.2.1 Experimental Setup

Figure 3.1 gives the schematic illustration of the experimental setup for the in-flight particle measurement in the 12-phase AC arc plasma system. The multi-phase AC arc generating setup has been descripted in Section 2.2.1. A powder feeder nozzle was installed above the chamber and cooled by water at flow rate of 7 L/min. The powder feeder (5MPE Series, Sulzer Metco) has vibrator assists gravity feeding of powders and help in powder fluidization. Raw materials of glass powders were supplied with carrier gas flow. A feed rate meter precisely measures, monitors and controls the powder feed rate. A tube was connected between the exit of the powder feeder and the feed nozzle. The exit of the powder feeder nozzle has a diameter of 3.8 mm and a distance of 150 mm over the upper electrode level. The raw materials were injected into the chamber with the carrier gas of air. The powders treated by the 12-phase AC arc were quenched and collected on the bottom at a distance of 766 mm below the electrode level.

In-flight particle diagnostics were performed with the optical system DPV-2000 from Tecnar (Canada). Measurement of the particle characteristics were carried out in the plume of the plasma at an axial distance of 80 mm down from the lower electrode level. In order to obtain the spatial characteristics of particles, the DPV-2000 instrument was fixed at each single point to get sufficient data and varied at a step of 5 mm along the radial direction. Emission spectrum was measured by a spectrometer (MicroHR, Horiba). Both the pyrometric and spectroscopic

measurements were focused on the same point and used the same optical components.

Different with the thermal spraying process which is usually operated in ambient air, the multi-phase AC arc plasma process is a closed system equipped with insulator inside the chamber, the water cooling and the exhaust gas system. The plasma velocity is much lower compared to other conventional thermal spray processes which use different types of plasma guns; therefore, the particle velocity is expected to be lower in the case of the 12-phase AC arc plasma process.

3.2.2 Raw Materials

Alkali-free glass has attracted attention owing to its excellent dielectric property, good rigidity and high intensity as well as good thermal and chemical stability. It has been widely applied in many fields, such as liquid crystal display (LCD) and electro luminescence (EL) display, thin film transistors (TFT), charge coupled devices (CCD), contact image sensors (CIS), solar cells, and glass fiber. In the in-flight melting technique, the granular glass raw materials were prepared by a spray dryer (Fig. 3.2). The granulation process of the spray dry method supplied by Asahi Glass Co., Ltd. is presented in Fig. 3.3 (Ohkawa et al. 2013). Reagents of fine powdered raw materials of boric acid (H_3BO_3), alumina (Al_2O_3) and barium carbonate ($BaCO_3$) were mixed in appropriate mass ratio and dispersed in water to form slurry. The slurry was sprayed through a disk type or nozzle type atomizer into a heated air cyclone at 270ºC to form spherical powders. In practical use the spray dryer is designed to be heated by the exhaust gas from the furnace. About 120 μm diameter granules with continuous small pores were for the alkali-free borosilicate glass (Asahi Glass Company, Limited 2011).

The composition of the raw material was adjusted to obtain the target of glass powders with composition of $50.2SiO_2$-$15.4B_2O_3$-$9.0Al_2O_3$-24.7BaO-$0.1Fe_2O_3$-0.3SrO in wt% (Table

3.1). Meanwhile, the glass raw material particles have substantially uniform constitution, and have a composition close to the desired liquid glass. Due to the batch composition adjustment before every spray drying, the constitution of the granulated particles for in-flight melting may have little difference. However, the same series of raw materials were used in each chapter. Figure 3.4 shows the representative microscope image of raw material of alkali-free glass particles. It has a spherical shape and ragged surface that is good for fluidity. The average diameter of raw materials comes from each batch after spray drying is slightly different. The representative of particle size distribution of raw material of alkali-free glass is given in Fig. 3.5.

3.2.3 Experimental Conditions

Experimental conditions for in-flight particle measurement by DPV-2000 are shown in Table 3.2. The typical parameters including electrode configuration of CW pattern, electrode distance of 100 mm and electrode diameter of 3.2 mm. Carrier gas flow rate was 20 L/min while the powder feed rate kept constant at 30 g/min for a good particle detection rate by DPV-2000. The spectrophotometer (MD-100, JASCO) was used for the calibration of thermal emission. The particle measurement position was focused at the center of the axis. It should be noted that the research for the calibration of particle temperature was done with our old experimental setup which has been used until the year of 2011. As already been discussed in Chapter 2, the electrode configuration and the electrode diameter have influence on the plasma spatial characteristics. Thus the particle spatial characteristics were investigated under different discharge conditions. The measurement height kept constant, while the central axis was defined as the 0 mm point in the radial distance and the sensor head moved horizontally to measure at five different radial distances as 10, 20, 30, 40 and 50 mm, respectively. Table 3.3 shows the experimental parameters for investigation of carrier gas flow rate. The spectrometer (MicroHR,

Horiba) was used for temperature calibration. The MicroHR provides a spectral resolution of 0.3 nm. Table 3.4 shows the experimental conditions for effect of electrode configuration in the particle characteristics. CW and FF patterns with the same discharge conditions were under investigation. Powder feed rate was at 30 g/min with carrier gas flow rate at 20 L/min. Experimental conditions for the effect of electrode diameter are given in Table 3.5. CW pattern with electrode diameter of 3.2 mm and 6 mm were used for comparison.

3.2.4 Experimental Procedures

The experiments of in-flight particle measurement by DPV-2000 were conducted in the following manner. The arc generation procedures were explained in Section 2.2.4.

- Preparation of electrodes
- Preparation of particle diagnostic system

1) Locate the DPV-2000 tool and operation table of the optical components.
2) Put on the laser diode alignment ON to make sure that the line array of fibers imaged on the disk in horizontal and the focus position is on the center of the axis.

- Preparation of arc ignition
- Arc generation

After the multi-phase AC arc is generated, adjust the electrode gap distance at 100 mm and keep the discharge for five minutes for stabilization.

- Powder injection

1) Open the gas cylinder of the air gas and regulate the pressure to 0.5 MPa.
2) Put in the power of the powder feeder. Introduce the Air vibration gas from the air compressor.
3) Introduce the Air carrier gas and turn on the switch (Powder ON/OFF switch) of the

powder feeder. Regulate the powder feed rate to the desired value.

- Particle measurement by DPV-2000

1) Remove the shading glass on the peephole to collect the particle thermal emission.

2) Run the software of DPV-2000 system and manipulate the parameters such as the “Trigger Level” and “Capture Depth” until the acquisition window shows a good number of “good signals”. The “good signal” means the percentage of particles that have been correctly collected by the diagnostic system. In the multi-phase AC arc processing, this value usually between 10% and 20%.

3) Save statistics of the measured particles. When the particles data is over 2000, stop the statistics saving.

4) Move the lens position to the next measurement point and repeat 4).

5) Change the experimental conditions such as carrier gas flow rate and repeat 4) and 5).

- Spectroscopic measurements

1) Remove the sensing head of DPV-2000 and place the sensor of the spectrometer.

2) Open the software of spectrometer and manipulate the parameters such as center wavelength, slit width, exposure time and accumulation.

3) Save the emission spectrum data.

4) Change the experimental conditions such as carrier gas flow rate and repeat 2) and 3).

- Stop the powder feeding

1) Decrease the powder feed rate to zero and turn off the air vibration tool.

2) Stop the Air carrier gas flow. Turn off the switch (Powder ON/OFF switch) of the powder feeder.

- Stop the arc discharge

3.2.5 Particle Measurement by DPV-2000

(a) Description of the DPV-2000 System

The DPV-2000 consists of three main parts (Salhi et al. 2005): (a) a sensing head collects the thermal radiation emitted by hot particles from the peephole, (b) a detection cabinet filters out the particle radiation which contained the photo detectors and optical components of the high speed pyrometry, (c) a computer equipped with the digitizing and computing boards compiles and displays the data. The velocity measurement is the most simple and precise one carried out by the DPV-2000. The conceptual diagram of velocity measurement principle is shown in Fig. 3.6. An optical two-slit photomask is inserted at the tip of the center fiber inside the sensing head. When a hot particle crosses the sensor measurement volume (<1 mm^3), a two-peak image is recorded through the photomask. By knowing the time of flight and the distance between the two slits, particle velocity can be calculated. The DPV-2000 is a high-speed, high precision two colors pyrometer. Surface temperature of the particles is measured based on Plank's radiation law. The conceptual diagram of temperature measurement is shown in Fig. 3.7. The two interference band pass filters chosen by DPV-2000 are λ_1=787±25 nm and λ_2=995±25 nm, respectively. The particle diameter is computed from the absolute radiation intensity at one wavelength and the temperature of the particle. A correction factor is applied to take into account of the particle emissivity. As the error on the temperature measurement is around 3%, and the error on surface area must be taken into account to estimate the accuracy of the diameter measurement (Moreau et al. 1994), the error for the diameter evaluation is between 7% and 15% (Pouliot et al. 1998).

(b) Temperature Measurement Principle

According to the Planck's radiation law, the spectrum of thermal radiation from a

blackbody is used to determine the particle surface temperature at the applied wavelengths:

$$I_\lambda = \varepsilon \frac{8\pi hc}{\lambda^5} \frac{1}{\exp\left(\frac{hc}{\lambda kT}\right) - 1} \tag{3.1}$$

where h is the Planck's constant which value is 6.62×10^{-34} J·s, c is the speed of light (3×10^8 m/s), ε is the surface emissivity, λ is the wavelength, k is the Boltzmann constant (1.38×10^{-23} J/K), T is the temperature. A real body that emits less thermal radiation than the blackbody has surface emissivity ε less than 1. Since the emissivities are unknown for many applications, the gray body assumption $\varepsilon(\lambda_1)=\varepsilon(\lambda_2)$ is used where it is hypothesized that the surface emissivity is independent of wavelength. Actually, this assumption is not fulfilled in many cases which can lead to temperature deviations (Fincke et al. 2001; Salhi et al. 2005; Mauer et al.2008).

Based on these approximations, the particle temperature T is obtained from the ratio of the radiation intensity and can be written in the version:

$$T = \frac{K_2(\lambda_1 - \lambda_2)}{\lambda_1 \cdot \lambda_2} \left[\ln \frac{TR_{\lambda 1}}{TR_{\lambda 2}} + 5 \ln \frac{\lambda_1}{\lambda_2} \right]^{-1} \tag{3.2}$$

where K_2 is the second radiation constant in Planck's law which value is 1.439×10^{-2} m·K, $TR_{\lambda 1}$ and $TR_{\lambda 2}$ are the thermal radiations emitted by a particle at λ_1 and λ_2, respectively.

3.3 Experimental Results and Discussion

3.3.1 Separation of Non-Thermal Signals

(a) Theoretical Considerations

As the high temperature field generated by the arc plasma could be valued as high as 5000-10000 ºC, the visibility of the particle radiative signal is reduced due to significantly direct and scattered plasma radiations. A cover with aperture was used to reduce 75% of the infrared radiation entering the DPV-2000 sensor to obtain a good particle detection rate. From Eq. (3.2),

the emission signals contained in the sensor measurement area are not only emitted by particles, but also other non-thermal emission signals. Failure to identify and remove the non-thermal signals leads to errors in calculating particle surface temperatures.

Figure 3.8 descripts all the possible emission sources which could be collected in the optical detector sampling volume including:

- Direct thermal radiation emitted by particles (solid red arrow);
- Direct thermal radiation from the insulator inside the chamber (solid green arrow);
- Thermal radiation from the insulator scattered by particles (dot green arrow);
- Direct line emission from plasma (solid blue arrow);
- Plasma emission scattered by particles (dot blue arrow)
- The line and continuum emission from the vaporized particle material.

The direct radiation from the insulator can be eliminated by using appropriate optics that will not collect this emission. The average temperature of particles was found to be constant while the temperature of insulator was increased. This means the particle-reflected radiation from insulator can be ignored. The detecting time for a particle by DPV-2000 sensor is considerably short compared with the fluctuation period of the multi-phase AC arc, and diagnostics were repeated until a statistically large number of particles were analyzed. Therefore, it is considered that the direct plasma line emission and fluctuation of arc discharge did not affect the total collected energy. The ratio of intensities is mostly affected by the plasma emission scattered by particles. Accordingly, the theoretical ratio of intensities radiated at two wavelength λ_1 and λ_2 which takes into account of the non-thermal emissions can be written as:

$$\frac{E(\lambda_1)}{E(\lambda_2)} = \frac{TR_{\lambda 1} + SPE_{\lambda 1}}{TR_{\lambda 2} + SPE_{\lambda 2}} \tag{3.3}$$

where $E(\lambda_1)$ is the total energy collected by the DPV lens at λ_1, and $SPE_{\lambda 1}$ is the intensity of plasma emission scattered by the particle.

As described in Eq. (3.3), the particle temperature obtained by DPV-2000 is not the real surface temperature. To quantify this error, a calibration method was investigated by a multichannel spectrophotometer (MicroHR, Horiba). The optical lens used for DPV-2000 and spectroscopic measurement were the same, and both of the sensors were focused at the same point which was at an axial distance of 80 mm down from the lower electrodes level (Fig. 3.1). The emission spectra were investigated at the center wavelength of λ_1=787 and λ_2=995 nm which were in accordance with the DPV-2000 detected ranges.

The particle velocity is obtained by measuring the time of flight between the two signals which are generated by a radiating particle passing through the two-slit mask. Combined with the distance of the two slits and the magnification factor of the optical lens, the velocity can be calculated. The precision on velocity is generally better than 5%.

(b) Spectroscopic Measurement

Figure 3.9(a) presents the emission spectrum at λ_1=787±25 nm recorded from the plasma without particle feed by the spectrometer (MD-100, JASCO). The curve shows a relatively weak continuum together with several noticeable spectral peaks. When the powder was feeding at 30 g/min, the emission spectrum was recorded as shown in Fig. 3.9(b). Line emissions from the vaporized particle material (Barium) were observed. Moreover, the emission intensity of Ar I increased compared with the case of no powder feeding. According to Planck's law, a hot particle will emit a continuum radiation over a wide range of wavelength, which the intensity is strongly dependent on its surface temperature. So, for the most accurate results, a red line was drawn to separate the continuum signal emitted by particles and other non-thermal radiations from the vaporized materials and scattered plasma emission. In this way, the intensity under the red line was assumed to be "$TR_{\lambda 1}$", while the whole intensity was assumed to be "$TR_{\lambda 1}$" plus

non-thermal emissions. Generally, it is considered that powder injection will lead to lower plasma emission intensity due to temperature decrease by heat transfer to powder from plasma (Hollis and Neiser 1998). Therefore the sources of the non-thermal radiations collected by the lens are primarily the scattered light by the particle from plasma, indicating that plasma light scattering is not negligible compared with particle emission. In this way, it is assumed that in the spectroscopic measurement, the influence of light emitted by plasma can be neglected in the measurement position when particles are feed. The thermal visibility of particle, which can be defined as the emission intensity ratio $R_{\lambda 1}$ can be given by the following equation:

$$R_{\lambda 1} = \frac{TR_{\lambda 1}}{TR_{\lambda 1} + SPE_{\lambda 1}} \tag{3.4}$$

So in the wavelength at λ_1=787±25 nm, the ratio of the particle thermal emission in the wholly taken emissions can be calculated by spectroscopic result, and the DPV-2000 actually measured the intensity of "TR_λ+SPE_λ". The approximation and subtraction of non-thermal signals provide improved estimation of the particle thermal emission so that the surface temperature can be determined.

Figure 3.10(a) presents the emission spectrum at λ_2=995±25 nm recorded from the plasma without particle feed. The intensity ratio of $R_{\lambda 2}$ can also be calculated from the spectroscopic result from Fig. 3.10(b) with the same method. The calculated value of $R_{\lambda 2}$=0.77 which was a little larger than the $R_{\lambda 1}$=0.60. The effect of carrier gas flow rate on the emission intensity ratio is given in Fig. 3.11. When increase the carrier gas flow rate, the temperature of particle decreases due to shorter residence time in the plasma region, thus the thermal radiation emitted by particle decreases. Combined with the Eqs. (3.3) and (3.4), the ratio of thermal radiation by particles emitted at each wavelength can be calculated as follows:

$$\frac{TR_{\lambda 1}}{TR_{\lambda 2}} = \frac{E(\lambda_1)}{E(\lambda_2)} \times \frac{R_{\lambda 1}}{R_{\lambda 2}} \tag{3.5}$$

Regarding of the above discussion, the intensity ratio of $E(\lambda_1)/E(\lambda_2)$ can be obtained from DPV-2000, while the ratio of $R_{\lambda 1}/R_{\lambda 2}$ can be obtained from the spectroscopic measurement. In conjunction with Wien's approximation of the Planck's law and the grey body assumption, Eqs. (3.2) and (3.5), the particle surface temperature can be determined by removing the non-thermal radiation from the DPV-2000 measurement.

3.3.2 Characteristics of In-Flight Particles

The characterization of in-flight particles is usually estimated from over 2000 particles. Figure 3.12 (a) gives the particle temperature distribution for the alkali-free glass powders obtained by the original data from DPV-2000 at powder feed rate of 30 g/min in the center position. The mean apparent temperature was 3000 K which did not take into account the contributions of non-thermal radiations. The true surface temperature distribution modified by Eq. (3.4) which removed the influence of non-thermal emissions is shown in Fig. 3.12 (b). The shape of the temperature distribution is approximately Gaussian. The average temperature of particles decreased and the distribution slightly shift to the left after calibration. This can be explained by the scattered plasma emission at the lower wavelength affects more strongly than the higher wavelength range. The smaller value of R_λ indicates the stronger effect of the scattered plasma emission. As the value of $R_{\lambda 1}$ was smaller than $R_{\lambda 2}$, the corrected temperature distribution has a totally different shape compared to the one before corrected.

Each data that obtained by DPV-2000 should do the temperature calibration as the example shown above. Figure 3.13 presents an example of overall distributions of particle diameter versus their temperatures obtained by DPV-2000. As may be expected from the particle surface to volume ratio, the smaller particles will be heated faster and will reach higher temperature than larger particles. According to the calculations, the melting temperature of

alkali-free glass is up to 2000 K. It can be observed from the result that most of the detected particles have surface temperature over the melting point, which means the majority of the in-flight particles are in partially molten state.

The tendency can be seen more clearly from the relationship between the mean values of particle diameter and the average velocity with standard deviation which is shown in Fig. 3.14. The error bars represent the standard deviation and have a magnitude of ±σ. Concerning the calculations, error bars have also an x component of ±22. The dispersion in the particle temperature is the biggest for the smallest particles. In thermal spraying process, powders with narrow particle size distributions are used to reduce size effect, which are known to enhance temperature, and velocity variances (Williamson et al. 2000). As the granulated glass raw materials had a certain size distribution from 50 to 300 μm, their temperature history in the plasma may also have a wide distribution. When particles are exposed into the high temperature atmosphere by plasma, the reaction and melting first occur on the surface of the particles, and then propagate into the inner solid. The viscosity of molten glass on the surface will delay the melting reaction and the removal of the decomposed gases inside the particles, namely, the temperature gradient within the particle is important during in-flight glass melting. At the same time, larger particles have higher thermal inertias will reach their maximum temperature values slower than smaller particles.

Figure 3.15 gives the plot of particle diameter versus velocity. The resolution of velocity measurement by DPV-2000 is relatively low, at 1 m/s. Figure 3.16 illustrates the relationship of particle mean diameter and average velocity with the standard deviation. A similar tendency to the temperatures can be observed—the larger the particle, the lower the mean velocity. The standard deviation is also largest for the smallest particles.

Figure 3.17 shows the relationship of particle velocity and temperature estimated by

DPV-2000. Generally, it is considered when at a constant flow rate, higher velocity particles will have a shorter residence time in the plasma hot region, which will cause a lower temperature of particles. However, Fig. 3.18, in which the particle velocity was plotted versus the particle temperature, confirms the particle size effect that all the particles having high velocities also have high temperatures.

Regarding these results, the profiles of the in-flight melted glass particles were successfully obtained by DPV-2000 measurement with adequate corrections. The typical average particle velocity, temperature and diameter measured at center axis are evaluated as 10 m/s, 2400 K and 90 μm, respectively. The results showed the particle size effect was the most critical point in this study rather than the residence time of particles in the plasma region. Small-size particles tend to reach higher velocity and heating to higher temperature, on the contrary, large-size particles had a lower speed of in-flight and lower surface temperature due to the higher thermal inertias. The most fundamental limitation of the measurement of temperature is the plasma light scattered by a particle. This scattered intensity was evaluated and quantified by the spectroscopic measurement which is thought to be justified. It can be concluded that the DPV-2000 did not detect low emissivity particles which depends on particle temperature and size. In the case discussed above, these particles probably have low velocity, low temperature or large diameter. A broader particle size distribution can result in large standard deviations, especially at higher temperatures.

3.3.3 Effect of Carrier Gas Flow Rate on the Spatial Characteristics of Particles

The experimental conditions are listed in Table 3.3. The effect of the carrier gas flow rate was studied considering three different values of 10, 20 and 30 L/min. The other processing parameters were kept at the same. Five different radial distances were measured from the center

of the plasma flame. For each position along the radial direction, the particle velocity, temperature and diameter were measured. Spectroscopic measurements were also conducted at different radial distances. Figure 3.19 shows the effect of carrier gas flow rate on the emission intensity ratio at different radial distances in CW pattern. The measurement position seems to have no effect on the value of emission intensity. Therefore, the average of the five points is used for the calibration of temperature.

Figure 3.20 shows variation of averaged particle axial velocity and dispersion against the radial distance for various carrier gas flow rate in CW pattern. At each constant flow rate, particles obtain maximum velocity in the center of plasma region and decrease along the radial position. This may be followed by the flow speed of plasma flame. The average particle velocity varies linearly with the radial distance. The discrepancy on the mean velocity is the largest at the central line. When increasing the carrier gas flow, the initial particle speed increases. Moreover, the difference of velocity in the radial direction at lower carrier gas flow rate becomes smaller due to the dispersing character and flow structure being improved.

As the granulated glass raw materials had a certain size distribution from about 50 to 300 μm, their temperature history in the plasma are also have a wide distribution. Linear relationship between particle surface temperature and radial distance was found as shown in Fig. 3.21. At a constant flow rate, the maximum of particle average temperature was obtained in the center of the particle flow. Particle temperature decreased with increasing the carrier gas flow rate due to the shorter residence time in the plasma region. The temperature difference between carrier gas flow rates of 10 and 20 L/min are not obvious, however, the temperature decrease rapidly at 30 L/min. This indicates that the particles at lower carrier gas flow conditions were well melted, thus the surface temperature was similar.

It is usually difficult to determine the exact particle size detection without precise

experiments (Larjo et al. 2003). As a result, the diameters measured by DPV-2000 in our experiments are not actual value but are relatively accurate. The effect of carrier gas flow rate on the in-flight particle diameter at different radial distances in CW pattern is shown in Fig. 3.22. Under each constant gas flow rate, the average diameter of particles detected at the center point is smaller than other radial positions. As been mentioned in Fig. 3.21, the particles detected at the center region has the highest temperature, thus the melting process was improved. Improved chemical reaction inside the particles would result in larger shrinkage of particles. However, result showed that the increase of carrier gas flow rate leads to smaller detected particles. This may be related to the change of particle distribution in the powder plume. According to this consideration, particle diameter versus surface temperature was further investigated as below.

Figure 3.23 shows the relationship of particle diameter and temperature measured at the center position in CW pattern with different carrier gas flow rates. It is assumed that larger particles preferably localized on the centerline of particle flow at injection time. Moreover, the spread of particle flux become narrow due to an increase of the carrier gas flow rate. Generally, it is considered that the higher carrier gas flow rate will cause a short residence time of particles in the plasma region. Thus the melted particles are expected to have larger diameter due to insufficient heating. However, the distribution of the *D-T* plot shifts to the smaller diameter indicates that the small-sized particles become easier to penetrate through the plasma plume center. This explains the drop of particle average size at flux center when increasing the carrier gas flow.

Figure 3.24 presents the relationship of particle diameter and temperature measured at different position with the same carrier gas flow rate in CW pattern. The distribution of the *D-T* plot shifts to the larger diameter when measured far away from the center. This phenomenon explains well the plasma flame temperature is high near the center and lower in the side.

In the above presented results, the effect of carrier gas flow rate on the particle spatial characteristics was experimentally confirmed by measuring the particle velocity, temperature and diameter at various radial positions. It emphasis that the particle velocity was most affected by the carrier gas flow rate and this effect is most significant in the central while weakened away from the axis. Particle temperature decreased with increasing the carrier gas flow rate due to short residence time in the plasma. Higher carrier gas flow rate impelled smaller particles inject through the center of plasma. The dispersing character of in-flight particles was largest in the center due to high flow speed and particle size effect.

3.3.4 Effect of Electrode Configuration on the Spatial Characteristics of Particles

The experimental conditions are listed in Table 3.4. Figure 3.25 shows the emission intensity ratio in FF pattern obtained from the spectroscopic measurement. The results of the CW pattern have already given in Fig. 3.19. At both measured wavelength ranges, the emission intensity ratio calculated in FF pattern is higher than that of CW pattern. This indicates the thermal radiation emitted by particle increases or the particle scattered plasma emission decreases.

Due to the particle detection number is insufficient far away from the center, the measurement radial distances in FF pattern were changed at 0, 5, 10, 15 and 20 mm. Figure 3.26 shows the effect of electrode configuration on the axial velocity of in-flight particles at different radial distances. CW pattern improves the particle velocity distribution along the radial direction. Particles have the highest velocity in the central position and decreased gradually along the radial distance. The plasma flame has the highest speed flow velocity in the central axis, thus the particles measured at the central obtained high speed. The average velocity of particles is similar and the dispersion on the velocity is 2~3, which is relatively large compared to its mean

value. The DPV-2000 is specially developed for the particle measurement in thermal spray where the general velocity is higher than 100 m/s. However, the particle velocity in the multi-phase AC arc treatment is usually about 10 m/s, thus the calculated standard deviation is large in our experiment. Anyhow, the measurement in the velocity has high accuracy based on this tool. It does not affect the obtained average data.

Average temperature and the standard deviation of particles in different electrode configuration are given in Fig. 3.27. It is obviously that CW pattern provides larger heat transfer from plasma to particles. According to the results obtained in Section 2.3.1, since the arc across the center area of plasma plume at diverse times in CW pattern, direct high-energy transfer from the arc to particles occurs frequently. Therefore, particles can be heated by both the arc and plasma flame in the CW pattern. On the contrary, the arc is constricted near the electrode region in FF pattern, thus particles fly into the center will not have chance to interact with arc and mainly be heated by the flame. This can explain why the average temperature measured at the center plume in CW pattern is higher. In addition, the dispersion of particle temperatures for FF pattern is smaller than that of CW pattern. The reason may be drawn from the Section 2.4.1, that the amplitude of plasma fluctuation in CW pattern is larger than FF pattern. The instability of arc characteristics is strong in CW pattern, resulted in a lower uniformity of the in-flight particle behavior. In a conclusion, FF pattern can be expected to achieve more uniform particle heating.

The results of particle diameters measured in different electrode configurations are shown in Fig. 3.28. Due to many uncertainties in the diameter calculation by DPV-2000 that has been explained in the principle, the calculated particle size is used for roughly estimation in this study. So the standard deviation on the data has no such important meaning that will not be given in this result. According to the above temperature results in Fig. 3.27, the higher temperature of particle leads to smaller diameter. The particles measured at the center position

have the smallest size due to the sufficient heating by plasma. Particles fly away from the central are in the lower temperature region of the plasma flame, so their surface temperature are lower, and particle size are larger.

The effect of electrode configuration on the particle characteristics at various positions was mainly due to the spatial distribution of high-temperature region. Accordingly, the particle temperature was different due to the heating efficiency in different electrode patterns. Besides, the electrode configuration does not play a major role in the particle velocity.

3.3.5 Effect of Electrode Diameter on the Spatial Characteristics of Particles

The experimental conditions are listed in Table 3.5. The effect of electrode diameter on the axial velocity of in-flight particles at various radial distances is presented in Fig. 3.29. The average velocity at each measured point has no significant difference between the two electrode diameters. Moreover, the particles along the center flow line have the highest velocity and decrease along the radial distance.

Figure 3.30 gives the particle temperature measured under different electrode diameters. The average value at each position is little higher with the large electrode diameter. Previous studies in Section 2.3.5 explained the arc swing with electrode diameter of 6 mm is narrow thus caused a more concentrate arc existence time in the central. This helps to transfer more energy from arc to the particles. Moreover, larger molten area leads to lower tip temperature. The average temperature in the plasma with small electrode diameter is lower than that of larger diameter. In a result, the particles treated in the 6 mm electrode achieved higher surface temperature. The arc distribution region is wider but more diffused with electrode size of 3.2 mm. According to this view, the particle temperature is little lower in the case of small electrode diameter.

Figure 3.31 presents the measured particle diameter with different electrode diameters. The lower average temperature caused larger diameter of melted particles with electrode size of 3.2 mm.

On the basis of experimental study of the effect of electrode diameter on the particle characteristics, it clearly showed a higher temperature and uniformity of particles can be observed using larger diameter of electrode. This result was in good agreement with the plasma spatial characteristics indicating larger diameter leads to higher plasma temperature.

3.4 Comparison of Spatial Characteristics of the Arc and Particles

The parameters of carrier gas flow rate, the electrode configuration and the electrode diameter are proved to have influence on the particle spatial characteristics. Moreover, the electrode configuration and the electrode diameter are known to significantly influence the plasma spatial properties. Experimental studies have identified that the spatial characteristics of particles are related with different electrode configurations. It is thought that the arc column has high viscosity. The detected particles were few far away from the central area probably due to high viscosity near the electrode region in FF pattern. The particle velocity is mainly decided by the carrier gas flow rate and injector diameter, therefore, no significant relation with the plasma spatial feature. Combined with the previous results for the plasma spatial characterization, the arc passes through the central region in CW pattern while no arc across the center in FF pattern. Therefore, the in-flight particles obtain energy from both of the arc and plasma flame in CW pattern, while particles are only heated by the flame in FF pattern. This resulted in the higher temperature in CW pattern than that of FF pattern. Additionally, the larger electrode size causes the higher plasma temperature, and the particle temperature was verified to be higher. The particle diameter is dependent on its surface temperature. The more heated, the more shrink of

melted particles.

Not all experimental data were given out for each parameter, therefore, the uniformity of the particle characteristics are summarized and compared in the case of CW patter (electrode size of 6 and 3.2 mm) and FF pattern (electrode size of 6 and 3.2 mm). The uniformity of in-flight particle velocity measured at the center flow at feed rate of 30 g/min and carrier gas flow rate of 20 L/min is shown in Fig. 3.32. The effect of the electrode diameter on the particle velocity dispersion seems more important than that of the electrode configuration. The relative spread with respect to mean velocities is 20%, 34%, 24% and 36%, respectively. It should be noted that the standard deviation of velocity is little higher in the multi-phase AC arc than the usual thermal spraying process. This is related to the low average velocity in the multi-phase AC arc processing and the resolution in velocity measurement by DPV-2000.

Figure 3.33 shows the measurement scatters around mean values in particle temperature with different arc discharge conditions. The effect of the electrode configuration on the particle temperature dispersion seems more important than that of the electrode diameter. The relative spread with respect to mean temperatures is 16%, 16%, 14% and 15%, respectively.

Figure 3.34 shows the standard deviation of measured diameters with different arc discharge conditions. The difference in the electrode diameter has greater influence on the particle diameter dispersion. The scatter around mean diameters is 34%, 40%, 28% and 41%, respectively.

Both of the electrode configuration and electrode diameter are demonstrated to have influence on the particle spatial characteristics. In the melting process, the instabilities of particle velocity and temperature are expected to be small, thus FF pattern with electrode diameter of 6 mm could be the appropriate condition.

3.5 Conclusion

In-flight particle diagnostics performed with optical system DPV-2000 and spectroscopic measurement were investigated theoretically and experimentally. A method was pointed out to estimate the accuracy of in-flight particle temperature by separating the non-thermal emissions. In addition, particles are experimentally detected within a large radial position in the plasma flame by varying the process parameters such as the carrier gas flow rate, the electrode configuration, and the electrode diameter. The research presented in this chapter yielded the following results.

1) The presence of plasma emission scattered by the particles can cause significant errors in temperature calculations using two-color pyrometry in multi-phase AC arc system. Therefore, to minimize the temperature errors, the intensity ratio of the particle thermal emission in the whole intensity taken by DPV-2000 should be considered.
2) The profiles of the in-flight melted glass particles were successfully obtained by DPV-2000 measurement with adequate corrections. The distributions of particle velocity, temperature and diameter were approximately Gaussian. The average temperature of particles decreased and the distribution was slightly narrowed after correction.
3) Granulated glass powders have relatively large size distribution and thus the size effect on the particle temperature and velocity variances is increased. The relationship between the mean values of particle diameter and the average velocity with standard deviation indicated the dispersion in the particle temperature is the biggest for the smallest particles. Small-sized particles tend to reach higher velocity and heating to higher temperature, on the contrary, large-sized particles had a lower speed of in-flight and lower surface temperature due to the higher thermal inertias.
4) The particle velocity was mostly dependent on the carrier gas flow rate. While the particle

temperature had relationship with the arc discharge conditions such as electrode configuration and electrode size. The particle diameter was related to its surface temperature, which is in accordance with the measurement principle. The higher temperature resulted in the smaller diameter.

5) The detection number of particles was small for the locations further away from the plasma centerline in FF pattern due to high viscosity near the electrode region in FF pattern.

6) In all the conditions that have been studied, the uniformity of overall particle characteristics was better in the FF pattern with electrode diameter of 6 mm.

7) The exact limits with DPV-2000 diagnostic system imposed by the issues described above are dependent on the size and emissivity of the particles. Additionally, there is also fundamental limitation of temperature measurement because the emissivities are not well known for the materials, and can change due to surface oxidation or other chemical reactions. Many particles do not pass the theoretical mask image plane also gave rejected signals of the detection algorithm. Therefore, a large number of good particles are essential to estimate particle characterization with a high degree of accuracy.

8) The in-flight particle temperature is critical to control the melting process. A narrow size distribution of raw materials can achieve a uniform temperature distribution. A proper selection of a proper raw material size distribution as well as good control of the residence time in the plasma high temperature region is expect to achieve a better melting result.

References

Fincke, J.R., D.C. Haggard and W.D. Swank. “Particle Temperature Measurement in the Thermal Spray Process.” *Journal of Thermal Spray Technology* **10**(2), 255-266 (2001).

Gougeon, P. and C. Moreau. “In-Flight Particle Surface Temperature Measurements: Influence of the Plasma Light Scattered by the Particles.” *Journal of Thermal Spray Technology* **2**(3), 229-234 (1993).

Hollis, K. and R. Neiser. “Analysis of the Nonthermal Emission Signal Present in a Molybdenum Particle-Laden Plasma-Spray Plume.” *Journal of Thermal Spray Technology* **7**(3), 383-391 (1998).

Larjo, J., E. Hamalainen and N. Kriikka. “In-flight particle imaging in thermal spraying with diode laser illumination.” Thermal Spray 2003: Advancing the Science and Applying the Technology. **2**, 1113-1116, (Eds.) B. R. Marple and C. Moreau, (Pub.) ASM Int. (2003)

Mauer, G., P. Gougeon, M. Lamontagne, V. Lacasse, G. Vandreuil and P. Cielo “On-Line Control of the Plasma Spraying Process by Monitoring the Temperature, Velocity and Trajectory of In-Flight Particles.” *NTSC Proceedings: Thermal Spray Industrial Applications*, 431-437, Boston (1994).

Mauer, G., R. Vaßen and D. Stöver. “Comparison and Application of DPV-2000 and Accuraspray-g3 Diagnostic Systems.” *Journal of Thermal Spray Technology* **16**(3), 414-424 (2007).

Ohkawa, S., C. Tanaka, S. Miyazaki, N. Shinohara and O. Sakamoto. “Application of the in-flight melting technology using RF plasma to alkaline free silicate glass.” *23rd International Congress on Glass* Prague, Czech Republic (2013).

Pouliot, L., J. Blain and F. Nadeau. “DPV 2000 Reference Manual-In Flight Particle Sensor for Thermal Spraying Systems.” Tecnar Automation Ltd., Canada (1998).

Sakuta, T. M.I. Boulos. “Novel Approach for Particle Velocity and Size Measurement Under Plasma Conditions.” *Review of Scientific Instruments* **59**(2), 285-291(1988).

Salhi, Z., P. Gougeon, D. Klein and C. Coddet. “Influence of Plasma Light Scattered by In-Flight Particle on the Measured Temperature by High Speed Pyrometry.” *Infrared Physics & Technology* **46**(5), p 394-399 (2005).

Williamson, R.L., J.R. Fincke and C.H. Chang. “A Computational Examination of the Sources of Statistical Variance in Particle Parameters During Thermal Plasma Spraying.” *Plasma Chemistry and Plasma Processing* **20**(3), 299-324 (2000).

Table 3.1 Batch formulation of alkali-free glass

Raw Material	SiO_2	Al_2O_3	B_2O_3	BaO	Fe_2O_3	SrO	Total
[wt%]	50.2	9.0	15.4	24.7	0.1	0.3	99.7

Table 3.2 Experimental conditions for in-flight particle measurement by DPV-2000

Discharge conditions	
Number of phase	12
Electrode configuration	Clockwise (CW) pattern
Power	40~50 kW
Current	320 A
Voltage	200 V
Electrode distance	100 mm
Ar flow rate (each electrode)	5 L/min
Tungsten electrode diameter	φ3.2 mm
Powder treatment conditions	
Powder	Alkali-free glass
Primary SiO_2 size	7~8 μm
Particle mean size	114 μm
Powder feed rate	30 g/min
Air carrier gas flow rate	20 L/min
Diagnostic methods	
Particle measurement	DPV-2000 (Tecnar)
Spectroscopic measurement	MD-100 (JASCO)
Measurement position	center of the axis

Table 3.3 Experimental conditions for effect of carrier gas flow rate

Discharge conditions	
Number of phase	12
Electrode configuration	Clockwise (CW) pattern
Power	40~50 kW
Current	320 A
Voltage	200 V
Electrode distance	100 mm
Ar flow rate (each electrode)	5 L/min
Tungsten electrode diameter	φ3.2 mm
Powder treatment conditions	
Powder	Alkali-free glass
Primary SiO_2 size	7~8 μm
Particle mean size	128 μm
Powder feed rate	30 g/min
Air carrier gas flow rate	10, 20, 30 L/min
Diagnostic methods	
Particle measurement	DPV-2000 (Tecnar)
Spectroscopic measurement	MicroHR (HORIBA)
Measurement position	0, 10, 20, 30, 40, 50 mm

Table 3.4 Experimental conditions for effect of electrode configuration

Discharge conditions		
Number of phase	12	12
Electrode configuration	Clockwise (CW) pattern	Flip-flop (FF) pattern
Power	40~50 kW	35~45 kW
Current	320 A	
Voltage	200 V	
Electrode distance	100 mm	
Ar flow rate (each electrode)	5 L/min	
Tungsten electrode diameter	φ3.2 mm	
Powder treatment conditions		
Powder	Alkali-free glass	
Primary SiO_2 size	7~8 μm	
Particle mean size	128 μm	
Powder feed rate	30 g/min	
Air carrier gas flow rate	20 L/min	
Diagnostic methods		
Particle measurement	DPV-2000 (Tecnar)	
Spectroscopic measurement	MicroHR (HORIBA)	
Measurement position	0, 10, 20, 30, 40 mm	0, 5, 10, 15, 20 mm

Table 3.5 Experimental conditions for effect of electrode diameter

Discharge conditions		
Number of phase	12	
Electrode configuration	Clockwise (CW) pattern	
Power	40~50 kW	40~50 kW
Current	320 A	
Voltage	200 V	
Electrode distance	100 mm	
Ar flow rate (each electrode)	5 L/min	
Tungsten electrode diameter	φ3.2 mm	φ6 mm
Powder treatment conditions		
Powder	Alkali-free glass	
Primary SiO_2 size	7~8 μm	
Particle mean size	128 μm	
Powder feed rate	30 g/min	
Air carrier gas flow rate	20 L/min	
Diagnostic methods		
Particle measurement	DPV-2000 (Tecnar)	
Spectroscopic measurement	MicroHR (HORIBA)	
Measurement position	0, 10, 20, 30, 40 mm	0, 10, 20, 30, 40, 50 mm

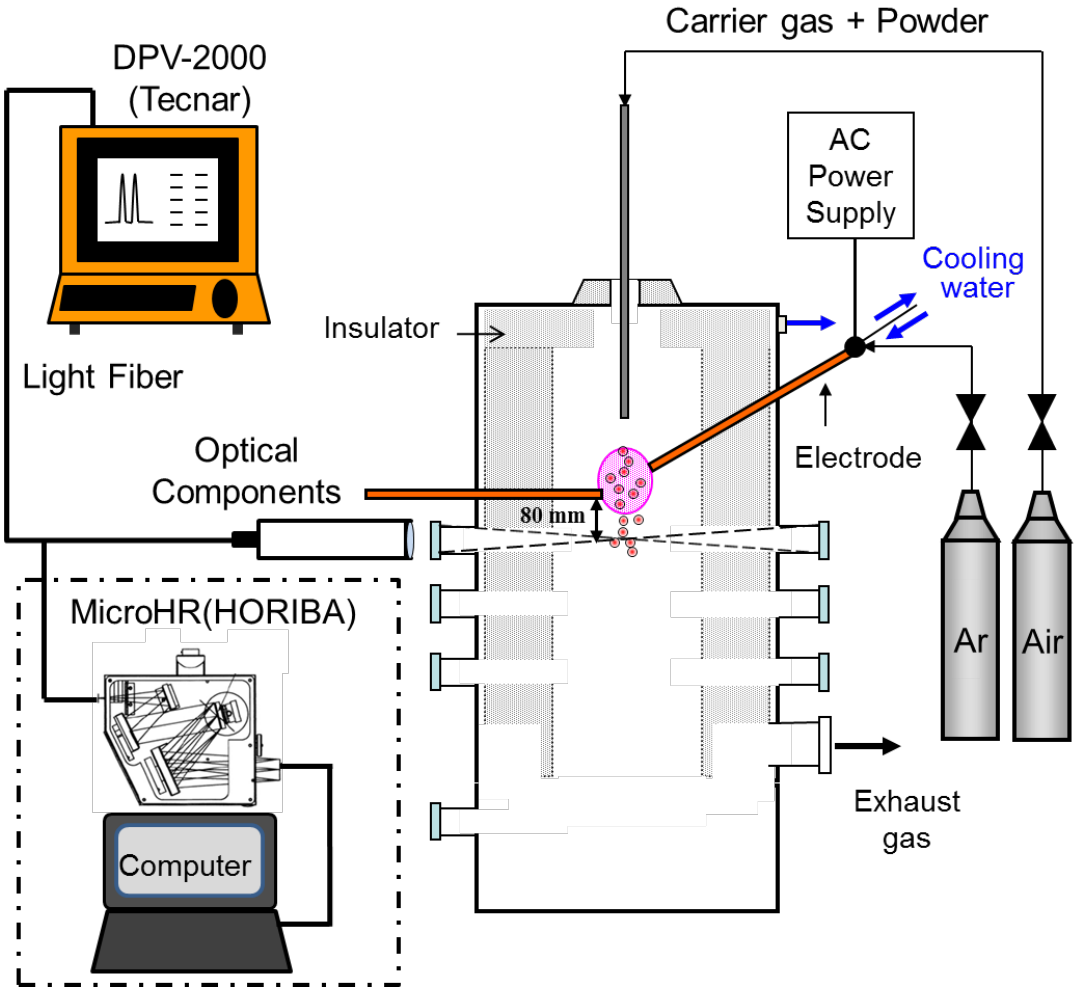

Fig. 3.1 The schematic arrangement of the system setup

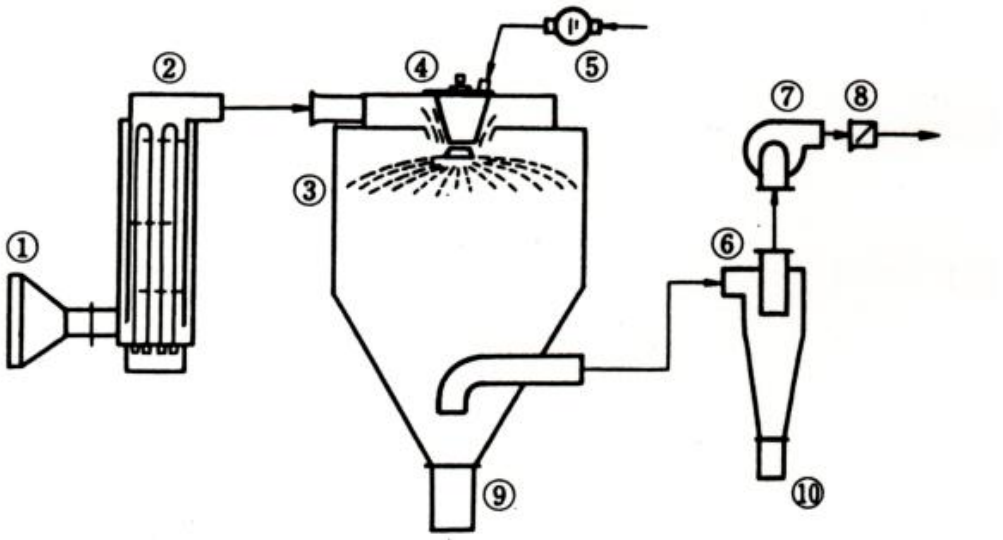

①air blower	②heater	③drying chamber
④atmizing device	⑤pomp	⑥dust collector
⑦blower	⑧exhaust filter	⑨separator
⑩recovery container		

Fig. 3.2 The schematic of the spray dryer

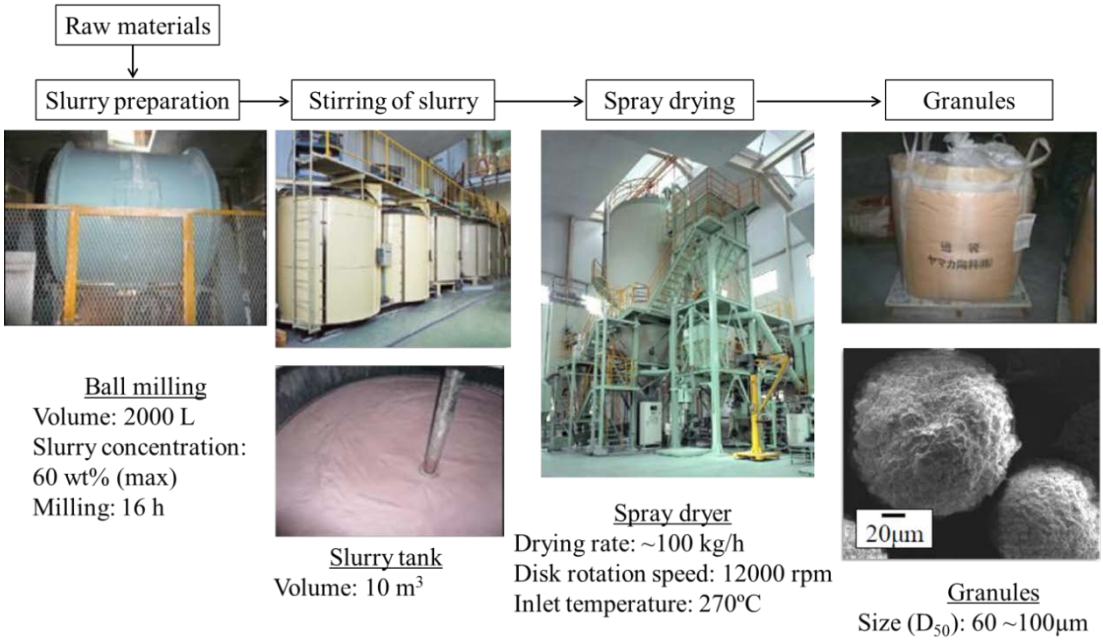

Fig. 3.3 Granulation process of spray dry method supplied by Asahi Glass Co., Ltd., Japan (Ohkawa et al. 2013)

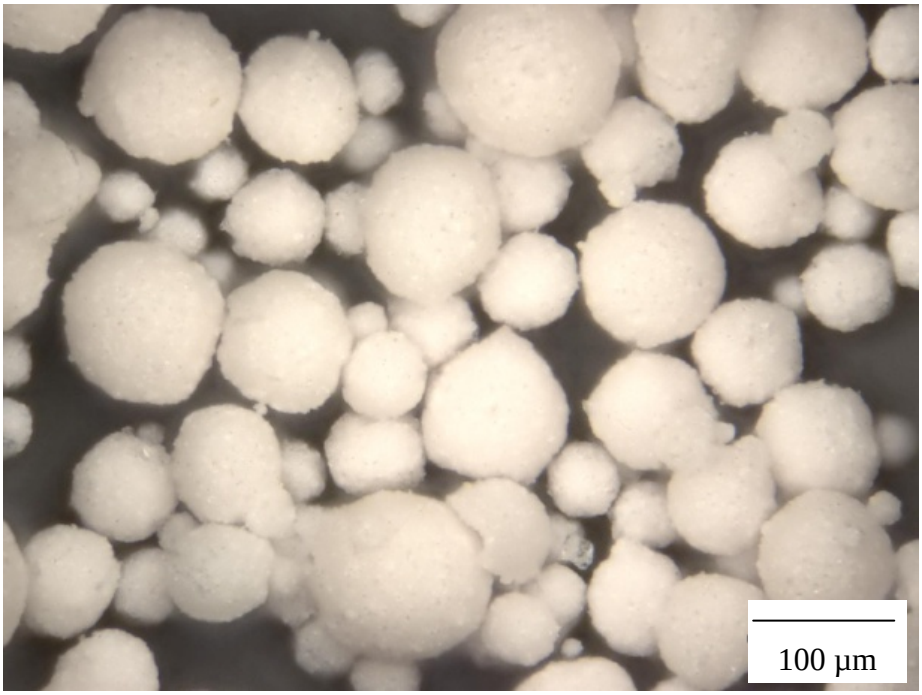

Fig. 3.4 The scope image of raw material of alkali-free glass

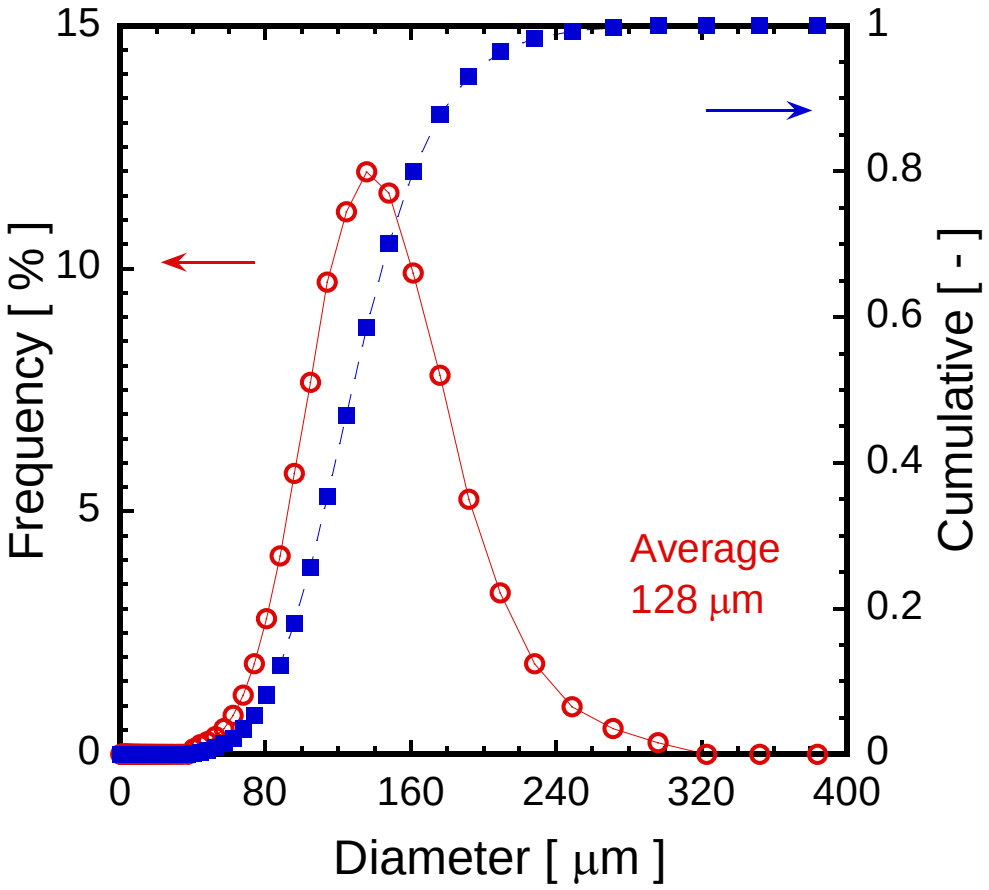

Fig. 3.5 Particle size distribution of raw material of alkali-free glass

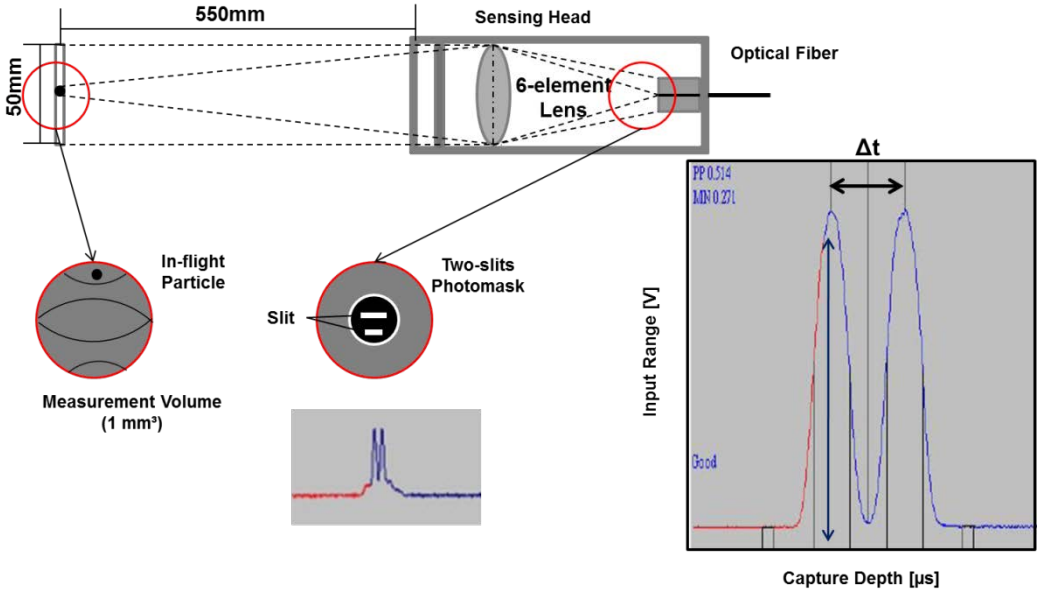

Fig. 3.6 The conceptual diagram of velocity measurement principle

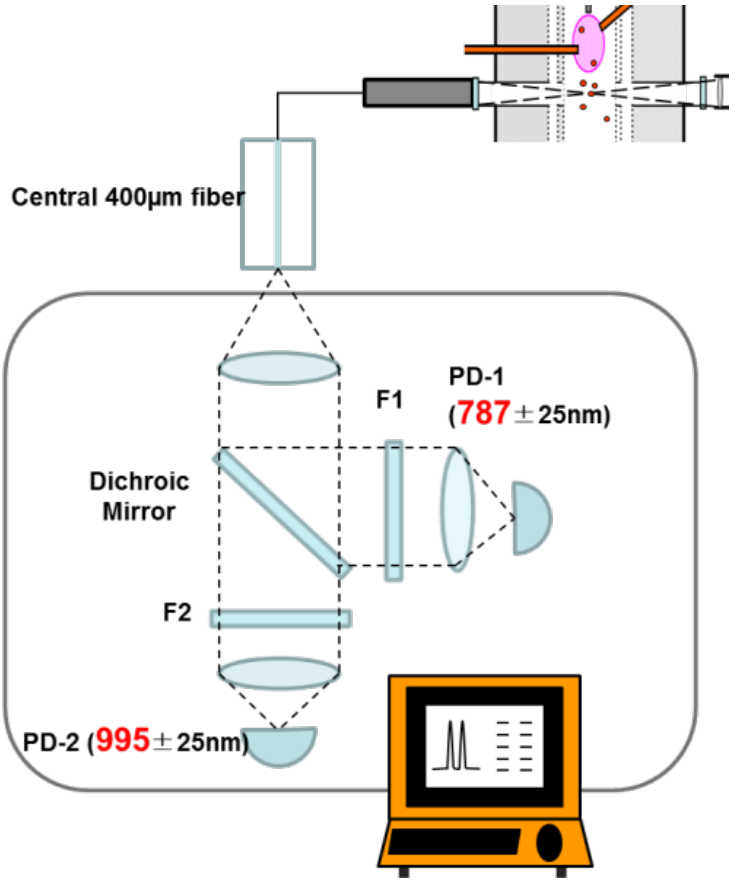

Fig. 3.7 The Conceptual diagram of temperature measurement principle

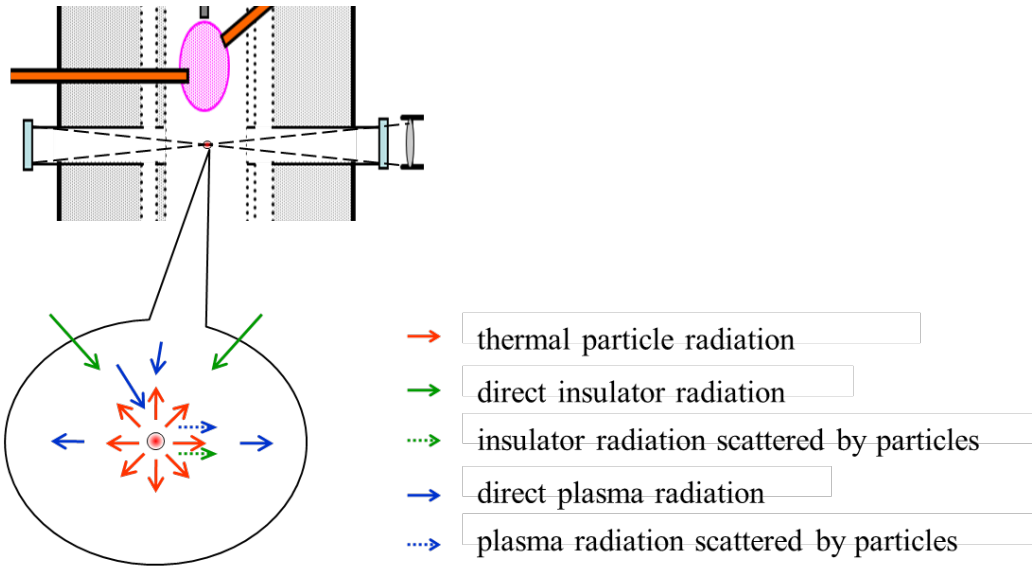

Fig. 3.8 Considered emissions taken in the particle measurement volume

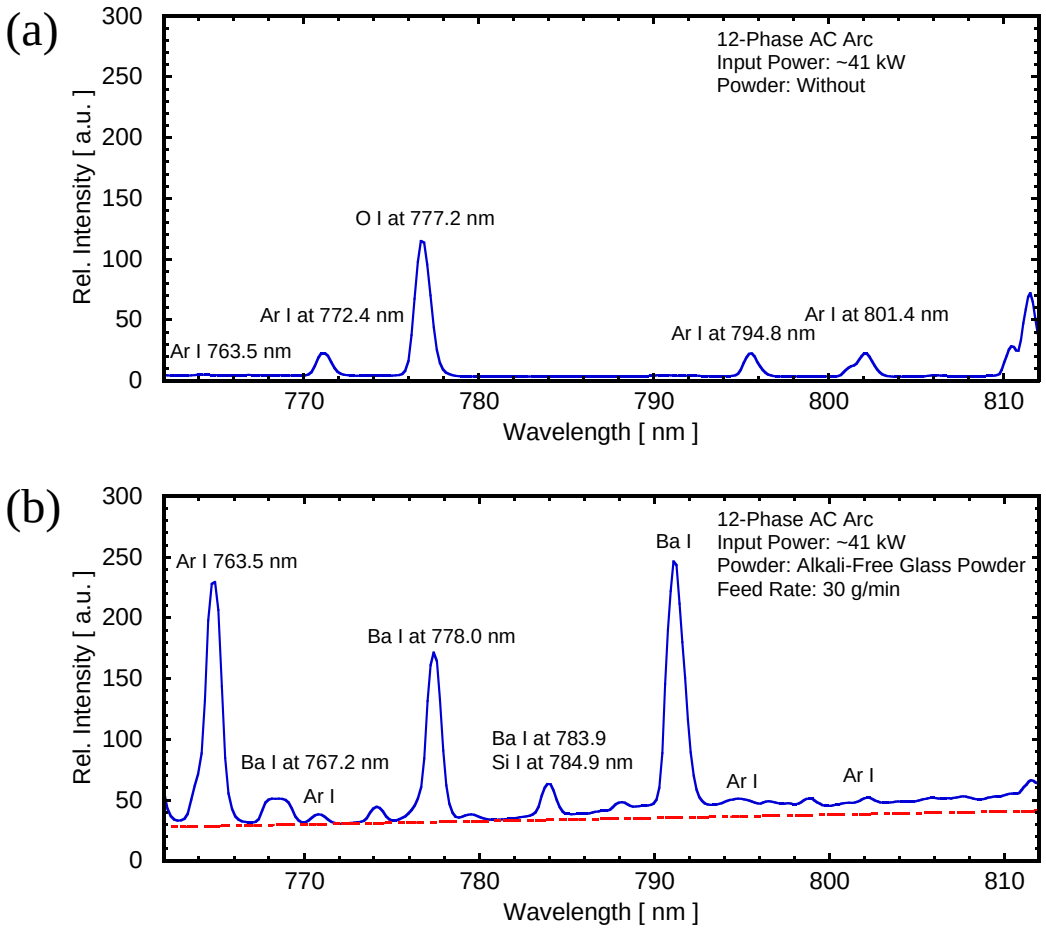

Fig. 3.9 Emission spectrum at λ_1=787±25 nm: (a) Without powder feeding and (b) With powder feeding

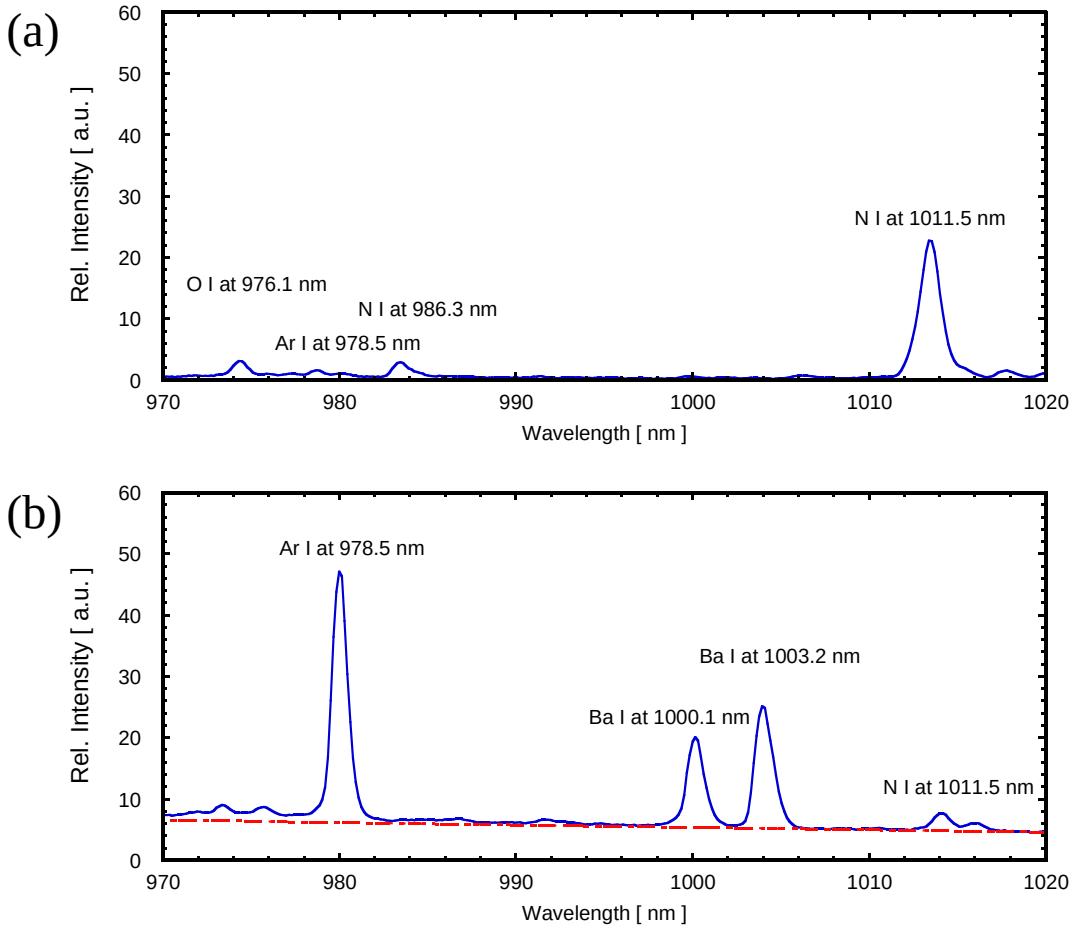

Fig. 3.10 Emission spectrum at λ_2=995±25 nm: (a) Without powder feeding and (b) With powder feeding

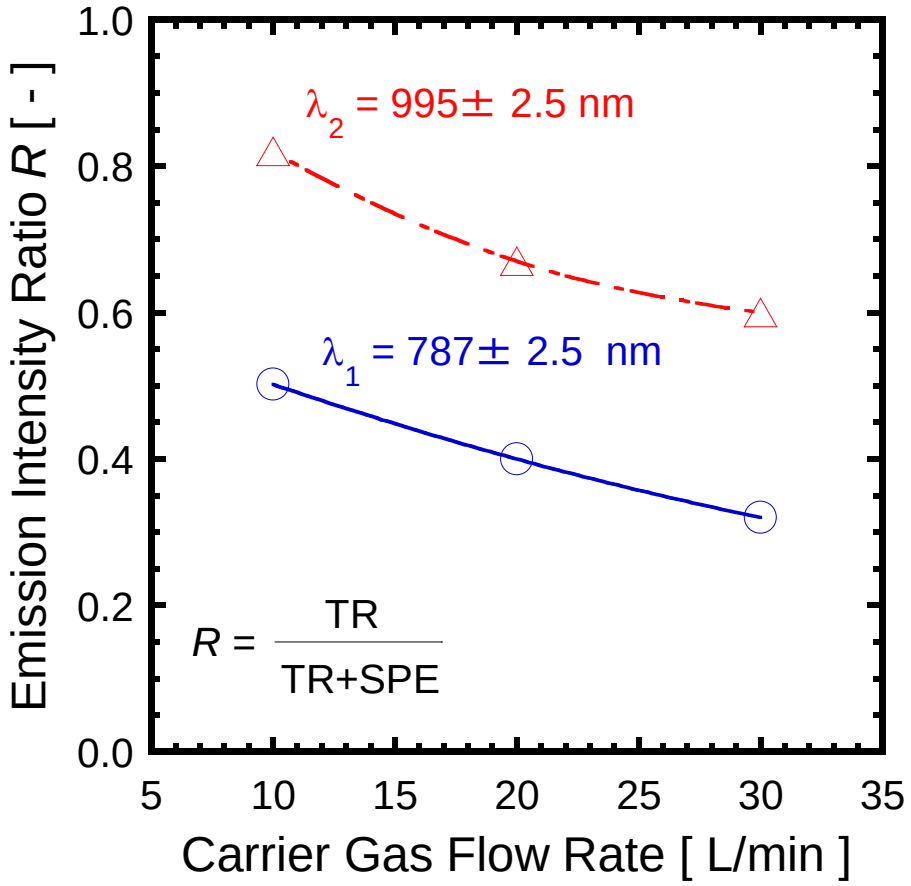

Fig. 3.11 Effect of carrier gas flow rate on the emission intensity ratio

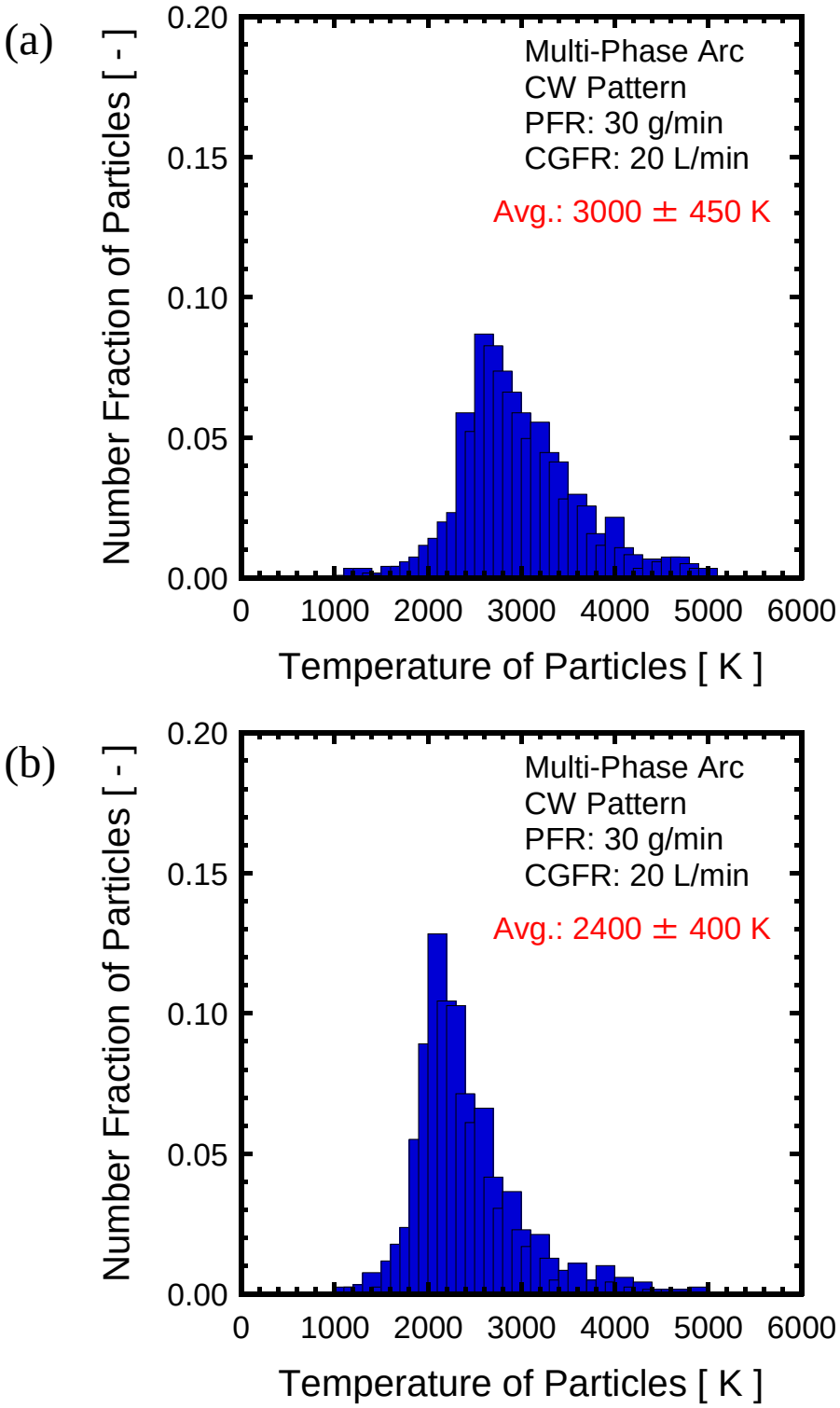

Fig. 3.12 Particle surface temperature distribution estimated by DPV-2000: (a) before correction and (b) after correction

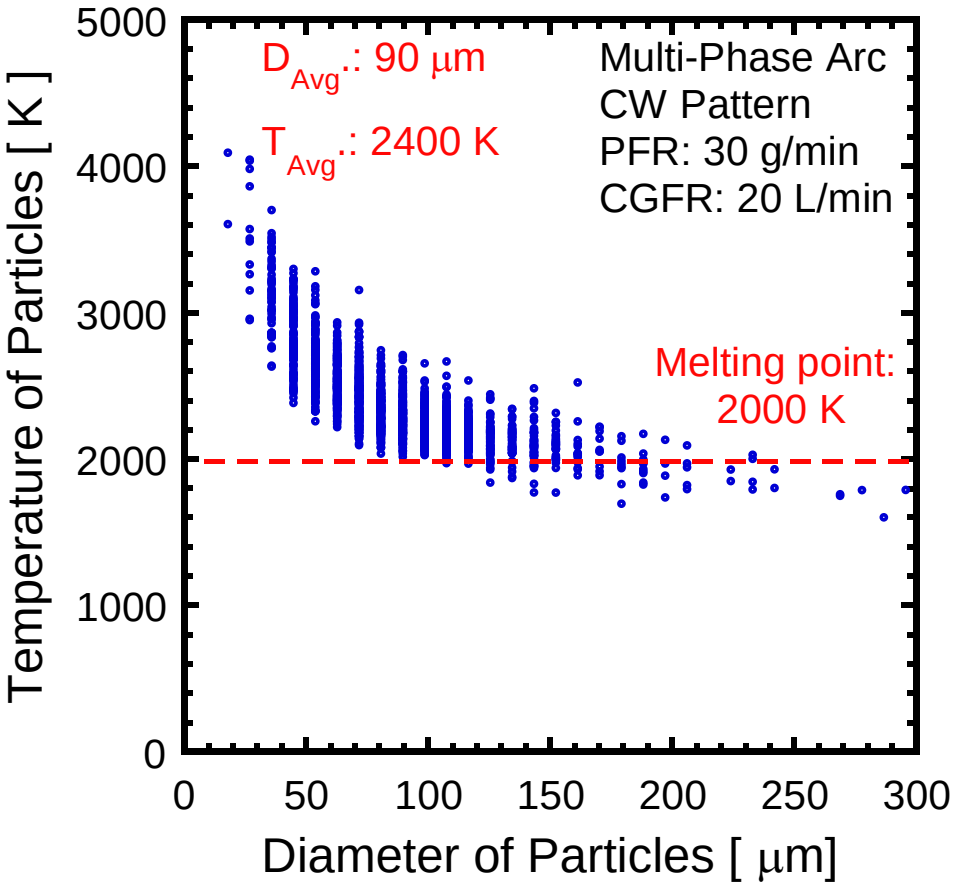

Fig. 3.13 Relationship of particle diameter and temperature estimated by DPV-2000

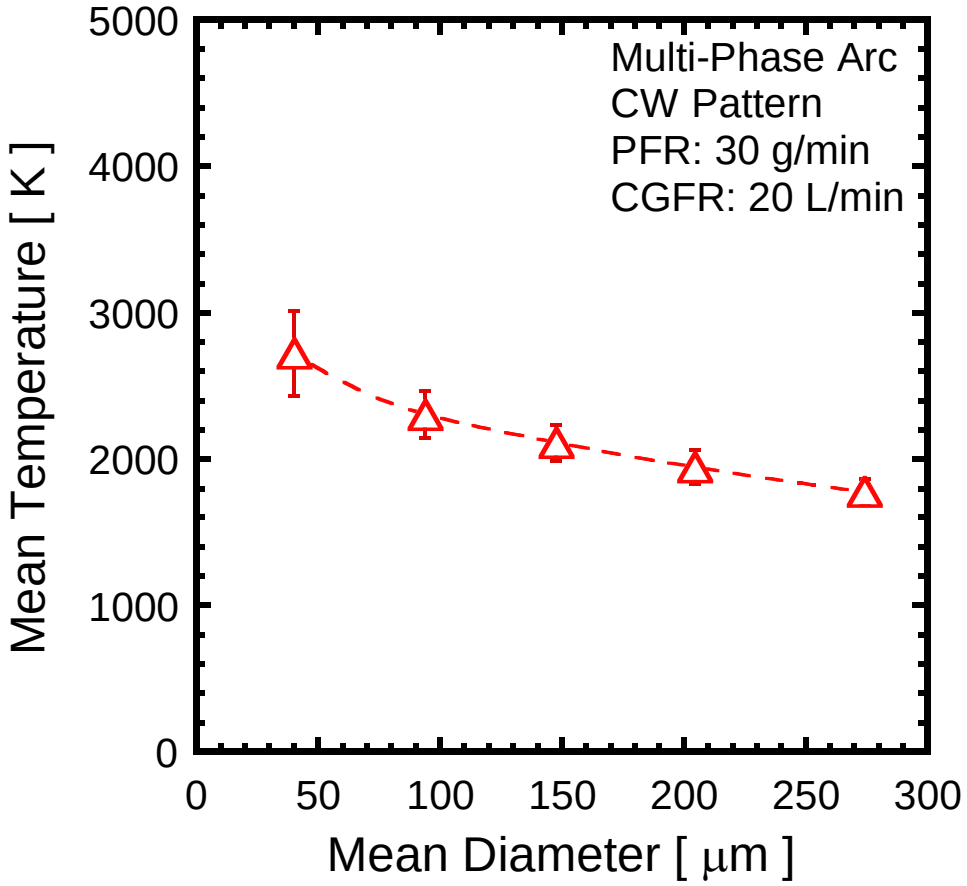

Fig. 3.14 Relationship of particle mean diameter and mean temperature estimated by DPV-2000

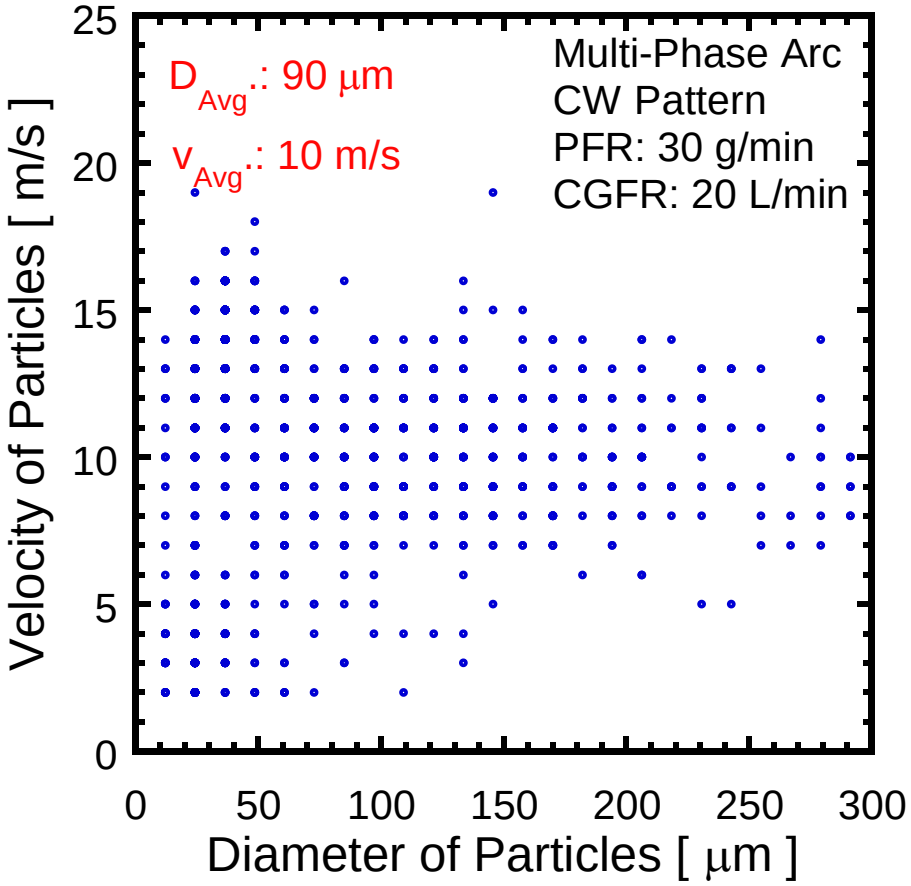

Fig. 3.15 Relationship of particle diameter and velocity estimated by DPV-2000

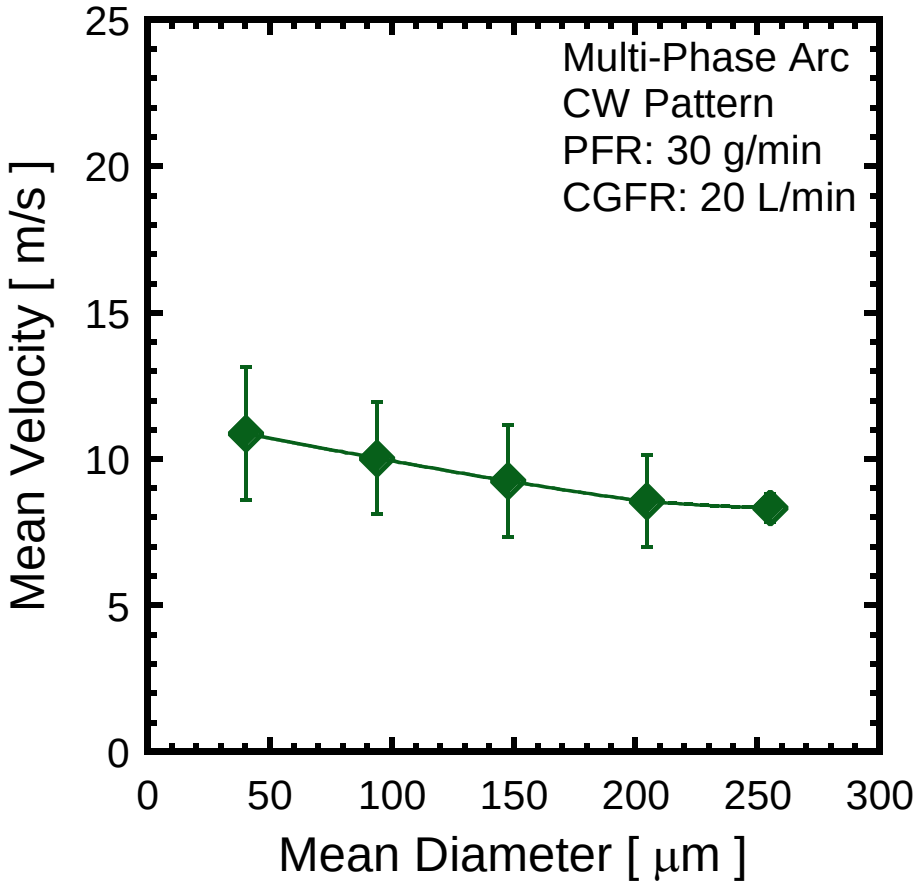

Fig. 3.16 Relationship of particle mean diameter and mean velocity estimated by DPV-2000

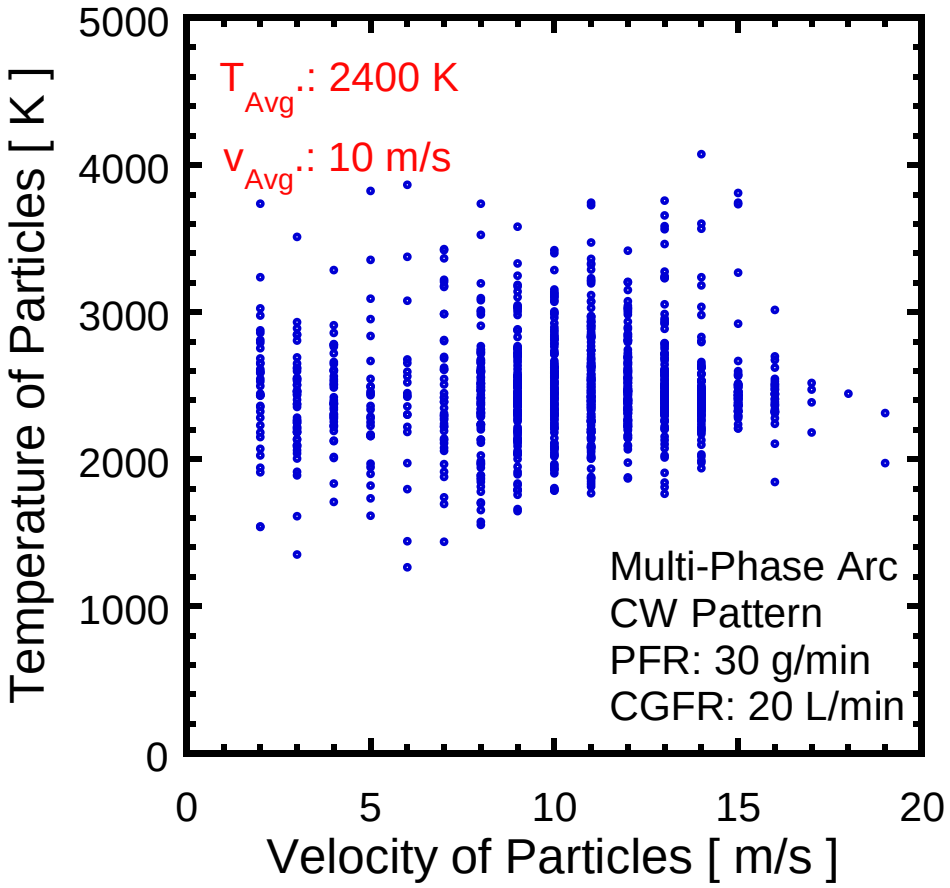

Fig. 3.17 Relationship of particle velocity and temperature estimated by DPV-2000

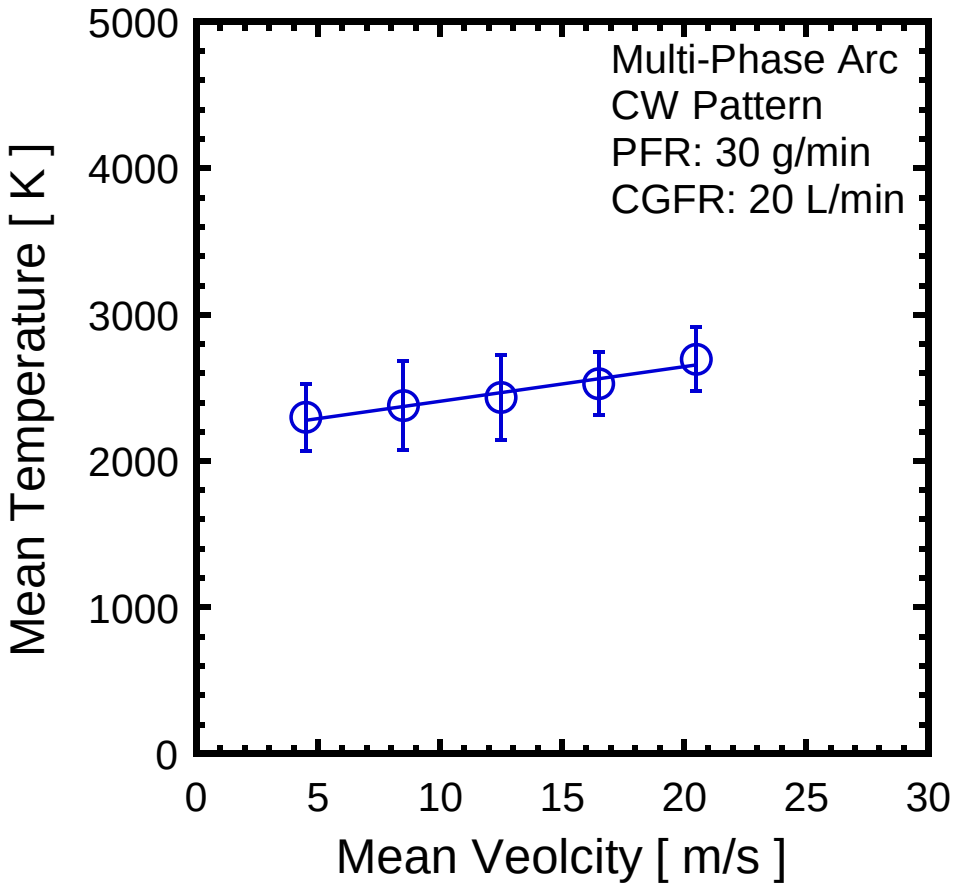

Fig. 3.18 Relationship of particle mean velocity and mean temperature estimated by DPV-2000

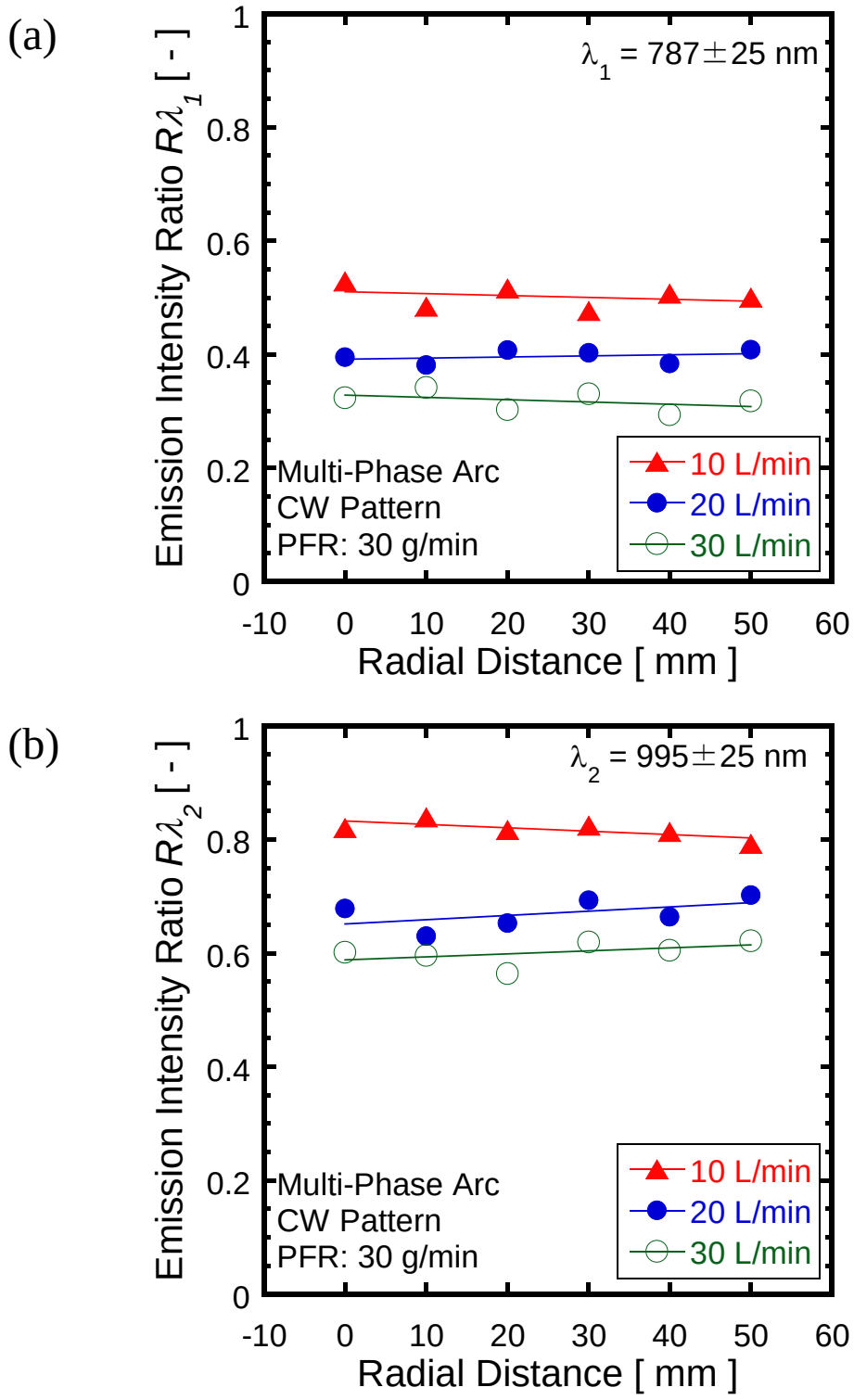

Fig. 3.19 Effect of carrier gas flow rate on the emission intensity ratio $R_{\lambda 1}$ and $R_{\lambda 2}$ at different radial distances in CW pattern

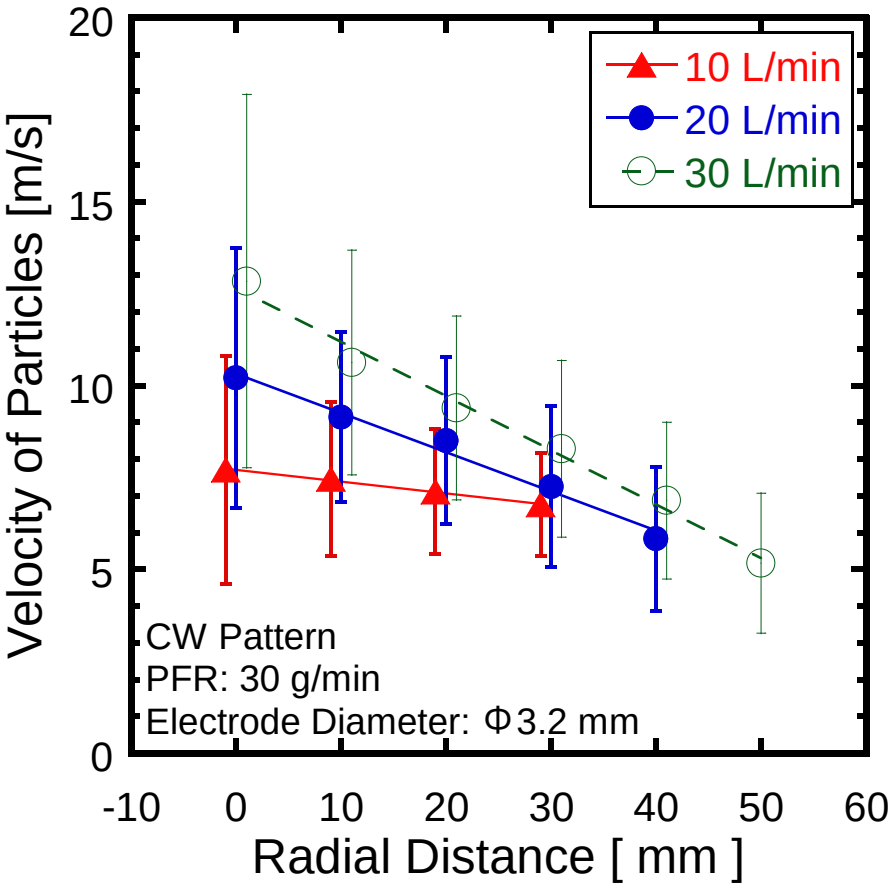

Fig. 3.20 Effect of carrier gas flow rate on the axial velocity of in-flight particles at different radial distances in CW pattern

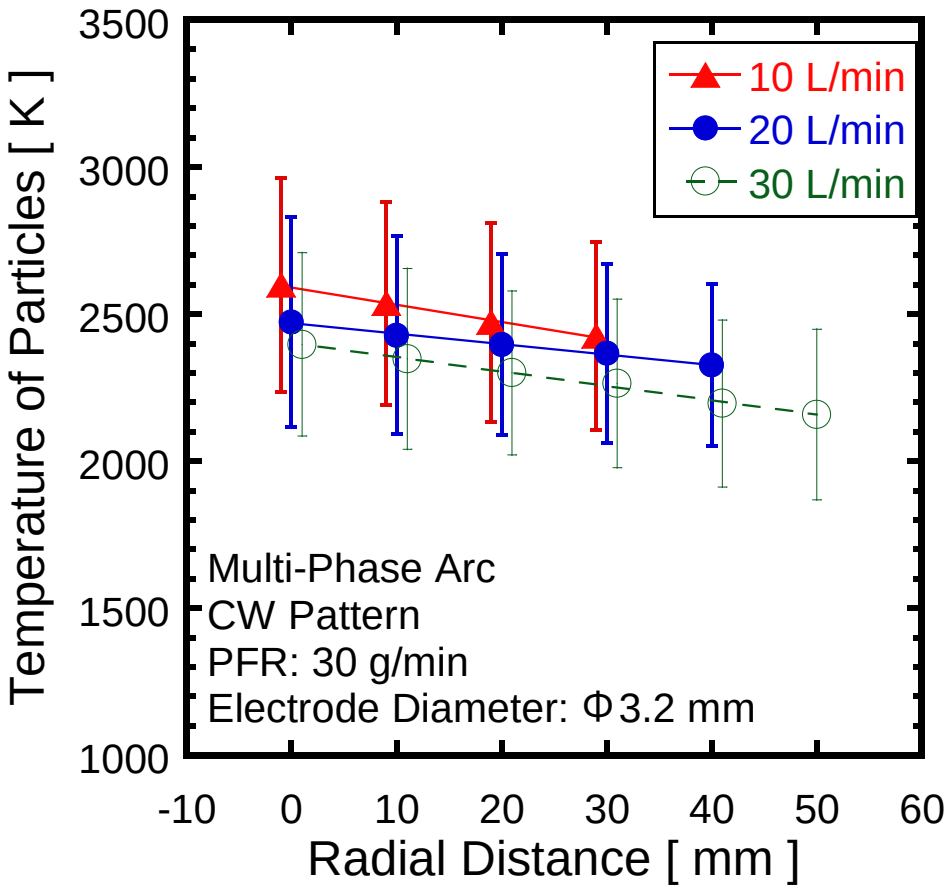

Fig. 3.21 Effect of carrier gas flow rate on the temperature of in-flight particles at different radial distances in CW pattern

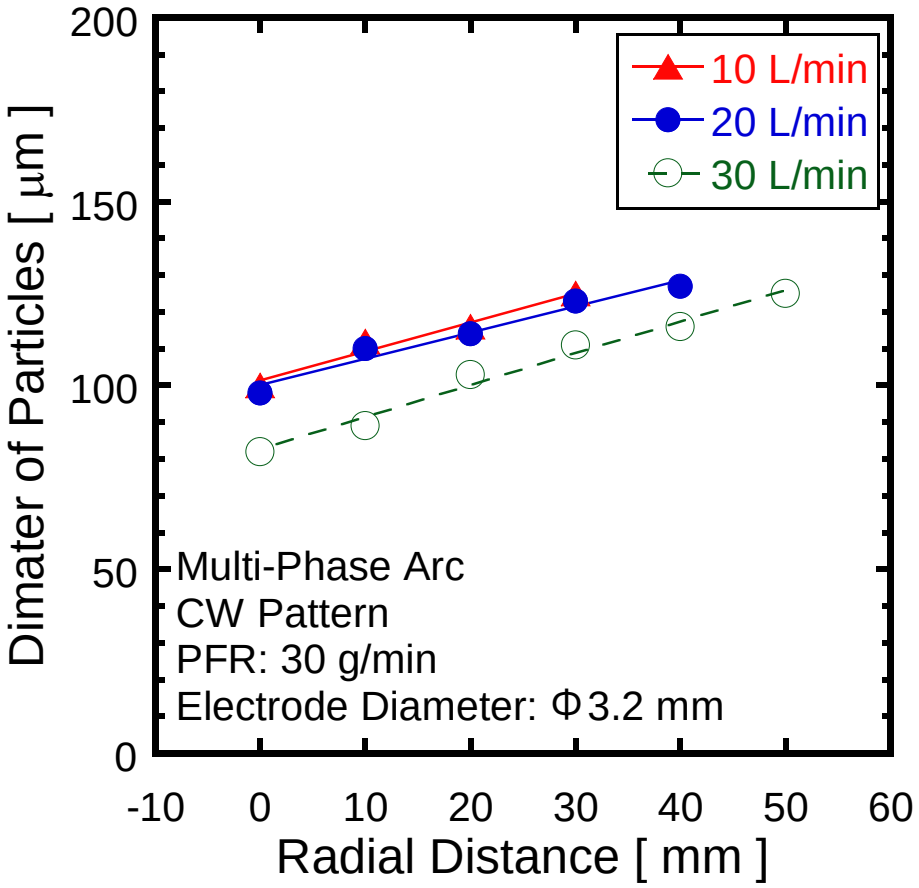

Fig. 3.22 Effect of carrier gas flow rate on the diameter of in-flight particles at different radial distances in CW pattern

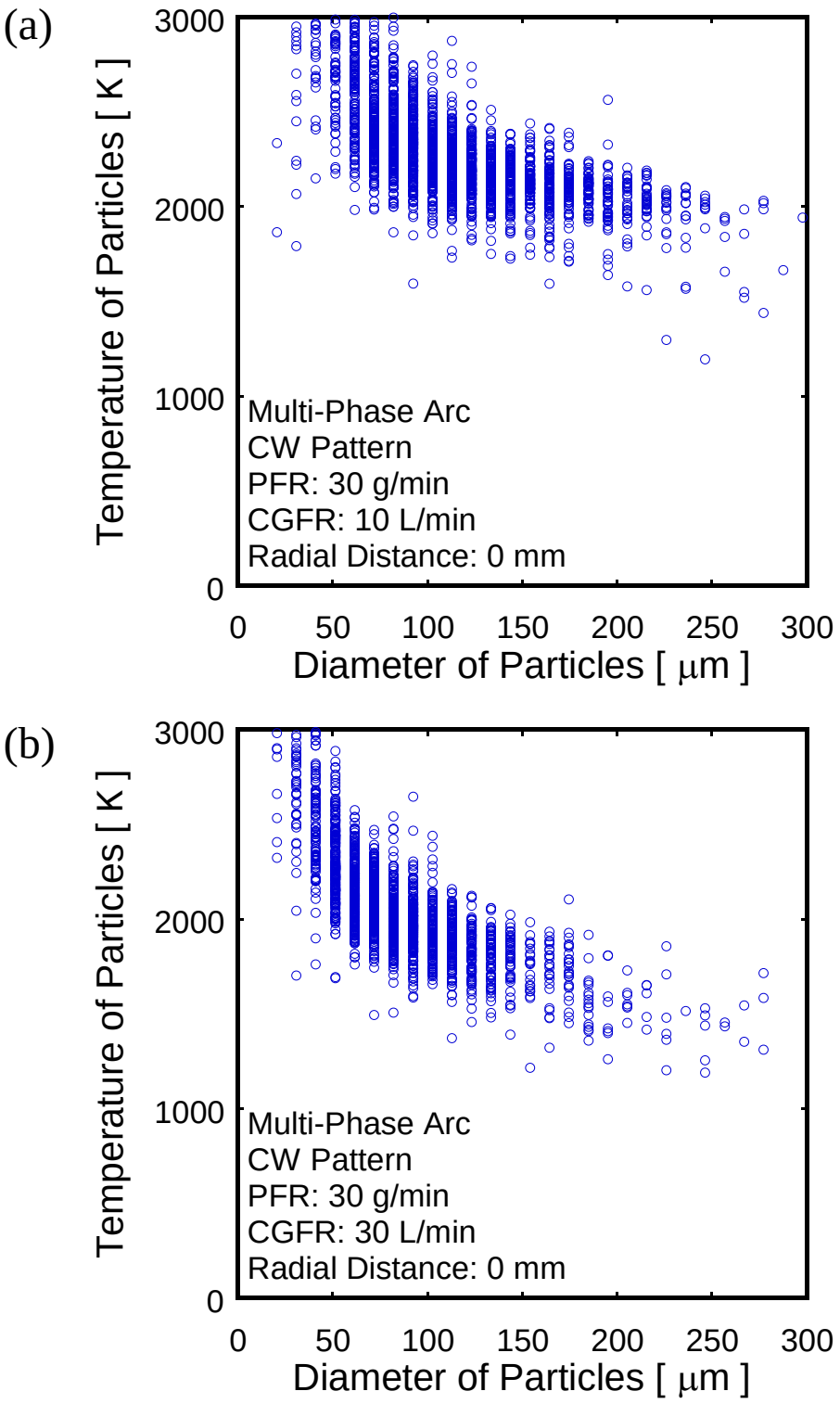

Fig. 3.23 Relationship of particle diameter and temperature estimated by DPV-2000 at the center position in CW pattern with carrier gas flow rate of (a) 10 L/min and (b) 30 L/min

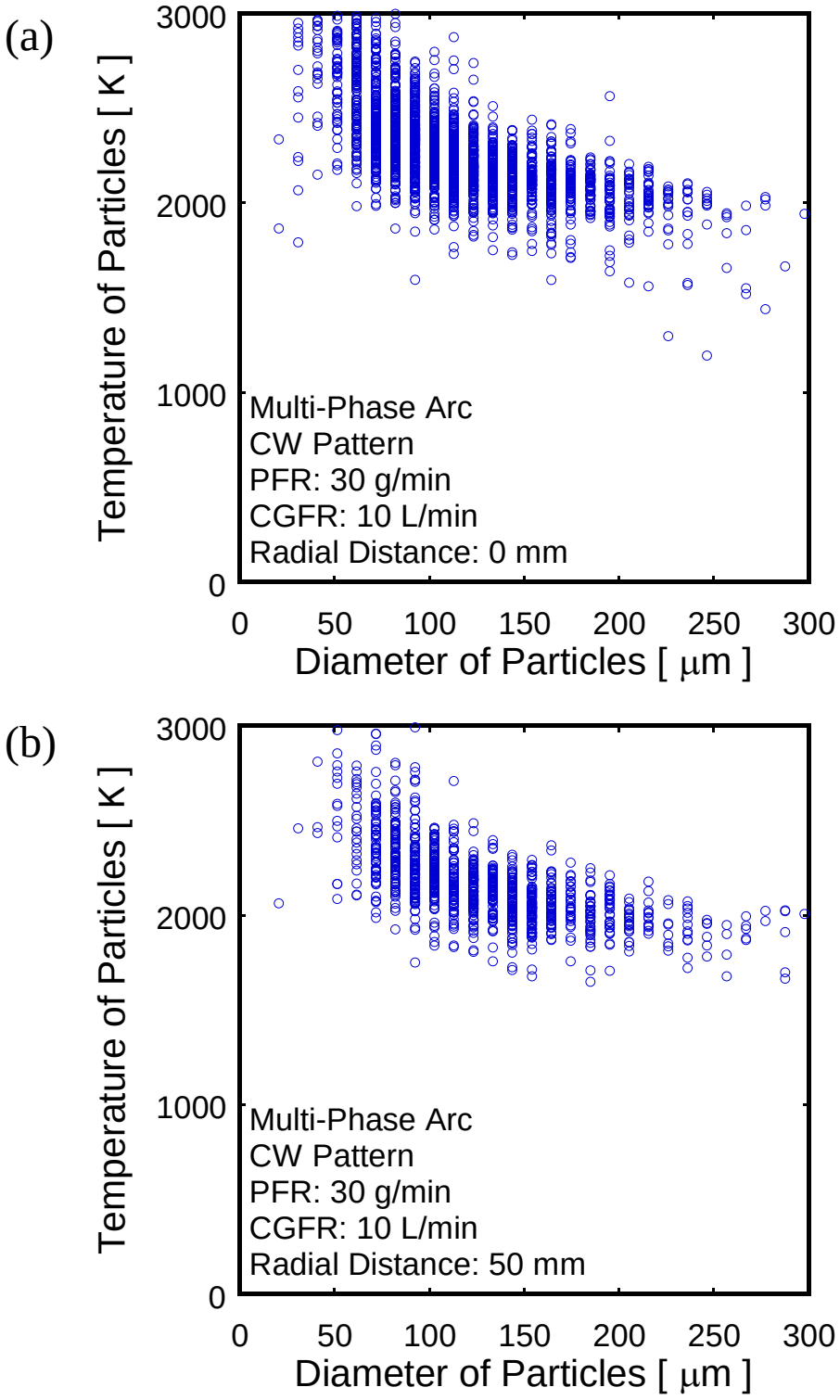

Fig. 3.24 Relationship of particle diameter and temperature estimated by DPV-2000 with carrier gas flow rate of 10 L/min in CW pattern at different radial positions: (a) 0 mm and (b) 50 mm

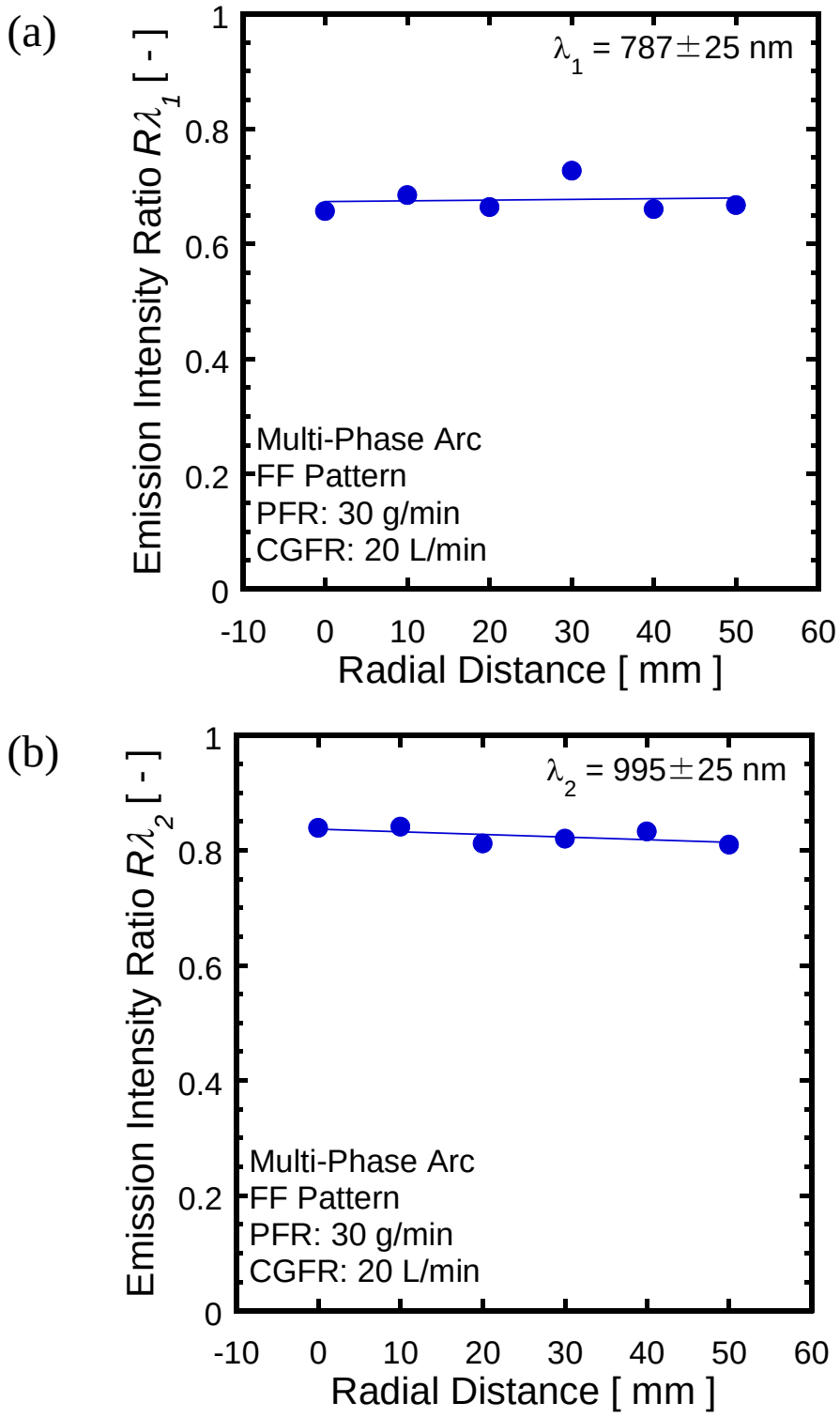

Fig. 3.25 Emission intensity ratio $R_{\lambda 1}$ and $R_{\lambda 2}$ at different radial distances in FF pattern

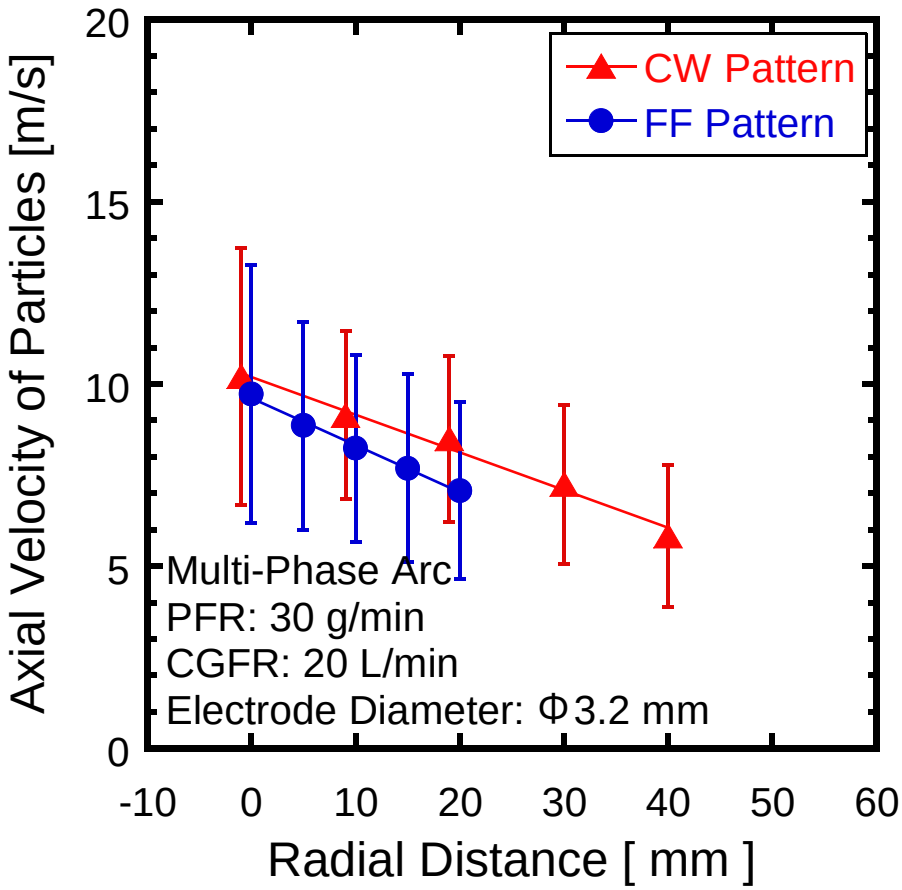

Fig. 3.26 Effect of electrode configuration on the axial velocity of in-flight particles at different radial distances

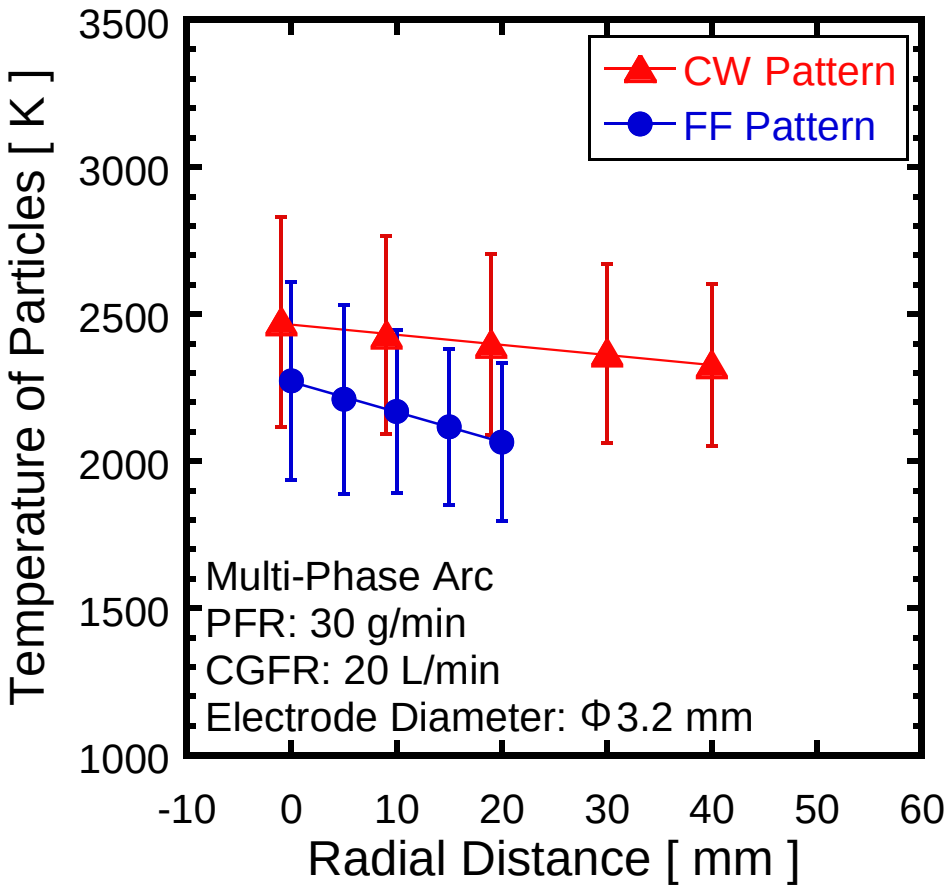

Fig. 3.27 Effect of electrode configuration on the temperature of in-flight particles at different radial distances

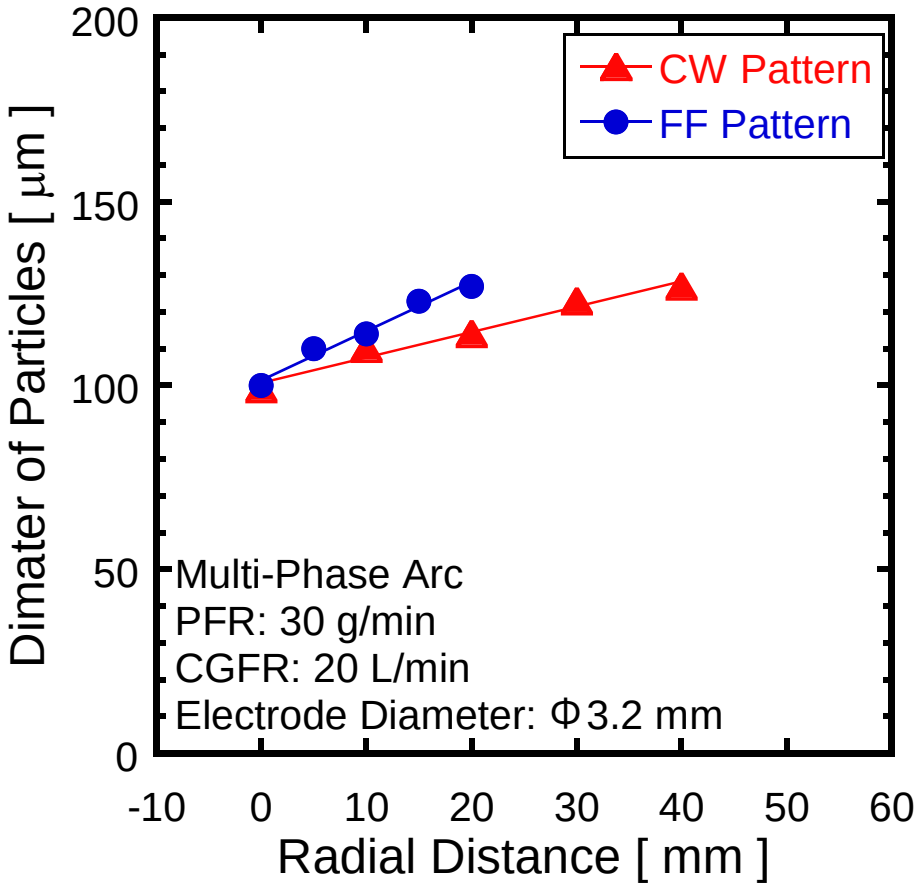

Fig. 3.28 Effect of electrode configuration on the diameter of in-flight particles at different radial distances

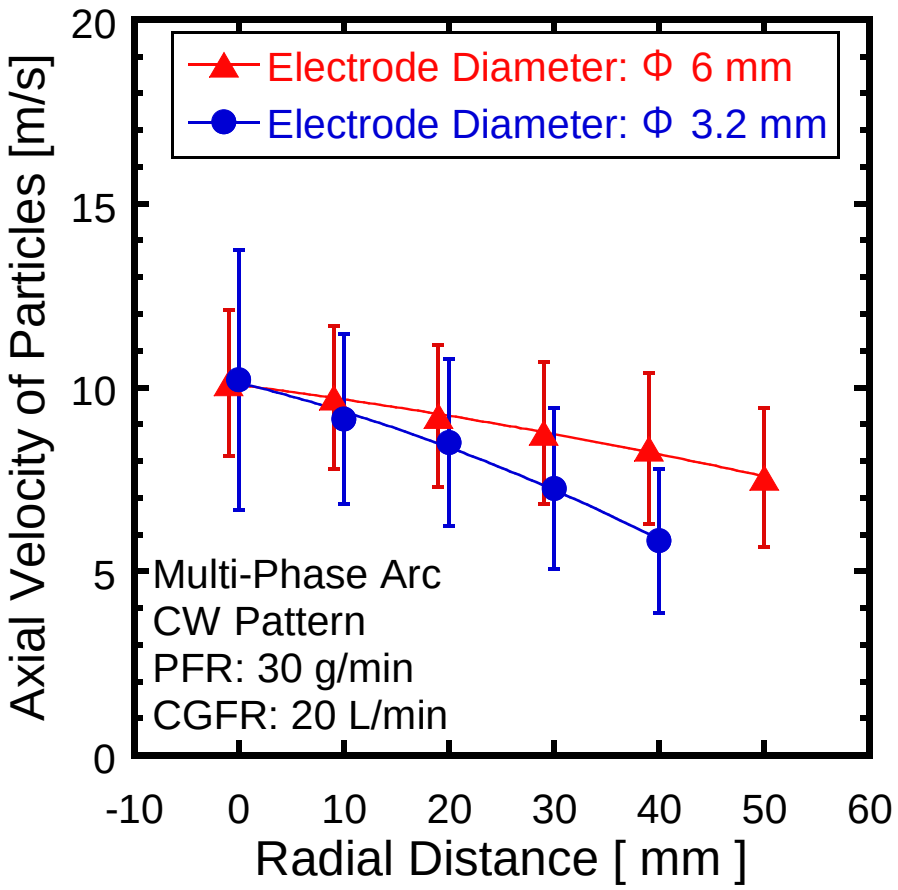

Fig. 3.29 Effect of electrode diameter on the axial velocity of in-flight particles at different radial distances in FF pattern

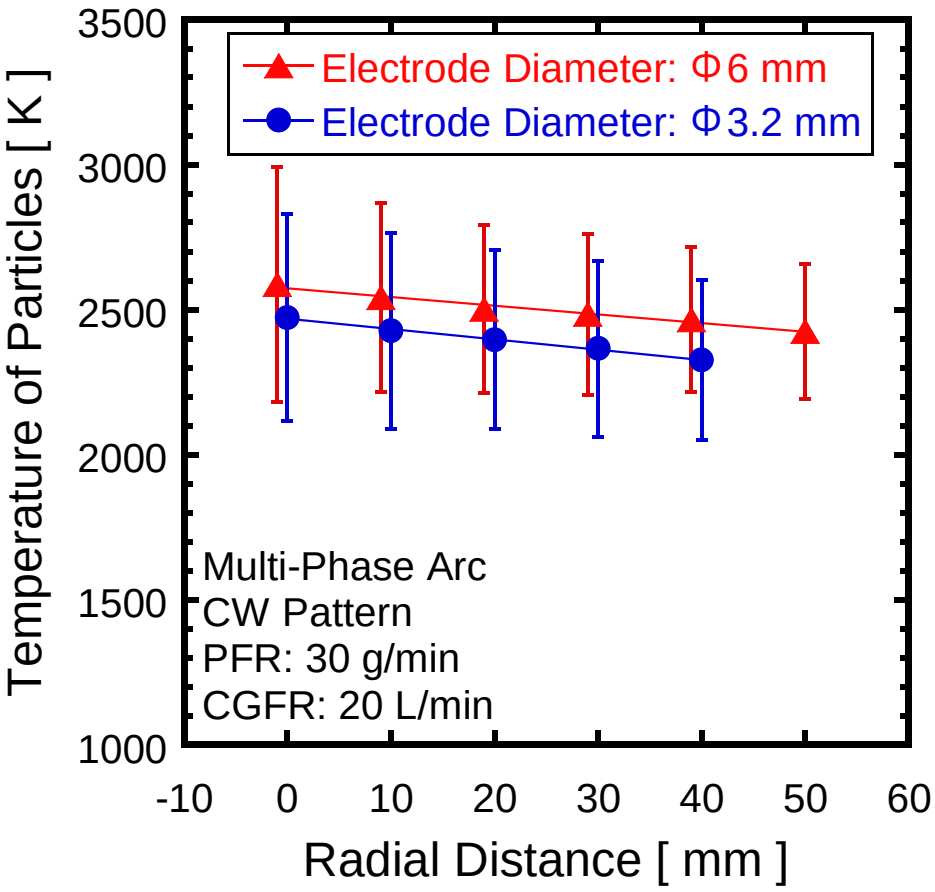

Fig. 3.30 Effect of electrode diameter on the temperature of in-flight particles at different radial distances in FF pattern

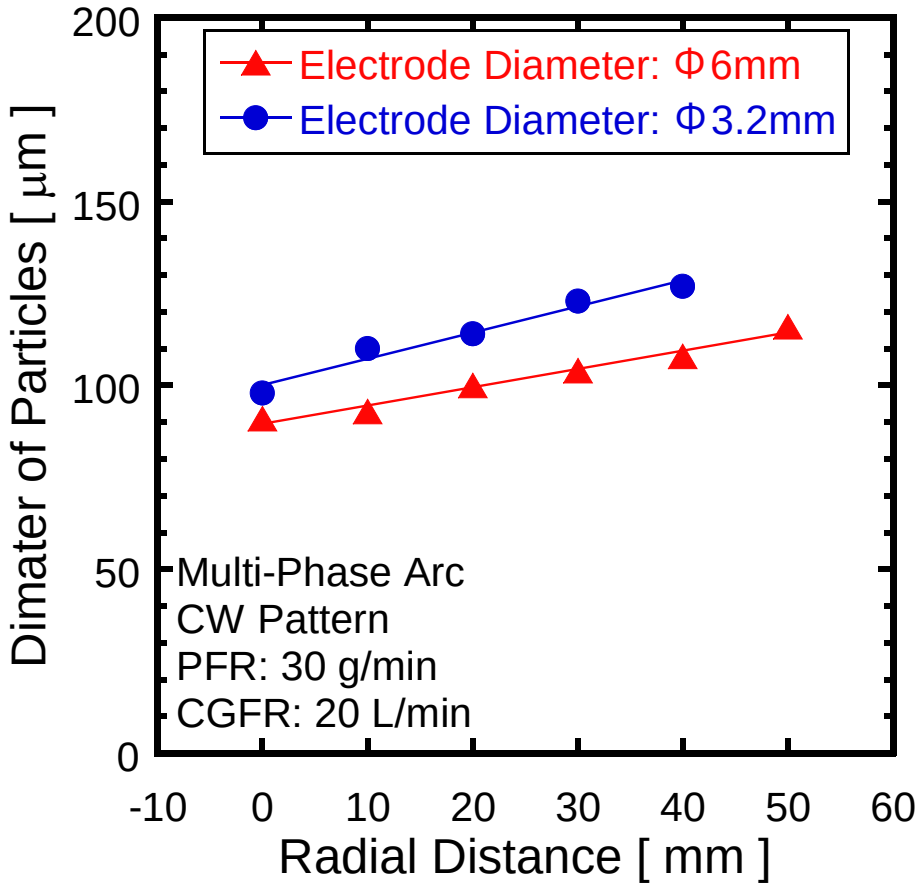

Fig. 3.31 Effect of electrode diameter on the diameter of in-flight particles at different radial distances in FF pattern

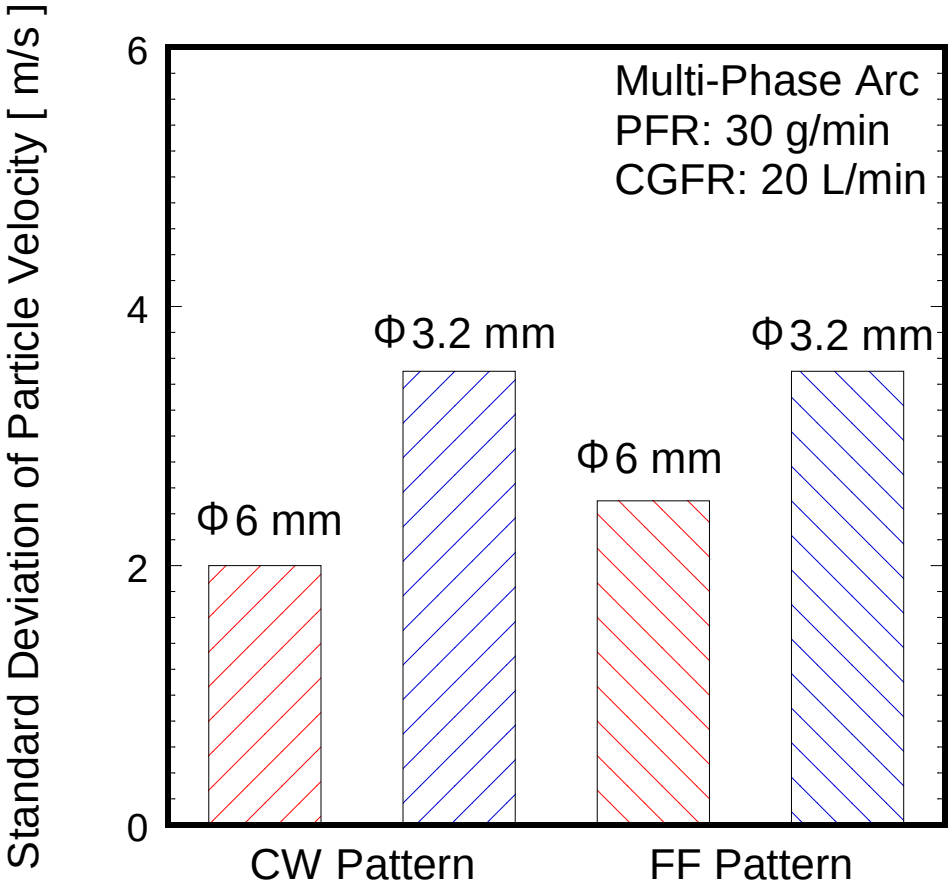

Fig. 3.32 Comparison of standard deviation of particle velocities in different patterns and electrode diameters

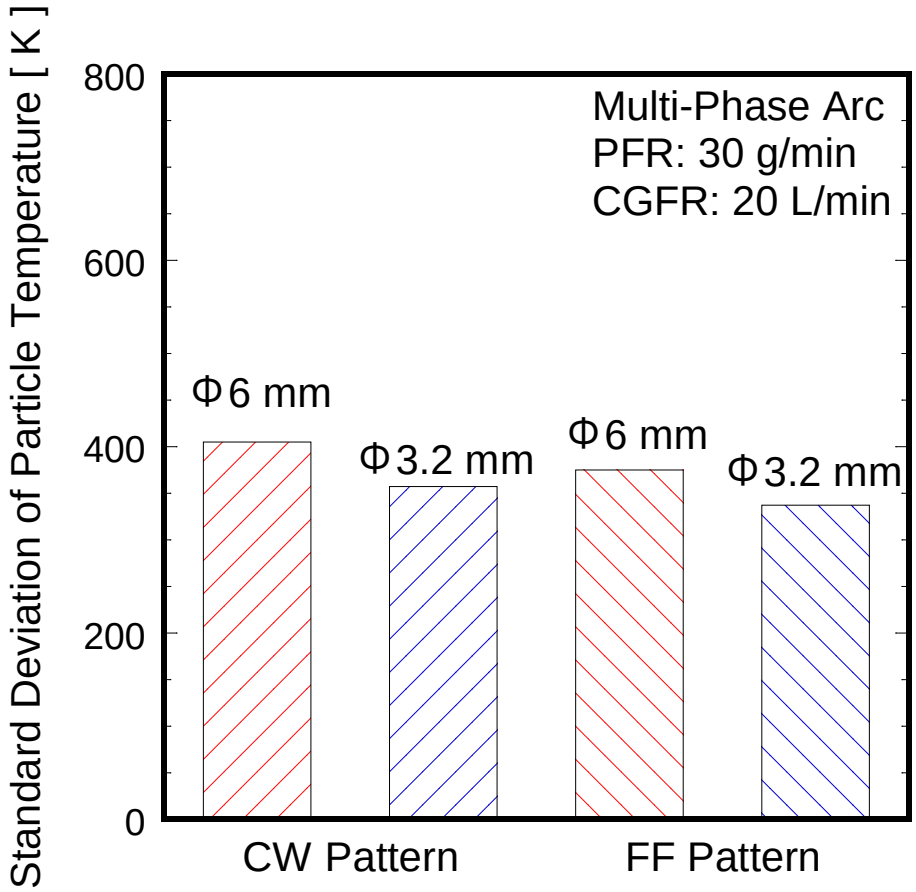

Fig. 3.33 Comparison of standard deviation of particle temperatures in different patterns and electrode diameters

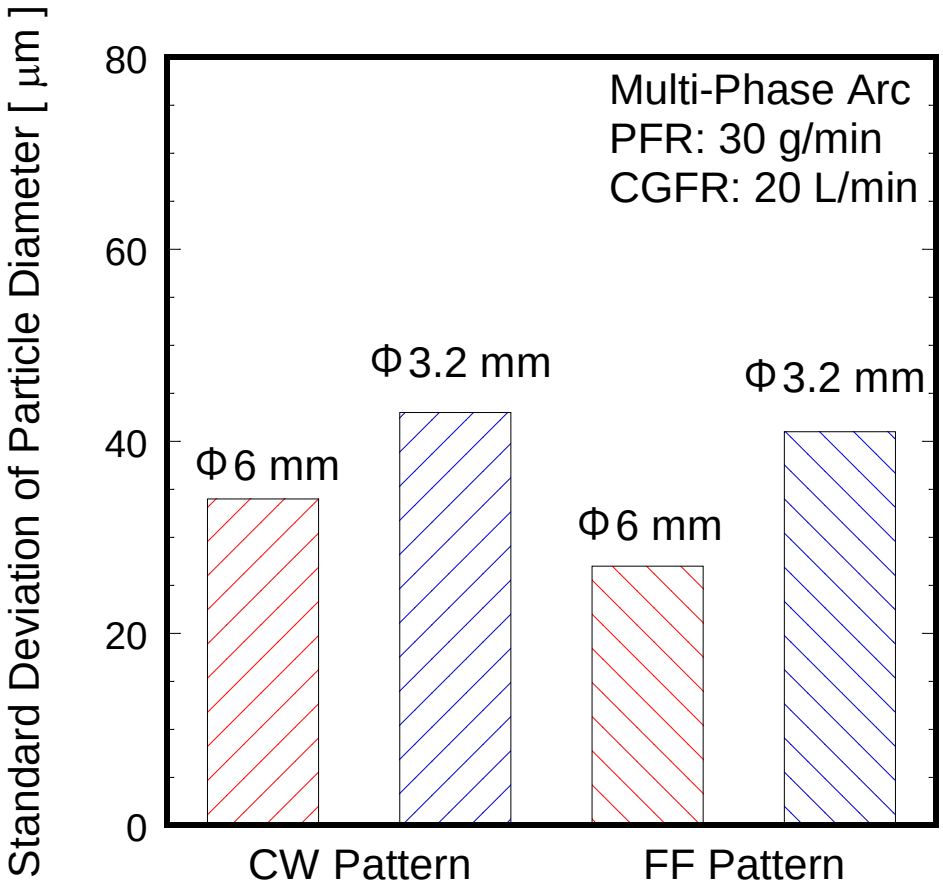

Fig. 3.34 Comparison of standard deviation of particle diameters in different patterns and electrode diameters

4. Investigation of Temporal Characteristics of the In-Flight Particles

The plasma fluctuation in the multi-phase AC arc has been reported in Chapter 2. However, up to date, very few studies have been undertaken to analyze the influence of multi-phase AC arc fluctuations on the particle characterization. This is mainly due to the complex interaction between the plasma and the injected particles. The particle diagnostic method by DPV-2000 can only measure single particle at a time. In this chapter, the fluctuation of particle temperature within millisecond in plasma region was studied by a high speed camera equipped with a band-pass filter system. The influence of the plasma fluctuation on the in-flight particle temperature was evaluated. Moreover, the effects of the electrode configuration, the carrier gas flow rate on the particle temperature fluctuation and the FFT characteristic were discussed.

4.1 Introduction

Ii is well known that a plasma jet ejecting from a direct current (DC) plasma torch displays strong fluctuations arising from the movement of the arc root on the anode wall. This gives rise to periodic plasma power oscillations, which may affect the in-flight particle state. Dussoubs et al. (1999) has shown that the spray jet trajectory varied with time delay by laser strobe technique, hence the particle trajectory can be affected by jet flow fluctuation. However, transient characteristics of individual in-flight particle were not measured. Park et al. (1999)

simulated the trajectories and temperature histories of yttrium stabilized zirconia (YSZ) particles in a N_2/H_2 plasma jet. Their results showed that the radial fluctuation affects the plasma conditions and particle behavior significantly, while the axial fluctuation leads to results closely resembling those of steady-state plasma jets. Bisson et al. (2003) analyzed the time-dependent alumina particle temperature and velocity variations by a modified DPV-2000 and spraying with Sulzer Metco F4 plasma gun. Fluctuations as large as 600 °C in temperature and 200 m/s in velocity were observed mainly due to the arc fluctuation. Correspondingly, their recorded fluctuations had the same frequency of 4500 Hz as that of the arc root. In addition, Goutier et al. (2008) found good correlation between the arc voltage and the particle temperature fluctuation when the plasma is operated with PTF4 and 3MB commercial plasma torches running on Ar-H_2 mixtures. While no relationship between arc and particle temperature was observed when using 3MB torch with N_2-H_2 mixture.

Different to DC arc plasmas, the periodic swinging motion of single electrode would be attributed to the rotational electromagnetic field in multi-phase AC arc plasma (Tanaka et al. 2011). The phase shifting period of multi-phase AC arc is 20 ms due to the frequency of power supply of 50 Hz, therefore the same arc discharge path is expected to repeat at the time interval of 20 ms. However, the periodicity of arc discharge phenomenon is still poorly understood. For particle treatment, the temporal fluctuation of plasma fluctuation caused by the transient discharge pattern from 12 electrodes may be a more important and interesting to be investigated. Obviously, this phenomenon is more complicated than the case of one electrode. As the particle dwell time in the plasma is considered as about 10~20 ms which is comparable to the period of a cycle, this may cause a variation in particle melting behavior.

Two-color pyrometry offers considerable advantages for measuring particle temperatures in flight. In our previous work, in-flight particle measurements on the surface temperature and

velocity were successfully performed by DPV-2000 system (Liu et al. 2011). Another implementation of two-color pyrometry for individual particle measurement involves the use of an electronically shuttered charge-coupled device (CCD) camera to image bright particles streaks over a large volume of the spray plume (Craig et al. 1999, 2000; Mates et al. 2002). Compared with DPV-2000, the use of high-speed camera provides many advantages including the selectivity of band-pass filters and temporal information of particles in millisecond. Furthermore, large amount of non-thermal emissions can be cut off to improve the accuracy of temperature measurement when narrow-band interference filters are used. Together with these results, time resolved observation of plasma discharge provides understanding of the plasma-particle energy exchange.

4.2 Experimental

4.2.1 Experimental Setup

In-flight particle diagnostics were undertaken by the same high-speed camera equipped with an interference filter system as shown in Fig. 4.1. In-flight particle diagnostics was performed at an axial distance of 80 mm down from the lower electrode level and the optical system was focused on the center of plasma plume. Voltage measurement was synchronized with the high-speed video observation. The powder was introduced into the plasma region with the help of air gas. The powder feeding used the same method as explained in Chapter 3.

4.2.2 Raw Materials

The composition of the alkali-free glass raw material is shown in Table 4.1 with $50.6SiO_2$-$9.1Al_2O_3$-$14.5B_2O_3$-$25.1BaO$-Fe_2O_3 in wt%. The particle size distribution of raw material is given in Fig. 4.2 with the average size of 126 μm.

4.2.3 Experimental Conditions

The process parameters of electrode configuration and carrier gas flow rate were investigated in multi-phase AC arc system. Experimental conditions for effect of electrode configuration on particle measurement are shown in Table 4.2. Electrode configuration of CW and FF patterns are used for comparison of the in-flight particle temperature fluctuation. In order to get individual information of particles, the data processing technique requires particle signals to be well separated from the others. For this reason, a low feed rate of powder, 30 g/min, was used to give an appropriate particle density without severe loading effect. The carrier gas flow rate was 20 L/min. The temporal characteristics of the in-flight particles are conducted by a high-speed camera (Photron, FASTCAM SA WTI, Japan) recorded at a speed of 10000 frames/s with a shutter speed of 100 μs. The choice of spectral bandwidths used to measure the two-color particle intensity signal should avoid the direct and scattered plasma light. As the glass particles are low emissivity ceramics, only a limited amount of radiation is available to measure. Figure 4.3 shows the line emission spectra of the plasma gas species and vaporized particle material (Barium) considered here. For a good sensitivity and to minimize the plasma radiation signal, the camera used a short wavelength band covering 785±2.5 and 880±5 nm. The oscilloscope (Yokogawa, ScopeCorder DL850, Japan) recorded at a sampling rate of 10^6 Hz. The air carrier gas flow rate varies at 10, 20 and 30 L/min and the effect on the particle temperature fluctuation was investigated. Tables 4.3 and 4.4 give the experimental conditions for effect of carrier gas flow rate on the particle measurement by high-speed camera in CW and FF pattern, respectively.

4.2.4 Experimental Procedures

The experiments of in-flight particle measurement by high-speed camera were

conducted in the following manner. Some of the parts have already been explained in Sections 2.2.4 and 3.2.4.

- Preparation of electrodes
- Preparation of particle diagnostic system

1) Locate the high-speed camera and set the band-pass filters.
2) Run the software of high-speed camera and focus the camera to view the center of the axis.

- Preparation of arc ignition
- Arc generation
- Powder injection
- Particle measurement by high-speed camera

1) Remove the shading glass on the peephole to take movie.
2) Adjust the camera such as zoom, lens aperture and focus to clearly observe the discharge behavior.
3) Set the frame rate and shutter speed of the camera and record the particle melting behavior.
4) Save statistics and change discharge conditions then repeat 3).

- Stop the powder feeding
- Stop the arc discharge

4.2.5 Particle Measurement by High Speed Camera

The optical system observes the plasma plume and splits the single object into two identical images simultaneously, as shown in Fig. 4.4, which is then filtered in separate spectral regions. Histograms of particle properties can be displayed in real time (>10^4 Hz). This two-color pyrometry method combined with the high-speed camera allows evaluating the fluctuation of the average particle temperature within millisecond in different electrode

configurations. Figure 4.5 gives a sample (dual) image of glass particles streaks. The camera focused on the centerline at the same height with DPV-2000 but the field of view was much wider. Although narrow band-pass filters were used, the fluctuation of the plasma flame can be seen periodically. If the carrier gas flow rate is higher than 30 L/min, the particles fly quickly through the measurement volume and it is impossible to separate the particles one by one. The sensor described here uses a commercially available 12-bit 1024×480 pixel CCD camera.

In a single measurement, up to 7531 images of particle streaks can be acquired at a rate of 10000 frames/s with the shutter speed of 100 μs. Images are stored in PC memory for subsequent processing. The high speed image process for calculating the particle surface temperature was conducted in the following procedures.

1) The captured dual images (from two band-pass filters) were selected separately at pixel of 252×100 in the same region and saved to individual images as JPEG files in an interval time of 0.1 ms. The pixels corresponding to the real size of 8.5×3.5 mm^2.
2) Convert each JPEG file to text document.
3) Import both of the JPEG and text files to the image analysis software of in-flight particles.
4) Analysis software scans the dual images of text files to identify individual particle and computes its velocity and temperature based on the Planck's law as already shown in Eq. 3.2. The thermal radiations emitted by a particle at λ_1 and λ_2, which represents the integrating pixel intensities in the video images. The sensor's spectral sensitivity was calibrated by a tungsten halogen lamp.
5) Each image corresponding to 0.1 ms in duration was analyzed to obtain the average temperature of all detected particles in the frame.
6) Since the phase shifting period of multi-phase AC arc is evaluated as 20 ms, the total calculated time for particle temperatures was over 10 periodic cycles of 200 ms.

4.3 Results and Discussion of Time-Dependent Particle Measurements

4.3.1 Effect of Electrode Configuration on the Particle Temperature

Figures 4.6 (a) and (b) give the particle temperature distribution estimated by the high-speed camera with CW and FF pattern, respectively. The powder feed rate was fixed at 30 g/min with carrier gas flow rate of 20 L/min. Both data were calculated from around 2 million particles. The shape of the temperature distribution is approximately Gaussian. The particle temperature obtained in the CW pattern is higher and distributed wider than that of FF pattern.

Figure 4.7 presents the average particle temperature in each calculated image as a function of time with different electrode configurations. The total average particle temperature in CW and FF pattern is 2470 K and 2270 K, respectively. As been reported in the Section 2.3.1, since the arc across the center area of plasma plume at diverse times in CW pattern, direct high-energy transfer from the arc to particles occurs frequently. This can explain why the average temperature measured at the center plume in CW pattern is higher. In addition, the dispersion of particle temperatures for FF pattern is 90 K, which is smaller than CW pattern of 150 K. This means more homogeneous particle treatment is expected in FF pattern rather in CW pattern due to the more uniform plasma temperature field. The difference in particle temperature fluctuation can also be explained by the Section 2.4.1. Compared with Fig. 2.28 which presents the arc luminance area fluctuation of CW and FF patterns, the particle temperature fluctuation intensity shows a common trend with the arc fluctuations. This means more homogeneous particle treatment is expected in FF pattern rather in CW pattern due to the more uniform plasma temperature field.

4.3.2 Effect of Carrier Gas Flow Rate on the Particle Temperature

The purpose of investigation of the particle temperature fluctuation is to verify the relationship with the plasma fluctuation. The frequency of the Fast Fourier Transform (FFT) analyses was conducted to find out the periodicity of particle temperature fluctuation and its relationship between the multi-phase AC arc fluctuations. As the particles were measured at the central axis, the analyzed diameter of arc luminance area was adapted to the particle diagnostic area. The frequency spectra of arc luminance area at analyzed diameter of 30 mm in CW and FF patterns are shown in Fig. 4.8. From the previous discussion in Section 2.4.2, CW pattern has a relatively strong fluctuation of luminance area near the central axis of the chamber, while FF pattern shows the strong fluctuation away from the axis. A significant peak of 100 Hz is observed in CW pattern which is expected to have an influence on the particle temperature.

Figure 4.9 shows the fluctuation of the calculated average temperature of particles in CW pattern with varies carrier gas flow rates. The total average temperature is decreased with increasing the carrier gas flow rate due to the decrease in residence time in plasma. The evaluated average particle temperature is 2500, 2470 and 2373 K in the carrier gas flow rate of 10, 20 and 30 L/min, respectively. Moreover, the fluctuation amplitude of the temperature becomes larger in the higher gas flow rate. The relative spread with respect to mean temperature is 5%, 6% and 9%, respectively.

Figure 4.10 shows the FFT spectra of particle temperature in CW pattern under different carrier gas flow rates of 10, 20 and 30 L/min, corresponding to the Fig. 4.9. A higher flow rate of carrier gas provides greater axial momentum to in-flight particles, resulting larger dispersion of particle flow in the axial direction. CW pattern presents a relatively strong arc fluctuation near the central axis due to the instability of arc path. The peak around 100 Hz is clearly visible in the case of 30 L/min. This may be explained by the carrier gas at higher flow rate decrease the residence time of particle, thus the temperature reflect the same periodicity of arc fluctuation,

which is in accordance with Fig. 4.8 (a). As the in-flight time of particle in the plasma region is similar or even shorter than a discharge cycle, the surface temperature of glass particle with a diameter of about 126 μm varied instantly. Despite the rapid rise in particle surface temperature, the high internal thermal resistance (high Biot number) of glass particles prevent the interior of the particle from being heated at the same rate.

In the case of FF pattern, the particle temperature fluctuation with different carrier gas flow rates is shown in Fig. 4.11. The calculated average temperature is about 2250, 2270 and 2180 K in accordance to the carrier gas flow rate of 10, 20 and 30 L/min. The difference in the fluctuation amplitude is not significant despite of the change in carrier gas flow rate.

The particle temperature FFT peak evolution versus carrier gas flow rate is shown in Fig. 4.12. There is no significant periodic signal for particle temperature can be observed regardless of carrier gas flow rate. According to Fig. 4.8 (b), the main peak of arc luminance spectrum is shown at 300 Hz. As the particle residence time in the plasma is considered long compared with this fluctuation period, is does not affect the temperature fluctuation of particles which penetrate the center region in FF pattern. The effect of carrier gas flow on the in-flight particle behavior demonstrated well that the particle temperature fluctuation depends on the arc discharge behavior.

Based on the above studies, the particle temperature fluctuation was demonstrated to be affected by the periodical arc fluctuation. The most successful example is the particle temperature fluctuation exhibits the same frequency of 100 Hz at the higher carrier gas flow rate in CW pattern. It explained well that particle reflect the same fluctuation if the particle residence time in the plasma is shorter than the periodical arc fluctuation.

The standard deviations of arc and particle temperature fluctuation for both patterns with carrier gas flow rate at 20 L/min are given in Fig. 4.13. It clearly shows that the different arc

discharge behaviors in CW and FF patterns determine the temporal characteristics of high-temperature region. The amplitude of the variation in the in-flight particle temperature depends on the amplitude of the arc fluctuation. As a comparison to the standard deviation of particle temperature measured by DPV-2000 presented in Fig. 3.33, the standard deviation in the temperature obtained by high-speed camera shows no more than 10%, which is rather smaller than the results obtained from DPV-2000. However, both of the measurements indicated that FF pattern leads to a more uniform heating treatment of in-flight particles.

4.4 Conclusion

The time-resolved diagnostics on individual particles in multi-phase AC arc were described in this chapter. The particle temperature fluctuations under different electrode configurations and carrier gas flow rates were investigated by a high-speed camera with band-pass filters. In addition, the correlations between plasma fluctuations with particle temperature have been discussed. The following conclusions can be drawn.

1) The particle temperature fluctuation depended on the arc fluctuation strongly. Higher fluctuation of arc luminance area caused larger dispersion of particle surface temperature.
2) The effect of carrier gas flow rate on the periodicity of particle temperature fluctuation was related to the arc discharge pattern. The particle temperature reflected the same periodicity of arc fluctuation at high carrier gas flow in CW pattern, while there was no significant periodic signal in FF pattern.
3) The particle temperatures evaluated by the high-speed camera were in good agreement with the DPV-2000 measurement results presented in Chapter 3. However, the standard deviation in the temperature obtained by high-speed camera was no more than 10%, which was rather smaller than the results obtained from DPV-2000.

References

Bisson, J. F., B. Gauthier and C. Moreau. “Effect of Plasma Fluctuations on In-Flight Particle Parameters.” *Journal of Thermal Spray Technology* **12**(1), 38-43 (2003).

Craig, J. E., R. A. Parker, D. Y. Lee, F. S. Biancaniello and S. D. Ridder. “A Two-Wavelength Imaging Pyrometer for Measuring Particle Temperature, Velocity and Size in Thermal Spray Processes.” *Proc. of the International Symposium on Advanced Sensors for Metal Processing*, Quebec, CAN. 369-380 (1999).

Craig, J. E., R. A. Parker, D. Y. Lee, F. S. Biancaniello, S. D. Ridder and S. P. Mates. “Particle Temperature Measurements by Spectroscopic and Two-Wavelength Streak Imaging.” Thermal Spray: Surface Engineering via Applied Research: *Proc. of the 1st International Thermal Spray Conference* Quebec, CAN. 51-56 (2000).

Dussoubs, B., G. Mariaux, A. Vardelle, M. Vardelle and P. Fauchais. “D.C. Plasma Spraying, Effect of Arc Root Fluctuations on Particle Behavior in the Plasma Jet.” *High Temperature and Materials Processes* **3**(2-3), 235-250 (1999).

Goutier, S., E. Nogues-Delbos, M. Vardelle and P. Fauchais. “Particle Temperature Fluctuations in Plasma Spraying.” *Journal of Thermal Spray Technology* **17**(5-6), 895-901 (2008).

Liu, Y., M. Tanaka, S. Choi and T. Watanabe. “In-Flight Particle Measurement of Alkali-Free Glass Raw Materials in 12-Phase AC Arc Plasma.” *Journal of Thermal Spray Technology* **21**(5), 863-872 (2011).

Mates, S. P., D. Basak, F. S. Biancaniello, S. D. Ridder, J. Geist. “Calibration of a Two-Color Imaging Pyrometer and Its Use for Particle Measurements in Controlled Air Plasma Spray Experiments.” *Journal of Thermal Spray Technology* **11**(2), 195-205 (2002).

Park, J. H., J. Heberlein, E. Pfender, Y. C. Lau, J. Ruud and H. P. Wang. “Particle Behavior in Fluctuating Plasma Jet.” *Annals of the New York Academy of Sciences* **891**(1), 417-424 (1999).

Tanaka, M., Y. Tsuruoka, Y. Liu, T. Matsuura and T. Watanabe. “Investigation of Multiphase AC Arc Behavior by High-Speed Video Observation.” *IEEE Transactions on Plasma Science* **39**(11), 2904-2905 (2011).

Table 4.1 Batch formulation of alkali-free glass

Raw Material	SiO_2	Al_2O_3	B_2O_3	BaO	Fe_2O_3	SrO	Total
[wt%]	50.6	9.1	14.5	25.1	0.1	0.3	99.7

Table 4.2 Experimental conditions for effect of electrode configuration on particle measurement by high-speed camera in multi-phase AC arc

Discharge conditions		
Number of phase	12	12
Electrode configuration	Clockwise (CW) pattern	Flip-flop (FF) pattern
Power	40~60 kW	40~55 kW
Current	320 A	
Voltage	200 V	
Electrode distance	100 mm	
Ar flow rate (each electrode)	5 L/min	
Tungsten electrode diameter	φ6 mm	
Powder treatment conditions		
Powder	Alkali-free glass	
Primary SiO_2 size	7~8 μm	
Particle mean size	126 μm	
Powder feed rate	30 g/min	
Air carrier gas flow rate	20 L/min	
Diagnostic methods		
High-speed camera	FASTCAM SA WTI (Photron)	
Frame rate	10000 fps	
Shutter speed	100 μs	
Band-pass filters	785±2.5 nm (left), 880±5 nm (right)	
Oscilloscope	ScopeCorder DL850 (Yokogawa)	
Sampling rate	10^6 Hz	

Table 4.3 Experimental conditions for effect of carrier gas flow rate on particle measurement by high-speed camera in CW pattern

Discharge conditions	
Number of phase	12
Electrode configuration	Clockwise (CW) pattern
Power	40~60 kW
Current	320 A
Voltage	200 V
Electrode distance	100 mm
Ar flow rate (each electrode)	5 L/min
Tungsten electrode diameter	φ6 mm
Powder treatment conditions	
Powder	Alkali-free glass
Primary SiO_2 size	7~8 μm
Particle mean size	126 μm
Powder feed rate	30 g/min
Air carrier gas flow rate	10, 20, 30 L/min
Diagnostic methods	
High-speed camera	FASTCAM SA WTI (Photron)
Frame rate	10000 fps
Shutter speed	100 μs
Band-pass filters	785±2.5 nm (left), 880±5 nm (right)
Oscilloscope	ScopeCorder DL850 (Yokogawa)
Sampling rate	10^6 Hz

Table 4.4 Experimental conditions for effect of carrier gas flow rate on particle measurement by high-speed camera in FF pattern

Discharge conditions	
Number of phase	12
Electrode configuration	Flip-flop (FF) pattern
Power	40~55 kW
Current	320 A
Voltage	200 V
Electrode distance	100 mm
Ar flow rate (each electrode)	5 L/min
Tungsten electrode diameter	φ6 mm
Powder treatment conditions	
Powder	Alkali-free glass
Primary SiO_2 size	7~8 μm
Particle mean size	126 μm
Powder feed rate	30 g/min
Air carrier gas flow rate	10, 20, 30 L/min
Diagnostic methods	
High-speed camera	FASTCAM SA WTI (Photron)
Frame rate	10000 fps
Shutter speed	100 μs
Band-pass filters	785±2.5 nm (left), 880±5 nm (right)
Oscilloscope	ScopeCorder DL850 (Yokogawa)
Sampling rate	10^6 Hz

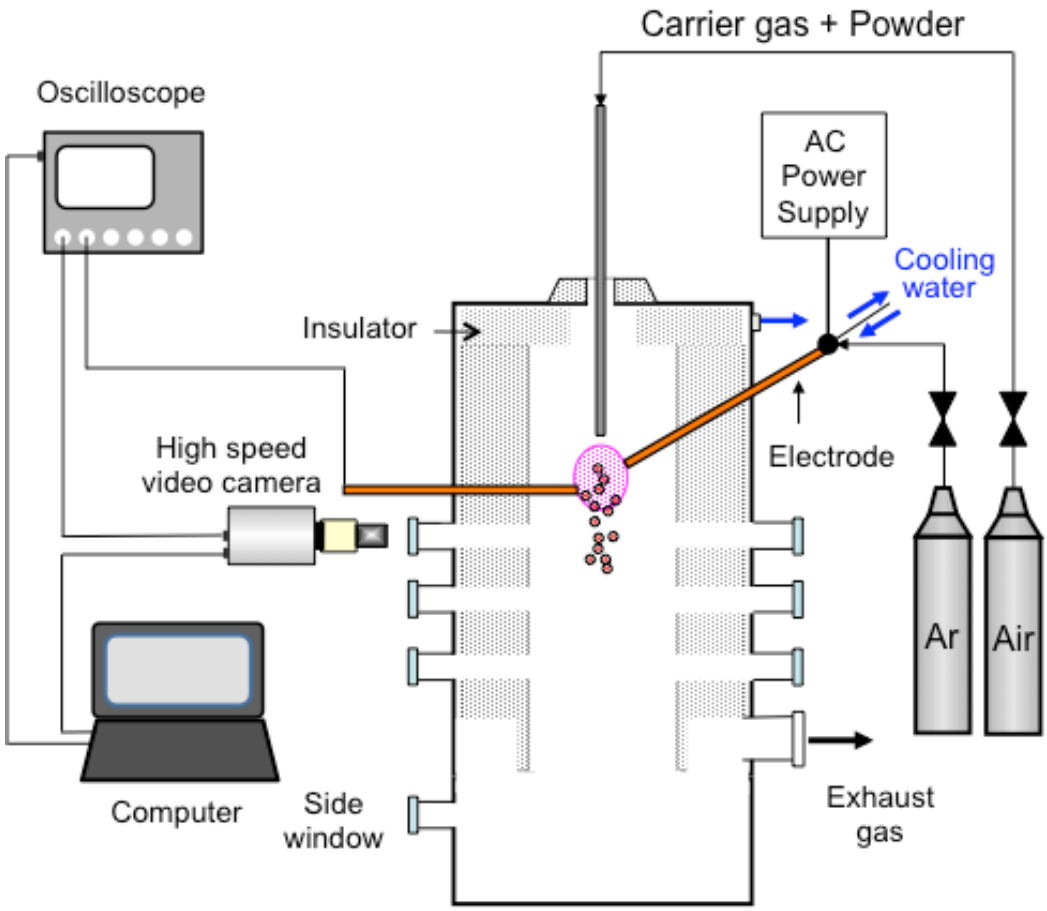

Fig. 4.1 The schematic of the particle measurement system with high-speed camera and band pass filter

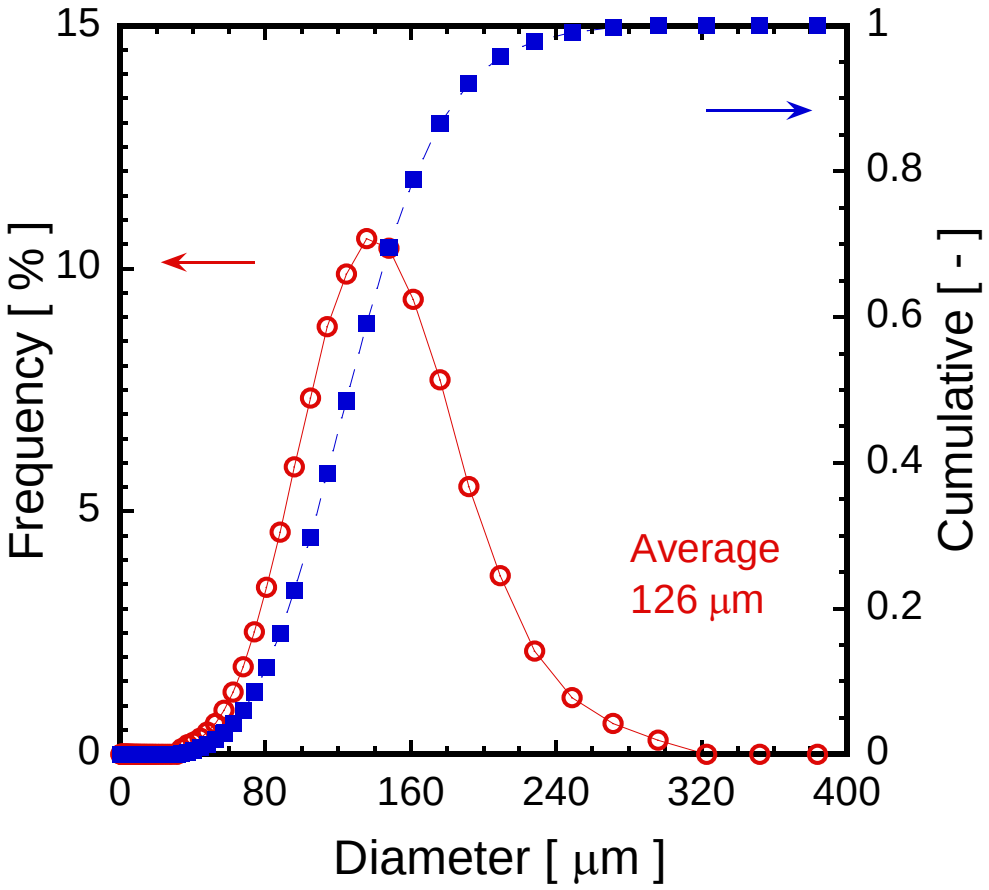

Fig. 4.2 Particle size distribution of raw material of alkali-free glass

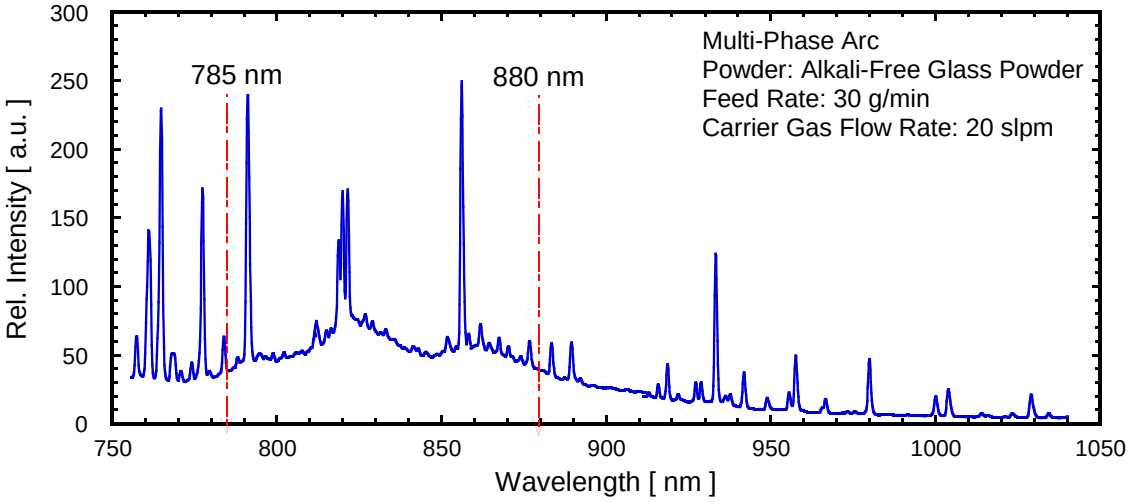

Fig. 4.3 Emission line spectrum of the 12-phase AC arc with powder injection

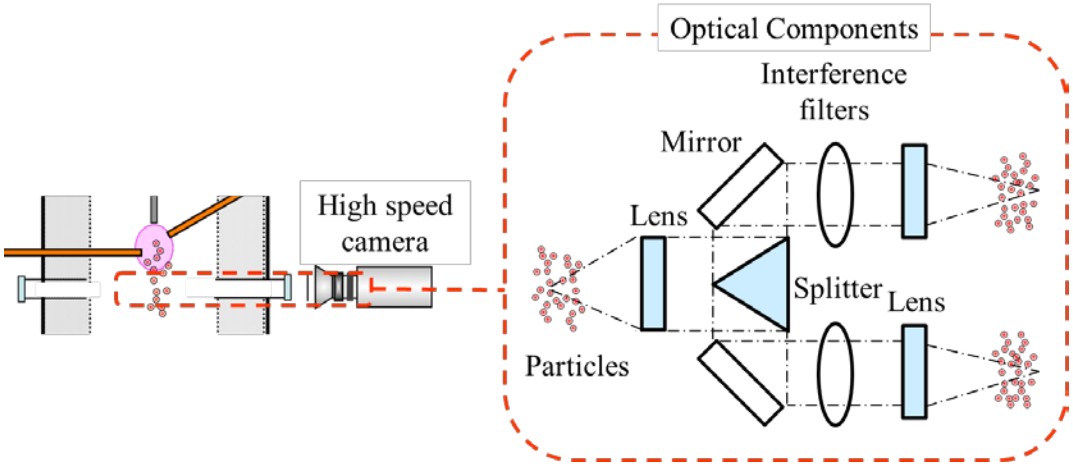

Fig. 4.4 The conceptual diagram of temperature measurement by high-speed camera

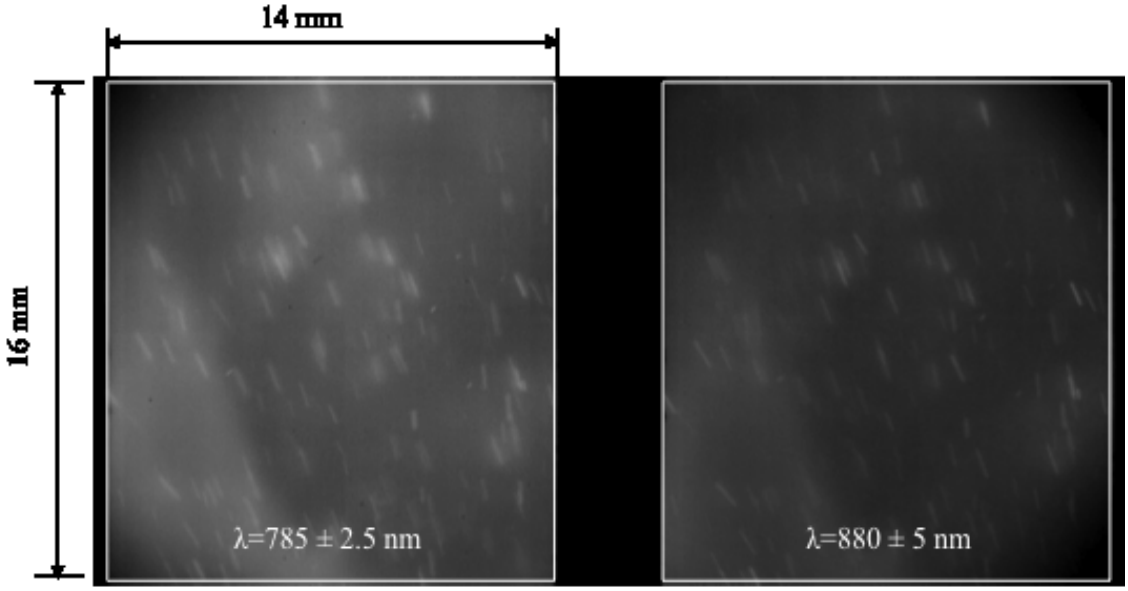

Fig. 4.5 The image of glass particle streaks obtained by two different band-pass filters, 785 ± 2.5 nm (Left) and 880 ± 5 nm (Right)

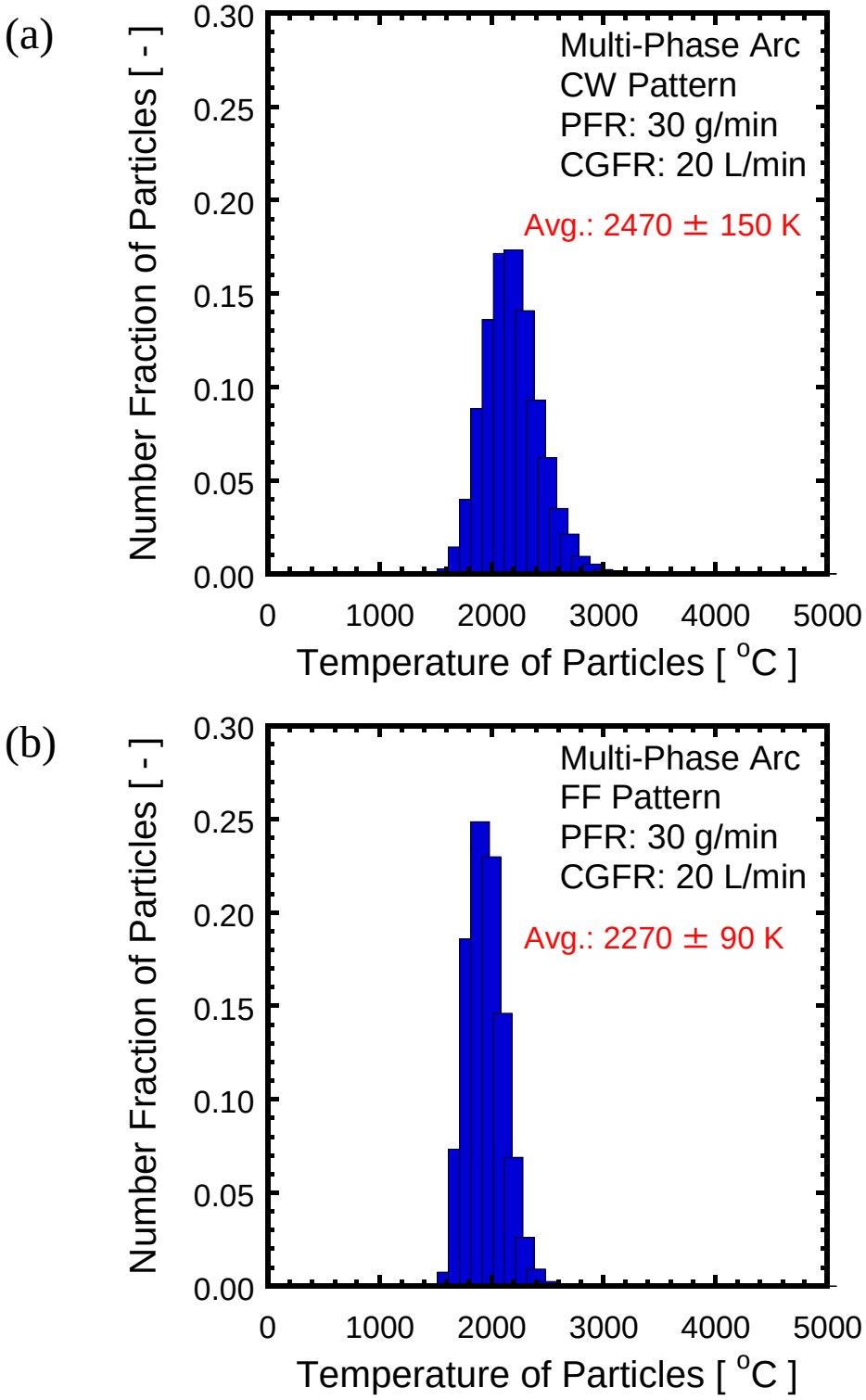

Fig. 4.6 Particle temperature distribution estimated by high-speed camera with different electrode configurations: (a) CW pattern and (b) FF pattern

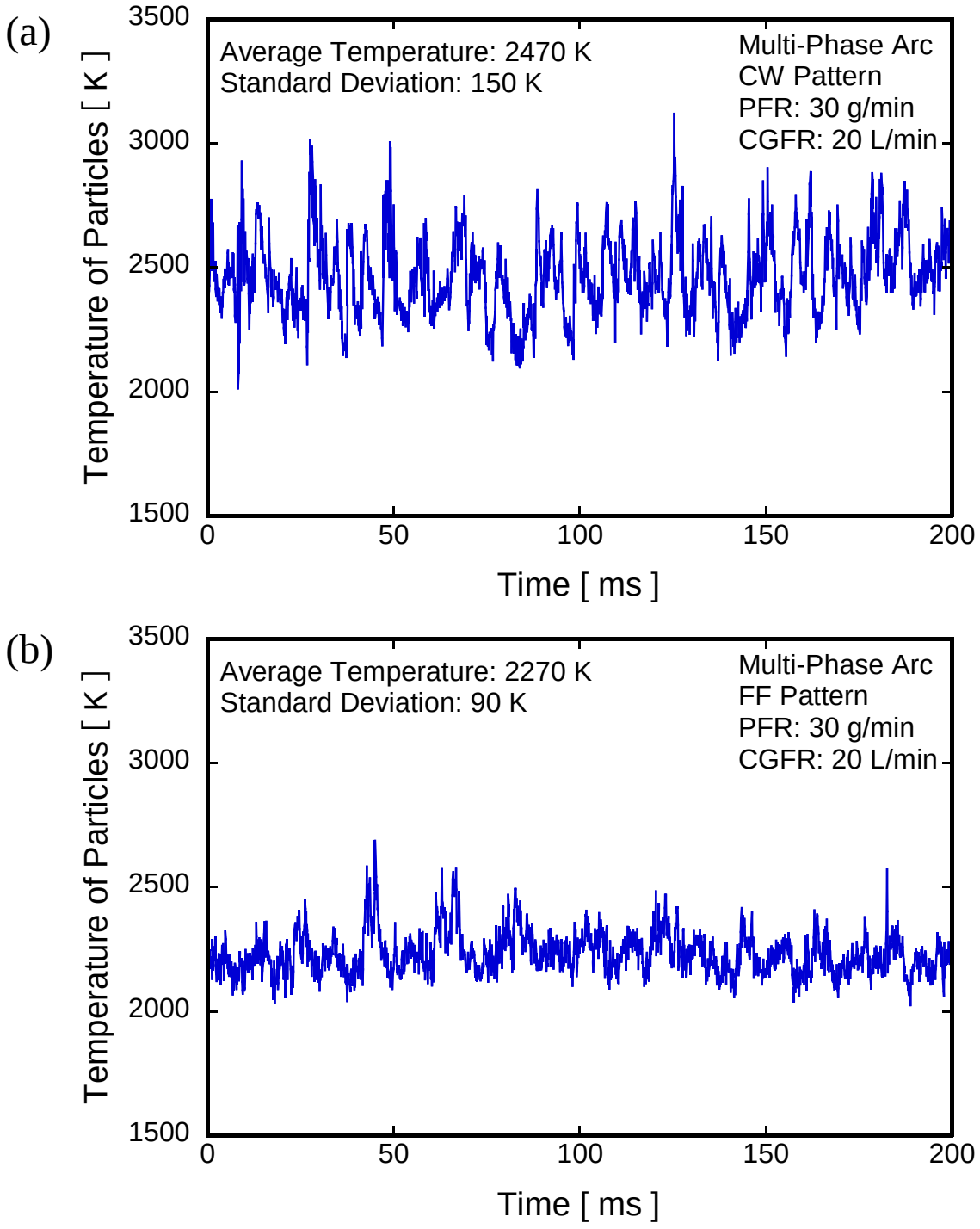

Fig. 4.7 Fluctuation of the average temperature of particles with different electrode configurations: (a) CW pattern and (b) FF pattern

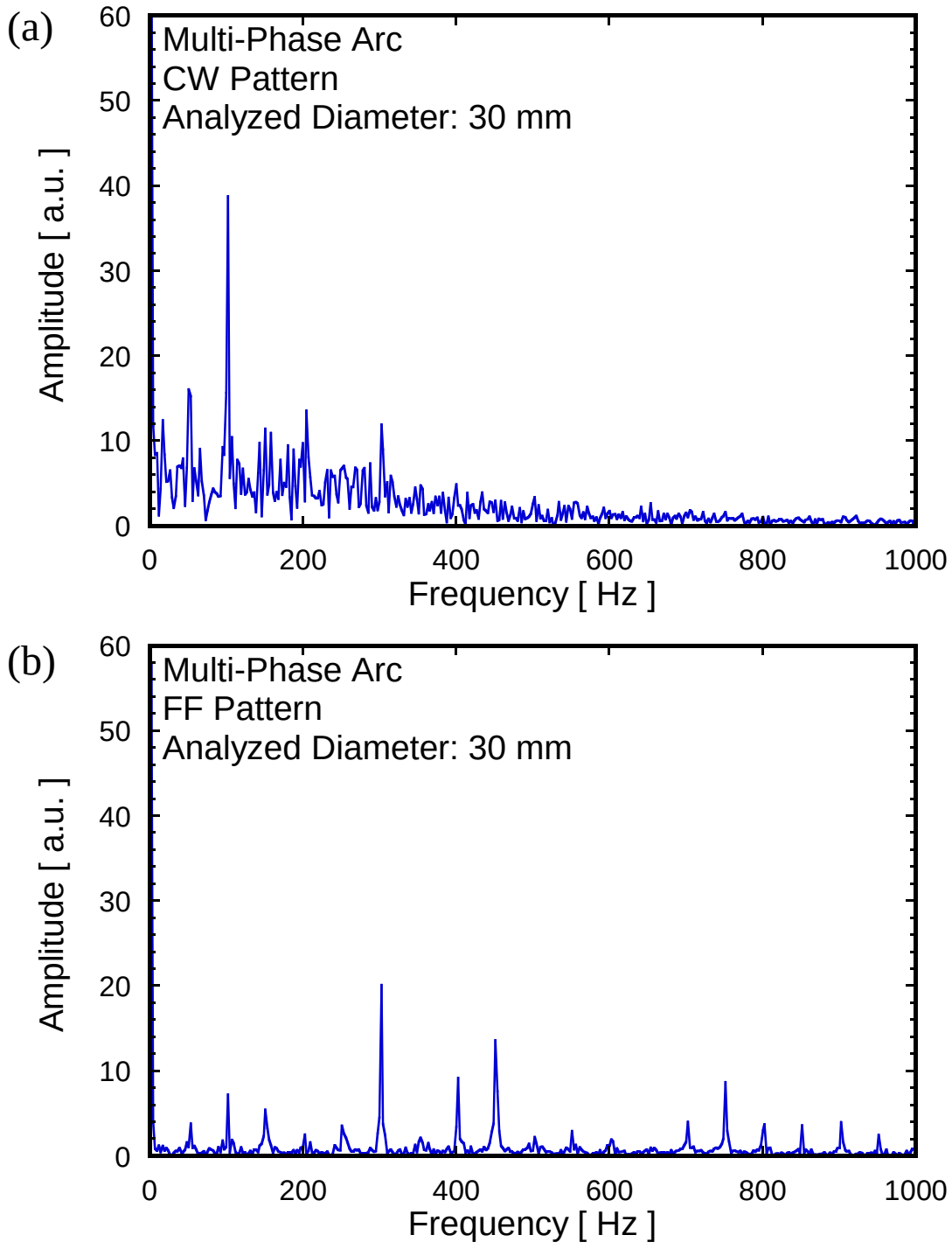

Fig. 4.8 Frequency spectra of arc luminance area at analyzed diameter of 30 mm in different electrode configurations: (a) CW pattern and (b) FF pattern

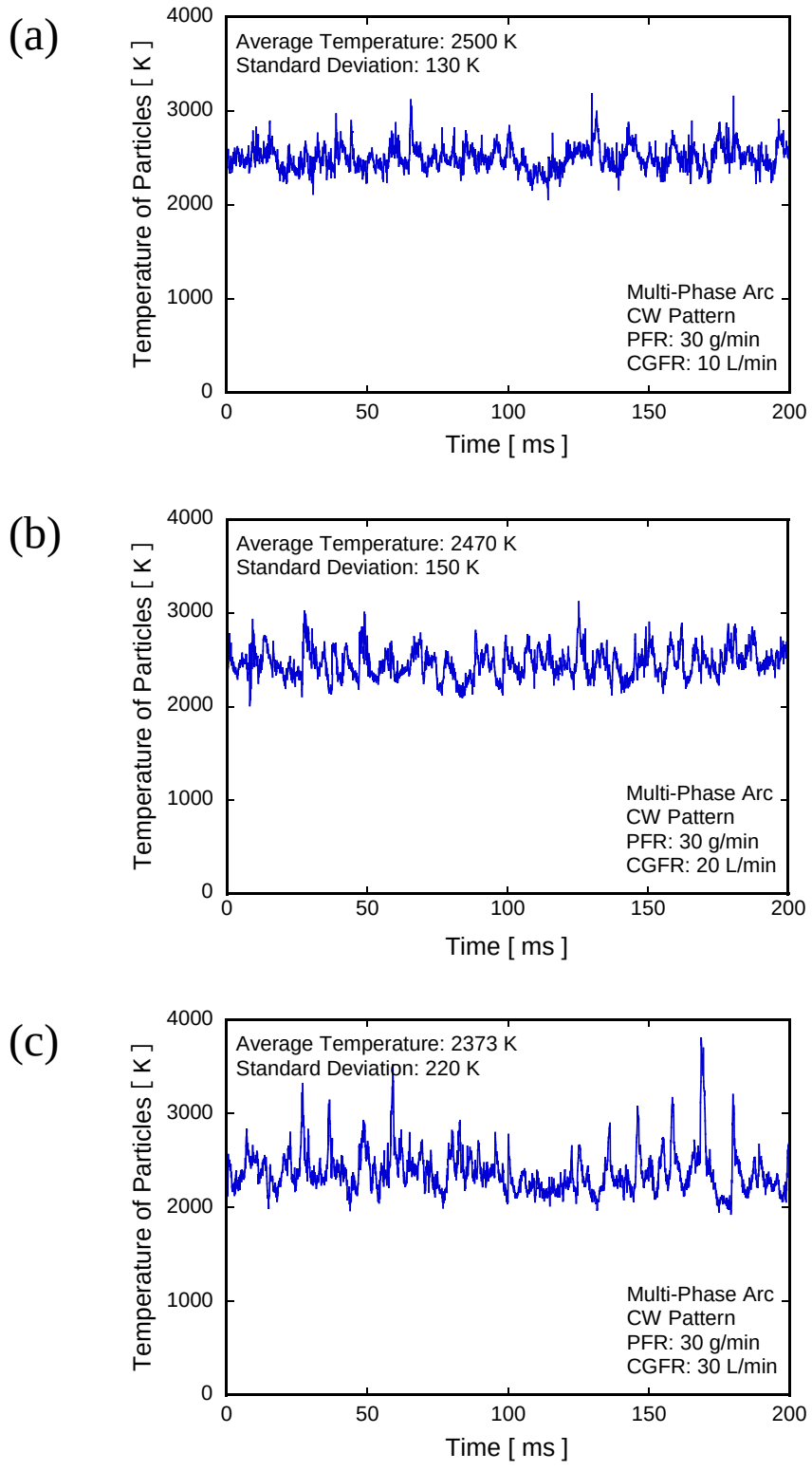

Fig. 4.9 Fluctuation of the average temperature of particles in CW pattern with different carrier gas flow rates: (a) 10 L/min (b) 20 L/min and (c) 30 L/min

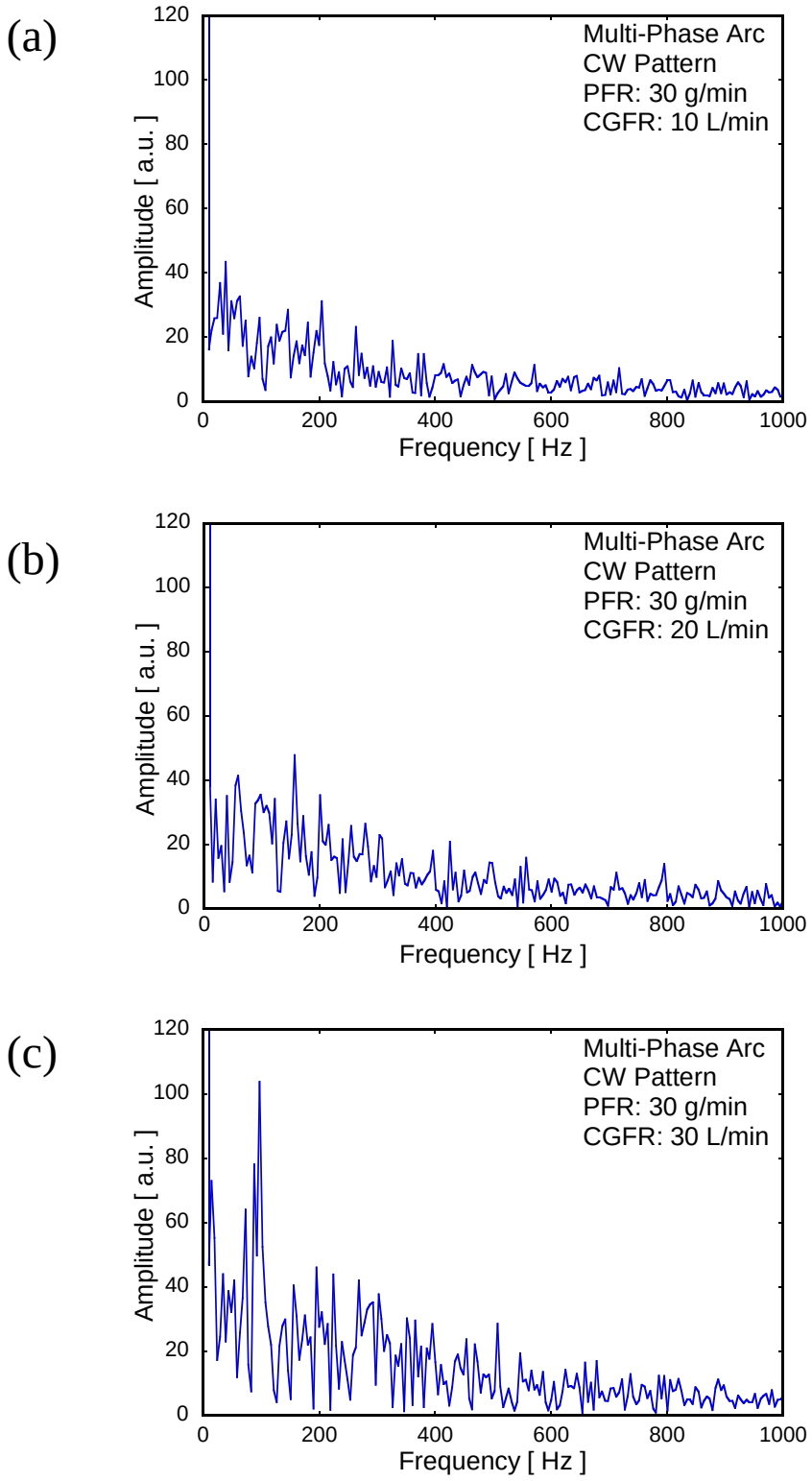

Fig. 4.10 Frequency spectra of fluctuation of particle temperature in CW pattern with different carrier gas flow rates: (a) 10 L/min (b) 20 L/min and (c) 30 L/min

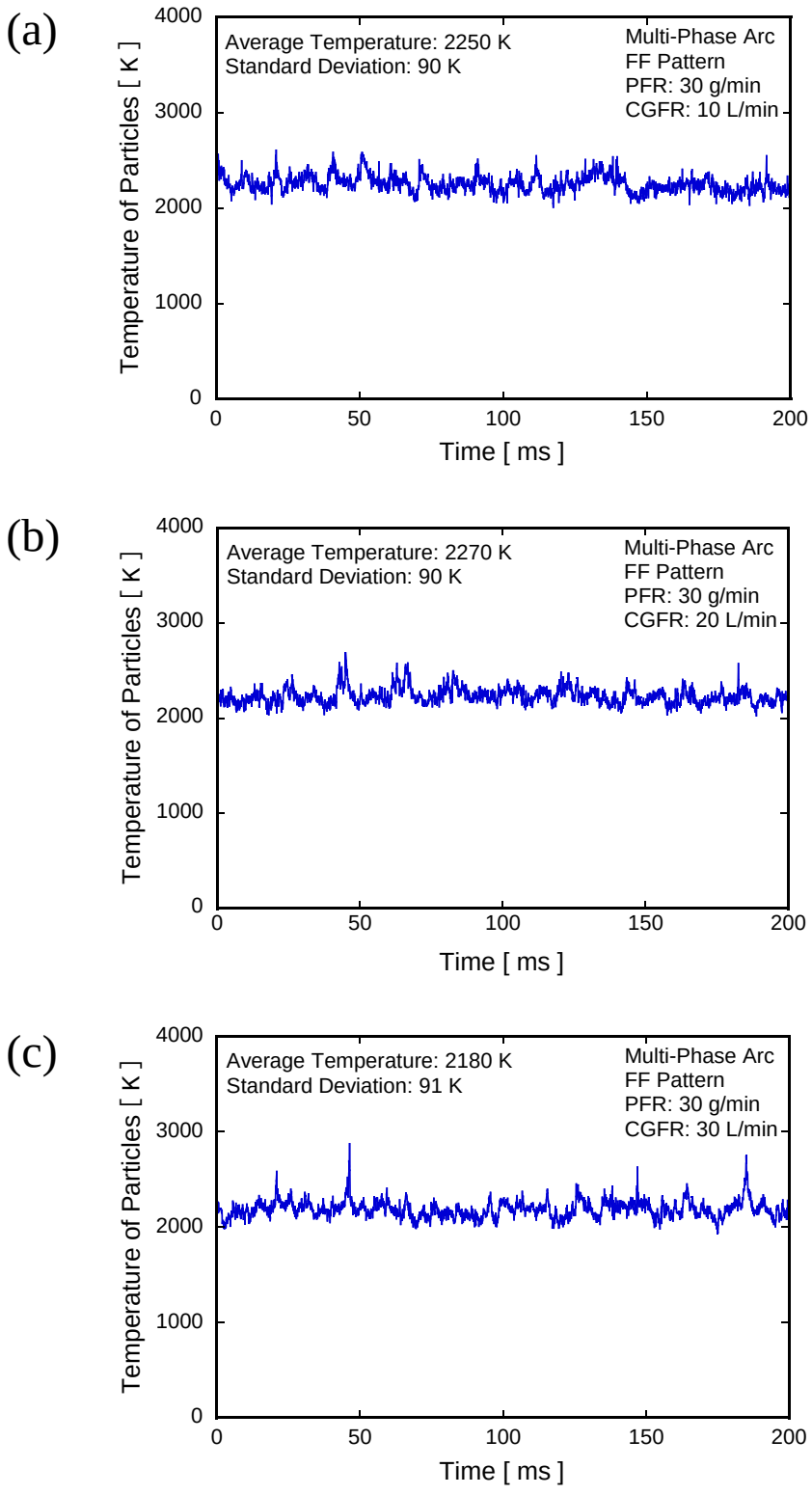

Fig. 4.11 Fluctuation of the average temperature of particles in FF pattern with different carrier gas flow rates: (a) 10 L/min (b) 20 L/min and (c) 30 L/min

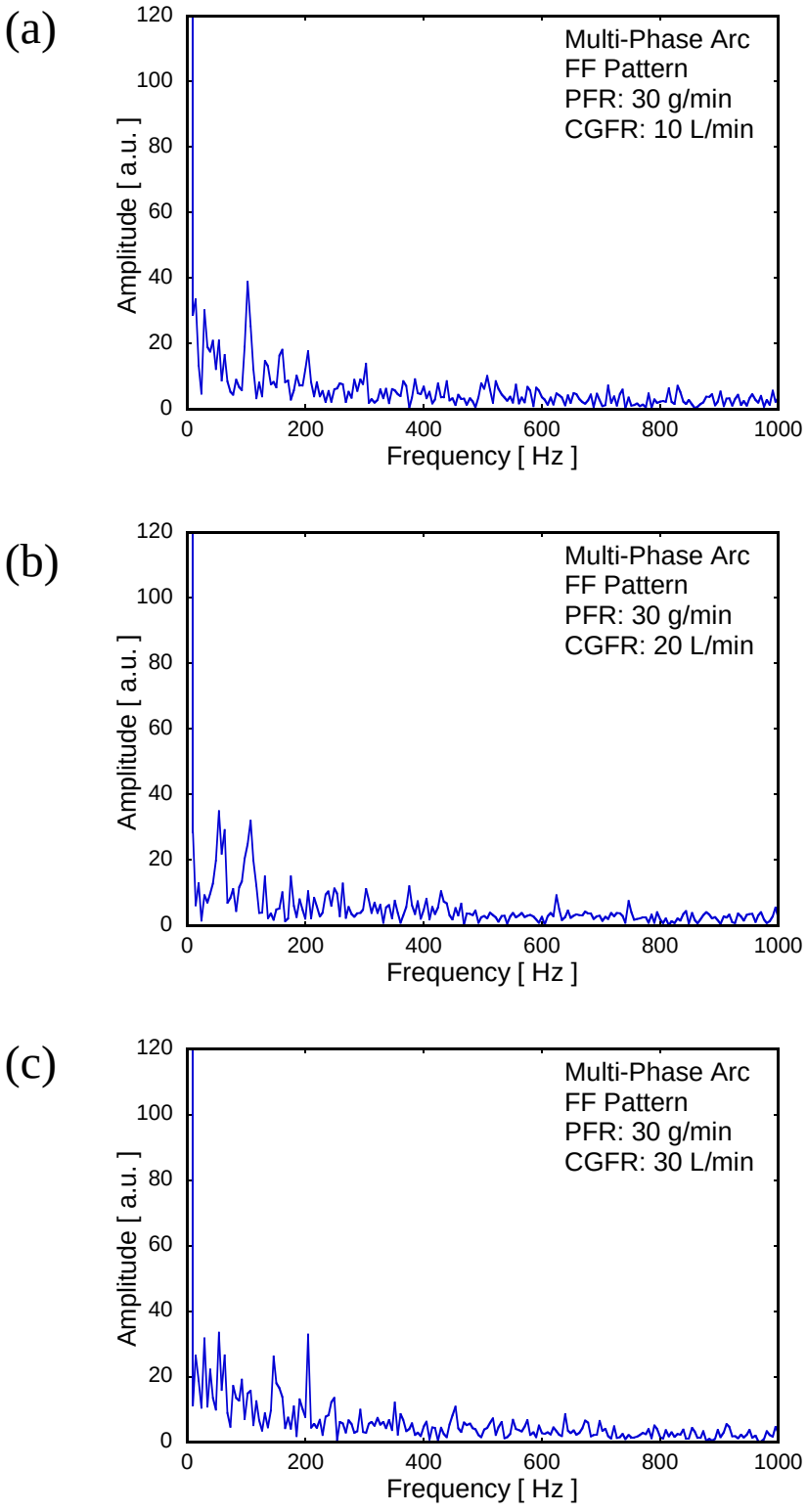

Fig. 4.12 Frequency spectra of fluctuation of particle temperature in FF pattern with different carrier gas flow rates: (a) 10 L/min (b) 20 L/min and (c) 30 L/min

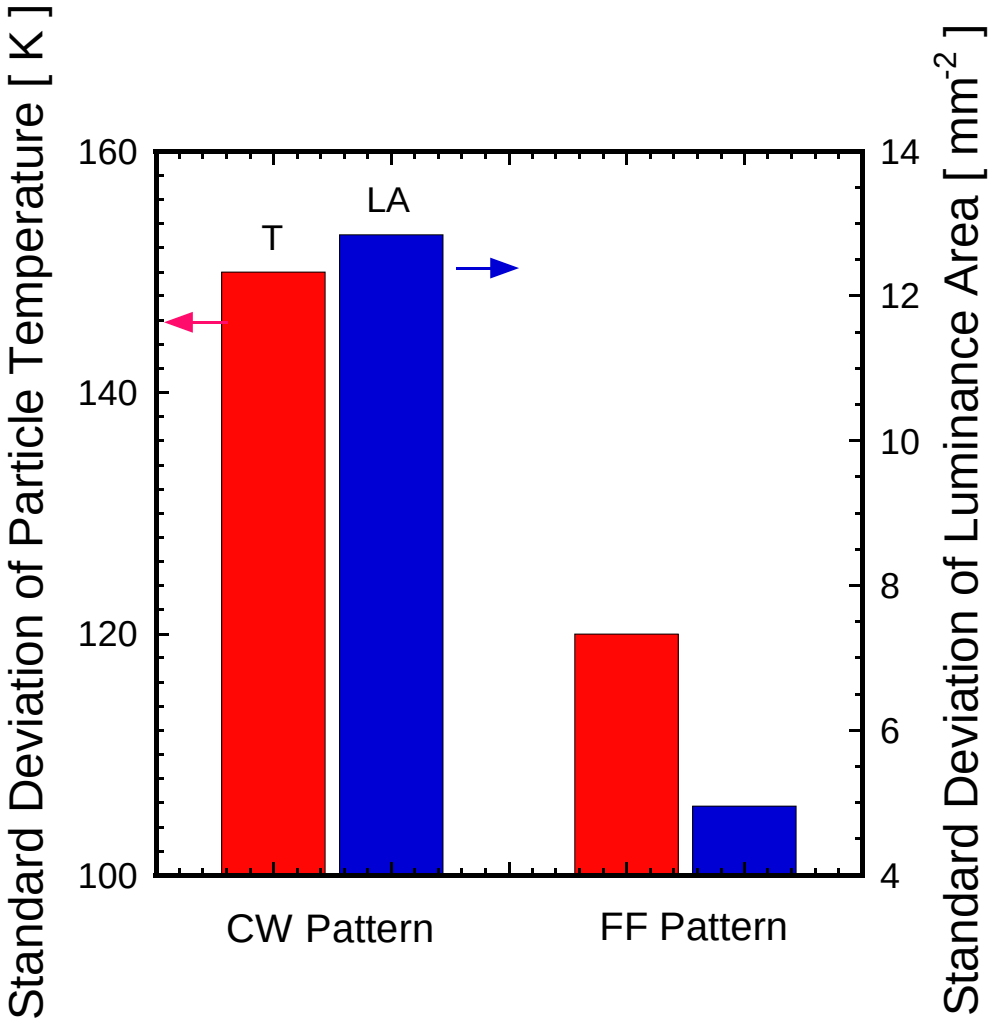

Fig. 4.13 Standard deviation of particle temperatures and arc luminance area of CW and FF patterns

5. Investigation of the Melting Behavior of Glass Powders by Multi-Phase AC Arc

In-flight melting is a method of melting glass materials in air using plasma combustion flames, that could reach up to 10,000ºC. This method enables the instant completion of the melting process, which usually consumes a lot of energy. Specially, granular materials with pre-adjusted composition are injected into the furnace from above and the materials pass through between the electrodes to be instantly melted by plasma combustion flames. By adopting in-flight melting to change the glass manufacturing method itself, it will be able to halve CO_2 emissions from glass manufacturing. Also, it will be able to downsize the melting tank to a width of several meters. The in-flight particle characterization in the multi-phase AC arc, as mentioned in Chapters 3 and 4, has shown that efficient thermal treatment of particles depends on the plasma conditions such as electrode configuration and others. The properties of melted glass powders are important to evaluate the feasibility of in-flight melting technology in future industrial application. This chapter will give an introduction of progress on the in-flight melting project and a summary of results of glass in-flight melting by multi-phase AC arc. Then the effect of electrode configuration, the carrier gas flow rate, and the different raw materials on the melting behavior was investigated. Results of the XRD patterns, the morphology, the particle size distribution, the vitrification degree and the composition of melted powders are given out.

5.1 Introduction

A feasibility study about in-flight-melting technology has been conducted from 2005 to 2007 and successfully melted the granular glass batch with an existing small facility. Commissioned by the New Energy and Industrial Technology Development Organization (NEDO), a new project was launched for the five-year period between 2008 and 2013, to identify the equipment necessary for practical use of the technology, and to study possible glass quality and the feasibility of mass production by the new melting method (Sakamoto et al. 2011; Shinohara 2011).

In the past five years, many researches have been done to investigate the proper heat source. The project has developed three different test furnaces, which are the 1t/day oxy-gas firing furnace (furnace-1), the 2000 kg/day oxy-gas firing-multi phase AC arc plasma hybrid furnace (furnace-2), and the 300 kg/day oxy-gas firing-RF plasma hybrid furnace (furnace-3). In the project, two kinds of glass compositions were employed for the melting testes. One is a standard commercial soda-lime-silica glass composition and the other is an alkali-free borosilicate glass composition similar to the Corning 7059 glass (Inoue et al. 2012). Because alkali-free glasses require higher melting temperature than the standard commercial silicate glasses, furnace-1 is usually used for the melting of standard silicate composition, while furnace-2 and 3 are used for the studies of both compositions. For the research of furnace-1, the modification of the burner design and the burner position was found very important to suppress the formation of foam layer on the glass melt. The key point of the optimization of the burner is the broadening and elongation of the flame which increases heating zone volume and flight time (Iwamoto et al. 2012).

Compared with the furnace-1, using thermal plasma in the in-flight melting technology are more challenging and difficult. The high power plasma glass melting can melt the glass

batches possessing high liquidus temperature which are difficult to melt in the Siemens type furnaces. Therefore the in-flight glass melting operated in the plasma heating will be able to produce the functional glasses containing the high melting point compounds. Many literatures reported both the numerically and experimentally of the in-flight behavior in induction thermal plasmas with soda-lime-silica glass particles (Yao et al. 2007a, b; Hossain et al. 2008,2009). It was found that the in-flight melting by RF plasma rather than oxy/gas combustion flame can increase both the residual amount of B_2O_3 and the vitrification degree. Moreover, the mechanical strength of granules was found to increase by using very fine primary raw materials (Sakamoto et al. 2012). A series of experiments showed that the vitrification proceeded homogeneously from the cross-section images (Yao et al. 2008a, b, 2009a). On the other hand, the risk of volatilization of Na_2O component during in-flight melting process increases due to the large specific surface of particles (Funabiki et al. 2008).

However, the use of RF plasma can only treat powders of a low feed rate usually at 5 g/min. The multi-phase AC arc possesses the advantage of large plasma volume attracted wide interest. Both of the soda-lime and alkali-free glass were treated by multi-phase (6- or 12-phase) AC discharge at the feed rate of 30 g/min (Yao et al. 2008c). Higher input power increase the vitrification of materials, thus decrease their particle size (Yao et al. 2009b). As the feed rate increases, the vitrification decreases as well as the volatilization of B_2O_3 (Yao et al. 2008c, d). The 12-phase AC arc provided the higher plasma temperature with larger volume and longer residence time during in-flight melting compared with RF plasma and oxygen burner (Yao et al. 2008e). The residence time of particle in the plasma region can be controlled by carrier gas flow rate and powder injection position (Yao et al. 2009c; Watanabe 2010). Soda-lime glass reached higher vitrification degree than the alkali-free glass due to its low viscosity (Yao et al. 2008c; Watanabe 2010).

5.2 Experimental

5.2.1 Experimental Setup

The experimental setup of in-flight glass melting by 12-phase AC arc is shown in Fig. 5.1. The details of the arc generation system have been introduced in Section 2.2. A powder feed nozzle was installed above the chamber and cooled by water at flow rate of 7 L/min. The exit of the feed nozzle has a diameter of 3.8 mm and a distance of 150 mm over the upper electrode level. The powders treated by the 12-phase AC arc were quenched and collected at the bottom of the chamber.

5.2.2 Raw Materials

The composition of the raw material is $51SiO_2$-$8.9Al_2O_3$-$15B_2O_3$-24.3BaO-0.1FeO in wt% (Table 5.1). The particle size distribution of alkali-free glass raw material is given in Fig. 5.2. The average size is 138 μm.

5.2.3 Experimental Conditions

The varied process parameters in the investigation of 12-phase AC arc discharge including the powder feed rate, the carrier gas flow rate, the electrode configuration, and the size of primary SiO_2 in raw material. The experimental conditions for effect of powder feed rate is shown in Table 5.2. CW electrode configuration with gap distance of 100 mm is the mostly used melting condition. The powder feed rate varied at 30, 50, 80, 110 g/min with constant air carrier gas flow rate at 20 L/min. Table 5.3 shows the experimental conditions for effect of carrier gas flow rate. 10, 20, 30 (maximum) L/min with typical powder feed rate of 30 g/min were conducted. Experimental conditions for effect of electrode configuration were presented in

Table 5.4. CW and FF pattern with powder feed rate at 30, 50, 80, 110 g/min under the carrier gas flow at 20 L/min were compared.

5.2.4 Experimental Procedures

The experimental procedures are shown in the following.

- Arc generation
- Powder injection

  The powder feeding time is depend on the powder feed rate. Considering of the recovery rate, the total weight of powder feeding is usually controlled at 400~500 g.
- Stop the powder feeding
- Stop the arc discharge

5.2.5 Analysis

The analyses as follows were carried out after the plasma experiments to investigate the characteristics of the melted glass particles.

i) Vitrification Degree Analysis by X-ray Diffractometry

The complicated process including many reactions which convert raw material into glass-like amorphous solid is called vitrification. In this research, the vitrification degree is simply defined as the reaction ratios of SiO_2 in the melted powders to the total crystal SiO_2 in the raw material by using X-ray diffractometry (XRD, Miniflex, Rigaku, Japan). The X radiation source is Cu Kα at 30 kV and 15 mA. The data were collected in the 2θ range 10-50º with a step size of 0.02 º and a scan speed of 4 º/min. The internal standard method was used to analyze the vitrification degree of raw material quantitatively, ZnO as the standard material.

Before analyze the melted powders, a calibration curve should be prepared. The mixtures of raw material and ZnO with various weight ratios (1:5, 1:2, 1, 2:1, 5:1) are used to obtain the calibration curve according to the peak intensities analyzed by XRD. The intensity ratios of SiO_2/ZnO can be obtained from their first intensity peaks ($2\theta=26.64^o$ for SiO_2 and $2\theta=36.24^o$ for ZnO). The calibration curve can be drawn with the relationship of weight ratio (SiO_2/ZnO) and intensity ratio (SiO_2/ZnO).

The mixture of the prepared powders (250 mg) and ZnO (50 mg) was analyzed by XRD to get respective peak intensities. Then the reacted SiO_2 (vitrification degree) can be accounted combining the calibration curve.

ii) Chemical Composition Analysis by X-ray Fluorescence Analyzer

The chemical composition of the obtained glass particles were analyzed for SiO_2, Al_2O_3 and BaO by the X-ray fluorescence analyzer (Rigaku Corp., ZSX Primus) using glass beads. The content of B_2O_3 in the glass was determined by wet analysis (JIS R2015). The analysis results were provided by Asahi Glass Co., Ltd.

iii) Morphology Observation by Optical Microscope

The morphology of the particles was performed with optical microscope on VHK-1000 (Keyence, Japan). The magnification was set as 500 times.

iv) Particle Size Distribution Analysis by Laser Scattering Measurement

The particle size distribution of the melted glass powders were measured by using laser diffraction particle size analyzer (Microtrack, Nikkiso Co., Ltd. MT3200) in a dry state. The analysis results were provided by Asahi Glass Co., Ltd.

5.3 Experimental Results

5.3.1 Effect of Powder Feed Rate on the Glass Melting Behavior

The XRD patterns of the raw material and the quenched powders with different feed rates (mixed with the ZnO) are shown in Fig. 5.3. The patterns show no obvious diffractive peaks except of the ZnO standard material in the samples of quenched powders, indicating the decomposition of carbonates was almost complete in the flight melting process. Compared with the raw material, the intensity of SiO_2 (101) of quenched powders decreases sharply after heating. As the feed rate decreases, the intensity of SiO_2 of quenched powders also decreases. Especially for the powder feed rate of 30 g/min, the patterns without any peaks except of the ZnO reveals that the powders are the whole amorphous structure with typical glass characteristic which means the reactions among compounds were complete during in-flight melting.

Figure 5.4 presents the microscope images of quenched glass particles prepared at different powder feed rates. The quenched particles completely melted like glass beads which have spherical shape, smooth surface and compact structure. While the unmelted particles still keep rough surface and opaque structure. As the powder feed rate of injected powders increases, the amount of unmelted particles increases due to lower particle temperature. Compared with the diameter of particles of raw material, the microscope images show that the particle shrank after melting.

Figure 5.5 illustrates the particle size distribution of quenched alkali-free glass particles at varying powder feed rates. With decrease the powder feed rate, the particle average size decreases. In addition, the particle size distribution becomes narrow and more uniform because of more energy transfer to each particle.

The particle vitrification degree as well as the average diameter under different powder feed rates is shown in Fig. 5.6. The particles after melting shrank due to high porosity of the raw materials and the decomposition of carbonate during vitrification reaction. Thus the shrinkage of particle diameter is related with the vitrification, higher vitrification causes more shrinkage of particle.

Table 5.5 summarized the results of chemical composition analysis under different powder feed rates. Compared with other components, B_2O_3 is the mainly volatilized part in the glass. The B_2O_3 in the alkali-free glass are the indispensable component to reduce the viscosity and softening point of each glass. Since B_2O_3 is volatile material which was introduced from the reagent of H_3BO_3, its residual content should be controlled at a certain level after treatment by plasma. The calculation of the B_2O_3 volatilization is based on the assumption that the amount of Al_2O_3 is not changed after melted because the boiling point of Al_2O_3 is 3000 ºC. The volatilization degree of B_2O_3 was estimated from the chemical composition of the raw materials and the melted powders.

Figure 5.7 shows the effect of powder feed rate on the B_2O_3 volatilization of quenched glass particles. With the powder feed rate increasing, the volatilization degree of B_2O_3 in the melted powders decreases, which indicates the maximum temperature of particles obtained in plasma decreased. Combined with Fig. 5.6, it is notable that the high vitrification degree accompanies with the high volatilization degree of B_2O_3. Thus the volatilization rate of B_2O_3 can reflect the particle temperature achieved in the process of in-flight melting.

The effect of powder feed rate on the glass melting properties was clearly through the above experiments. Lower powder feeding leads to a more sufficient reaction inside the particle. The well treated glass particles have characteristics of amorphous structure, transparent morphology and small diameter. The vitrification degree and volatilization degree are the most

effective factors to evaluate the in-flight melting process. Decrease the powder feed rate caused higher vitrification which indicated the improved melting speed, but also leads to larger volatilization of component.

5.3.2 Effect of Carrier Gas Flow Rate on the Glass Melting Behavior

Figure 5.8 shows the XRD patterns of the powders treated by multi-phase AC arc at powder feed rate at 30 g/min with different carrier gas flow rates. The powders prepared under the three conditions have amorphous structure because no clear peaks are remained except of the standard material. The intensity of SiO_2 main peak was decreased at the lower carrier gas flow rate due to the reaction of crystal SiO_2 with other compounds.

The microscope images of prepared particles at carrier gas flow rate of 10, 20 and 30 L/min are shown in Fig. 5.9 to observe the particle morphology. Due to a low feed rate at 30 g/min, the particles in all conditions are well vitrified. Especially in the carrier gas flow rate of 10 L/min, almost all of the quenched particles have small size, spherical shape and transparent structure. In the case of 30 L/min, some incompletely melted particles with irregular shape and the structure closed to the raw material can be observed.

Results of the particle size distributions treated at carrier gas flow rate of 10, 20 and 30 L/min are presented in Fig. 5.10. The particle size distribution shifts to the left side at lower gas flow rate, indicating the average size becomes smaller.

Figure 5.11 shows the effect of carrier gas flow rate on the vitrification degree and particle size. Larger flow rate leads to lower plasma temperature due to more energy exchange between plasma and carrier gas, then lower plasma temperature brings less heat transferred to particles. Besides, increase of the gas flow rate will decrease the particle residence time in the plasma flame because of higher velocity of particle which caused by more momentum. As a

result, the vitrification degree decreases. Correspondingly, the particle average diameters become larger. However, the figure shows a high vitrification degree of 92% at the highest flow rate of carrier gas.

Table 5.6 shows the chemical compositions of melted particles with different carrier gas flow rates. The effect of carrier gas flow rate of volatilization degree of B_2O_3 is presented in Fig. 5.12. The volatilization degree of B_2O_3 in the melted powders decreases with increasing the carrier gas flow rate. It indicates the less heat transfer from plasma to particle under higher gas flow rate.

The carrier gas flow rate is another important parameter to decide the powder injection condition. Its effect on the glass melting properties was clearly shown. Increase the carrier gas flow rate results in the higher particle velocity, thus shorter residence time passing through the plasma region. In this case, particles have no sufficient time to be heated and melted.

As the multi-phase AC arc shows variety adaptability on the powder treatment, several external parameters were demonstrated to influence the multi-phase AC arc characteristics which presented in Chapter 2. One of the most important parameter is the electrode configuration.

5.3.3 Effect of Electrode Configuration on the Glass Melting Behavior

In-flight particle melting behavior was investigated in multi-phase AC arc with the FF pattern. Figure 5.13 shows the XRD patterns of melted particles in FF configuration at different powder feed rates. The results are similar with the CW pattern in Fig. 5.3. However, the peak of SiO_2 (101) in the FF pattern is lower than that of CW pattern. Figure 5.14 gives the particle morphology observed by optical microscope treated in FF pattern. Higher powder feed rate leads to the larger particle size as well as more number of unmelted particles.

Figures 5.15 (a) to (c) give the particle size distribution of treated powders with FF pattern at feed rate of 30, 50 and 80 g/min, respectively. The peak of size distribution becomes narrower with decreasing the powder feed rate, which indicates the reaction inside the particle are promoted thus the diameter reduces.

The vitrification degree of powders treated by CW and FF pattern with different powder feed rates are compared in Fig. 5.16. In both patterns, the increase of powder feed rate leads to a decrease in vitrification degree. At lower rate of powder feeding, the vitrification degree with CW pattern is higher than that of FF pattern. While increased the powder feeding over 40 g/min, CW pattern caused lower vitrification degree than the FF pattern. It can be explained by the spatially distribution of in-flight granulated particles. Most granulated particles pass through the central region of the arc in the case of lower powder feeding. On the other hand, with increasing the feed rate, the powder spread prior to the electrode region due to the expansion of powder flux. The different trend of vitrification degree indicated that the different spatial characteristics of discharge patterns, which has been mentioned in Section 2.3.2. In FF pattern, the high-temperature region was most effectively constricted toward the nozzle axis. Hence, the expansion of in-flight powders will enhance the melting efficiency due to high-temperature region.

Table 5.7 gives the analysed chemical compositions of melted particles in FF pattern. Then the volatilization degree of B_2O_3 is calculated and compared with CW pattern. The result is presented in Fig. 5.17. The volatilization degree in CW pattern at powder feed rate of 30 g/min is higher than that of FF pattern. With the powder feed rate increases, the volatilization degree of B_2O_3 in the melted particles decreases, which indicates the maximum temperature of particle obtained in plasma decreased. At feed rate of 110 g/min, FF pattern leads to higher vitrification degree as well as lower volatilization degree compared with the CW pattern. This

can be related to the arc discharge behavior in different patterns. Although the CW pattern resulted in a wider arc existence region, its great temporal fluctuation affected the particle melting behavior (Chapter 4). On the other hand, FF pattern maintained a small variation of the high temperature distribution, thus the powders could be treated uniformly. This is in good agreement with the lower fluctuation of particle temperature in FF pattern measured by high-speed camera (Section 4.3.1). These experimental results indicated that the spatial variation behavior originated from arc discharge caused different particle melting characteristics in the two electrode patterns.

5.4 Discussion

The multi-phase AC arc possesses the advantage of high energy efficiency compared to other thermal plasmas such as RF plasma. The primary used electricity power of 12-phase AC input can be calculated from voltage (195 V), current (290 A) and power factor of 0.8. The total power of the 12-phase AC arc come from the electricity is evaluated with efficiency of 70~80% because of the energy loss in the transformers. Thus the input power of Joule heating for multi-phase AC arc system is about 55 kW. From the calculation of energy balance in the melting system, 45% of the energy transferred to out gas and 40% of the energy transferred to cooling water in electrodes, plasma torches, reaction chamber and powder feeder. In the case of RF thermal plasma torch, there are energy losses due to the electron-impact excitation and ionization of gas atoms and plasma heat conduction. The input power come from the electricity is evaluated with efficiency of about 50%. 20% of the energy goes to cooling water and 30% of the energy losses by radiation. Compared with these two thermal plasma sources, multi-phase AC arc has higher energy efficiency than that of RF plasma, thus more suitable for material processing.

Glass melting is a complicated process, containing many physical and chemical changes during heating. The main chemical reactions include the decomposition of barium carbonates ($BaCO_3$), formation of aluminosilicate melt, and forming an amorphous of SiO_2. The granular raw materials have pores of submicrometer order are considered to be formed by the drying of water in the slurry droplets, and the large voids can be attributed to bubbles inside the slurry droplets. When particles are exposed into the high temperature atmosphere by plasma, the reaction and melting first occur on the surface of the particles, and then propagate into the inner solid. The viscosity of molten glass on the surface will delay the melting reaction and the removal of the decomposed gases inside the particles, namely, the temperature gradient within the particle is important during in-flight glass melting. The bubbles remained in the melted particles originated from the initial voids, otherwise come from the decomposition reaction and the CO_2 cannot escape from the inside.

The vitrification degree and volatilization degree of B_2O_3 are the most important evaluations of the glass quality by in-flight melting process. As the raw materials size dispersion could affect their melting state, raw material with smaller particle sizes, or particles that can pass through high temperature area are easy to melt completely. The particles after treatment in CW pattern with powder feed rate at 30 g/min were sieved and classified into three size ranges, smaller than 75 μm, 75~150 μm and larger than 150 μm, respectively. There XRD patterns are presented in Fig. 5.18. From the morphology of raw materials and each sieved particle group which is shown in Fig. 5.19, it can be seen that smaller particles have a smooth surface and a characteristic of glass with transparent structure which indicated completely melted. On the other hand, the larger particles show rough surface and similar morphology to the raw powders are represented for the incompletely melted.

The chemical compositions of quenched powders with different sieved sizes are shown

in Table 5.8. The vitrification degree and volatilization degree of B_2O_3 as a relationship to the particle diameter are presented in Fig. 5.20. As the particle size effect is more critical than the residence time in the plasma region, it was considered that the heat transfer to larger particles is the same with smaller particles. However, larger heat capacity of larger particles makes the increase of particle temperature slow. The granulated particles are considered to fly separated from each other in the thermal plasma, and be heated by the surrounding atmosphere from all directions. The short residence time in the hot plasma region was sufficient for small-size particles to be melted, but the surface of the flying particles can be a reaction field of the volatilization phenomena. The particles have a much large specific surface area and all of them are in contact with a high-temperature atmosphere. It would be reasonable to caused an over volatilization of B_2O_3 than the traditional batch melting method. The thermal energy that one particle receives from the thermal plasma depends on the plasma condition as well as the particle size. The vitrification ratio of the large particles would be considerable affected by their flying condition. When consider the suppression of volatilization of B_2O_3 from the particles, it also have to take into account the depression of the reaction of SiO_2.

5.5 Conclusion

The in-flight treatment of alkali-free glass raw materials by multi-phase AC arc was conducted. The effect of powder feed rate, the electrode configuration, and the carrier gas flow rate on the melting behavior was investigated. On the basis of the experimental results, the following major conclusions can be drawn from this chapter.

1) An innovative in-flight melting technology using the stable 12-phase AC arc was successfully developed to melted granulated alkali-free glass raw materials. High vitrification of powders can be achieved within short in-flight time of 20 milliseconds.

2) The high vitrified glass particles are characterized by XRD pattern with no obvious diffractive peaks compared to the raw material, indicating the glass-like amorphous solid which is free of crystalline structure.

3) The shrinkage of particle is strongly related to the vitrification degree. Larger powder rate or higher carrier gas flow rate results in lower heat transfer to particles.

4) The volatilization rate of B_2O_3 can reflect the particle temperature achieved in the process of in-flight melting.

5) The spatial variation behavior originated from arc discharge caused different particle melting characteristics in the two electrode patterns. Increase the powder feed rate implies the expansion of powder flux, thus the FF pattern leads to higher vitrification degree than that of CW pattern because the arc is concentrated away from the central. Moreover, FF pattern maintained a small variation of the high temperature distribution according to the luminance area of arc, thus a uniform treated powder with prohibited volatilization degree can be obtained at high feed rate.

References

Funabiki, F., T. Yano, Y. Yao and T. Watanabe. “In-flight-melted soda-lime-silica glass by RF induction thermal plasma.” *Journal of the American Ceramic Society* **91**(12), 3908-3914 (2008).

Hossain, M. M., Y. Yao and T. Watanabe. “A numerical analysis of plasma-particle heat exchange during in-flight treatment of granulated powders by argon-oxygen induction thermal plasmas.” *Thin Solid Films* **516**(19), 6634-6639 (2008).

Hossain, M. M., Y. Yao, T. Watanabe, F. Funabiki and T. Yano. “In-flight thermal treatment of soda-lime-silica glass powders for glass production by argon-oxygen induction thermal plasmas.” *Chemical Engineering Journal* **150**(2-3), 561-568 (2009).

Inoue, S., T. Watanabe, T. Yano, O. Sakamoto, K. Satoh, S. Kawachi and T. Iseda. “Future of Glass Melting Through the In-Fight Melting Technique.” *Processing, Properties, and Applications of Glass and Optical Materials: Ceramic Transactions* **231**, 37-44, (Eds.) A. K. Varshneya, H. A. Schaeffer, K. R. Richardson, M. Wightman and L. D. Pye (2012).

Iwamoto, M., K. Satoh, Y. Ebihara, O. Sakamoto, C. Tanaka and H. Segawa. “Test results of the in-flight glass melting using one-ton/day large scale experimental melter.” Processing, Properties, and Applications of Glass and Optical Materials: Ceramic Transactions, **231**, 51-58, (Eds.) A. K. Varshneya, H. A. Schaeffer, K. A. Richardson, M. Wightman and L. D. Pye (2012).

Sakamoto, O., C. Tanaka, S. Miyazaki and S. Ohkawa. “Glass-melting furnace, process for producing molten glass, apparatus for producing glass products and process for producing glass products.” U. S Patent, 8,544,298 (2011).

Sakamoto, O., C. Tanaka, S. Miyazaki, N. Shinohara and S. Ohkawa. “Application of the in-flight melting technology to an alkaline free borosilicate glass.” Processing, Properties, and Applications of Glass and Optical Materials: Ceramic Transactions, **231**, 45-49, (Eds.) A. K. Varshneya, H. A. Schaeffer, K. A. Richardson, M. Wightman and L. D. Pye (2012).

Shinohara, N. “Process for production of glass raw material granules, and process for production of glass product.” Patent, EP2,620,416 A1 (2011).

Watanabe, T., K. Yatsuda, Y. Yao, T. Yano and T. Matsuura. “Innovative in-flight glass-melting technology using thermal plasmas.” *Pure Appl. Chem.*, **82**(6), 1337-1351 (2010).

Yao, Y., M. M. Hossain, Y. Oyamatsu, T. Watanabe, F. Funabiki and T. Yano. “In-flight melting of granulated powders in thermal plasmas for glass production.” *Transactions of the Materials Research Society of Japan* **32**(2), 509-512 (2007a).

Yao, Y., M. M. Hossain, Y. Oyamatsu, T. Watanabe, F. Funabiki and T. Yano. “Plasma-Particle Heat Transfer Mechanism for In-Flight Melting of Powders in Induction Thermal Plasmas.” *Proc. 1st Asian Symposium on Computational Heat Transfer and Fluid Flow* Xi’an, China (2007b).

Yao, Y., M. M. Hossain, T. Watanabe, T. Tsujimura, F. Funabiki and T. Yano. “Effects of feed rate and particle size on the in-flight melting behavior of granulated powders in induction thermal plasmas.” *Thin Solid Films* **516**(19), 6622-6627 (2008a).

Yao, Y., M. M. Hossain, T. Watanabe and F. Funabiki. “Application of in-flight melting technology by RF induction thermal plasmas to glass production.” *Plasma Science and Technology* **10**(3), 344-347 (2008b).

Yao, Y., M. M. Hossain, T. Watanabe, T. Matsuura, F. Funabiki and T. Yano. “A multi-phase AC arc discharge and its application in in-flight thermal treatment of raw glass powders.” *Chemical Engineering Journal* **139** (2), 390-397 (2008c).

Yao, Y., K. Yatsuda, T. Watanabe, F. Funabiki and T. Yano. “Investigation on in-flight melting behavior of granulated alkali-free glass raw material under different conditions with 12-phase AC arc.” *Chemical Engineering Journal* **144**(2), 317-323 (2008d).

Yao, Y., T. Watanabe, T. Yano, T. Iseda, O. Sakamoto, M. Iwamoto and S. Inoue. “An innovative energy-saving in-flight melting technology and its application to glass production.” *Science and Technology of Advanced Material* **9**(2), 1-8 (2008e).

Yao, Y., M. M. Hossain and T. Watanabe. “Numerical and Experimental Investigation on the In-Flight Melting Behavior of Granulated Powders in Induction Thermal Plasmas.” *Plasma Science and Technology* **11**(1), 71-77 (2009a).

Yao, Y., K. Yatsuda, T. Watanabe, T. Matsuura and T. Yano. “Characteristics of multi-phase alternating current arc for glass in-flight melting.” *Plasma Chemistry and Plasma Procssing* **29**(5), 333-346 (2009b).

Yao, Y., K. Yatsuda, T. Watanabe and T. Yano. “Effect of injection position on in-flight melting behavior of granular alkali-free glass raw material in 12-phase AC arc plasma.” *Plasma Science and Technology* **11**(6), 699-703 (2009c).

Table 5.1 Batch formulation of alkali-free glass

Target	SiO_2	Al_2O_3	B_2O_3	BaO	Fe_2O_3	Total
[wt%]	51	8.9	15	24.3	0.1	99.4
Raw material	SiO_2	Al_2O_3	H_3BO_3	$BaCO_3$	Fe_2O_3	Total
[wt%]	51	8.9	26.6	32.2	0.1	118.8

Table 5.2 Experimental conditions for effect of powder feed rate by multi-phase AC arc

Discharge conditions	
Number of phase	12
Electrode configuration	Clockwise (CW) pattern
Power	50~55 kW
Current	320 A
Voltage	200 V
Electrode distance	100 mm
Ar flow rate (each electrode)	5 L/min
Tungsten electrode diameter	φ6 mm
Powder treatment conditions	
Powder	Alkali-free glass
Primary SiO_2 size	7~8 μm
Particle mean size	138 μm
Powder feed rate	30, 50, 80, 110 g/min
Air carrier gas flow rate	20 L/min
Distance from powder injection position to electrodes	300 mm

Table 5.3 Experimental conditions for effect of carrier gas flow rate by multi-phase AC arc

Discharge conditions	
Number of phase	12
Electrode configuration	Clockwise (CW) pattern
Power	50~55 kW
Current	320 A
Voltage	200 V
Electrode distance	100 mm
Ar flow rate (each electrode)	5 L/min
Tungsten electrode diameter	φ6 mm
Powder treatment conditions	
Powder	Alkali-free glass
Primary SiO_2 size	7~8 μm
Particle mean size	138 μm
Powder feed rate	30 g/min
Air carrier gas flow rate	10, 20, 30 L/min
Distance from powder injection position to electrodes	300 mm

Table 5.4 Experimental conditions for effect of electrode configuration by multi-phase AC arc

Discharge conditions		
Number of phase	12	
Electrode configuration	Clockwise (CW) pattern	Flip-flop (FF) pattern
Power	50~55 kW	50~55 kW
Current	320 A	320 A
Voltage	200 V	200 V
Electrode distance	100 mm	100 mm
Ar flow rate (each electrode)	5 L/min	5 L/min
Tungsten electrode diameter	φ6 mm	φ6 mm
Powder treatment conditions		
Powder	Alkali-free glass	
Primary SiO_2 size	7~8 μm	
Particle mean size	138 μm	
Powder feed rate	30, 50, 80, 110 g/min	
Air carrier gas flow rate	20 L/min	
Distance from powder injection position to electrodes	300 mm	

Table 5.5 Chemical compositions of the alkali-free glass powders with different powder feed rate by multi-phase AC arc in CW pattern

Powder feed rate	SiO_2 (wt%)	Al_2O_3 (wt%)	B_2O_3 (wt%)	BaO (wt%)	Fe_2O_3 (wt%)
30 g/min	51.8	11.2	8.8	27.4	0.1
50 g/min	52.3	9.8	11.7	25.4	0.1
80 g/min	51.8	9.6	13	24.9	0.1
110 g/min	51.1	9.5	13.4	25.3	0.1

Table 5.6 Chemical compositions of the alkali-free glass powders with different carrier gas flow rate by multi-phase AC arc in CW pattern

Carrier gas flow rate	SiO_2 (wt%)	Al_2O_3 (wt%)	B_2O_3 (wt%)	BaO (wt%)	Fe_2O_3 (wt%)
10 L/min	52.5	10.4	10.3	26.2	0.1
20 L/min	51.8	11.2	8.8	27.4	0.1
30 L/min	52.9	9.8	11.4	25.3	0.1

Table 5.7 Chemical compositions of the alkali-free glass powders with different powder feed rate by multi-phase AC arc in FF pattern

Powder feed rate	SiO_2 (wt%)	Al_2O_3 (wt%)	B_2O_3 (wt%)	BaO (wt%)	Fe_2O_3 (wt%)
30 g/min	52.6	10.2	10	26.4	0.1
50 g/min	52.4	9.7	11.8	25.4	0.1
80 g/min	52.1	9.5	12.8	24.9	0.1
110 g/min	51.8	9.6	12.7	25.2	0.1

Table 5.8 Chemical compositions of the alkali-free glass powders with different sieved sizes by multi-phase AC arc in CW pattern

Sieved size	SiO_2 (wt%)	Al_2O_3 (wt%)	B_2O_3 (wt%)	BaO (wt%)	Fe_2O_3 (wt%)
<75 μm	55.1	11.6	4.8	27.6	0.1
75~150 μm	53.8	9.3	11.3	24.8	0.1
>150 μm	51.5	8.7	14.9	22.2	0.1

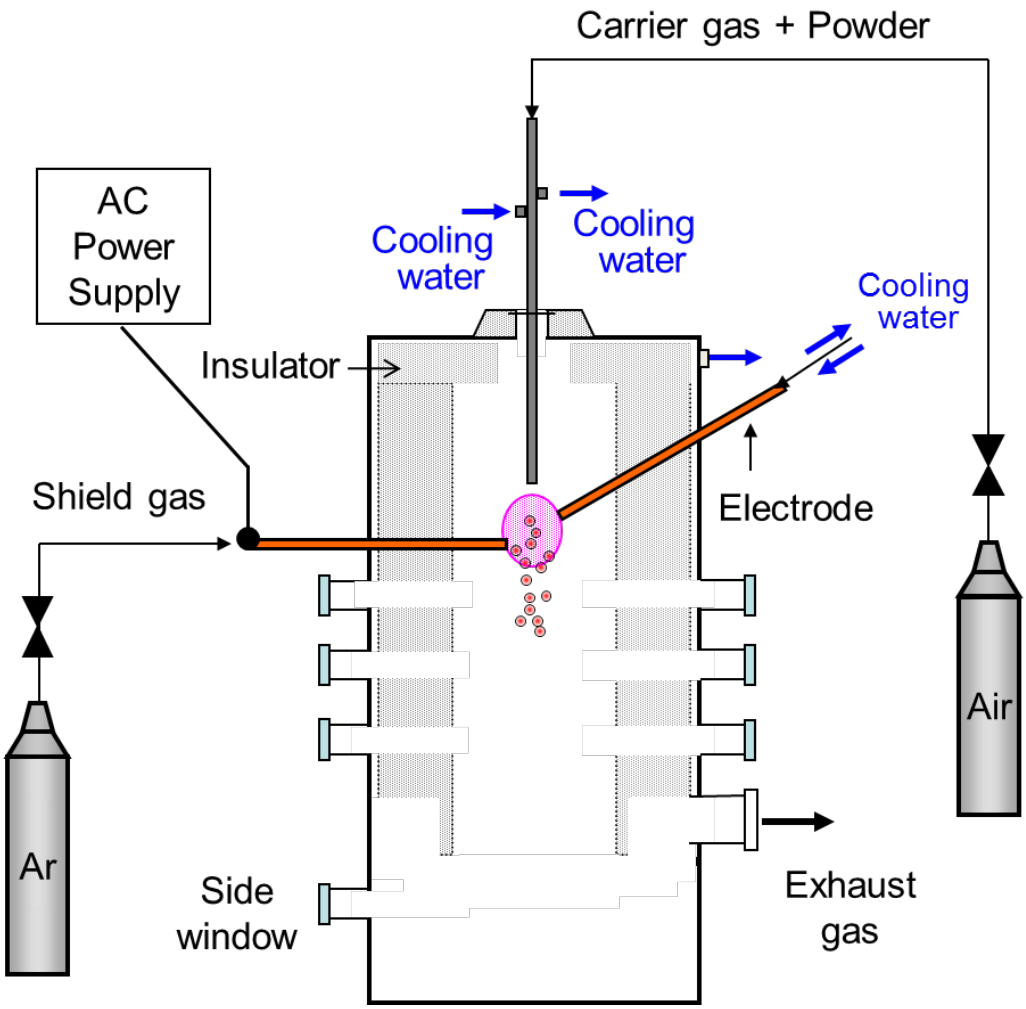

Fig. 5.1 The schematic of the in-flight melting by multi-phase AC arc

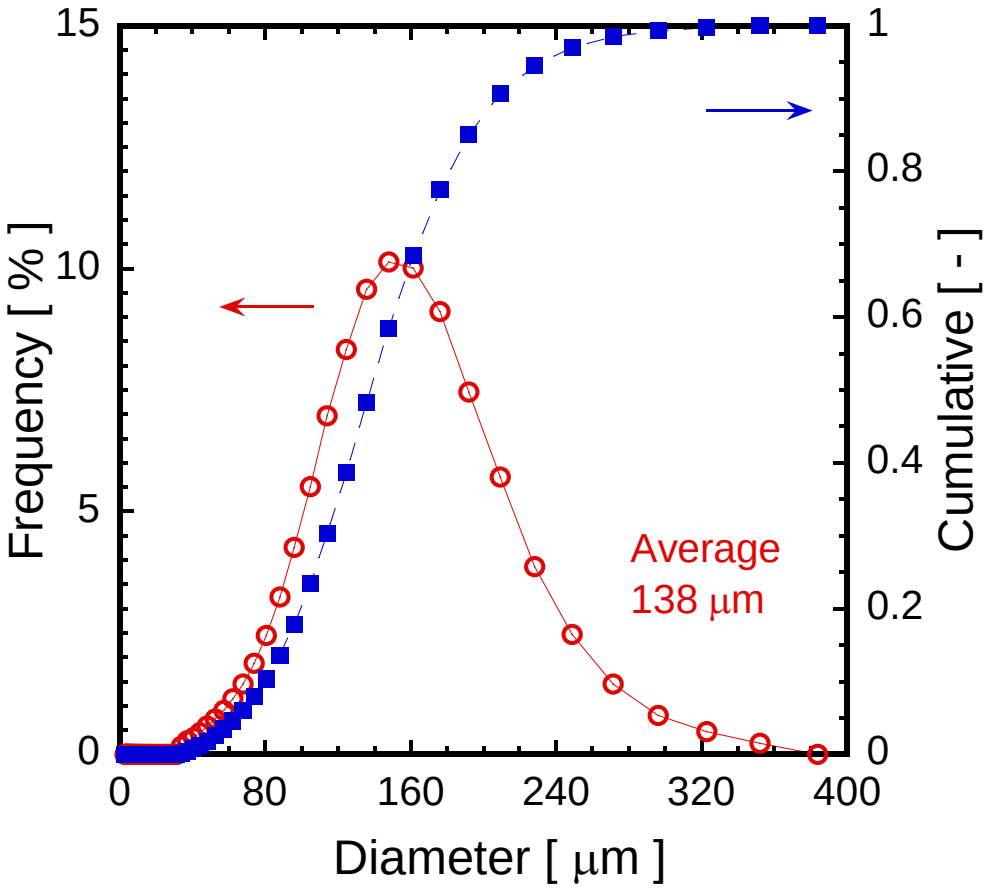

Fig. 5.2 Particle size distribution of raw material of alkali-free glass

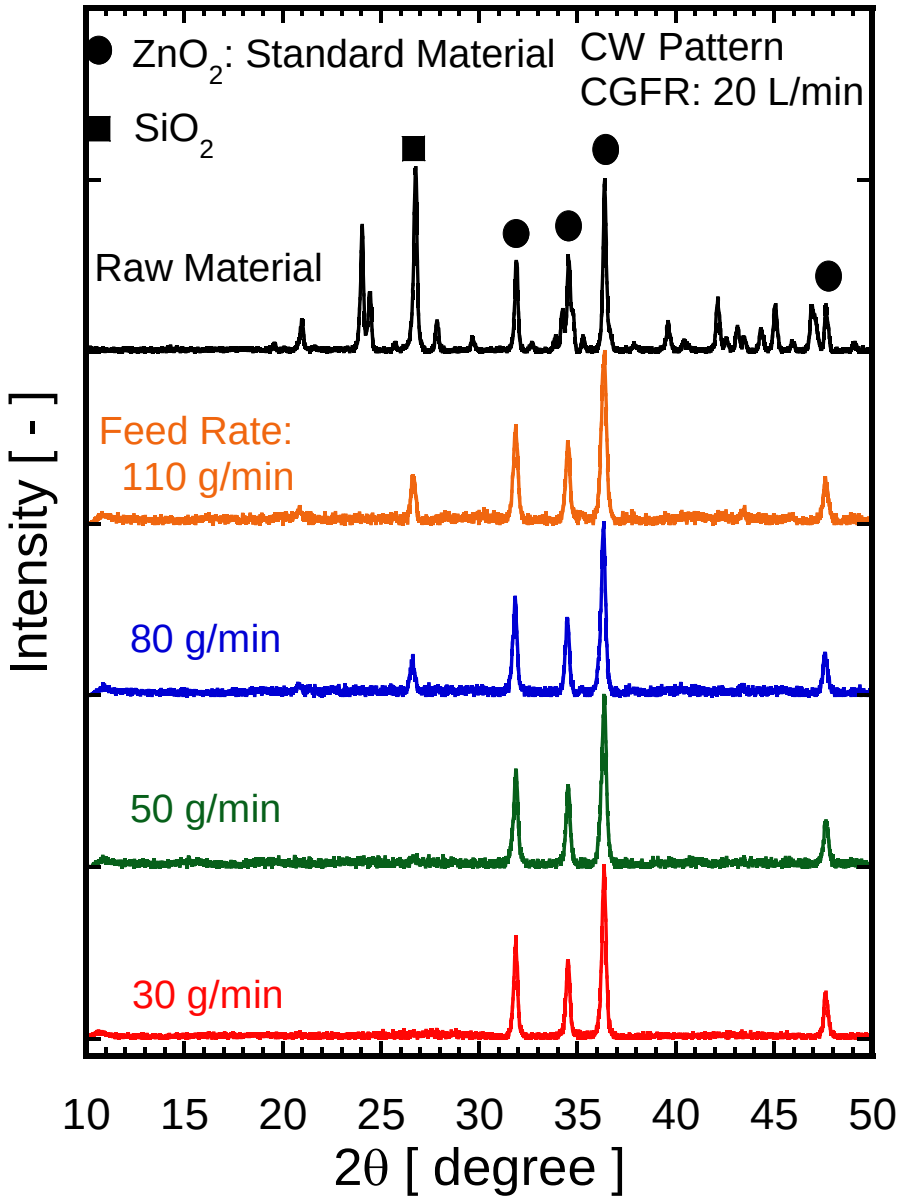

Fig. 5.3 XRD patterns of melted alkali-free glass particles by multi-phase AC arc with CW pattern at different powder feed rates

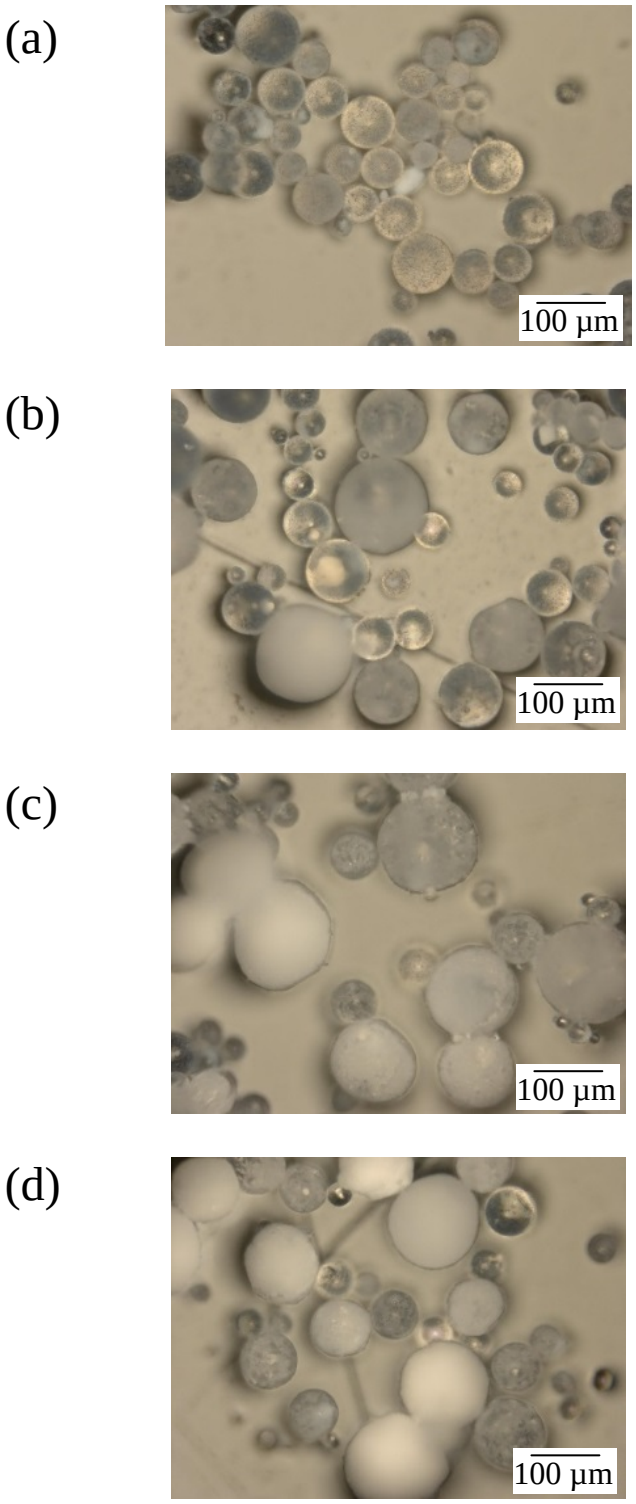

Fig. 5.4 Microscope images of melted alkali-free glass particles by multi-phase AC arc with CW pattern at different powder feed rates: (a) 30 g/min, (b) 50 g/min, (c) 80 g/min and (d) 110 g/min

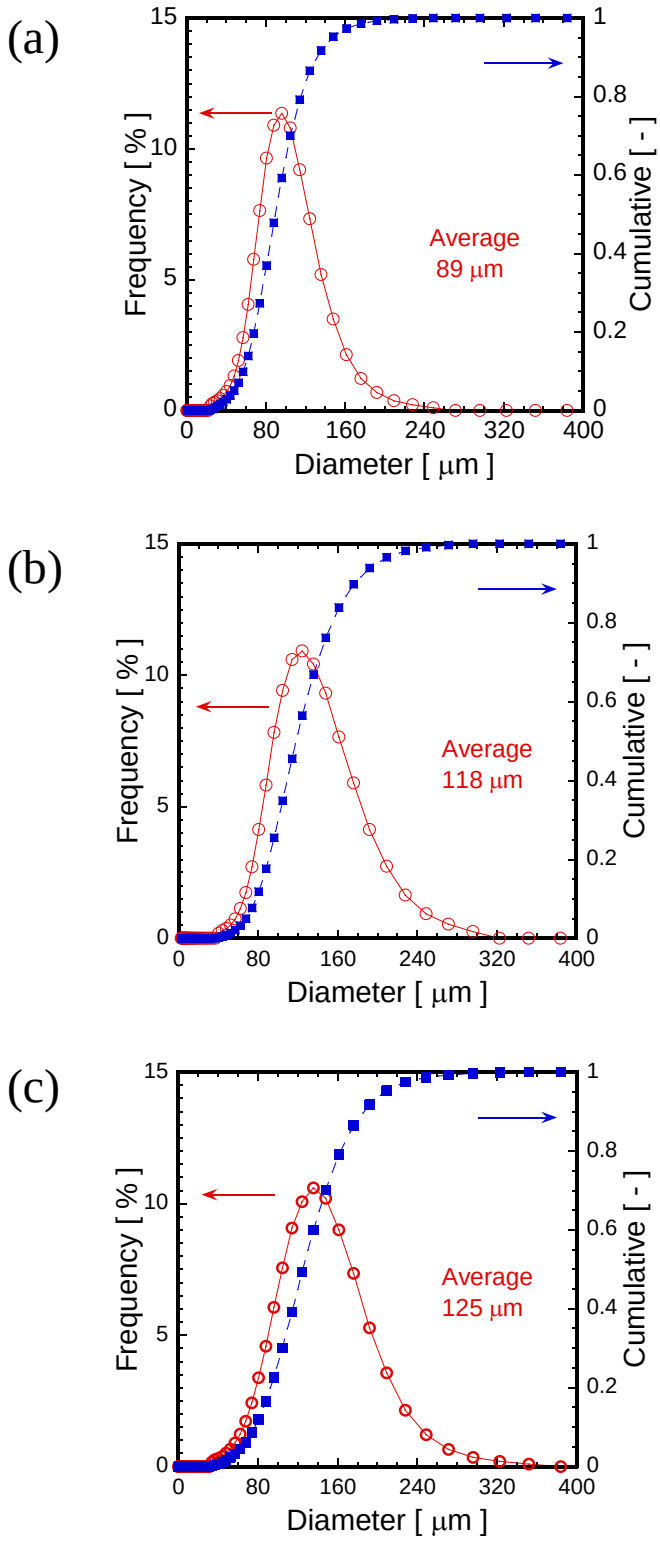

Fig. 5.5 Particle size distributions of melted alkali-free glass particles by multi-phase AC arc with CW pattern at different powder feed rates: (a) 30 g/min, (b) 50 g/min and (c) 80 g/min

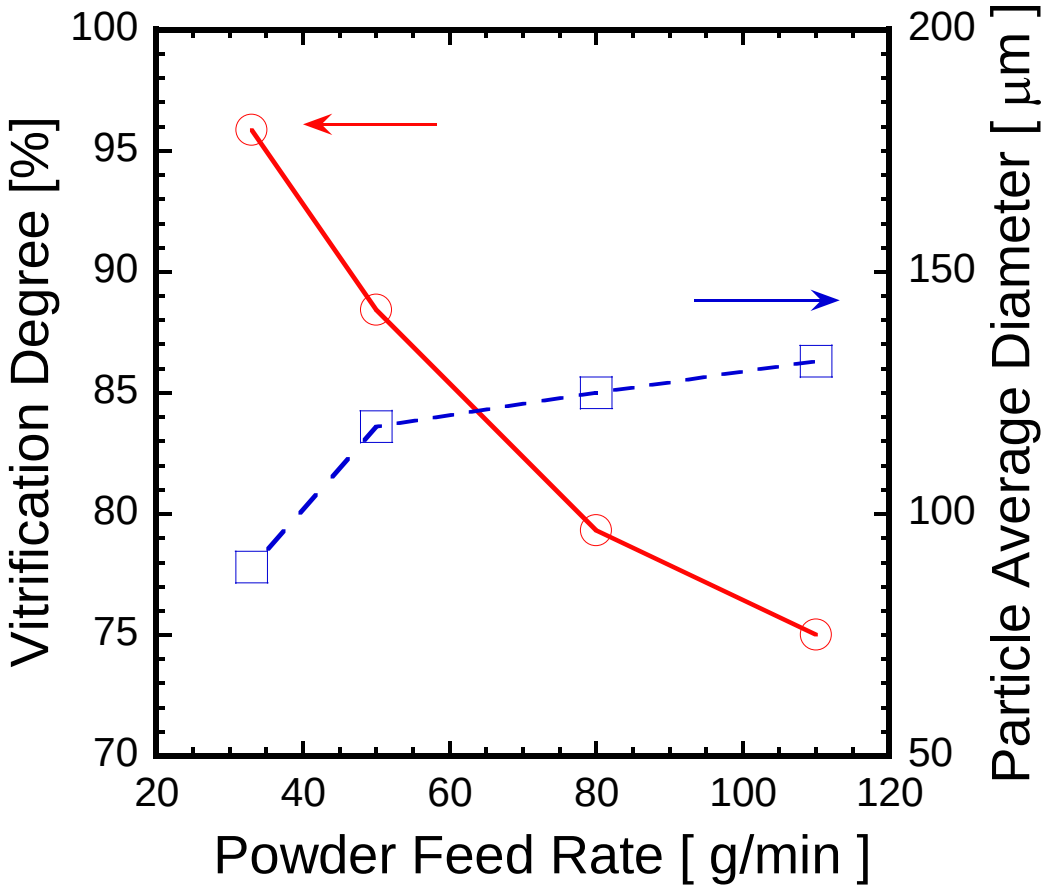

Fig. 5.6 Effect of powder feed rate on vitrification degree and particle average diameter of melted alkali-free glass particles by multi-phase AC arc with CW pattern

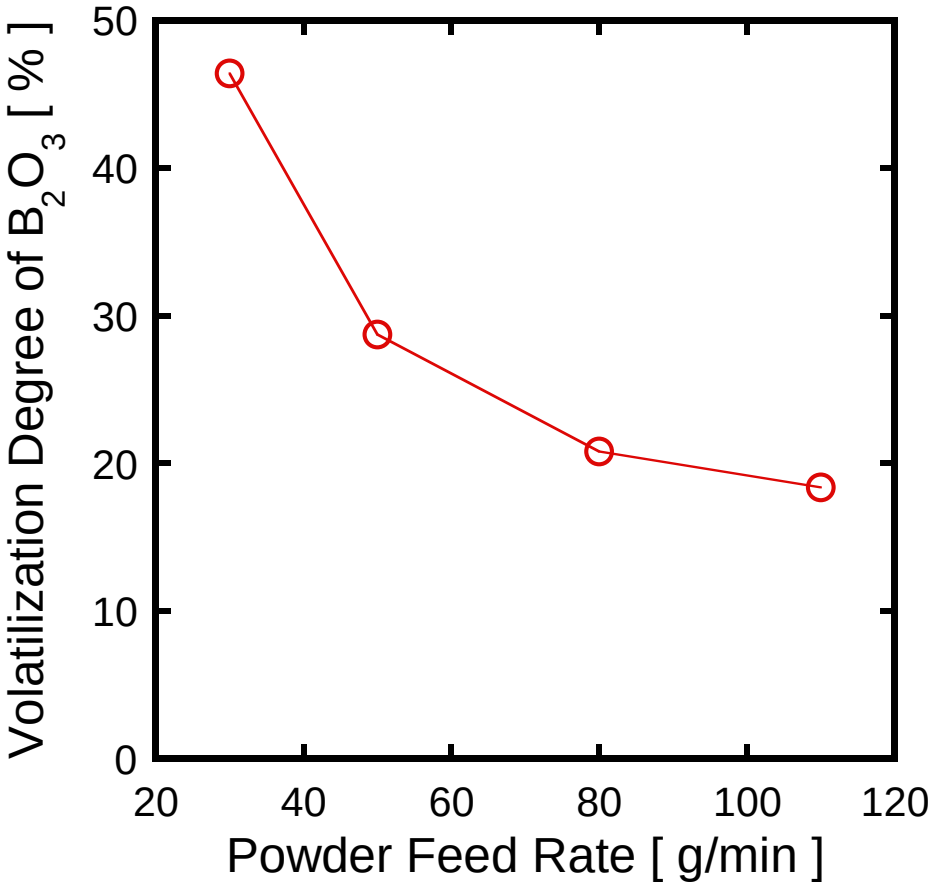

Fig. 5.7 Effect of powder feed rate on B_2O_3 volatilization of melted alkali-free glass particles by multi-phase AC arc with CW pattern

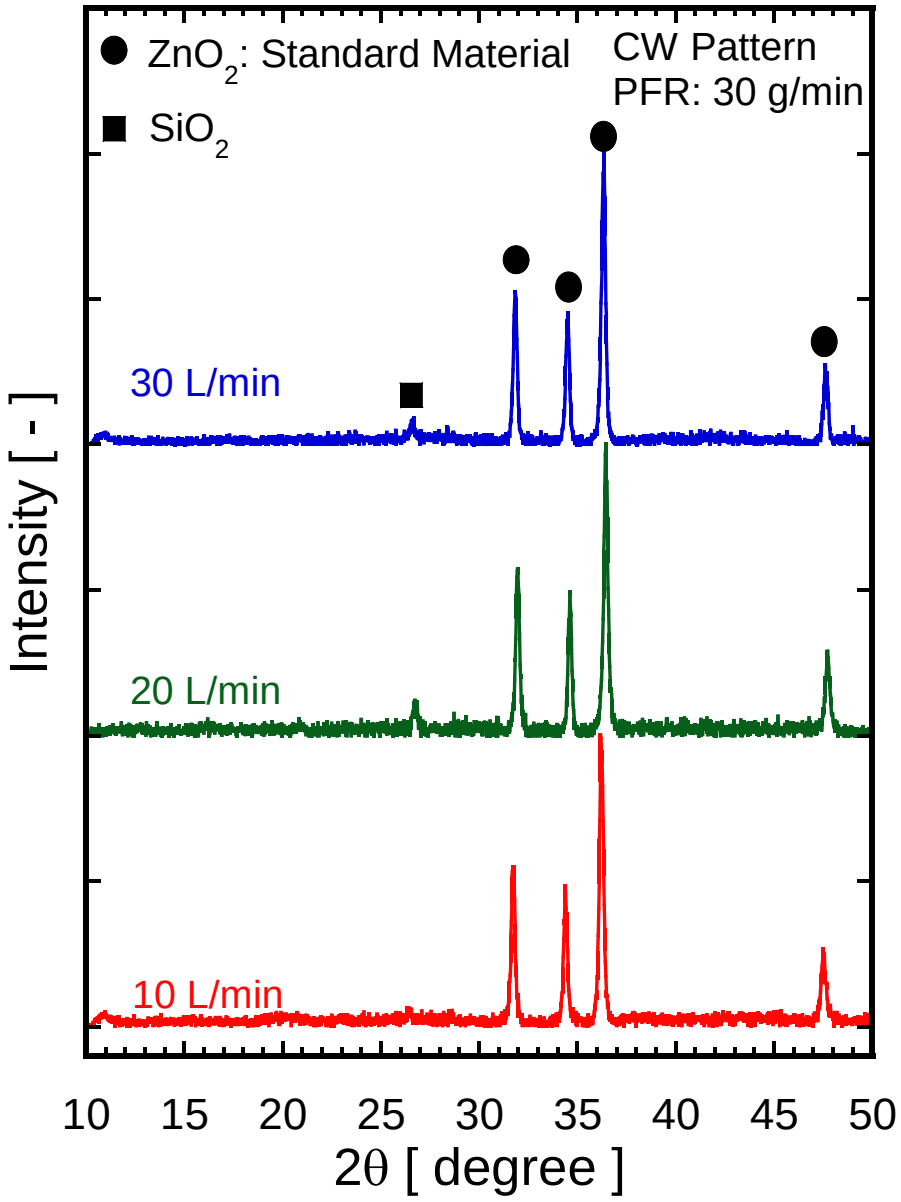

Fig. 5.8 XRD patterns of melted alkali-free glass particles by multi-phase AC arc with CW pattern at different carrier gas flow rates

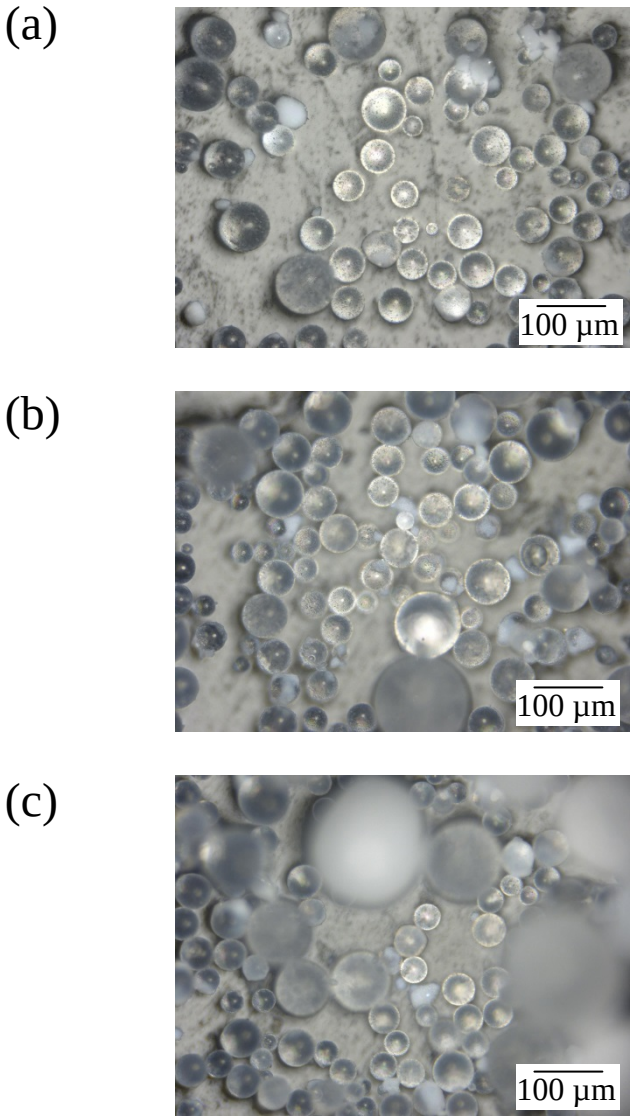

Fig. 5.9 Microscope images of melted alkali-free glass particles by multi-phase AC arc with CW pattern at different carrier gas flow rates: (a) 10 L/min, (b) 20 L/min and (c) 30 L/min

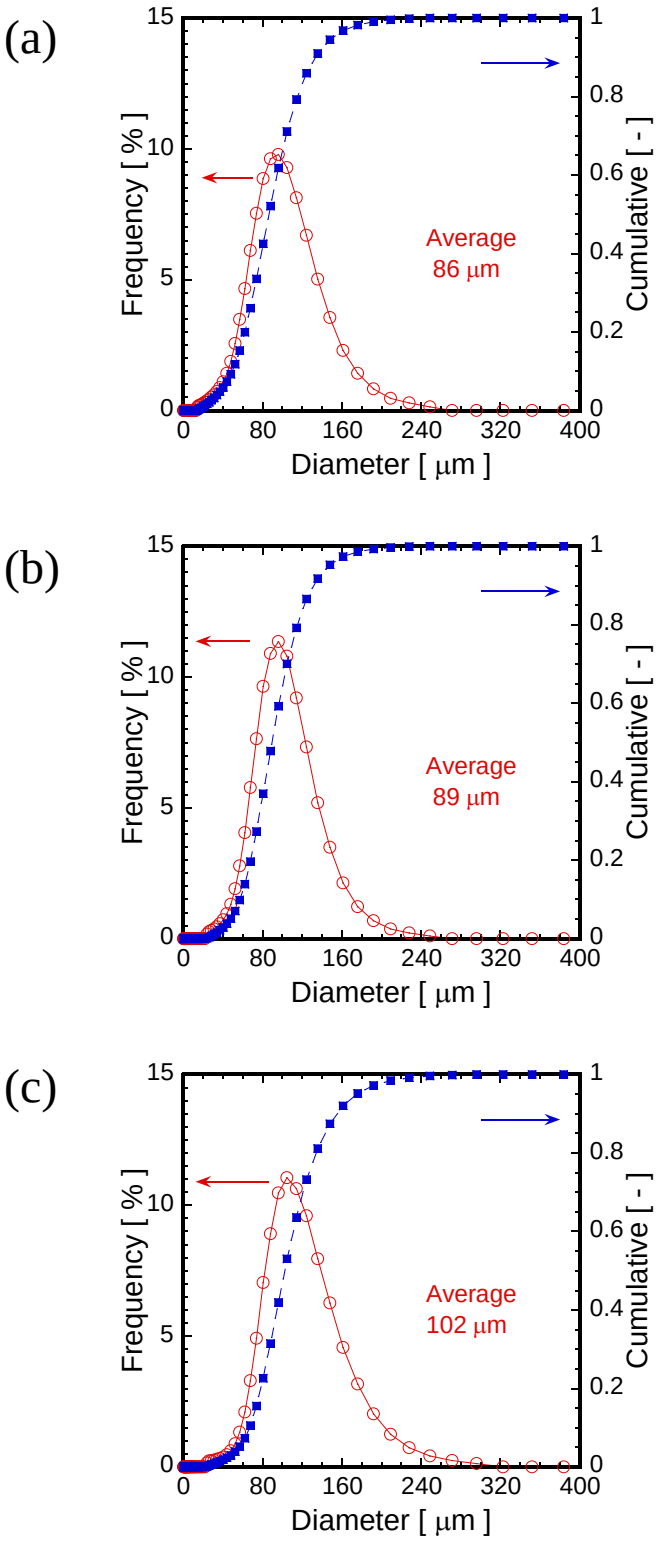

Fig. 5.10 Particle size distributions of melted alkali-free glass particles by multi-phase AC arc with CW pattern at different carrier gas flow rates: (a) 10 L/min, (b) 20 L/min and (c) 30 L/min

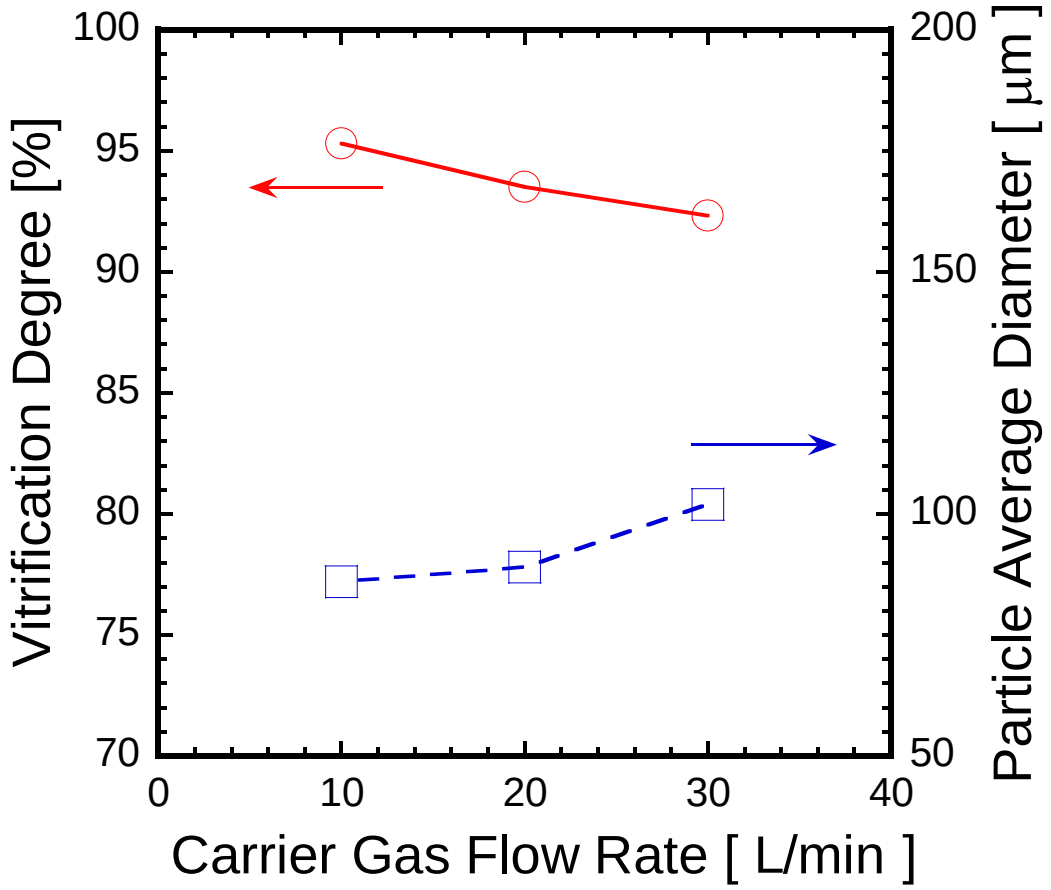

Fig. 5.11 Effect of carrier gas flow rate on vitrification degree and particle average diameter of melted alkali-free glass particles by multi-phase AC arc with CW pattern

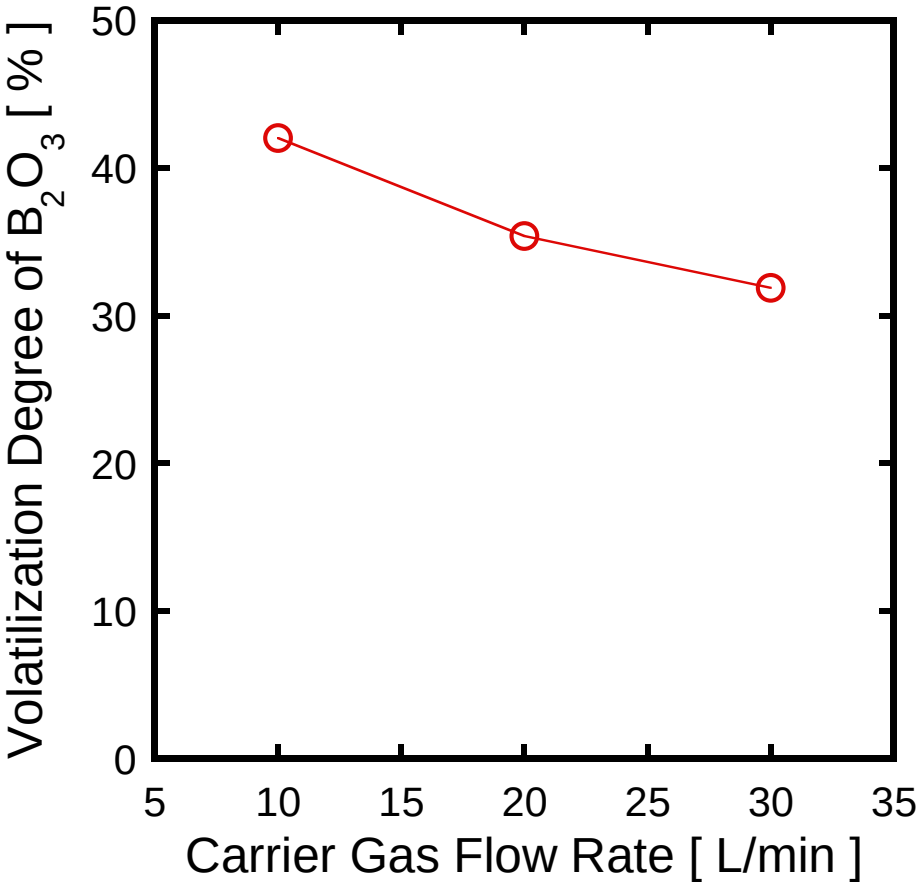

Fig. 5.12 Effect of carrier gas flow rate on B_2O_3 volatilization of melted alkali-free glass particles by multi-phase AC arc with CW pattern

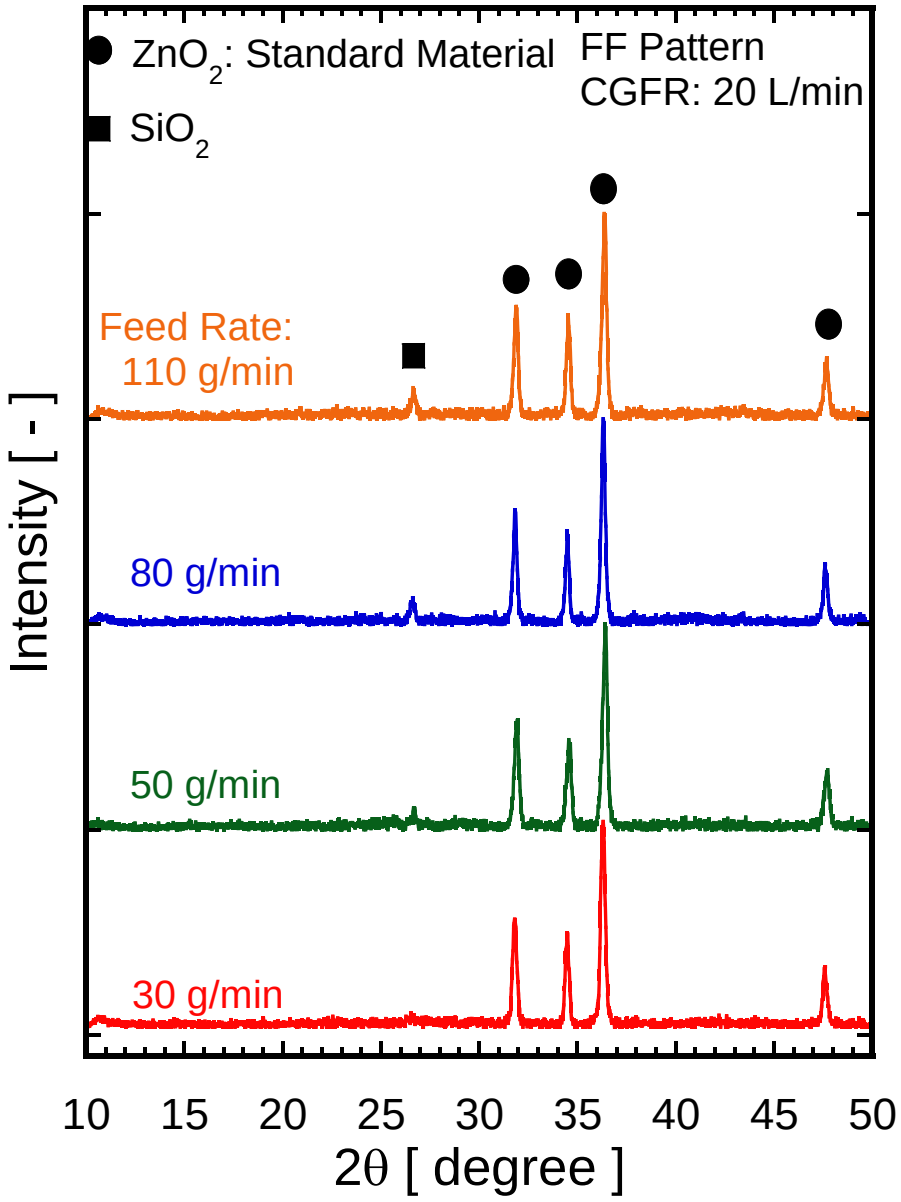

Fig. 5.13 XRD patterns of melted alkali-free glass particles by multi-phase AC arc with FF pattern at different powder feed rates

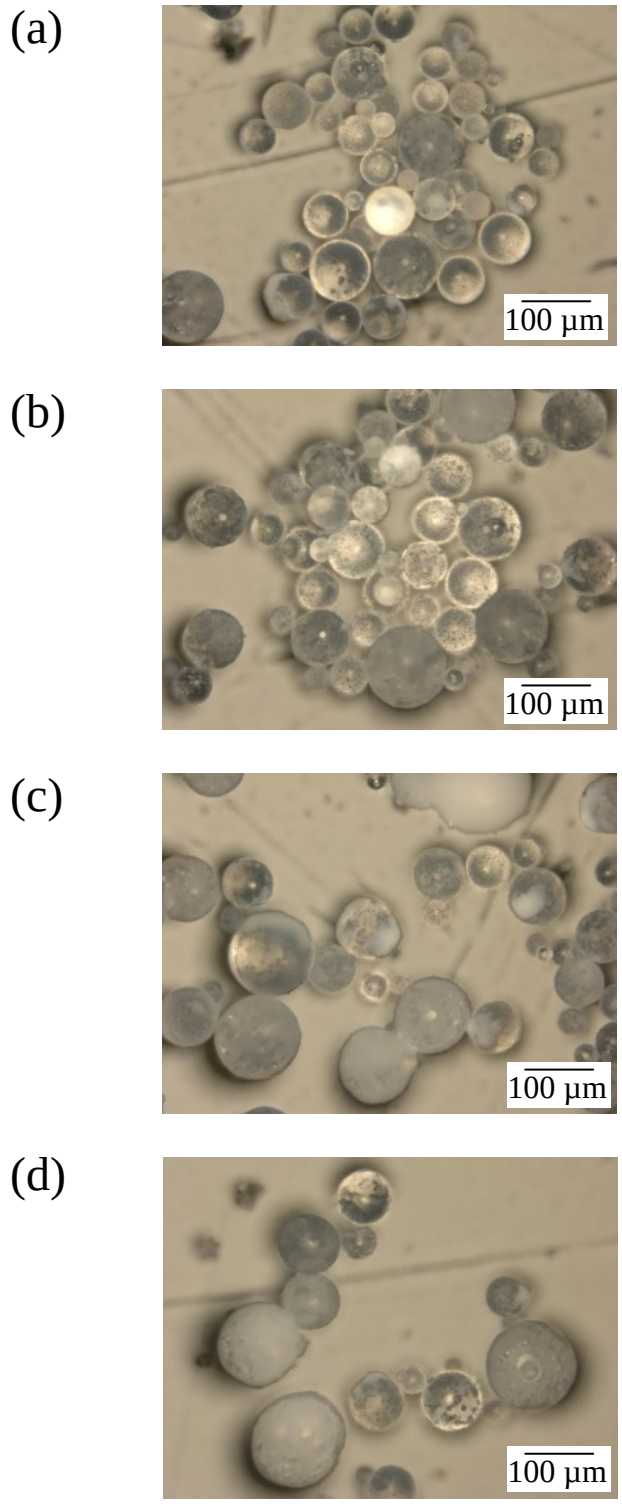

Fig. 5.14 Microscope images of melted alkali-free glass particles by multi-phase AC arc with FF pattern at different powder feed rates: (a) 30 g/min, (b) 50 g/min, (c) 80 g/min and (d) 110 g/min

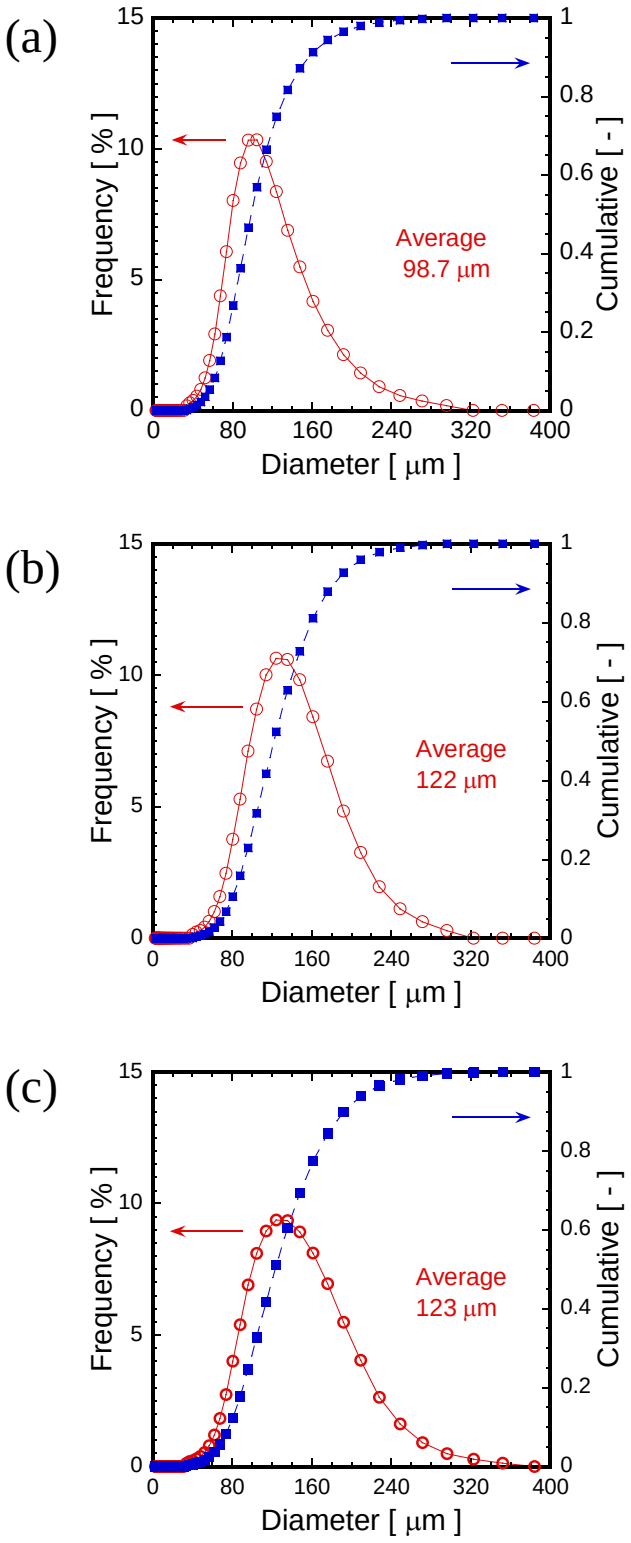

Fig. 5.15 Particle size distributions of melted alkali-free glass particles by multi-phase AC arc with FF pattern at different powder feed rates: (a) 30 g/min, (b) 50 g/min and (c) 80 g/min

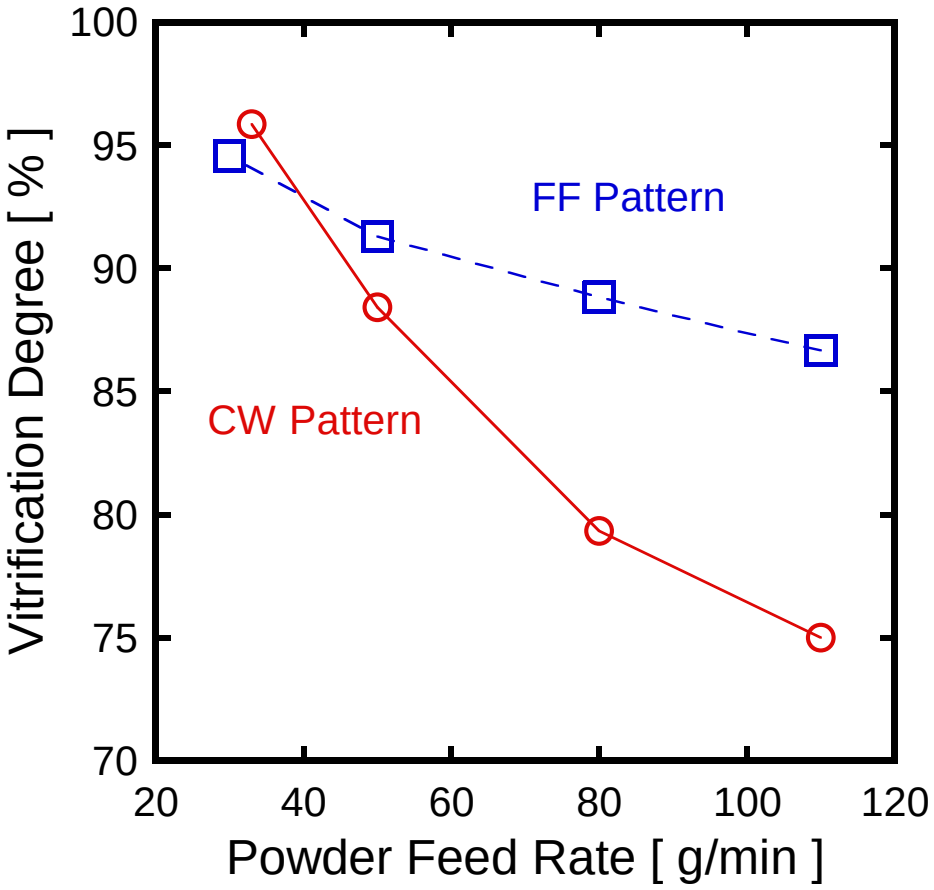

Fig. 5.16 Effect of electrode configuration on vitrification degree of melted alkali-free glass particles by multi-phase AC arc at different powder feed rates

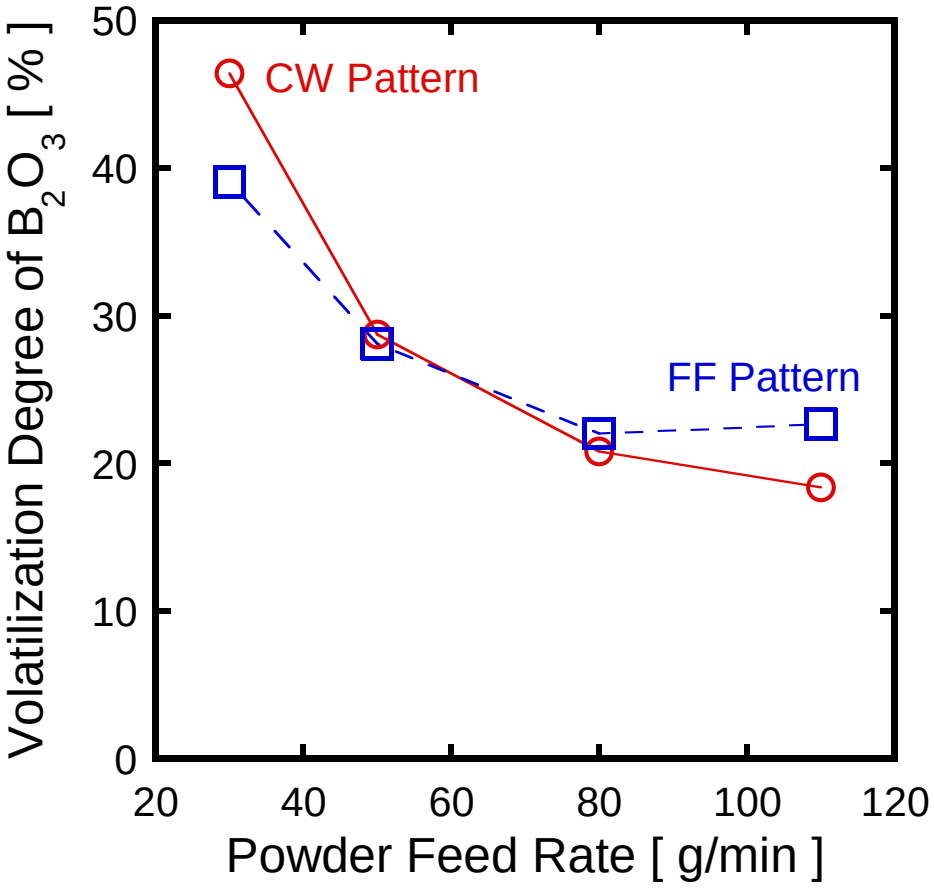

Fig. 5.17 Effect of electrode configuration on B_2O_3 vitrification of melted alkali-free glass particles by multi-phase AC arc at different powder feed rates

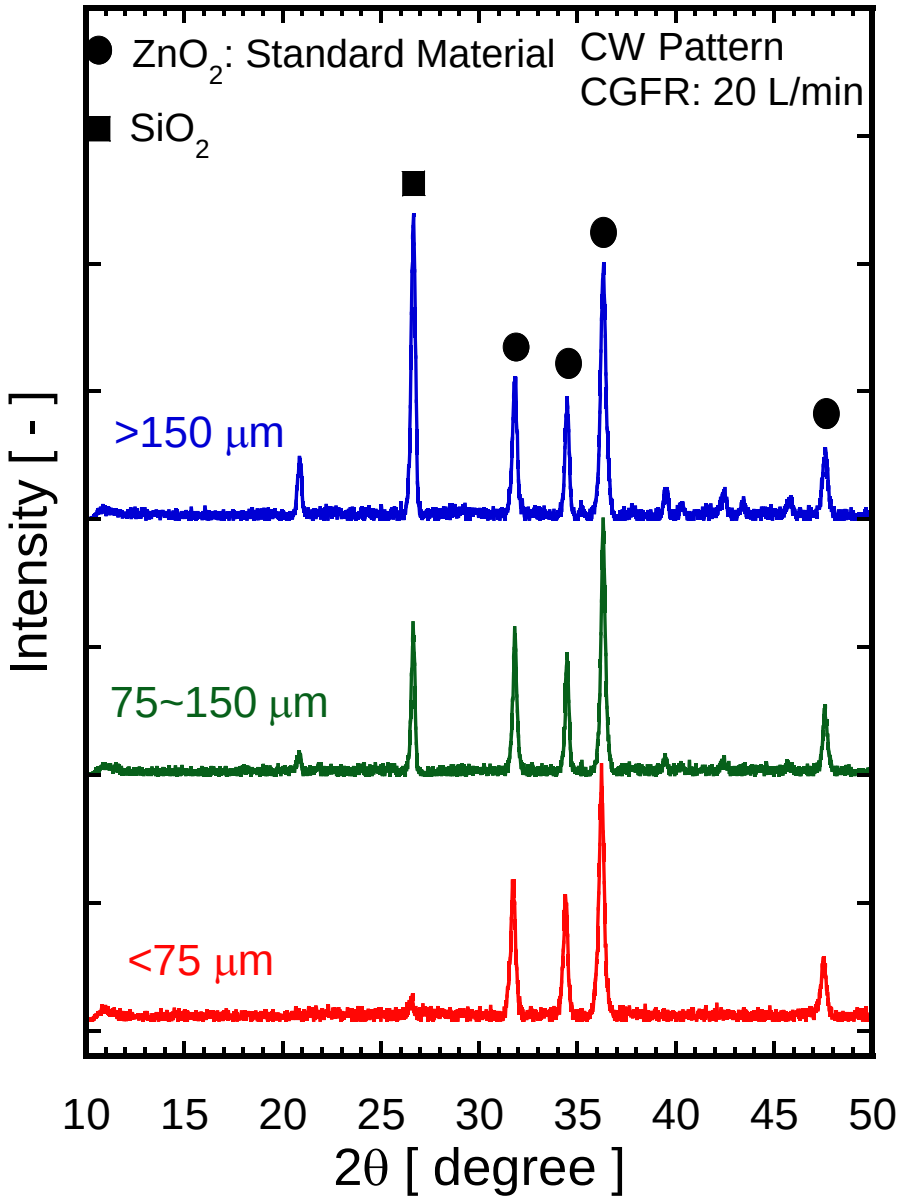

Fig. 5.18 XRD patterns of melted alkali-free glass particles by multi-phase AC arc in CW pattern with different sieved sizes

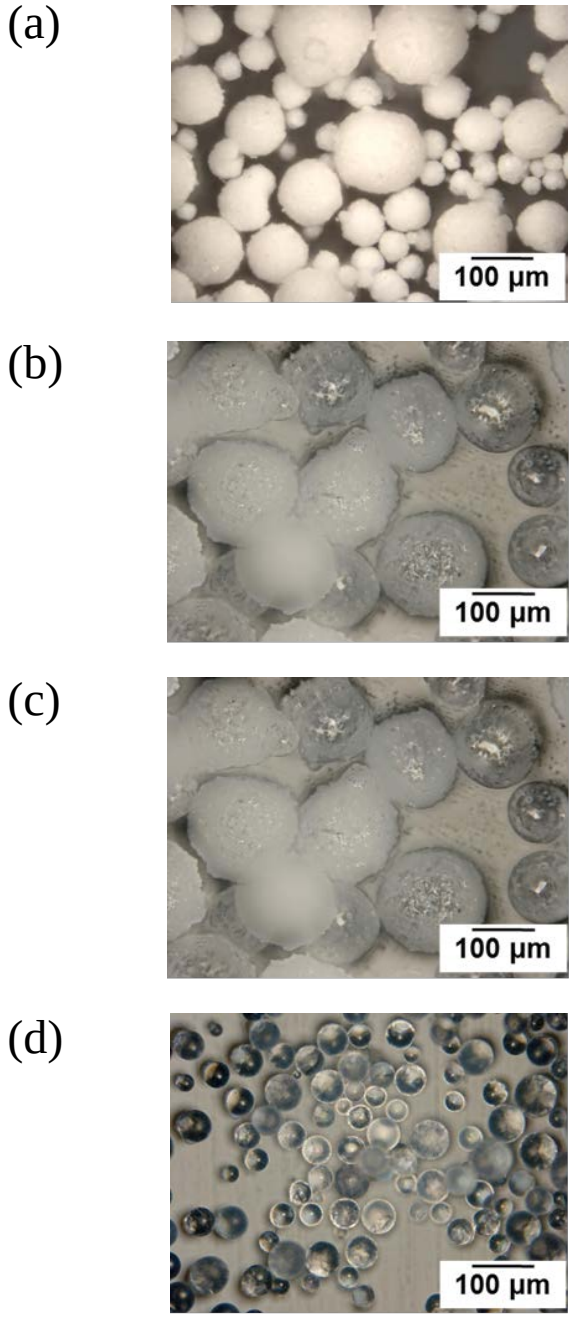

Fig. 5.19 Morphology of (a) raw alkali-free glass particles, and melted particles with different sieved sizes of (b) >150 μm, (c) 75~150 μm and (d) <75 μm

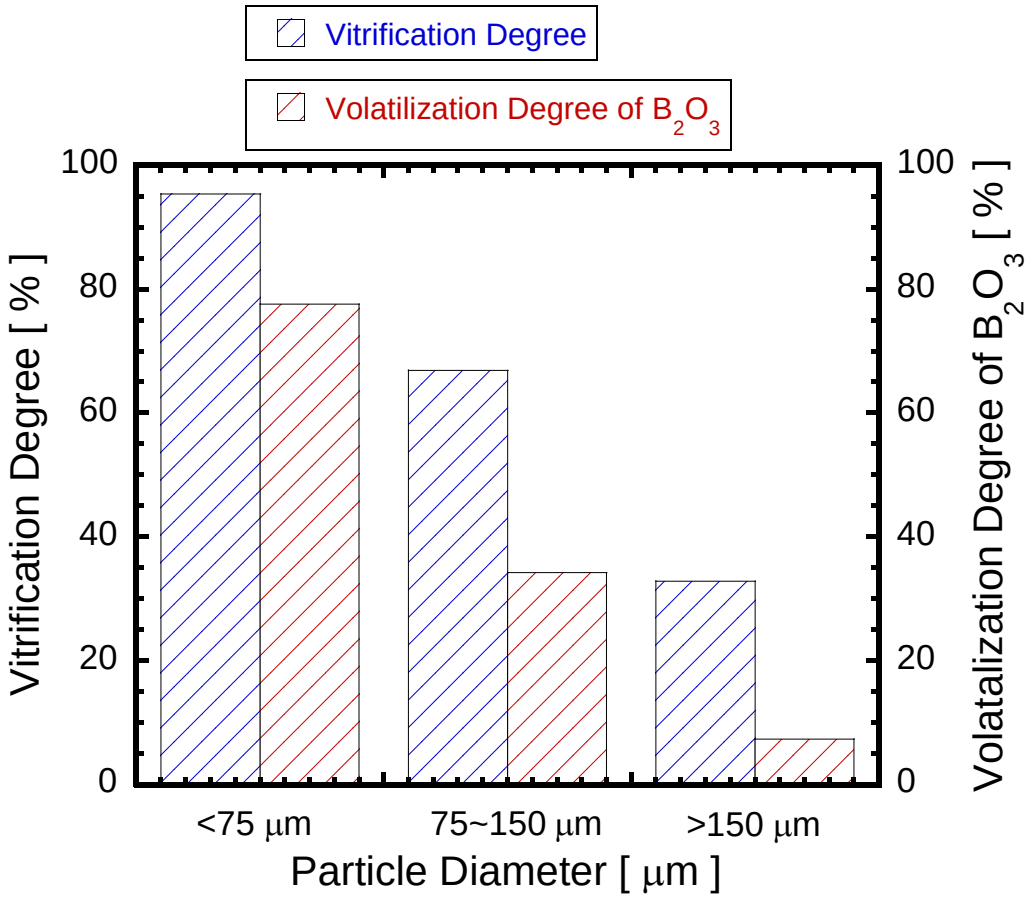

Fig. 5.20 Effect of particle size on vitrification degree and volatilization degree of B_2O_3

6. Comparison of Melting Behavior of Glass Powders by Multi-Phase AC Arc and Hybrid Plasmas

The 12-phase AC arc provides the higher plasma temperature with larger volume and longer residence time that is advantageous to the in-flight glass melting process. Chapter 5 has reported the granulated raw materials been injected into the plasma region and vitrified within milliseconds. Different parameters on the powder homogeneity treatment were discussed. Results showed that the temperature and residence time are the two most important factors during in-flight melting treatment, thus they depend the glass vitrification, volatilization and glass composition as well. For the multi-phase AC arc, the most effective way to control of the high-temperature region is using different electrode configuration. The approach to govern the residence time is to regulate the carrier gas flow rate. In this chapter, a hybrid heating method combined with the oxygen burner and the multi-phase AC arc to enhance the melting of glass materials was proposed. It offers another possibility to control the high temperature and residence time of the heat source. The experiments results using this so-called “hybrid plasmas” were compared with the multi-phase AC arc. Furthermore, the effect of primary size of SiO_2 in the raw material on the melting process was investigated. The different melting behaviors due to the high temperature region and residence time in the two heat sources were discussed.

6.1 Introduction

The research results acquired in the past three years indicates that the multi-phase AC arc has been successfully applied to melt the granulated glass materials. Improvement of the experimental setup such as analysis of electrode erosion mechanism (Tanaka et al. 2013a, b) and arc stability (Tanaka et al. 2011a) achieved a more in-depth understanding of multi-phase AC arc system. This is also allowed to obtain a more stable multi-phase AC arc. As been introduced in Section 1.2.2, the oxygen burner can be combined with a multi-phase AC arc to enhance the melting of glass materials according to the project proposal. The heating method called “hybrid plasma” combines multi-phase AC arc with oxygen burner is expected to improve glass quality and increase productivity with minimum energy consumption. This hybrid plasmas aims at exploiting the benefits of both heating sources of multi-phase AC arc and oxygen burner. It has the advantages of both high temperature and long residence time approved to be a better heat source in the future. The technology has not been fully researched due to the development of multi-phase AC arc in the past few years. Although previous researches revealed that the hybrid plasma can melt granulated glass raw materials during in-flight processing (Tanaka et al. 2011b; Liu et al. 2011), the in-flight melting behavior of the glass particles, especially alkali-free glass, by the hybrid plasma has not been sufficiently understood yet. This chapter will give the latest research results of in-flight melting by hybrid plasmas and its comparison with multi-phase AC arc. The in-flight particle diagnostics in the hybrid plasma system conducted by DPV-2000 as well as high-speed camera were firstly presented. The effects of different heat sources, the primary SiO_2 size in the raw material, the powder feed rate on the melting behaviors were investigated. The particle morphology, the size distribution, the particle vitrification degree and the volatilization degree were given out.

6.2 Experimental

6.2.1 Experimental of Setup

The schematic illustration of the in-flight melting by hybrid plasma apparatus is shown in Fig. 6.1. It combines a multi-phase AC arc plasma reactor with an oxygen burner installed above the furnace chamber. The combustion energy of oxygen burner was 9 kW. Raw materials of glass powders were supplied with carrier gas flow rate of 20 L/min by the powder feeder (5MPE Series, Sulzer Metco). A tube was connected between the exit of the powder feeder and the oxygen burner. The exit of the feeder nozzle of the burner has a diameter of 5.5 mm and a distance of 300 mm over the upper electrode level. The schematic of the in-flight melting by multi-phase AC arc is the same with Chapter 5. The exit of the feeder nozzle has a diameter of 3.8 mm and a distance of 150 mm over the upper electrode level.

6.2.2 Oxygen Burner

The photograph of the oxygen burner is shown in Fig. 6.2. The schematic of nozzle tip of oxygen burner is illustrated in Fig. 6.3 which consists of a nozzle with cooling water, fuel, oxygen and powder feeding system. Propane (C_3H_8) was used as the fuel. The flow rates of C_3H_8 gas, the primary oxygen and the secondary oxygen were 6, 6, and 24 L/min, respectively. The oxygen is divided into two lines in order to easily control the length and radial expansion of the oxygen flame. There are several types of nozzle with different oxygen gas injection angles. The nozzle type used in this chapter is direct parallel flow of the primary and second oxygen gas.

6.2.3 Raw Materials

The raw materials of alkali-free glass were supplied by Asahi Glass Co., Ltd., Japan. The

components of the raw material were prepared from SiO_2, H_3BO_3, Al_2O_3, and $BaCO_3$ by spray dry method as shown in Fig. 6.4. Two kinds of the granulated raw materials were prepared from SiO_2 particles with different sizes (7~8 μm and 1~2 μm). There morphologies taken by microscopy are shown in Figs. 6.5 and 6.6, respectively. The compositions of the raw materials are given in Tables 6.1 and 6.2, respectively. The particle size distributions of raw materials with primary SiO_2 size of 7~8 μm and 1~2 μm are shown in Figs. 6.7 and 6.8, respectively. The average diameters of these granulated raw materials were 114 μm and 105 μm, respectively.

6.2.4 In-Flight Particle Measurement

Figure 6.9 shows the schematic of the hybrid plasma apparatus with particle measurement system by DPV-2000 and spectroscopy. The particle diagnostic system and analysis method are the same with explained in the Chapter 3. The experimental conditions are given in Table 6.3. Alkali-free glass raw material with primary SiO_2 size of 7-8 μm was used for measuring.

The schematic illustration of the hybrid plasma apparatus with particle measurement system by high-speed camera is shown in Fig. 6.10. The experimental conditions for in-flight particle measurement by high-speed camera in hybrid plasma system are given in Table 6.4. The effect of the carrier gas flow rate on the particle temperature fluctuation was investigated. The temporal characteristics of the in-flight particles are conducted by a high-speed camera (Photron, FASTCAM SA WTI, Japan). As the background of the plasma with oxygen burner is so bright that the particle thermal emission is weak to be recorded by the camera. Figure 6.11 shows the emission line spectrum of hybrid plasma with powder injection. The band-pass filters were selected at 785±5 and 880±5 nm for the left and right. In the hybrid plasma system, the camera was set at a rate of 5000 frames/s with the shutter speed of 200 μs. The oscilloscope (Yokogawa,

ScopeCorder DL850, Japan) recorded at a sampling rate of 10^6 Hz.

6.2.5 Experimental Conditions

The experimental conditions for powder treatment by hybrid plasmas are given in Table 6.5. The electrode configuration in hybrid plasma condition is CW pattern and electrode distance is 80 mm to decrease the instability. Tungsten electrode diameter of 3.2 mm is used due to its lower re-ignition voltage than 6 mm. Two different raw materials are used for comparison. The powder feed rates are varied at 30, 50, 80, 100 and 150 g/min. Table 6.6 shows the experimental conditions for powder treatment by multi-phase AC arc. The arc discharge conditions are the same with hybrid plasma except of no use of oxygen burner. Powders are injected into the plasma at feed rates of 30, 50, 80, 130 and 150 g/min through the feeder.

6.2.6 Experimental Procedures

The experimental procedure with multi-phase AC arc is the same as already explained in Section 5.2.4. The experiments with hybrid plasma system are shown in the following.

- Preparation of oxygen burner

1) Flow the cooling-water of burner and put in the breaker of the operator control panel of flow meter for oxygen burner.
2) Open the gas cylinder of the oxygen gas and regulate the pressure to 0.8 MPa.
3) Open the gas cylinder of the nitrogen gas and regulate the pressure to 0.1 MPa.
4) Open the gas cylinder of the propane gas and regulate the pressure to 0.1 MPa.

- Arc generation
- Oxygen burner ignition

Introduce the primary, secondary oxygen and propane gas into the burner at the same time.

Regulate the flow meter until the gas feeding at 6, 6, and 24 L/min, respectively.

- Powder injection

  The powder feeding time is depend on the powder feed rate. Considering of the recovery rate, the total weight of powder feeding is usually controlled at 400~500 g.

- Stop the powder feeding
- Stop arc discharge
- Stop oxygen burner

1) Stop the propane gas flow immediately.
2) Introduce the nitrogen gas flow into the burner to eliminate the flame and remove the propane gas remained in the tube.
3) Stop the nitrogen gas flow.
4) Stop the oxygen gas flow.

6.3 Experimental Results

6.3.1 In-Flight Particle Measurements in Hybrid Plasmas

(a) Particle Characteristics by DPV-2000

In our experiment, the lens of the DPV-2000 was placed at a constant position so it only focused on the small measurement volume (about 1 mm^3) of the center. The measurement procedure and particle characterization principles have already been presented in Chapter 3. Figures 6.12 (a) and (b) show the particle velocity distributions estimated by DPV-2000 in hybrid plasma and multi-phase AC arc, respectively. The particle initial velocity is expected to be higher in the hybrid plasma due to the gas flow of oxygen and propane. However, the nozzle diameter of oxygen burner is 5.5 mm, which is larger than the powder feed nozzle used in multi-phase AC arc. The distance from the nozzle exit to the electrode level is longer than in the

case of multi-phase AC arc. The result shows mean velocities are 10 m/s and 9 m/s in hybrid plasma and multi-phase AC arc, respectively.

Figure 6.13 presents particle surface temperature distribution obtained from DPV-2000 in hybrid plasma and multi-phase AC arc. As the particle velocity in hybrid plasma is little higher thus decrease the residence time in the plasma region, the measured temperature is about 2350 K, little lower than the multi-phase AC arc. However, the particle diagnostic by DPV-2000 in hybrid plasma system is rather difficult compared with multi-phase AC arc. The visibility of the radiative signal by particles is relatively weak due to the strong intensity of the background. Therefore, it takes much time to obtain sufficient “good signal” of in-flight particles.

(b) Particle Characteristics by High Speed Camera

A sample of dual image recorded by high-speed camera in hybrid plasma is shown in Fig. 6.14. The calculated range of the image was 200×200 pixels which corresponding to the real size of 11×11 mm^2. In a single measurement, up to 1051 images of particle streaks can be acquired. The high speed image process for calculating the particle surface temperature can be found in Section 4.2.5. Considering for the particle velocity and an appropriate estimation, every five images (represent for 1 ms) were calculated to obtain the average temperature value of particles. Since the fluctuation period of multi-phase AC arc is evaluated as about 20 ms, the total calculated time for particle temperature was over five periodic cycles of 100 ms.

Figure 6.15 shows the effect of carrier gas flow rate on the particle average temperature and velocity estimated by high-speed camera in hybrid plasma. The particle velocity is mostly dependent on the carrier gas flow rate. The particle velocity varied from 7.6 to 9.0 m/s, indicated that the carrier gas flow does not change the velocity much compared to the multi-phase AC arc (Fig. 3.20). This is because the nozzle exit of burner has a larger diameter

than the powder feeder nozzle, thus the influence was not significant. The temperature of particles decreased due to shorter residence time in plasma region.

Figure 6.16 presents the temperature fluctuation and average value under different carrier gas flow rate measured by high-speed camera in hybrid plasma. Each point was obtained from calculation the average of all the particles over five images. The calculated average temperature is about 2750, 2480 and 2300 K in accordance to the carrier gas flow rate of 10, 20 and 30 L/min.

Moreover, a gradual decrease in the periodicity of fluctuation as a function of carrier gas flow rate can be understood by considering their Fourier amplitude spectra, which is shown in Fig. 6.17. The particle temperature exhibited a principle periodicity of 100 Hz that caused by the fluctuation of multi-phase AC arc. The amplitude of the frequency at 100 Hz was the largest with carrier gas flow rate at 10 L/min, indicating the particle residence time in the plasma was comparable to the plasma fluctuation time. In a result, particles were affected by the plasma fluctuation. In addition, the periodicity decreased with increasing the carrier gas flow rate, which is different in the case of multi-phase AC arc (Fig. 4.10). When the carrier gas flow rate increased to 30 L/min, the particles had velocity of about 9 m/s. However, due to the high speed flow of oxygen burner, the periodicity of arc discharge seems to be affected by the burner flame. Thus the surface temperature is difficult to reflect the periodical characteristics from the plasma.

The in-flight particle measurement in hybrid plasma system was conducted by DPV-2000 and high speed camera. The obtained particle temperature values are in good agreement by the two diagnostic methods. The in-flight particle diagnostics in the hybrid plasmas showed more accurate data obtained by high speed camera with band-pass filters. On the other hand, the DPV-2000 measurement was found to be difficult because of the strong emission from the plasma and oxygen burner. The measured particle velocity was little higher

than that in the multi-phase AC arc due to higher gas flow rate.

6.3.2 Effect of Different Heat Sources on the Glass Melting Behavior

Figure 6.18 give the XRD patterns of raw materials and quenched powders treated by multi-phase AC arc and hybrid plasma at a feed rate of 30 g/min. The intensity of the SiO_2 peak indicates the vitrification process. Compare with the two different heat sources, the pattern without any peaks except of the standard material treated by hybrid plasma reveals that the powders are the whole amorphous structure.

Figure 6.19 shows the optical micrograph images of the glass raw material (a) and the particles with primary SiO_2 size of 7-8 μm after in-flight heat treatment by multi-phase AC arc (b) and hybrid plasma at powder feed rate of 30 g/min (c). While the glass raw materials have bumpy shape and no optical transparency, the melted particles have spherical shape and optical transparency, which indicates the raw materials were well-vitrified during the in-flight heat treatment. Moreover, there are still some unmelted particles can be found after melting by multi-phase AC arc. This is consistent with the above diffraction peak analysis that the reaction between crystal SiO_2 with other components is not completed inside the particles. However, the particles melted by hybrid plasma have smooth surface and transparent structure.

The particle size distributions of the melted particles by different heat sources with powder feed rate at 30 g/min are presented in Fig. 6.20. The particles after melting shrank due to high porosity of the raw materials and the decomposition of carbonate during vitrification reaction. The average particle size treated by hybrid plasma is smaller than that of multi-phase AC arc.

The total input energy of the hybrid plasma is higher than that of multi-phase AC arc as the energy of the oxygen burner is included. To compare two different heat sources equally, the

relationship between the input energy per unit weight of the raw materials and the vitrification degrees of the powders melted by the multi-phase AC arc and the hybrid plasma are presented in Fig. 6.21. The vitrification degree of the powders melted by the hybrid plasma is obviously higher than that of the multi-phase AC arc. This is because the residence time in the hybrid plasma heat treatment would be longer than that in the multi-phase AC arc treatment due to the oxygen flame, which has longer high temperature region than that of the multi-phase AC arc. Consequently, the obtained results indicated that the chemical reactions inside the particles were more effectively in the hybrid plasma than the multi-phase AC arc.

The chemical compositions of the melted powders by hybrid plasma with different powder feed rates are shown in Table 6.7, while the result in the multi-phase AC arc is given in Table 6.8. The estimation of volatilization degrees indicated that the only volatilization of B_2O_3 was not ignorable whereas volatilizations of other components were ignorable. Therefore, volatilization of B_2O_3 is focused. Figure 6.22 shows the relationship between the input energy and the volatilization degree of B_2O_3 As well as the vitrification degree, the volatilization degree of the powders melted by the hybrid plasma is higher than the particles treated by the multi-phase AC arc.

The volatilization of B_2O_3 from the in-flight melted glass powders is desired to be decreased together with the higher vitrification degree. Figure 6.23 shows the relationship between the vitrification degree and the volatilization degree of the powders after heat treatment by different heat sources. Increasing the vitrification degree leads to the higher volatilization degree, resulting from the increase of the energy transfer from the heat sources to the particles. The hybrid plasma heating leads to the lower volatilization degree than the multi-phase AC arc in the case with the same vitrification degree. This is because the different temperature history and the residence time between the hybrid plasma and the multi-phase AC arc heating.

The vitrification and volatilization reflect the reaction rate and the mass transfer rate inside the particles respectively, and they should have different correlations with the temperature of particles. In the hybrid plasma treatment, the particles are firstly heated by the burner flame before they enter the high temperature plasma zone. The particles experience low temperature heating and short residence time in the burner flame. These would be the differences between the hybrid plasma treatment and the multi-phase AC arc treatment. Therefore, it must be important to control the temperature history and the residence time of particles for the in-flight melting method. Considering the different characteristics of the multi-phase AC arc and the oxygen burner, it is expected to decrease the power of the multi-phase AC arc as well as enlarge the heating region of the oxygen burner. This can be realized by increasing the power or changing the height position of the burner.

6.3.3 Effect of Primary SiO_2 Size on the Glass Melting Behavior

Figure 6.24 shows the XRD patterns of the melted particles with different primary SiO_2 sizes treated by hybrid plasma at feed rate of 150 g/min. When using small primary size of SiO_2 raw material, the homogeneous reaction in the particles is almost completely even under a high feed rate of powder. The smaller size of SiO_2 leads to the higher degree of mixing of raw materials, and this situation can cause the rapid transformation from the granulated raw materials to the uniformly vitrified products.

Figure 6.25 shows the microscope images of melted particles corresponding to the XRD results. The quenched particles used raw materials of larger primary SiO_2 size still contain some proportion of partly melted particles. While the using of smaller primary SiO_2 size leads to well melted particles for majority. Figure 6.26 illustrates the particle size distribution of quenched particles treated by hybrid plasma using different raw materials. The average diameter obtained

from the smaller primary sizes of SiO_2 is about 93 μm, which is smaller than that of larger primary sizes of SiO_2.

Figure 6.27 shows the relationship between the input energy and the vitrification degree of the melted powders by the hybrid plasma for different primary sizes of SiO_2. The vitrification degrees of the melted powders from the both raw materials with larger and smaller SiO_2 were more than 90% in the range of the input energy more than 50 kJ. Contrastingly, it is notable that the vitrification degree of the powders with smaller primary size of SiO_2 was still more than 90% in the range of the input power less than 50 kJ, while that with larger SiO_2 drastically decreased with decreasing the input energy. This result suggests the smaller size of SiO_2 leads to the higher reaction rate than larger primary SiO_2 due to the rapid transformation from the granulated raw materials to the vitrified products.

Table 6.9 gives the chemical compositions of quenched particles treated by hybrid plasma using primary SiO_2 size of 1-2 μm. The relationship between the input energy and the volatilization degree of B_2O_3 by hybrid plasma for different sizes of primary SiO_2 particles is presented in Fig. 6.28. The volatilization degrees of B_2O_3 of 7-8 μm SiO_2 is higher than that of 1-2 μm SiO_2. This is because the volatilization of B_2O_3 was mainly occurred at the surface of primary B_2O_3 which was introduced from the reagent of H_3BO_3. The B_2O_3 vapor diffuses through the initial voids between the primary particles in the granulated powders. If the larger sizes of the primary SiO_2 are used, the voids between the raw materials become larger due to geometrical reason. Then the diffusivity of the B_2O_3 vapor becomes larger.

Fig. 6.29 shows the relationship between the vitrification degree and the volatilization degree of the melted powders by hybrid plasma heating for different sizes of primary SiO_2. Smaller size of primary SiO_2 leads to higher vitrification degree than larger one in the case with the same volatilization degree. This is because the primary size of SiO_2 is important on the

reaction rate inside the individual particles during the in-flight melting process as discussed in previous paragraph.

The obtained results indicate that the optimization of the particles size and the primary size of the species (SiO_2) must be important to produce well-vitrified glass without excessive volatilization of the species during in-flight melting heat-treatment, as well as the optimization of the temperature history and the residence time by the improvement of the hybrid plasma-heating system.

6.4 Discussion

In 12-phase AC arc, the phase transition time was 1.67 ms from one electrode to next one and takes 20 ms for a periodic cycle. Although the multi-phase AC arc has the merit of high temperature, there is a possibility that some particles cannot receive enough energy from the plasma due to the short residence time in the high temperature region. The oxygen burner with 9 kW can preheat the raw materials in a low temperature as well as enlarge the particle residence time in the flame. The temperature and residence time are the two most important factors during in-flight melting treatment, thus they depend the glass vitrification, volatilization and glass composition as well. In a word, the objective in the in-flight melting technology is to produce high vitrification with low volatilization degree under the same energy cost for unit weight of the raw materials. The hybrid plasma can increase adjustable parameter than just using multi-phase AC arc to control the high-temperature region and residence time of particles. It is expected as a promising technology for application in the in-flight melting process. The multi-phase AC arc with different electrode configuration combined with oxygen burner under appropriate condition can produce the desired glass particles in diverse needs.

6.5 Conclusion

This chapter introduced a more efficient heating source as the hybrid plasma. The in-flight melting experiments were conducted by comparing the two methods. The melted particle properties in different heat sources are compared from the particle morphology, the size distribution, the vitrification and the volatilization degree. The obtained results are summarized as follows.

1) The in-flight particle diagnostics in the hybrid plasma system showed more accurate measurement data were obtained by high-speed camera with band-pass filters than DPV-2000. Results indicated that under conditions of powder feed rate at 30 g/min with carrier gas flow rate of 20 L/min, the particle velocity was 10 m/s with the surface temperature of about 2480 K. The velocity was little higher than that in the multi-phase AC arc.
2) The comparison between the different heat sources suggested the hybrid plasma heating leads to higher vitrification degree than the multi-phase AC arc in the case with the same volatilization degree.
3) The comparison between the different primary sizes of SiO_2 in the granulated raw materials indicated that the primary SiO_2 greatly affect to the vitrification and volatilization during in-flight melting process. The optimization of the particle size and the primary SiO_2 size would be important to melt the glass in-flight processes.
4) The vitrification and volatilization reflect the reaction rate and the mass transfer rate inside the particles respectively. The optimization of the balance between the multi-phase AC arc and the oxygen burner is promising to produce glass powders with high vitrification as well as low volatilization degree.

References

Liu, Y., Y. Tsuruoka, M. Tanaka, T. Ichihashi, T. Yano and T. Watanabe. “In-flight Melting Behavior of Different Glass Raw Materials by Hybrid Heating of Twelve-Phase AC Arc with Oxygen Burner.” *Thin Solid Films* **519** (20), 7005-7008 (2011).

Tanaka, M., Y. Tsuruoka, Y. Liu, T. Matsuura and T. Watanabe. “Stability Analysis of Multi-Phase AC Arc Discharge for In-Flight Glass Melting.” *Current Applied Physics* **11** (5), S35-S39 (2011a).

Tanaka, M., Y. Tsuruoka, Y. Liu and T. Watanabe. “Investigation of In-Flight Melting Behavior of Granulated Glass Raw Material by Multi-Phase AC Arc Plasma and Hybrid Plasma.” *IOP Conference Series: Materials Science and Engineering* **18**, 112010 (2011b).

Tanaka, M., T. Ikeba, Y. Liu, S. Choi and T. Watanabe. “High-Speed Visualization of Electrode Erosion in Multi-Phase Alternating Current Arc.” *Journal of Fluid Science and Technology* **8** (2), 160-171 (2013a).

Tanaka, M., T. Ikeba, Y. Liu, S. Choi and T. Watanabe. “Investigation of Electrode Erosion Mechanism of Multi-Phase AC Arc by High-Speed Video Camera.” *Journal of Physics: Conference Series* **441**, 012015 (2013b).

Table 6.1 Batch formulation of alkali-free glass with primary SiO_2 size of 7~8 μm

Raw material	SiO_2	Al_2O_3	B_2O_3	BaO	Fe_2O_3	Total
[wt%]	51	8.6	15.9	24	0.1	99.6

Table 6.2 Batch formulation of alkali-free glass with primary SiO_2 size of 1~2 μm

Raw material	SiO_2	Al_2O_3	B_2O_3	BaO	Fe_2O_3	Total
[wt%]	49.5	8.9	15	26	0.1	99.5

Table 6.3 Experimental conditions for in-flight particle measurement by DPV-2000 in hybrid plasma

Hybrid plasma conditions	
Number of phase	12
Electrode configuration	Clockwise (CW) pattern
Power of multi-phase AC arc	50~60 kW
Current	320 A
Voltage	200 V
Electrode distance	80 mm
Ar flow rate (each electrode)	5 L/min
Tungsten electrode diameter	φ3.2 mm
Power of oxygen burner	9 kW
Propane gas flow rate	6 L/min
Primary O_2 gas flow rate	6 L/min
Second O_2 gas flow rate	24 L/min
Powder treatment conditions	
Powder	Alkali-free glass
Primary SiO_2 size	7~8 μm
Particle mean size	114 μm
Powder feed rate	30 g/min
Air carrier gas flow rate	20 L/min
Distance from powder injection position to electrodes	300 mm
Diagnostic methods	
Particle measurement	DPV-2000 (Tecnar)
Spectroscopic measurement	MicroHR (HORIBA)

Table 6.4 Experimental conditions for in-flight particle measurement by high-speed camera in hybrid plasma

Hybrid plasma conditions	
Number of phase	12
Electrode configuration	Clockwise (CW) pattern
Power of multi-phase AC arc	50~60 kW
Current	320 A
Voltage	200 V
Electrode distance	80 mm
Ar flow rate (each electrode)	5 L/min
Tungsten electrode diameter	φ3.2 mm
Power of oxygen burner	9 kW
Propane gas flow rate	6 L/min
Primary O_2 gas flow rate	6 L/min
Second O_2 gas flow rate	24 L/min
Powder treatment conditions	
Powder	Alkali-free glass
Primary SiO_2 size	7~8 μm
Particle mean size	114 μm
Powder feed rate	30 g/min
Air carrier gas flow rate	10, 20, 30 L/min
Distance from powder injection position to electrodes	300 mm
Diagnostic methods	
High-speed camera	FASTCAM SA WTI (Photron)
Frame rate	5000 fps
Shutter speed	200 μs
Band-pass filters	785±5 nm (left), 880±5 nm (right)
Oscilloscope	ScopeCorder DL850 (Yokogawa)
Sampling rate	10^6 Hz

Table 6.5 Experimental conditions for powder treatment by hybrid plasma

Conditions of hybrid plasma		
Number of phase	12	
Electrode configuration	Clockwise (CW) pattern	
Power	50-65 kW	
Current	320 A	
Voltage	190 V	
Electrode distance	80 mm	
Ar flow rate (each electrode)	5 L/min	
Tungsten electrode diameter	φ3.2 mm	
Conditions of oxygen burner		
Power	9 kW	
Gas flow rate	C_3H_8: 6 L/min	
Primary O_2 flow rate	O_2: 6 L/min	
Second O_2 flow rate	O_2: 24 L/min	
Conditions of powder treatment		
Powder	Alkali-free glass	
Primary SiO_2 size	7~8 μm	1~2 μm
Particle mean size	114 μm	105 μm
Powder feed rate	30, 50, 80,150 g/min	30, 50, 70, 100, 150, 200 g/min
Air carrier gas flow rate	20 L/min	
Distance from powder injection position to electrodes	300 mm	

Table 6.6 Experimental conditions for powder treatment by multi-phase AC arc

Discharge conditions	
Number of phase	12
Electrode configuration	Clockwise (CW) pattern
Power	50~60 kW
Current	320 A
Voltage	200 V
Electrode distance	80 mm
Ar flow rate (each electrode)	5 L/min
Tungsten electrode diameter	φ3.2 mm
Powder treatment conditions	
Powder	Alkali-free glass
Primary SiO_2 size	7~8 μm
Particle mean size	114 μm
Powder feed rate	30, 50, 80, 130, 150 g/min
Air carrier gas flow rate	20 L/min
Distance from powder injection position to electrodes	150 mm

Table 6.7 Chemical compositions of the alkali-free glass powders with primary SiO_2 size of 7~8 μm at different powder feed rates by hybrid plasma

Powder feed rate	SiO_2 (wt%)	Al_2O_3 (wt%)	B_2O_3 (wt%)	BaO (wt%)	Fe_2O_3 (wt%)
30 g/min	45.3	15.7	5.69	32.4	0.08
50 g/min	51.3	12.8	6.15	29.1	0.09
80 g/min	53.7	11.2	7.29	27.3	0.09
150 g/min	53.7	10	10.1	25.7	0.09

Table 6.8 Chemical compositions of the alkali-free glass powders with primary SiO_2 size of 7~8 μm at different powder feed rates by multi-phase AC arc

Powder feed rate	SiO_2 (wt%)	Al_2O_3 (wt%)	B_2O_3 (wt%)	BaO (wt%)	Fe_2O_3 (wt%)
30 g/min	54.3	10.0	9.8	25.5	0.09
50 g/min	53.5	9.6	11.4	25.1	0.09
80 g/min	52.9	9.3	12.5	24.9	0.09
130 g/min	52.7	9.1	12.3	25.1	0.10
150 g/min	51.4	9.0	14.8	24.1	0.08

Table 6.9 Chemical compositions of the alkali-free glass powders with primary SiO_2 size of 1~2 μm at different powder feed rates by hybrid plasma

Powder feed rate	SiO_2 (wt%)	Al_2O_3 (wt%)	B_2O_3 (wt%)	BaO (wt%)	Fe_2O_3 (wt%)
30 g/min	44.6	17.1	4.39	32.5	0.08
50 g/min	49.9	11.5	6.88	30.9	0.08
70 g/min	49.9	12.2	6	31.2	0.08
100 g/min	52.8	10.3	9.8	26.3	0.10
150 g/min	51.2	9.5	11.3	27.4	0.07
200 g/min	51.7	9.8	12.2	25.5	0.10

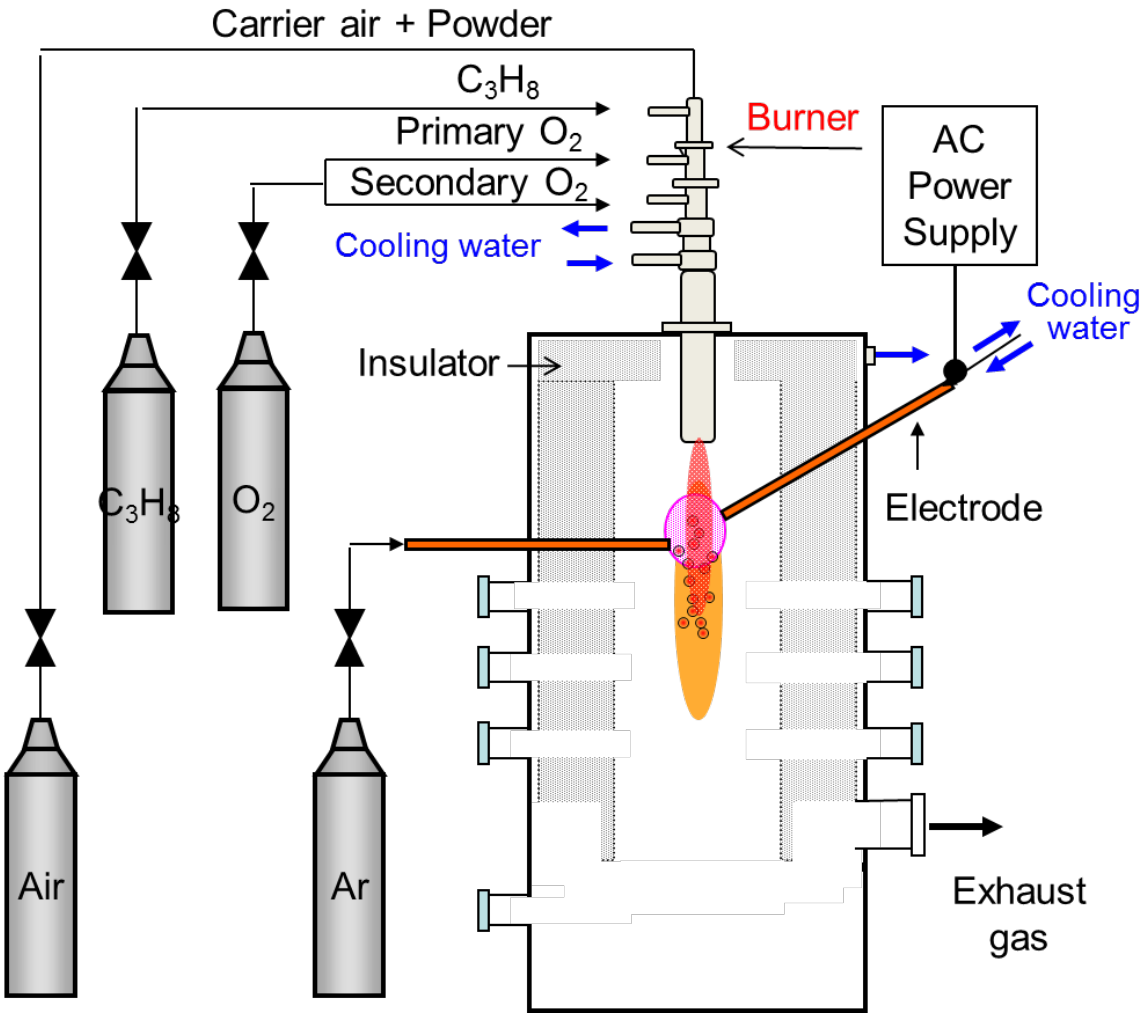

Fig. 6.1 The schematic of the in-flight melting by hybrid plasmas

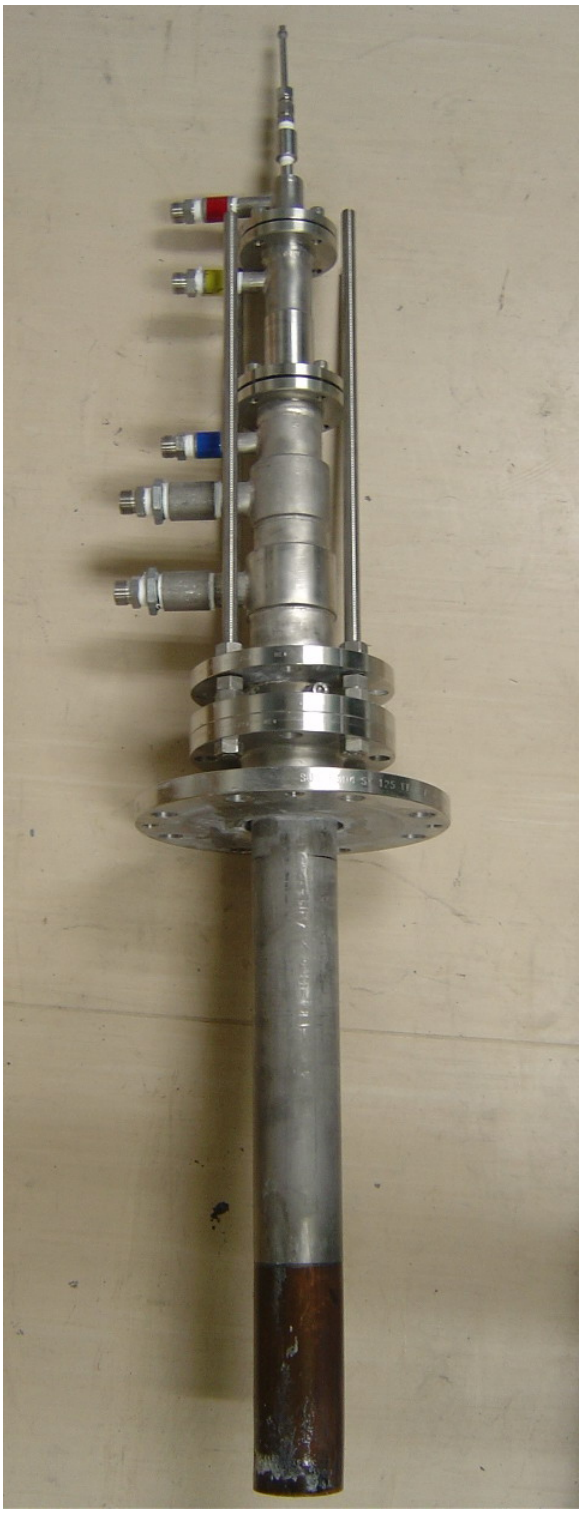

Fig. 6.2 The photograph of the oxygen burner

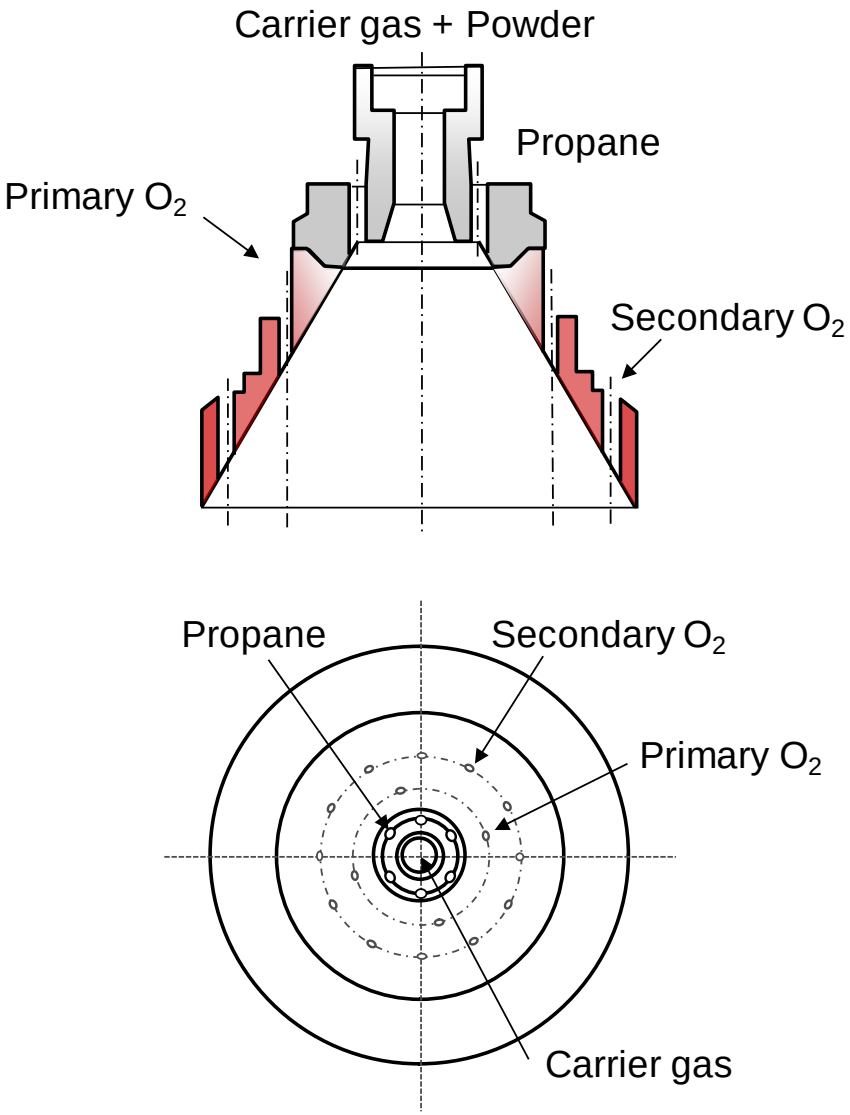

Fig. 6.3 The schematic of nozzle tip of oxygen burner

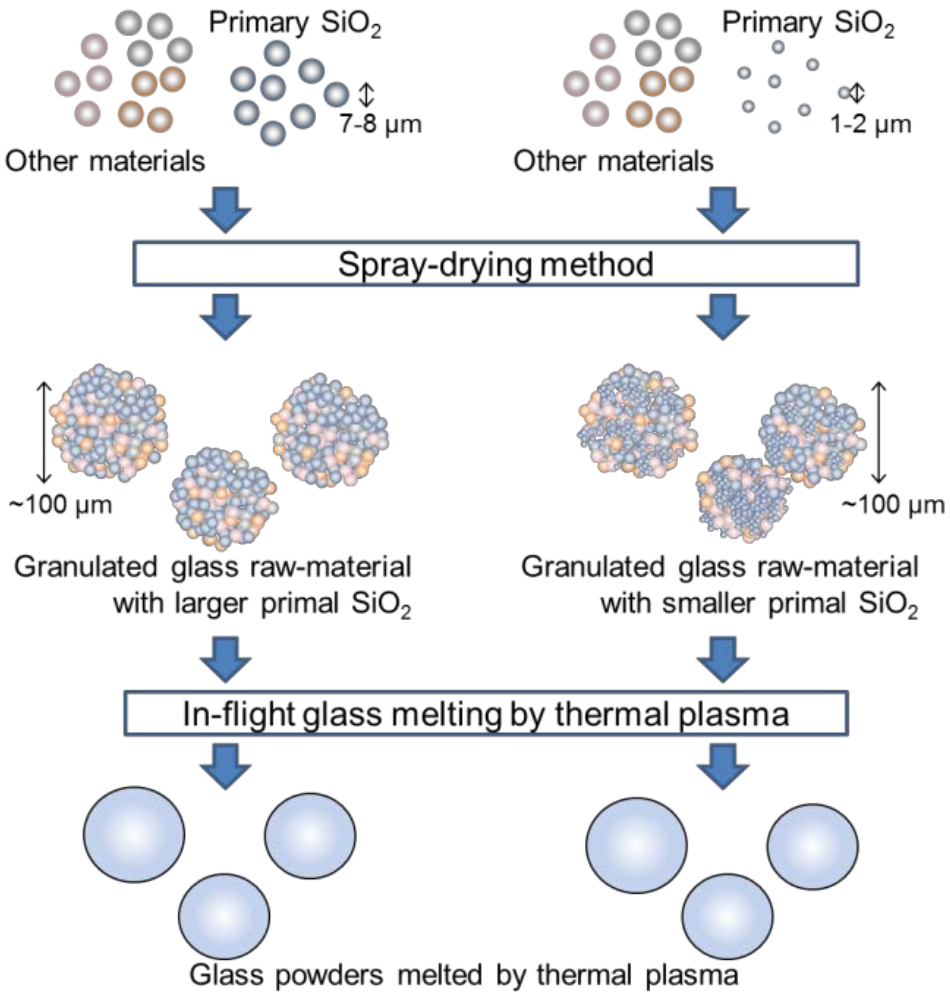

Fig. 6.4 Granulation process of spray dry method supplied by Asahi Glass Co., Ltd., Japan

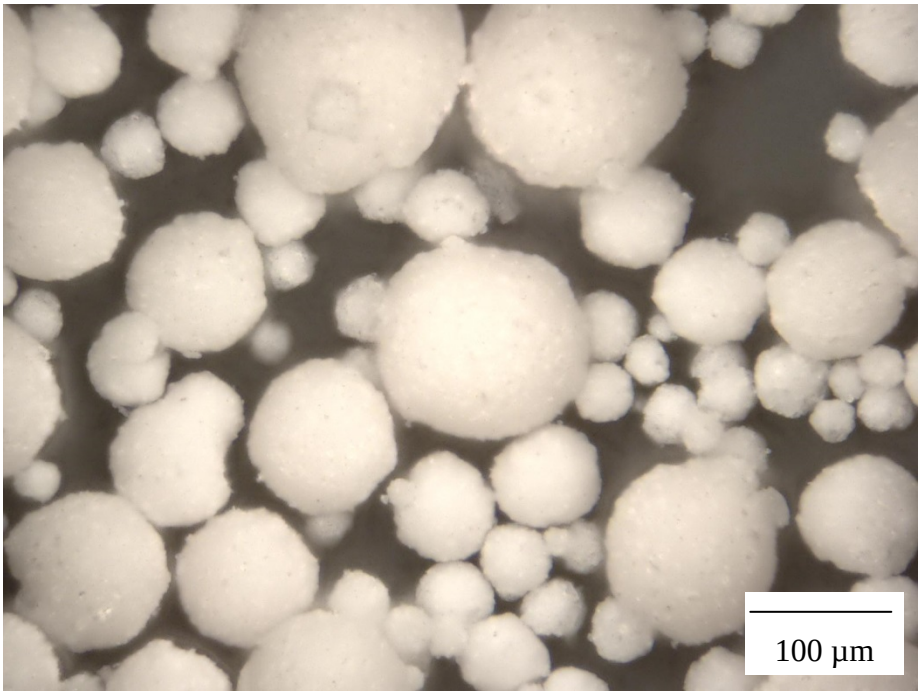

Fig. 6.5 Microscope image of raw material of alkali-free glass with primary SiO_2 size of 7~8 µm

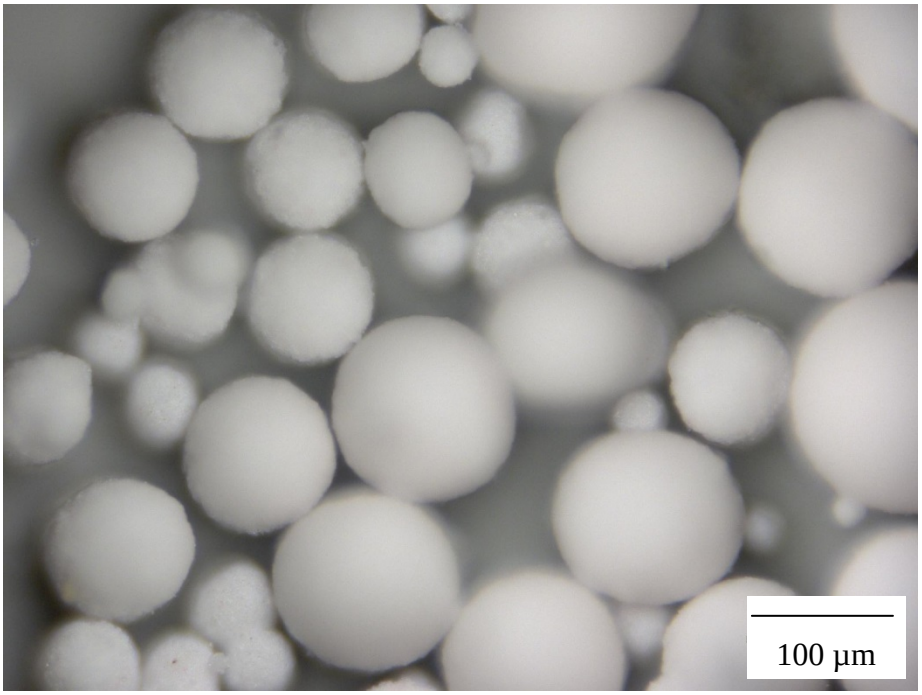

Fig. 6.6 Microscope image of raw material of alkali-free glass with primary SiO_2 size of 1~2 µm

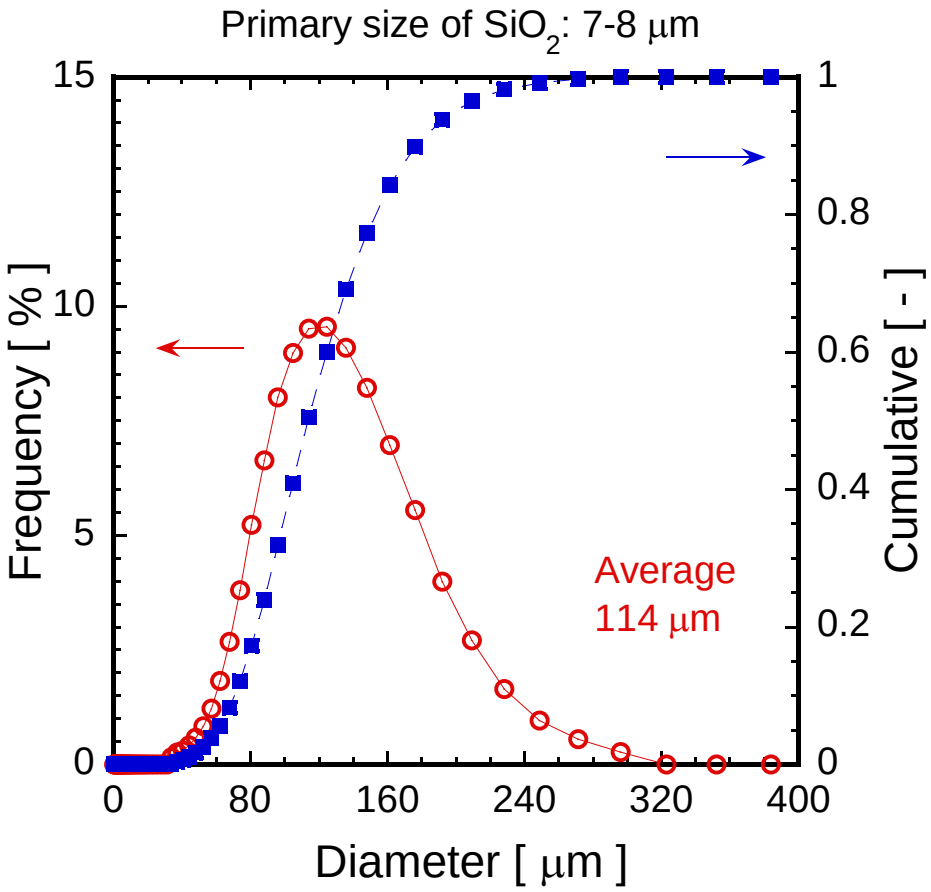

Fig. 6.7 Particle size distribution of raw material of alkali-free glass with primary SiO_2 size of 7~8 μm

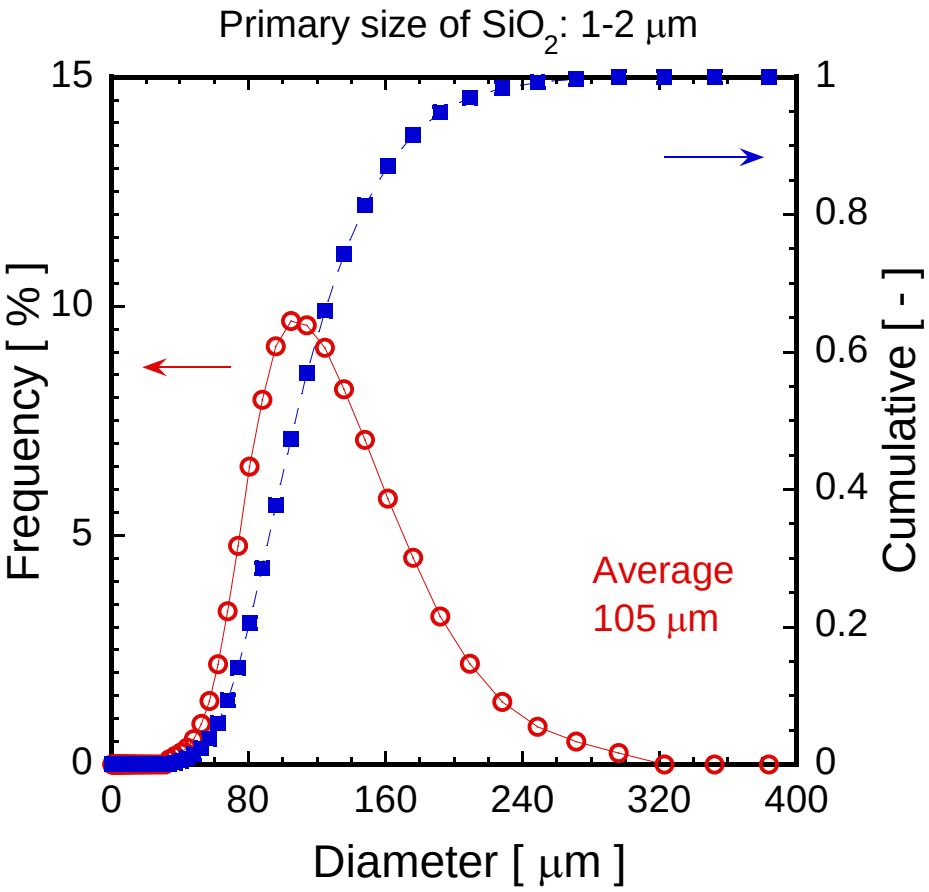

Fig. 6.8 Particle size distribution of raw material of alkali-free glass with primary SiO_2 size of 1~2 μm

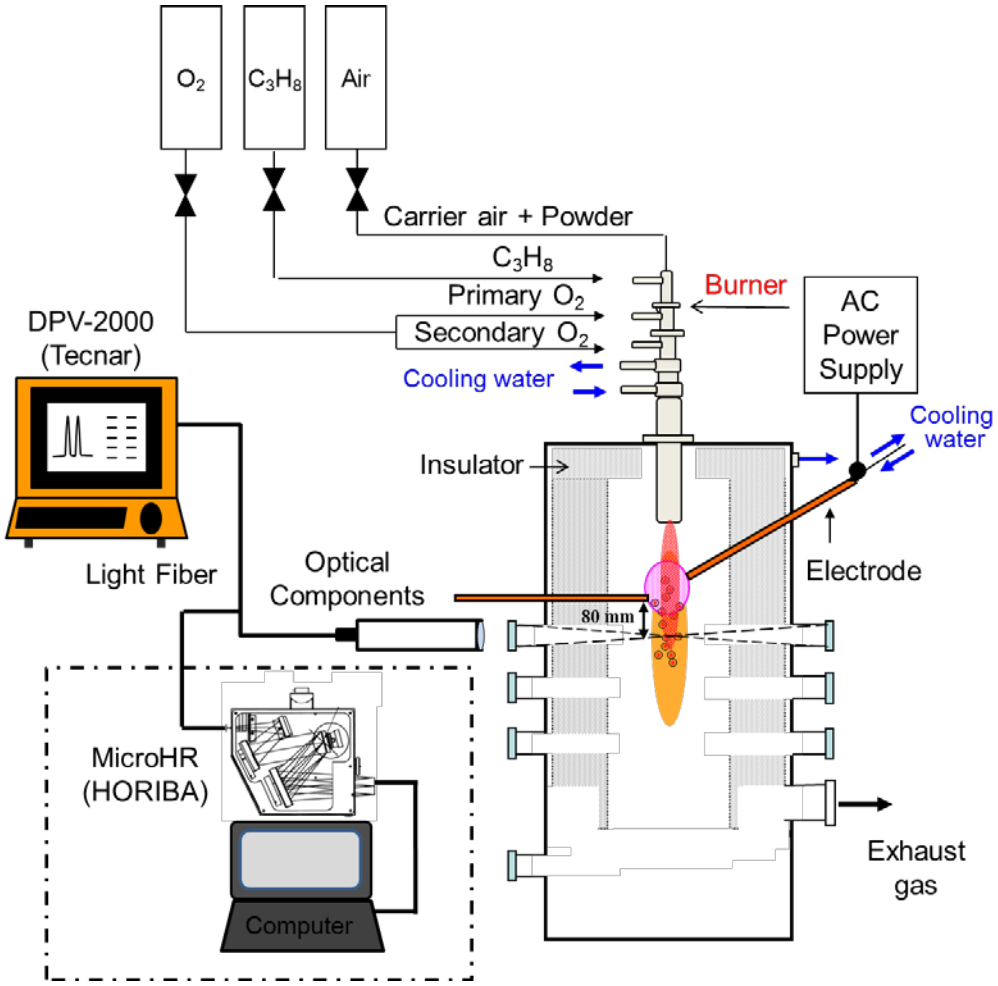

Fig. 6.9 The schematic of the hybrid plasma apparatus with particle measurement system by DPV-2000 and spectroscopy

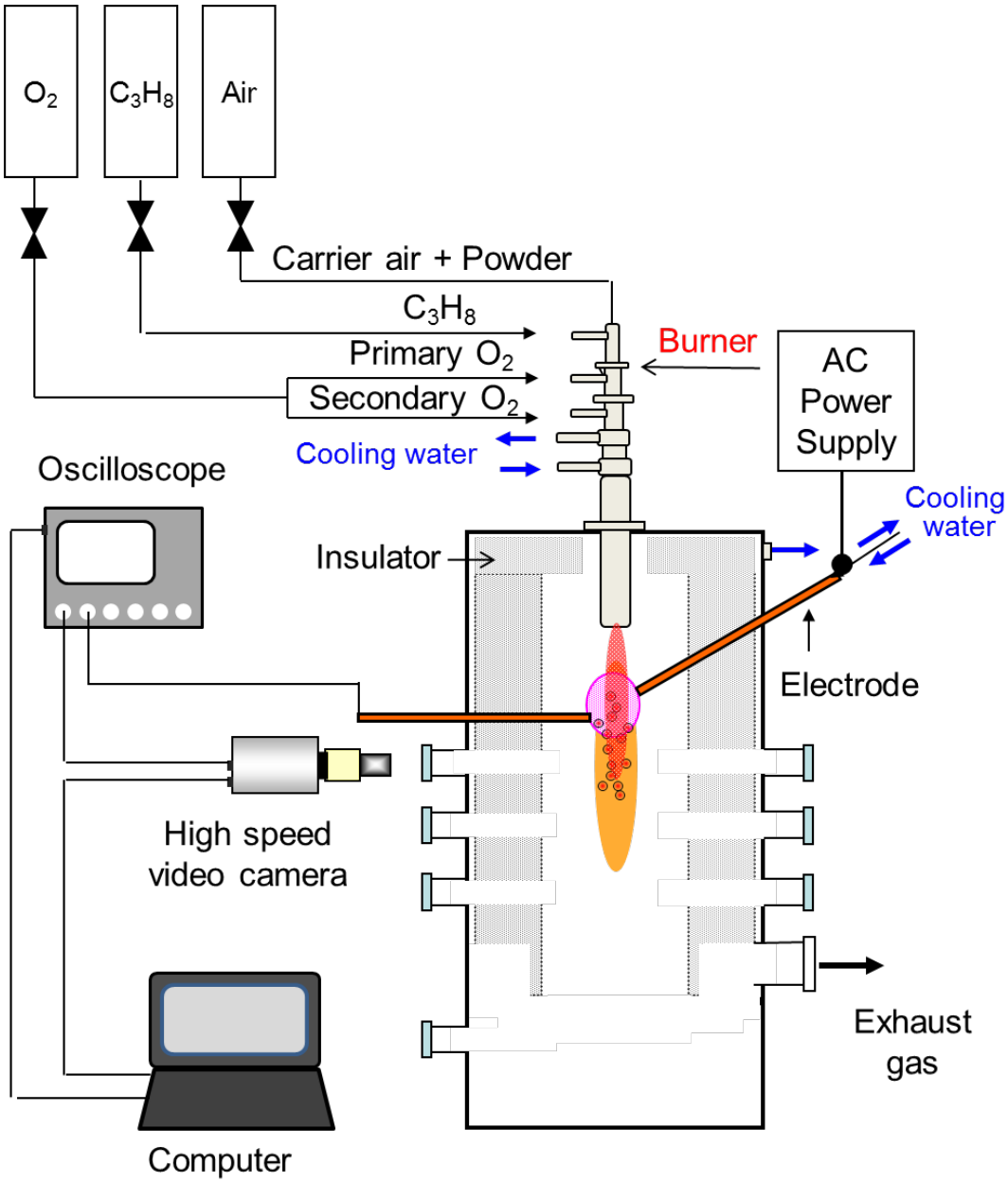

Fig. 6.10 The schematic of the hybrid plasma apparatus with particle measurement system by high-speed camera

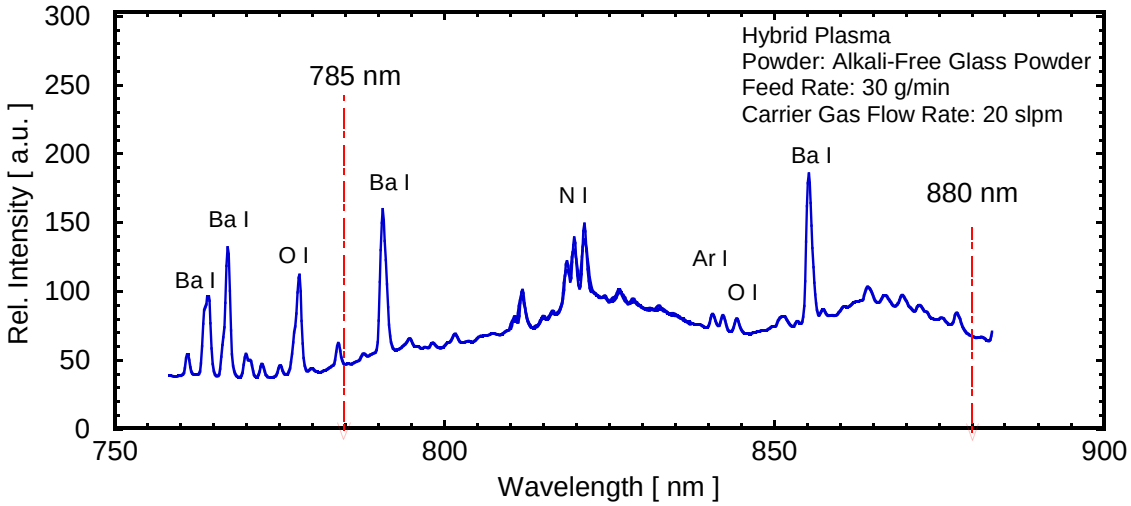

Fig. 6.11 Emission line spectrum of hybrid plasma with powder injection

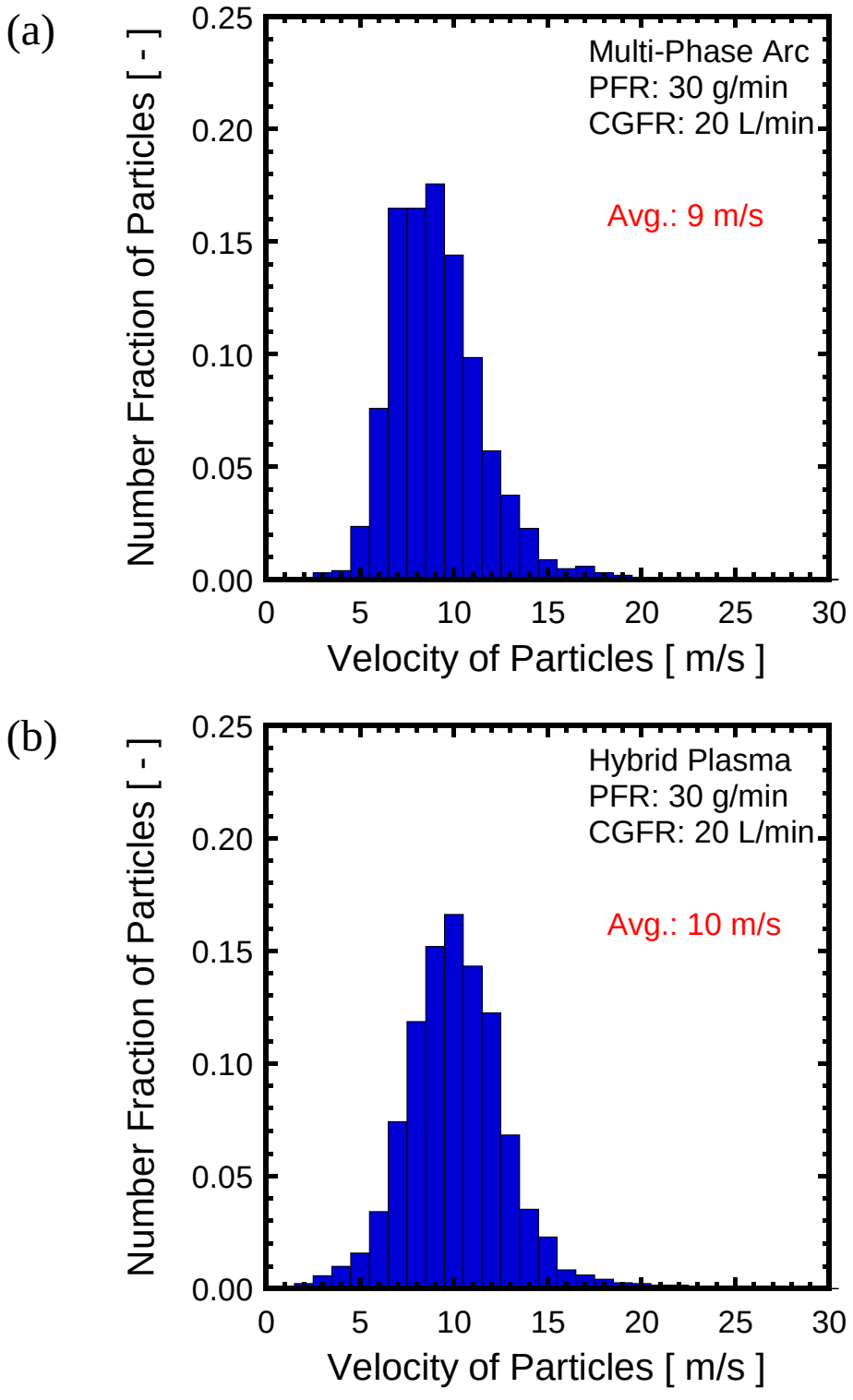

Fig. 6.12 Particle velocity distribution estimated by DPV-2000 in (a) hybrid plasma system and (b) multi-phase AC arc system

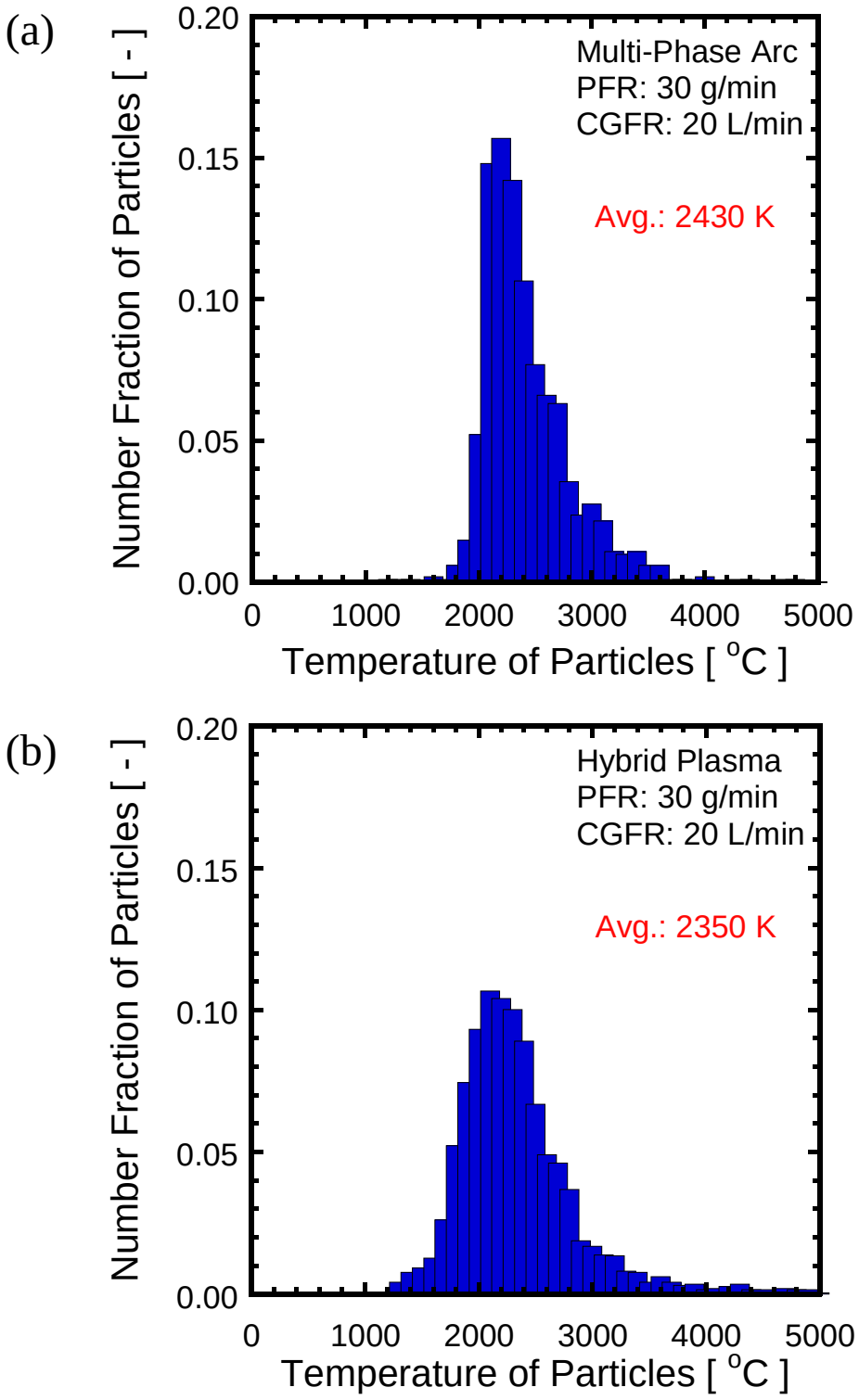

Fig. 6.13 Particle surface temperature distribution estimated by DPV-2000 in (a) hybrid plasma system and (b) multi-phase AC arc system

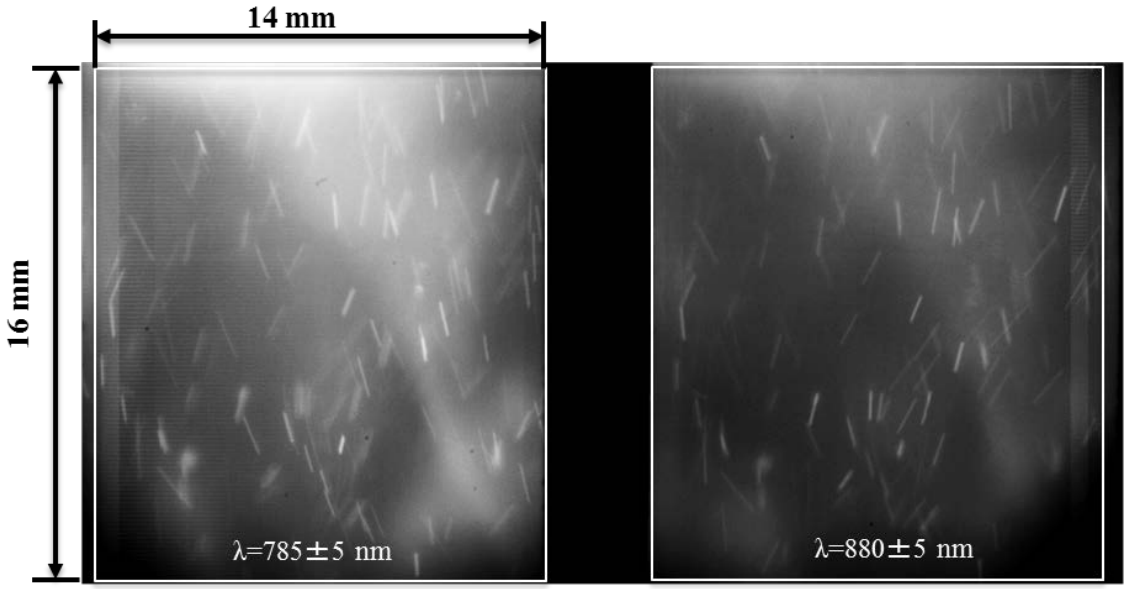

Fig. 6.14 Image of glass particle streaks obtained by two different band-pass filters in hybrid plasmas, 785 ± 5 nm (Left) and 880 ± 5 nm (Right)

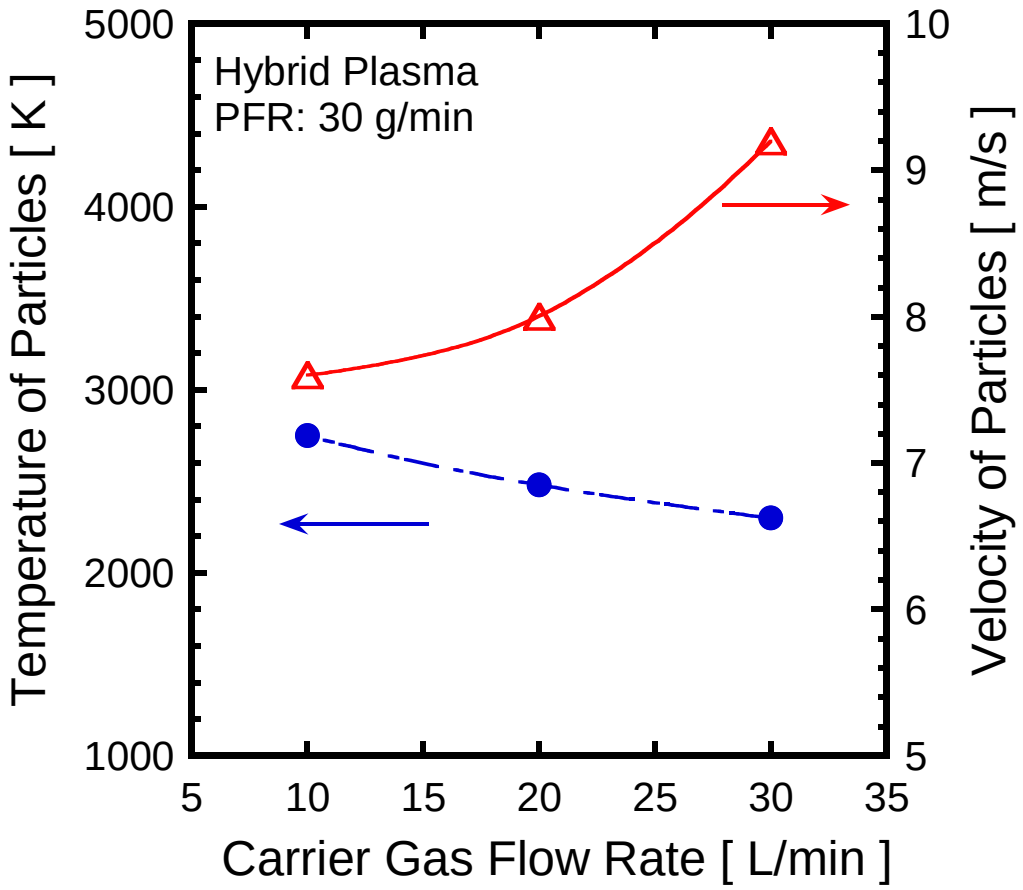

Fig. 6.15 Effect of carrier gas flow rate on the particle average temperature and velocity estimated by high-speed camera in hybrid plasma

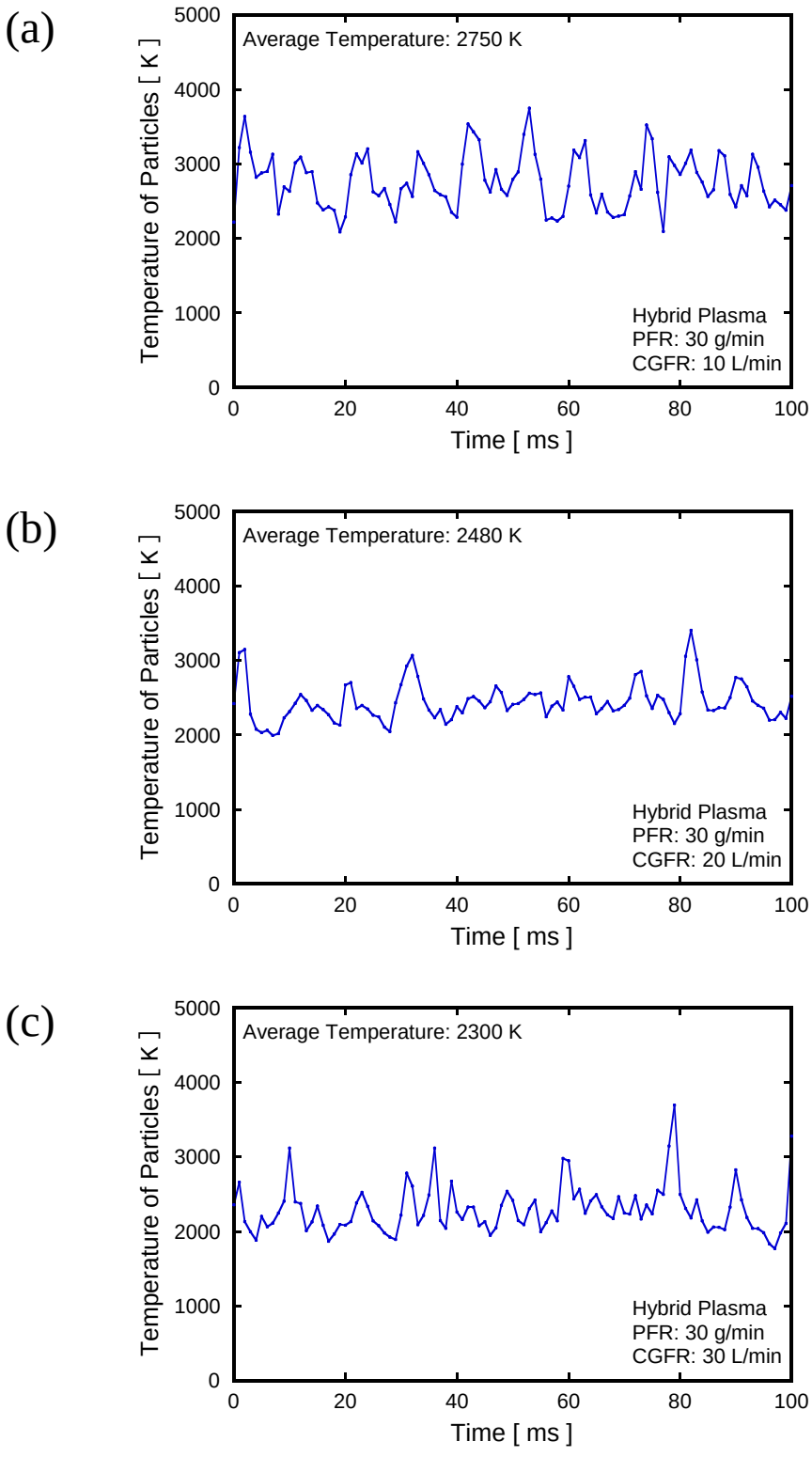

Fig. 6.16 Fluctuation of average temperature of particles in hybrid plasmas with different carrier gas flow rates: (a) 10 L/min (b) 20 L/min and (c) 30 L/min

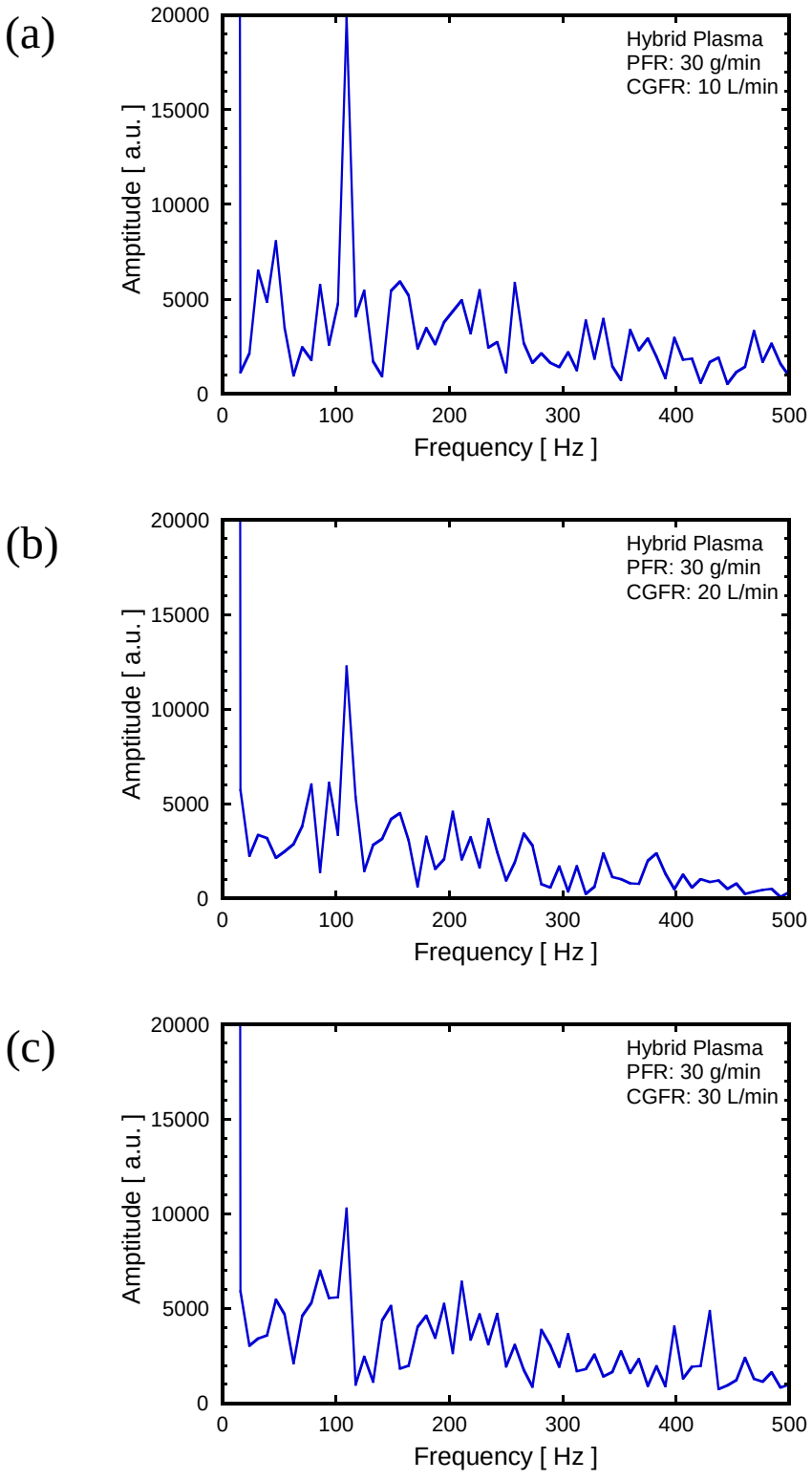

Fig. 6.17 Frequency spectra of fluctuation of particle temperature in hybrid plasmas with different carrier gas flow rates: (a) 10 L/min (b) 20 L/min and (c) 30 L/min

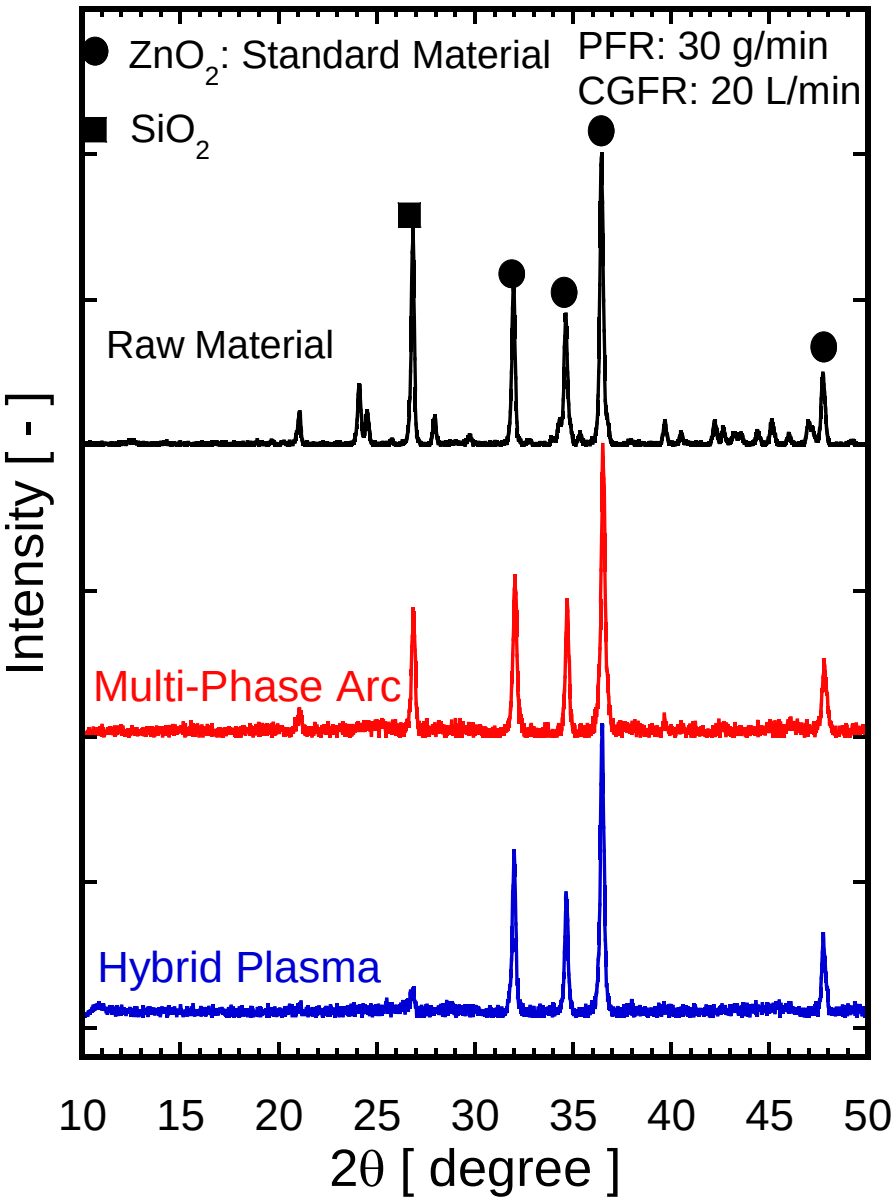

Fig. 6.18 XRD patterns of alkali-free glass raw materials and prepared powders treated by multi-phase AC arc and hybrid plasma at a feed rate of 30 g/min

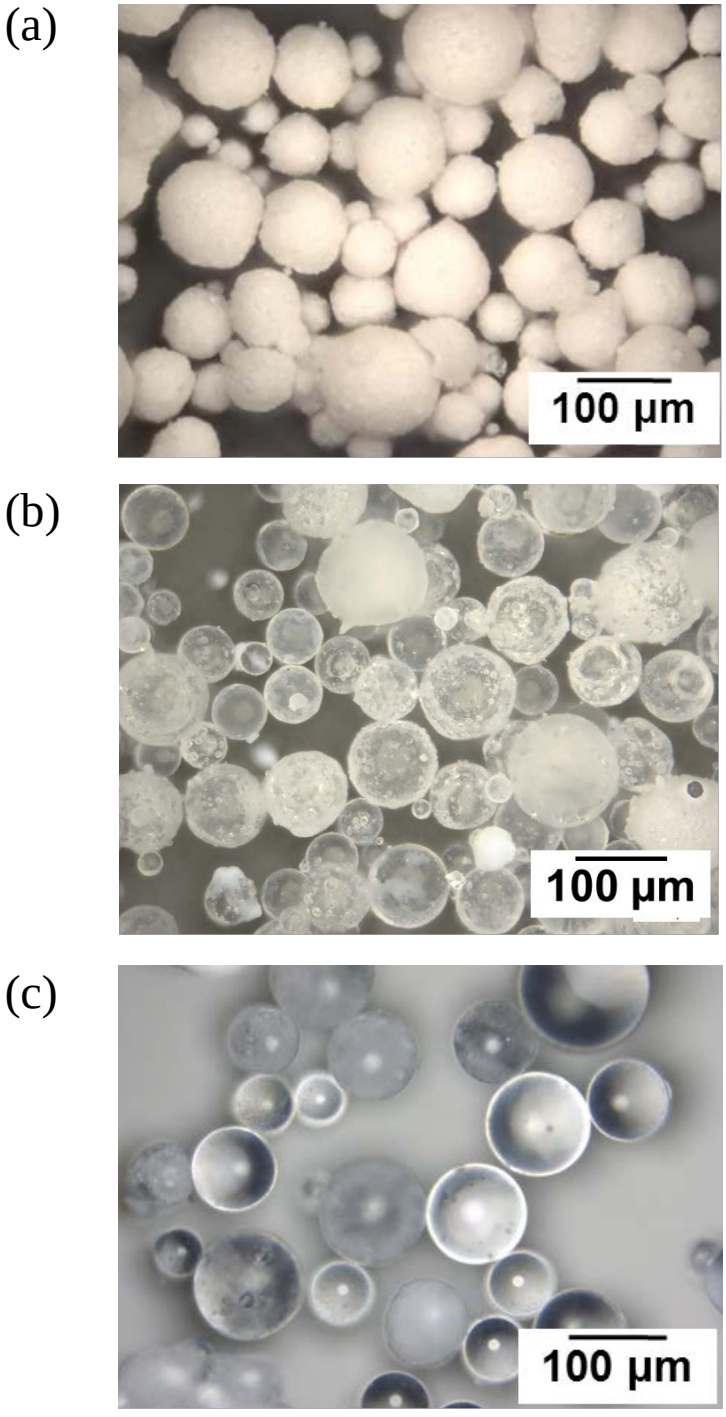

Fig. 6.19 Optical microscope images of (a) the raw material, (b) the melted particles by multi-phase AC arc and (c) the melted particles by hybrid plasma at feed rate of 30 g/min

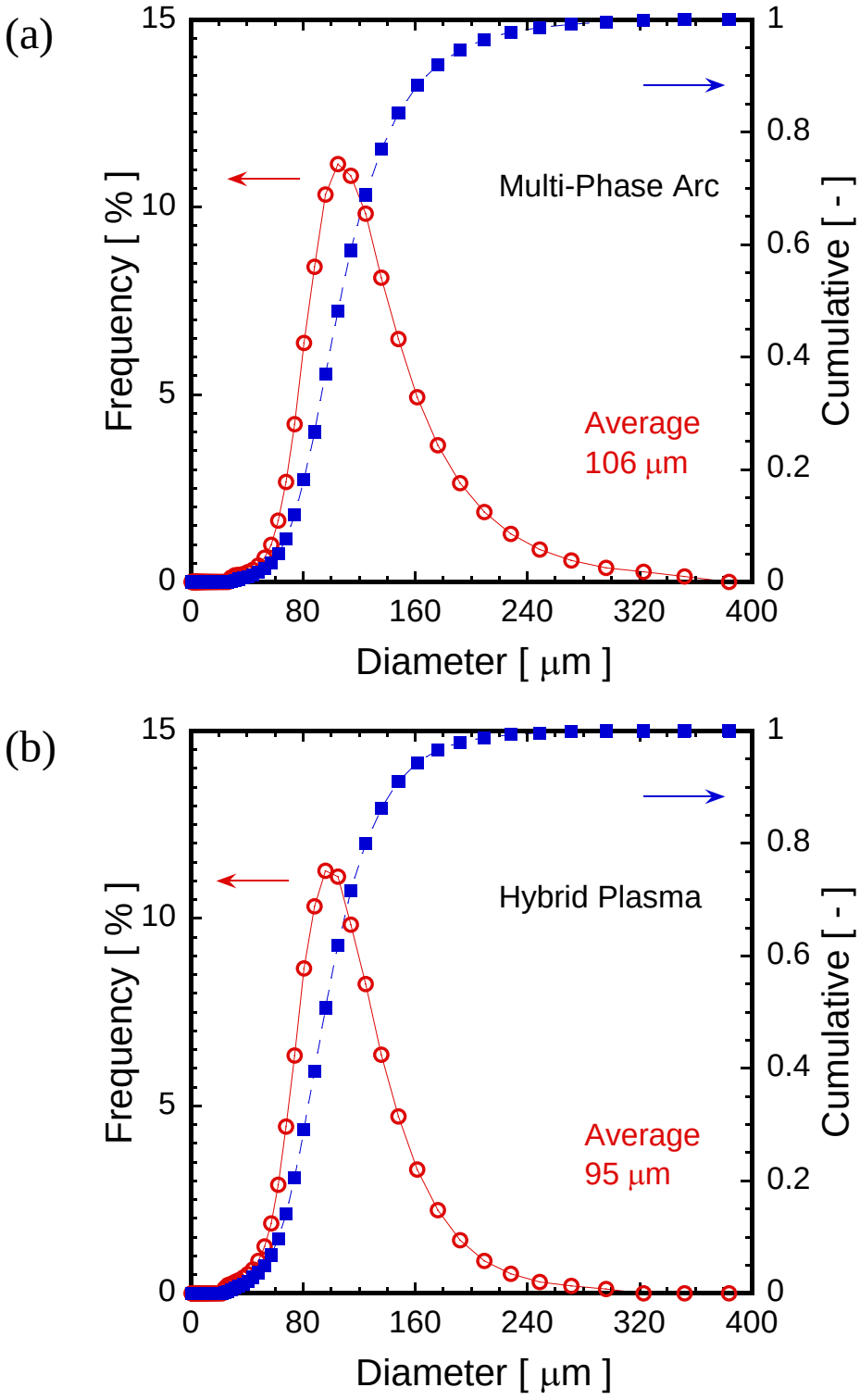

Fig. 6.20 Particle average size of the melted powders by different heat sources

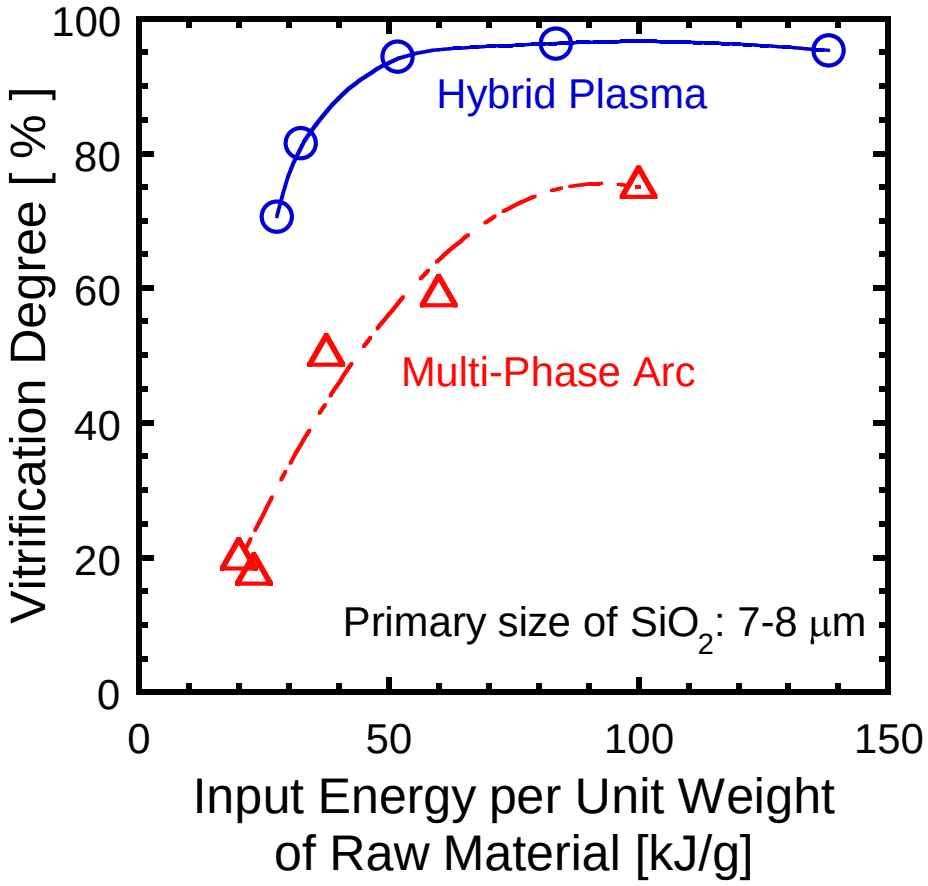

Fig. 6.21 Relationship between the input energy and the verification degree of the powders melted by different heat sources

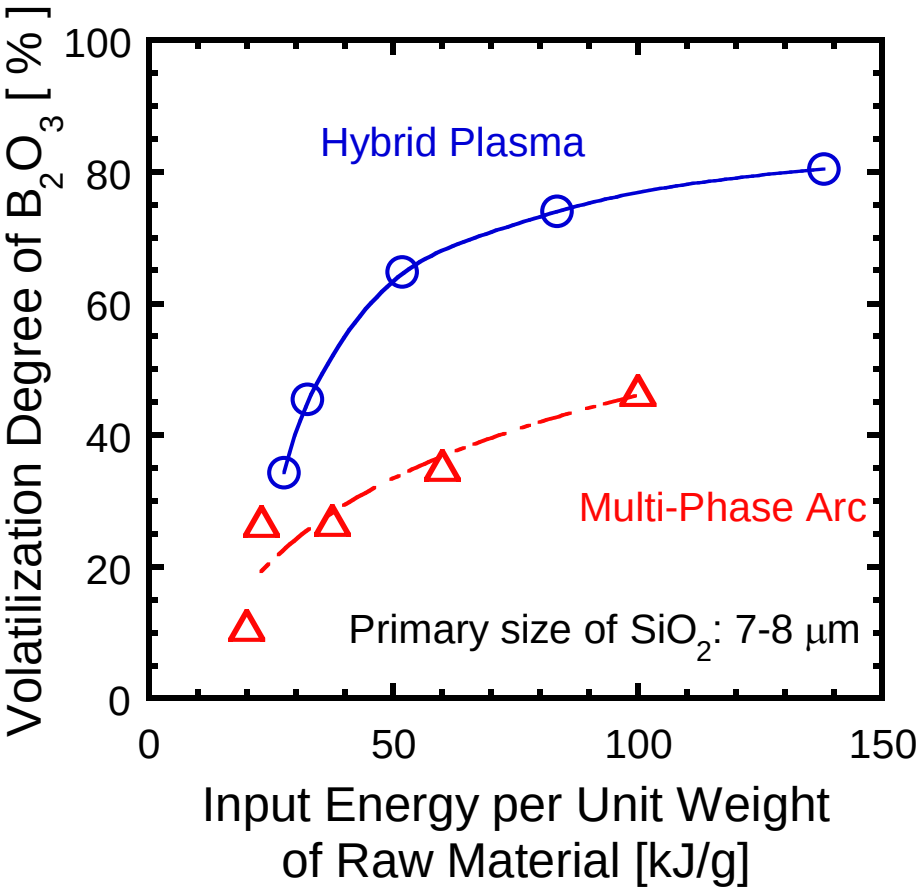

Fig. 6.22 Relationship between the input energy and the volatilization degree of the powders melted by different heat sources

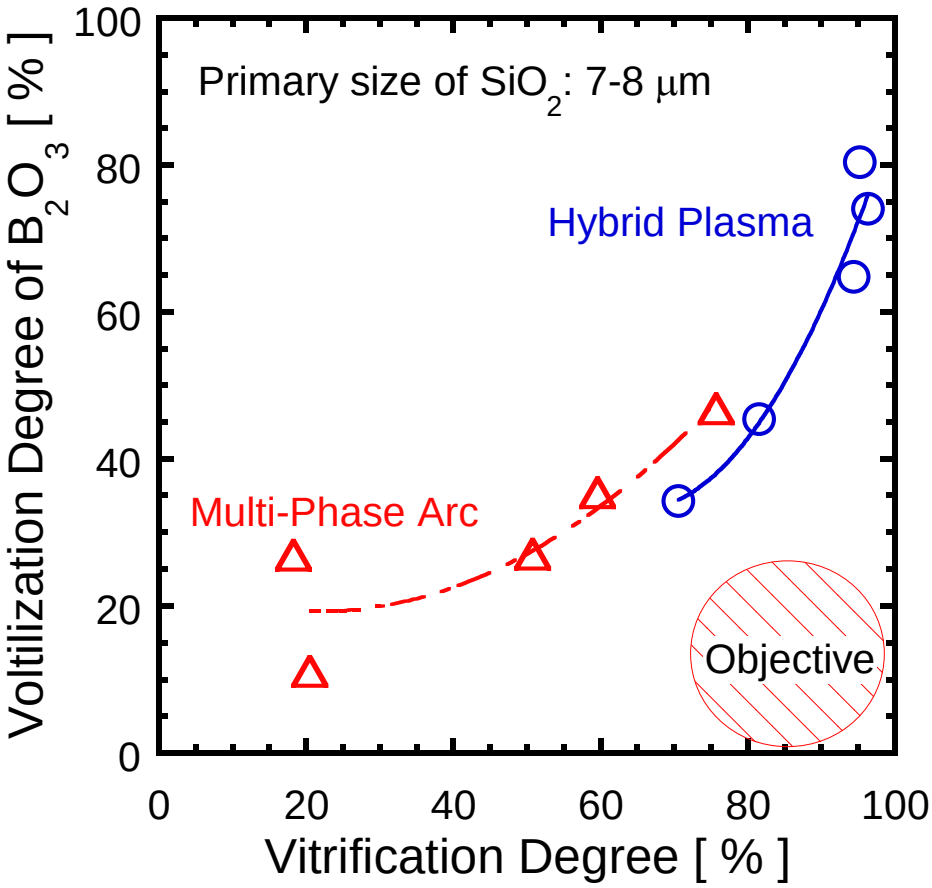

Fig. 6.23 Relationship between the vitrification degree and the volatilization degree of B_2O_3 for larger size of primary SiO_2 particles

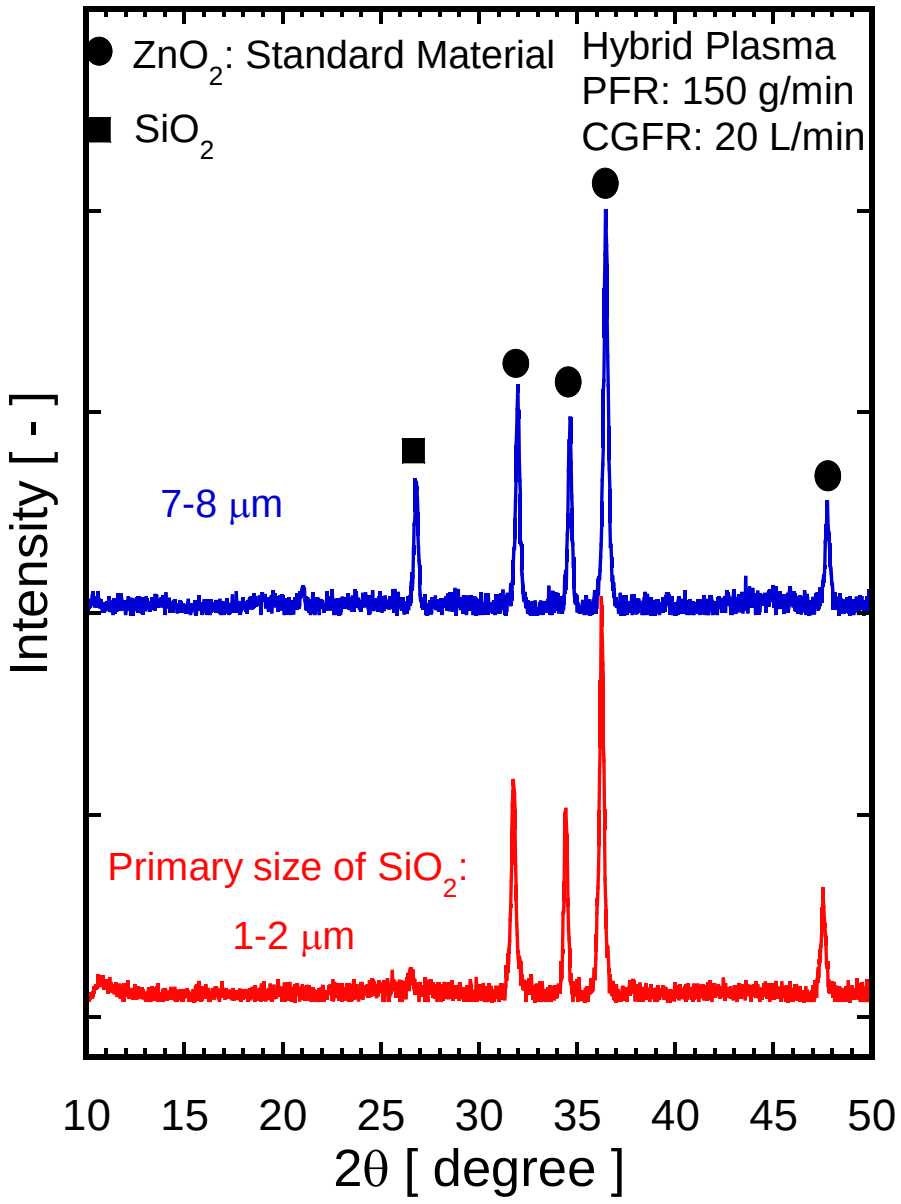

Fig. 6.24 XRD patterns of alkali-free glass raw materials with different primary size of SiO_2 treated by hybrid plasma at a feed rate of 150 g/min

(a)

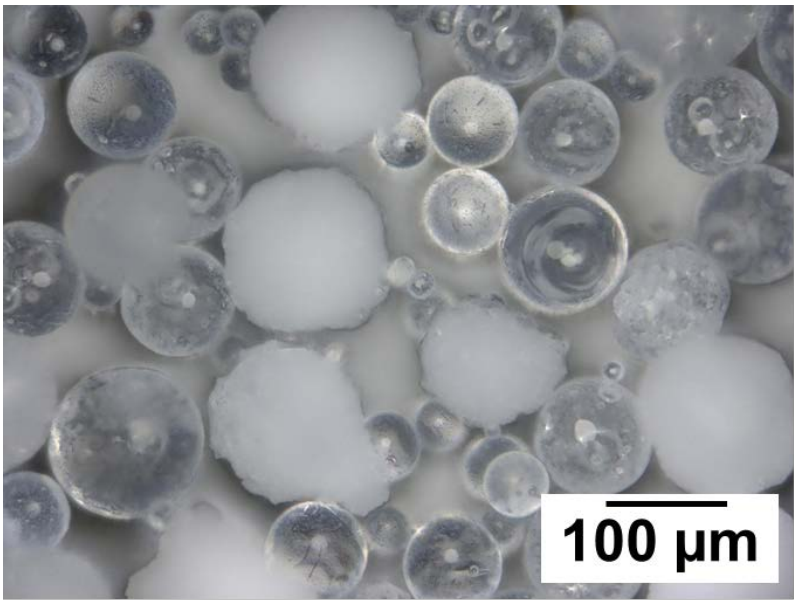

(b)

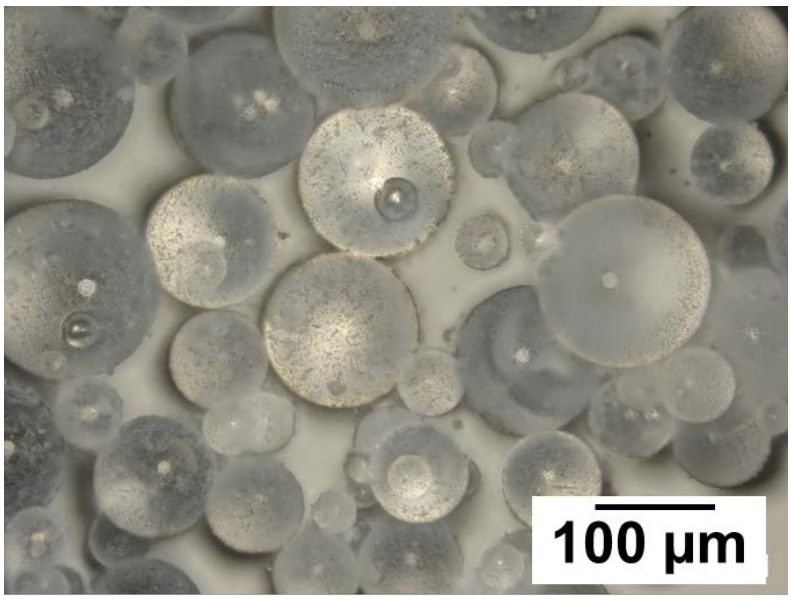

Fig. 6.25 Optical microscope images of melted particles by hybrid plasma with different raw materials at feed rate of 150 g/min: (a) primary SiO_2 size of 7~8 μm and (b) primary SiO_2 size of 1~2 μm

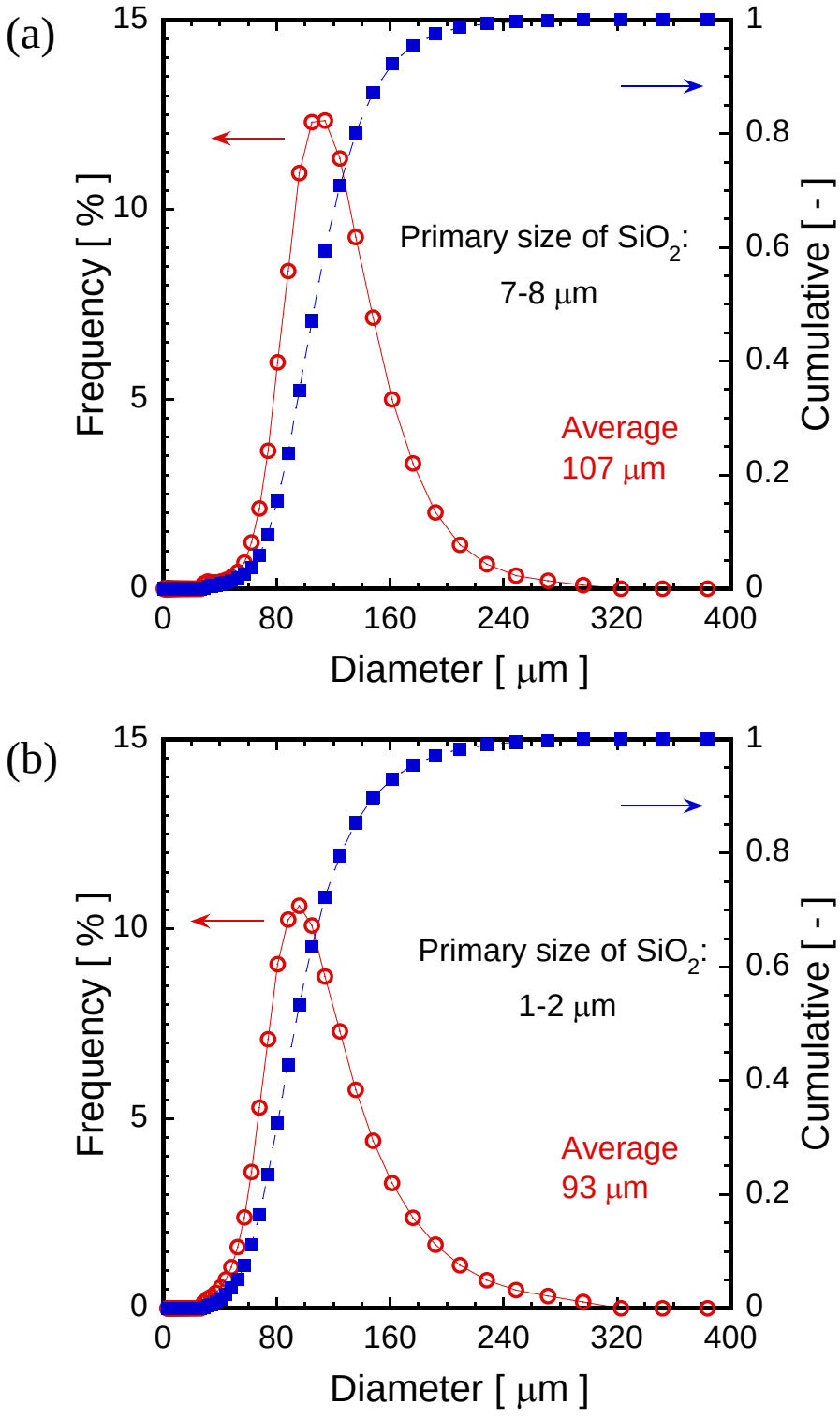

Fig. 6.26 Particle size distributions of melted alkali-free glass particles by hybrid plasma at feed rate of 150 g/min with different raw materials: (a) primary SiO_2 size of 7~8 μm and (b) primary SiO_2 size of 1~2 μm

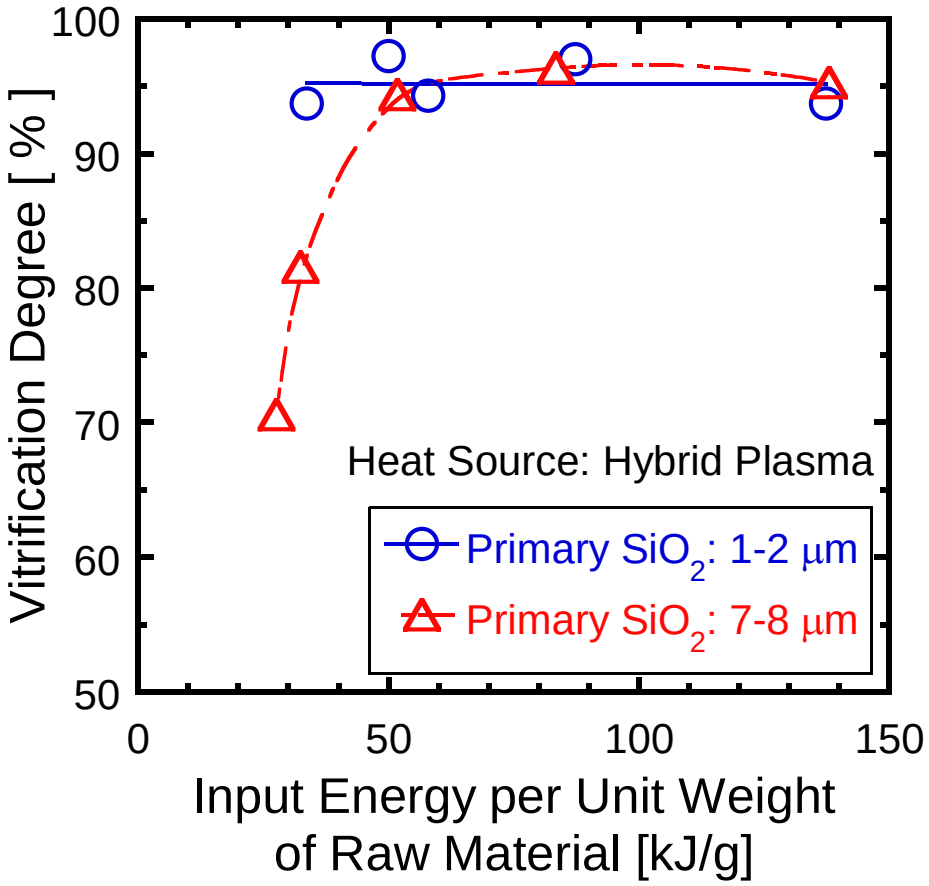

Fig. 6.27 Relationship between the input energy and the vitrification degree of the powders melted by hybrid plasma for different sizes of primary SiO_2 particles

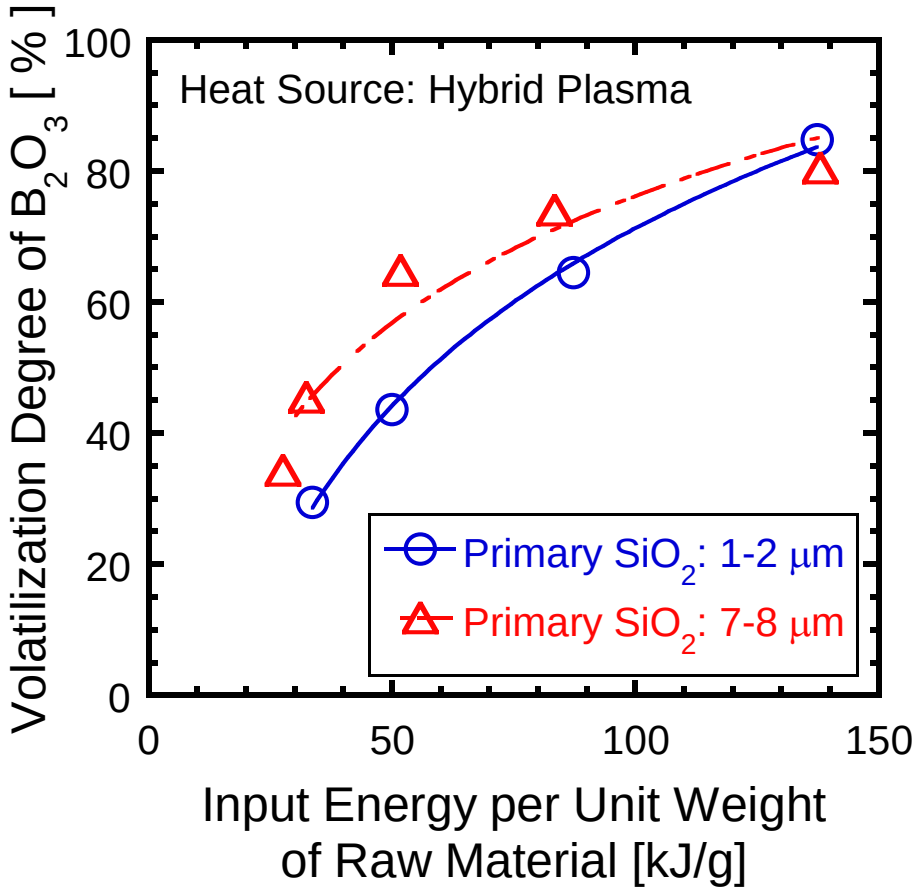

Fig. 6.28 Relationship between the input energy and the volatilization degree of the powders melted by hybrid plasma for different sizes of primary SiO_2 particles

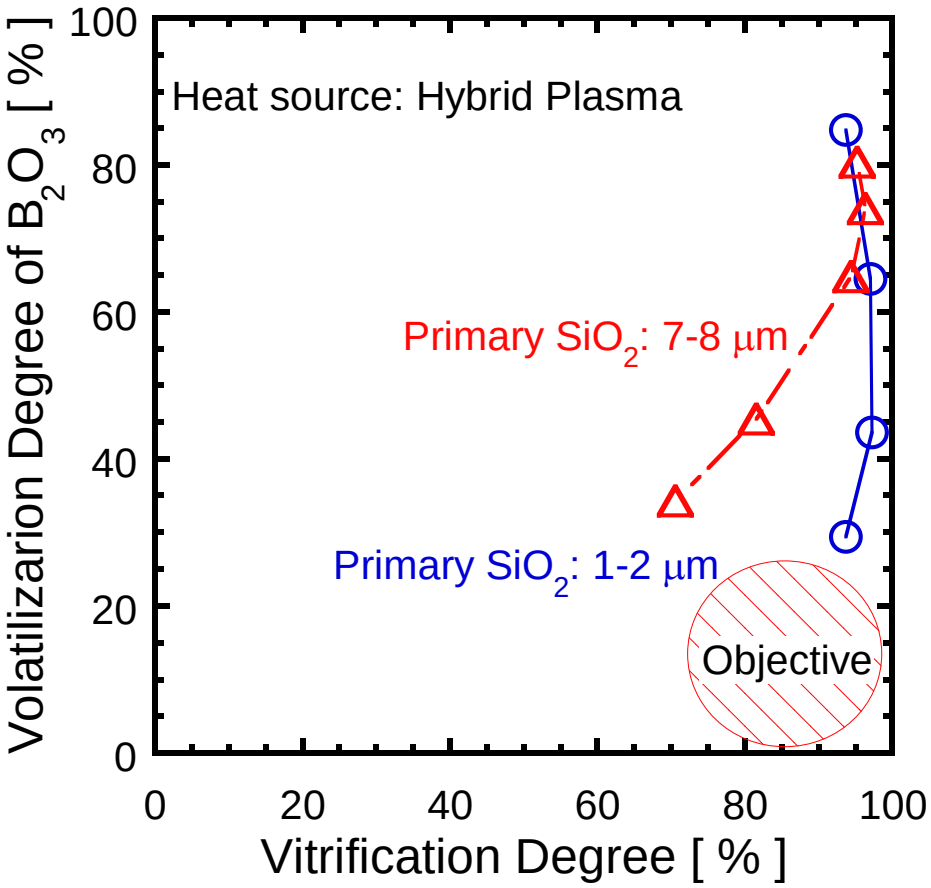

Fig. 6.29 Relationship between the vitrification degree and the volatilization degree of melted powders by hybrid plasma

7. Conclusions

7.1 Summary and Conclusion of Dissertation

The objective of this dissertation was to investigate the innovative in-flight glass melting technology by the multi-phase AC arc plasma. The experimental approaches including the characterization of multi-phase AC arc discharge behavior and analysis of the spatial and temporal properties. Another purpose of this work was to investigate the relationship between multi-phase AC arc and in-flight glass melting behavior. Finally, the feasibility for the in-flight glass melting using multi-phase AC arc as well as the hybrid plasmas was discussed. Theoretical and the experimental investigations were conducted to achieve the purpose in this dissertation.

In Chapter 1, the research direction of material processing by thermal plasmas was reviewed after a brief introduction of the principle thermal plasma physics. The conventional glass melting technology was mentioned with indicating that the traditional method is time and energy consuming. Several trials of introducing the thermal plasma into glass melting have been made in the history but none of them was commercialized. The background of the innovative in-flight melting technology and the five-year project was then introduced.

In Chapter 2, the spatial and temporal uniformity of multi-phase AC arc discharge were investigated by a high-speed camera observation. The arc luminance area obtained from high-speed image analysis was used to evaluate the plasma fluctuation and spatial uniformity. Experimental results showed that the electrode configuration attributes to the arc discharge behavior and fatherly affect the plasma characteristics temporally and spatially. CW pattern was

characterized by the main arc between opposite electrodes rotating in the clockwise direction combined with several small alternative arc paths. On the other hand, FF pattern had a couple of strong and short discharged arc. High-temperature area of CW pattern was found wider than that of FF pattern due to the wider swing angle on the arc spot. The high-temperature region in the central area can be enlarged by reducing the electrode distance or increase the Ar gas flow rate. Moreover, the swirl gas flow of Ar extends the arc length in the axial direction thus made the plasma distribution more concentrated to the central area. The temporal uniformity of multi-phase AC arc was also investigated. Experimental results have shown that large fluctuation in CW pattern was caused by the transient variation of different discharge paths. In the case of FF pattern, the arc length is regular resulted in the smaller fluctuation of luminance area in the whole discharge region. The fluctuation of arc showed periodical frequency of 300 Hz of 12-phase AC arc that originated from the supply frequency of 50 Hz. Based on these studies, the uniformity of arc distribution and instability of discharge are expected to have great influence on the in-flight particles during the short time of several milliseconds.

In Chapter 3, in-flight particle diagnostics performed with optical system DPV-2000 and spectroscopic measurement were investigated theoretically and experimentally. The accuracy of in-flight particle temperature was estimated by separating the non-thermal emissions from spectroscopic measurement. The profiles of the in-flight melted glass particles were successfully obtained by DPV-2000 measurement with adequate corrections. Obtained results showed that the particle velocity was mostly dependent on the carrier gas flow rate. Small-sized particles tend to reach higher velocity and heating to higher temperature, on the contrary, large-sized particles had a lower speed of in-flight and lower surface temperature due to the higher thermal inertias. The measured particle diameter was related to its surface temperature. The dispersion in the particle temperature was the biggest for the smallest particles. The influence of plasma

spatial uniformity on the particle characteristics was investigated. The particle spatial characteristics were different in CW and FF patterns. Results indicated that the detection number of particles was small for the locations further away from the plasma centerline in FF pattern due to high viscosity near the electrode region in FF pattern. Plasma spatial uniformity was demonstrated to have influence on the particle spatial characteristics. In a result, FF pattern with electrode diameter of 6 mm is expected to achieve better uniform melting characteristics.

The particle measurement by DPV-2000 indicated the following facts; (i) there is fundamental limitation of temperature measurement because the emissivities are not well known for the materials, (ii) DPV did not detect low emissivity particles which depended on particle temperature and size, (iii) a broader particle size distribution can result in large standard deviations, especially at higher temperatures. The data obtained by DPV-2000 should be carefully analysed and calibrated, especially in a background with strong non-thermal emission.

In Chapter 4, the fluctuation of particle temperature within millisecond in plasma region was studied by a high speed camera equipped with a band-pass filter system. The influence of the plasma fluctuation on the in-flight particle temperature was evaluated. The obtained results showed the particle temperature fluctuation depends on the arc fluctuation strongly. Higher fluctuation of arc luminance area caused larger dispersion of particle surface temperature. The effect of carrier gas flow rate on the periodicity of particle temperature fluctuation was related to the arc discharge pattern. The particle temperature reflects the same periodicity of arc fluctuation at high carrier gas flow in CW pattern, while there is no significant periodic signal in FF pattern. It indicated that more homogeneous particle treatment can be obtained in FF pattern due to small instability.

In Chapter 5, the properties of melted glass powders by multi-phase AC arc were analysed to evaluate the feasibility of in-flight melting technology in future industrial

application. The analysis methods including the XRD patterns, the morphology, the particle size distribution and the composition of melted powders. The obtained results showed the high vitrified glass particles are characterized by XRD pattern with no obvious diffractive peaks compared to the raw material, indicating the glass-like amorphous solid which is free of crystalline structure. Particle size shrank after melted and the final diameter was strongly related to the vitrification degree. The vitrification degree and the volatilization rate of B_2O_3 were the most important parameters to evaluate the glass quality using in-flight melting technology. They also can reflect the particle temperature achieved in the process of in-flight melting. The spatial variation behavior originated from arc discharge caused different particle melting characteristics in the two electrode patterns. Increase the powder feed rate implies the expansion of powder flux, thus a uniform treated powder with prohibited volatilization degree can be obtained at high feed rate in FF pattern.

In Chapter 6, another heating method called “hybrid plasma” combines multi-phase AC arc with oxygen burner was introduced. It has the advantages of both high temperature and long residence time approved to be a better heat source in the future. The in-flight particle measurement in the hybrid plasmas showed higher particle velocity and lower surface temperature at the detected position. The in-flight melting experiments of granulated powders were conducted by multi-phase AC arc and hybrid plasmas. The comparison between the different heat sources suggested the hybrid plasma heating leads to higher vitrification degree than the multi-phase arc in the case with the same volatilization degree. Different primary sizes of SiO_2 in the granulated raw materials were used for investigation of the particle vitrification and volatilization process. The experimental results indicated that smaller size of primary SiO_2 leads to higher vitrification degree due to the fast mixed with of the raw materials. It also reduce the volatilization of B_2O_3 due to smaller voids between the primary raw materials decreased the

diffusivity of the B_2O_3 vapor.

7.2 Future Research Subjects

The experimental and theoretical investigation in this dissertation showed the characterization of multi-phase AC arc and its relationship to the in-flight glass melting behavior. Interesting opportunities emerge for further research to better understand the in-flight melting process by multi-phase AC arc and particle characteristics based on the studies conducted in this dissertation. Some suggestions are presented here for further consideration.

7.2.1 Further Investigation of the Plasma Properties

Fundamental researches of multi-phase AC arc are required such as arc stability, temperature and velocity field. Moreover, control the plasma distribution by measuring its real temperature is a challenge work in the future. Investigation of the plasma instability by multi-phase AC arc with various discharge conditions will be needed to improve the possibility of industrial application. A wide variety of electrode configurations are possible, many of which have not been described before. Examining other multi discharge configurations would be an interesting topic in the future. This dissertation put forward several methods and directions to evaluate the arc fluctuation in the time range and the relatively existence time overall plasma distributed region.

7.2.2 Further Investigation of the Plasma-Particle Interaction

Particles were characterized mainly by the distribution and mean value of velocity, temperature and diameter by DPV-2000 diagnostic system. Although it is one of the most widely used approaches, it has some limitation in the measurement principle such as particle

diameter. Improved calibration on diameter measurement can be obtained by a sieved small amount of powder to a narrow size range (e.g. 80-90 μm).

Particle surface temperature is not adequate to describe the melting state thus particles may partially molten or fully molten. Improvements to the definition of particles are needed to describe the melting states of the particles and enable improved understanding of the plasma-particle interaction. A molten fraction can be defined from the calculate data based on the in-flight temperature, residence time and particle size.

The in-flight particle diagnostics described in this dissertation were all based on the single measurement method thus low powder feed rate was used. Ensemble methods observe large numbers of particles simultaneously and yield an estimated mean temperature directly, but cannot provide information on the shape or width of the particle temperature distribution. However, it can provide the temperature of particle with large powder feed rate.

Further investigation need to reduce the overall process variability. Variability has been defined as the difference between the maximum and minimum values of the measured response parameters (such as particle temperature, etc.) and normalized to the average value of that parameter.

Acknowledgements

First of all, it is a pleasure to thank Prof. Takayuki Watanabe for giving me the opportunity to do my Ph.D. at the Tokyo Institute of Technology. The excellent working conditions, the topic of my research and the opportunities to participate in several international conferences and meetings were all made available by Pro. Watanabe forming the basis of this work. His research philosophy and methodology give me deep impression. Importantly, I have learnt a lot from him, I am sure, which will be especially useful at my different life stages. I am really grateful for his suggestive and the fruitful discussion.

Secondly, I want to express my gratitude to Dr. Manabu Tanaka, a special assistant professor of the Department of Environmental Chemistry and Engineering, Tokyo Institute of Technology. This work would not exist without his plenty of hard work and persistence. I derived inspiration to pursue research and gained confidence to do Ph.D. from Dr. Manabu Tanaka. He also has enriched all aspects of my experience living in Japan. I cannot express my gratitude in words for him.

I would also like to thank Dr. Sooseok Choi, a special assistant professor of the Department of Environmental Chemistry and Engineering, Tokyo Institute of Technology, who helped me in various ways. He is an academically talented researcher and a very nice person came from Korea. His help suggestion in my experiments and encouragement given to me are memorable.

I want to say my thanks to many professors, colleagues and young researchers at

international conferences. Especially, discussions and interactions with Dr. Masaya Shigeta, Associate Professor of Department of Energy Control Processing, Osaka University, have helped me professionally.

I would like to express my sincere appreciation to Dr. Shintaro Morisada, Associate Professor of the Department of Chemistry and Applied Chemistry, Saga University for his help during his stay in Tokyo Institute of Technology and his encouragements and supports.

It is necessary to mention that my cordial thanks should be given to all the staffs and members of Watanabe lab for their cooperation and help in these four years. Especially, I am grateful to Mr. Feng Liang and Ms. Yingying Chen for enjoying academic researching and daily life together. I am very pleased to express my gratitude to my colleagues, Mr. Yosuke Tsuruoka and Mr. Tomoki Ikeba, for their important roles during my master-doctor period and efforts in my research project.

The financial support from the NEDO is highly acknowledged. Thanks to the collaborative research with Asahi Glass Co., Ltd, I have got chances to learn experience from various people who have a broad knowledge. The continuing private financial support from Tsuji Asia Scholarship Foundation during my doctoral period is greatly appreciated.

Last but not least, I would like to express my deepest appreciation to my father, mother and my sister who live in China for their love, tolerance, understandings and heartfelt support.

January, 2014

Yaping Liu